

DOCTORAL THESIS

Mechanobiological origins of bone porosity and elasticity: An experimental and computational multiscale approach

submitted in satisfaction of the requirements for the degree
Doctor of Science in Civil Engineering
of the Vienna University of Technology, Faculty of Civil Engineering

DISSERTATION

Mechanobiologische Herkunft der Knochen-Porosität und -Elastizität: Ein experimenteller und computergestützter Mehrskalen-Ansatz

ausgeführt zum Zwecke der Erlangung des akademischen Grades eines
Doktors der technischen Wissenschaften
eingereicht an der Technischen Universität Wien, Fakultät für Bauingenieurwesen

von

Dipl.-Ing. **Maria-Ioana Pastrama**
Matrikelnr.: 0827044
Neubaugasse 5/2/18H, 1070 Wien, Österreich

Gutachter:

Univ. Prof. Dipl.-Ing. Dr. techn. **Christian Hellmich**
Institut für Mechanik der Werkstoffe und Strukturen
Technische Universität Wien
Karlsplatz 13/202, 1040 Wien, Österreich

Univ. Prof. Dipl.-Ing. Dr. sc. nat. **Philipp J. Thurner**
Institut für Leichtbau und Struktur-Biomechanik
Technische Universität Wien
Getreidemarkt 9, 1060 Wien, Österreich

Prof. **Hans Van Oosterwyck**
Department of Mechanical Engineering – Biomechanics Section
Katholieke Universiteit Leuven
Celestijnenlaan 300 C, B-3001 Leuven, Belgium

Wien, im November 2016

.....

Abstract

Bone mechanobiology comprises all the processes by which bones “sense” and “react on” mechanical loading, through the corresponding activity of biological cells and biochemical factors. In this context, the transfer of mechanical loads from the macroscopic scale down to the cellular level is governed by the hierarchical interaction of bone, as well as its mechanical properties; thereby, elasticity and porosity play a particularly eminent role. The latter two quantities, shortly reviewed in **Chapter 1**, as well as the interdependencies of these properties and their relationship with bone mechanobiology are investigated in the present thesis, by means of experiments and computer simulations. Notably, both approaches are guided by the concept of multiscale continuum (poro)micromechanics, an essential theoretical framework when dealing with a multiscale, hierarchically structured material such as bone.

In **Chapter 2**, a multiscale mathematical model for simulation of bone remodeling is presented, describing the porosity-specific processes and relationships between bone cells, biochemical factors, and mechanical loads occurring at the level of the vascular and lacunar pores. Particularly, the mechanical stimuli acting on the bone cells involved in bone remodeling are quantified in terms of hydrostatic pore pressures, estimated from the macroscopic loading by means of a continuum (poro)micromechanics representation of bone. The model is then validated quantitatively and qualitatively with experimental data from literature, showing the influence of different mechanical loading conditions on bone adaptation for various animal species.

Chapters 3 and **4** deal with determination of the elastic modulus of bone by means of a new method which, based on the concept of statistical nanoindentation and an evolutionary algorithm, can distinguish between damaged and undamaged material phases – or, more generally, between indents where the elastic half space theory applies, or not (e.g., due to the presence or initiation of microcracks). More precisely, in **Chapter 3**, the elastic modulus of undamaged, cortical bone, at the scale of the extracellular matrix, is determined throughout different plane sections through the midshaft of a human femur, and the differences in stiffness between endosteal and periosteal regions, as well as between loaded and not loaded areas are investigated. In **Chapter 4**, Young’s modulus of intact bovine extracellular femur bone is investigated. In both chapters, the hypothesis that nanoindentation testing may also deliver elasticity values related to damaged material is checked, by imaging microcracks with a Scanning Electron Microscope (SEM).

Finally, in **Chapters 5** and **6**, experimental methods are employed for determination of the mechanical properties of ceramic materials for bone tissue engineering scaffold production, namely baghdadite ($\text{Ca}_3\text{ZrSi}_2\text{O}_9$) and Bioglass[®]. Ideally, such scaffolds should reproduce the properties of bone as closely as possible. In the case of baghdadite, scaffolds seeded with bone cells have shown good biological properties *in vivo*, but research on their mechanical properties are scarce. In **Chapter 5**, by means of statistical nanoindentation combined with ultrasonic tests, the elasticity of porous baghdadite is characterized across a wide range of material porosities. In the case of Bioglass[®] scaffolds, mechanical properties have been measured before, and require improvement in order to come close to those of trabecular bone. The study in **Chapter 6** investigates, by means of multiscale ultrasound-nanoindentation measurements, the possibilities of enhancing the stiffness of these scaffolds by coating them with various types of polymers.

Kurzfassung

Knochen-Mechanobiologie umfasst alle Prozesse, bei denen Knochen durch die Aktivität von Zellen oder biochemischen Faktoren eine mechanische Belastung erfahren. In diesem Sinne ist die Lastübertragung von makroskopischer zu zellulärer Ebene von hierarchischen Knochen-Interaktionen, sowie von mechanischen Eigenschaften geleitet; dabei spielen die Elastizität und die Porosität eine wesentliche Rolle. In dieser Arbeit werden diese beiden Eigenschaften (kurz erläutert in **Kapitel 1**), ihre gegenseitige Abhängigkeit, sowie ihre Zusammenhänge mit Knochen-Mechanobiologie durch Experimente und computergestützte Simulationen untersucht. Beide Vorgehen basieren auf der Theorie der mehrskaligen Kontinuums-(Poro)Mikromechanik, einem wesentlichen Ansatz bei der Untersuchung von mehrskaligen, hierarchisch strukturierten Materialien wie Knochen.

In **Kapitel 2** wird ein mehrskaliges mathematisches Modell für die Simulation von Knochenremodellierung vorgestellt, das die Porosität-spezifischen Prozesse und Zusammenhänge zwischen Zellen, biochemischen Faktoren und mechanischen Belastungen beschreibt, die auf Ebene der vaskularen Poren und Lakunen stattfinden. Die mechanischen Stimuli, die auf die in Knochen-Remodellierung involvierten Zellen wirken, werden als hydrostatische Porendrücke quantifiziert, und von der makroskopischen Belastung mit Hilfe einer kontinuums-(poro)mikromechanischen Darstellung von Knochen berechnet. Das Modell wird anschließend quantitativ und qualitativ mit auf Literatur basierenden experimentellen Werten validiert, die den Einfluss von unterschiedlichen mechanischen Belastungsbedingungen auf Knochenadaptierung für verschiedenartige Tierspezies belegen.

Die **Kapitel 3** und **4** behandeln die Bestimmung des Elastizitätsmoduls von Knochengewebe mittels einer neuen Methode, die – basierend auf dem Konzept der statistischen Nanoindentation und einem evolutionären Algorithmus – zwischen beschädigten und unbeschädigten Materialphasen unterscheiden kann – oder, im Allgemeinen, zwischen Indents, bei denen die Theorie des elastischen Halbraums gültig oder ungültig (z.B. aufgrund existierender oder neugebildeter Mikrorisse) ist. In **Kapitel 3** wird der Elastizitätsmodul von unbeschädigtem menschlichem Femur auf extrazellulärer Ebene bestimmt und an verschiedenen anatomischen Positionen und Belastungsrichtungen verglichen. Die Unterschiede in Steifigkeit zwischen Endost und Periost, sowie zwischen belasteten und unbelasteten Regionen werden untersucht. In **Kapitel 4** wird der Elastizitätsmodul von intaktem Rinder-Femur auf extrazellulärer Ebene ermittelt. In beiden Kapiteln wird die Hypothese, dass Nanoindentations-

Tests auch Elastizitätswerte von beschädigtem Material liefern, durch Abbildung von Mikrorissen mit einem Scanning Electron Microscope (SEM) untersucht.

Schlussendlich werden in den **Kapiteln 5** und **6** experimentelle Methoden zur Bestimmung der mechanischen Eigenschaften von keramischen Materialien für die Produktion von Tissue Engineering Knochengerüsten, Baghdadite ($\text{Ca}_3\text{ZrSi}_2\text{O}_9$) und Bioglass[®], angewandt. Idealerweise sollten diese Gerüste die Eigenschaften von Knochen so genau wie möglich reproduzieren. Für Baghdadite zeigten mit Knochenzellen besetzte Gerüste *in vivo* gute biologische Eigenschaften, jedoch sind ihre mechanischen Eigenschaften kaum erforscht. In **Kapitel 5** wird die Elastizität von Baghdadite unterschiedlicher Porosität mit statistischer Nanoindentation und Ultraschall-Tests charakterisiert. Für Bioglass[®] Gerüste wurden bereits mechanische Eigenschaften gemessen; diese müssen jedoch verbessert werden, um den Eigenschaften von trabekulärem Knochen möglichst genau zu entsprechen. Die Studie in **Kapitel 6** untersucht, wie die Steifigkeit dieser Gerüste durch verschiedene Polymer-Beschichtungen mittels mehrskaliger Ultraschall-Nanoindentations-Messungen verbessert werden kann.

Before 1892, it was often thought that bone architecture was determined by magic or God, we could never understand it, and perhaps it verged on blasphemy to try to understand such handiwork.

Harold M. Frost

Acknowledgements

I would like to thank my supervisor, Christian Hellmich, for his support and inspiration, setting an example for dedication and excellence in science, and giving me the opportunity to participate in conferences and meetings with many brilliant scientists. Further thanks go to Profs. Hans Van Oosterwyck and Philipp Thurner, for taking the time to be reviewers of my thesis; to Stefan Scheiner, for being resourceful with any Matlab or modeling issue I had, and the funny conversations; and to Prof. Peter Pivonka, for his help and advice.

I am very thankful for the support of my colleagues, that were always ready to discuss anything from scientific matters to German grammar to life matters, but also enjoy a nice lunch in the sun or a movie evening. I would especially like to mention the “old-library crew”, Patricia Hasslinger and Aleš Kurfürst, for their kindness and moral support; Markus Königsberger and Luis Zelaya, for their fun company; Hawraa Kariem, for her friendship and patience in answering my many questions; and Romane Blanchard, for being a friend and scientific help both in Vienna and during my stay in Melbourne. My appreciation goes also to Gabriele Ostrowski, Martina Pöll, and Astrid Schuh for always being kind and positive and solving any issue in a matter of minutes.

I am grateful for the support of my parents, who have lived my happy and not-so-happy moments with the same intensity as I have, always encouraging me; and that of my friends, whether they were in Vienna, Bucharest, London, or any other part of the world.

To Maria, who is not around anymore, but whose kind heart continues to guide me.

Finally, to Chris, for understanding, reasoning, and caring.

Contents

1	Introduction	19
1.1	Bone structure	19
1.2	Bone porosity	21
1.3	Bone elasticity	23
1.3.1	Young's modulus	23
1.3.2	Stiffness homogenization	24
1.4	Bone adaptation and mechanobiology	27
1.4.1	Bone modeling	27
1.4.2	Bone remodeling	28
1.4.3	Bone cells and biochemical factors	29
1.4.4	The mechanical usage windows of bone	32
1.4.5	Mechanical stimulus	34
1.4.6	Mathematical modeling of bone (re)modeling	35
1.5	Bone replacement materials	36
1.6	Appendix: Energy considerations for bone adaptation	37
2	Multiscale systems biology of bone, accounting for pore space-specific mechanosensation	42
2.1	Introduction	43
2.2	Multiscale organization of bone remodeling	45
2.3	Mathematical model combining multiscale systems biology with poro-micromechanics	48
2.3.1	Model representation of bone tissue	48
2.3.2	Introduction of pore space-specific concentrations	50
2.3.3	Cell evolution in changing vascular pore space	51
2.3.4	Effects of $TGF\beta$ on osteoblast differentiation and osteoclast apoptosis	52
2.3.5	Mechanical stimulation of osteoblast precursor proliferation	53
2.3.6	Mechanical inhibition of osteoclast precursor differentiation	55
2.4	Model calibration and validation	55

2.4.1	Simulation of bone formation and bone resorption occurring upon loading of mouse tibiae	55
2.4.2	Independent model check: simulation of bone resorption in tibiae of tail-suspended rats	58
2.4.3	Simulation of bone resorption resulting from exposure to microgravity	58
2.5	Parameter studies	60
2.5.1	Study of mechanoregulatory model features	60
2.5.2	Effects of temporary disuse in aging bone	61
2.5.3	Mechanoresponsiveness without osteocytes – example of fish bone	64
2.6	Discussion	66
2.7	Acknowledgements	67
2.8	Appendix A: Abbreviations and nomenclature	67
2.9	Appendix B: Poromicromechanics model	70
2.10	Appendix C: Mass kinetics equations and definition of vascular concentrations of biochemical factors	72
2.11	Appendix D: Parameter values	78
3	Spatial variation of longitudinal and transverse elastic properties in mid femur cortical cross sections, as assessed by statistical nanoindentation	79
3.1	Introduction	80
3.2	Materials and methods	83
3.2.1	Sample preparation	83
3.2.2	Cutting protocol	84
3.2.3	Polishing protocol for nanoindentation	84
3.2.4	Nanoindentation	85
3.2.5	Scanning electron microscopy	87
3.2.6	Statistical tests	88
3.3	Results	88
3.3.1	Longitudinal direction	88
3.3.2	Tangential direction	88
3.4	Discussion	91
3.4.1	Difference between endosteal and periosteal bone stiffness	94
3.4.2	Difference in bone stiffness between the anteroposterior and mediolateral directions	95
3.4.3	Difference in bone stiffness between the longitudinal and tangential directions	95

3.4.4	Difference in extent of damage in the longitudinal and tangential directions	95
3.5	Acknowledgements	96
4	A new nanoindentation protocol for identifying the elasticity of undamaged extracellular bone tissue	97
4.1	Introduction	98
4.2	Materials and methods	100
4.2.1	Sample preparation	100
4.2.2	Roughness determination	101
4.2.3	Nanoindentation	102
4.3	Results	104
4.3.1	Microscopic surface investigation and roughness measurements	104
4.3.2	Undamaged elastic modulus of bovine bone	106
4.4	Discussion	106
4.5	Acknowledgements	108
4.6	Appendix: Abbreviations and nomenclature	109
5	Micro-poro-elasticity of baghdadite-based bone tissue engineering scaffolds: A unifying approach based on ultrasonics, nanoindentation, and homogenization theory	111
5.1	Introduction	112
5.2	Materials and methods	113
5.2.1	Weighing and ultrasonic tests, for porosity and elasticity determination	113
5.2.2	Polycrystal micromechanics – elastic properties of pure (dense) baghdadite	115
5.2.3	Nanoindentation	116
5.3	Results	120
5.3.1	Porosity and elasticity determination	120
5.3.2	Elastic properties of pure (dense) baghdadite	120
5.4	Discussion	126
5.4.1	Simple, but sufficient microelastic representation of porous baghdadite	128
5.4.2	Separation of scales, wavelength, and ultrasonic sample size .	130
5.4.3	Nanoindentation: size effects, damage, and creep	131
5.4.4	Anisotropy effects of single baghdadite crystals	133
5.4.5	Perspectives	134
5.5	Acknowledgements	134
5.6	Appendix: Evolutionary algorithm	134

6	Ultrasonic elasticity determination of 45S5 Bioglass[®]-based scaffolds: Influence of polymer coating and crosslinking treatment	137
6.1	Introduction	138
6.2	Materials and methods	141
6.2.1	Materials	141
6.2.2	Fabrication of Bioglass [®] -based scaffolds	141
6.2.3	Polymer coating procedure	141
6.2.3.1	PHBV coated Bioglass [®] -based scaffolds	142
6.2.3.2	Gelatin coated Bioglass [®] -based scaffolds	142
6.2.3.3	Crosslinked gelatin coated Bioglass [®] -based scaffolds	142
6.2.3.4	Alginate coated Bioglass [®] -based scaffolds	142
6.2.3.5	Crosslinked alginate coated Bioglass [®] -based scaffolds	142
6.2.4	Fabrication of polymer films and Bioglass [®] disk	143
6.2.5	Characterization methods	143
6.2.5.1	Density of polymers and sintered Bioglass [®]	143
6.2.5.2	Density and porosity of scaffolds	143
6.2.5.3	Surface morphology	144
6.2.5.4	Ultrasonic measurement of elastic properties of scaffolds	144
6.2.6	Measurement of elastic modulus of polymers and Bioglass [®] by nanoindentation	145
6.2.7	Statistical analysis	145
6.3	Results	145
6.3.1	Density of polymers and Bioglass [®]	145
6.3.2	Nanoindentation-derived elastic modulus of polymers and sintered Bioglass [®]	146
6.3.3	Structure characterization	146
6.3.4	Ultrasound characterization of scaffolds	147
6.4	Discussion	150
6.5	Conclusions	153
6.6	Acknowledgements	154
7	Conclusions and outlook	155
	Bibliography	158
	Appendix A: Matlab code for simulation of bone remodeling	192
	Appendix B: Matlab code for deconvolution of nanoindentation results with an evolutionary algorithm	220
	Curriculum Vitae	232

List of Figures

1.1	Hierarchical levels of structural organization of the human long bone, reproduced from Hellmich et al. (2004a) and (Fritsch et al., 2009b): (a) Macrostructure: whole bone; (b) Macrostructure: section through long bone; (c) Microstructure: osteons in cortical bone; (d) Microstructure: trabecular struts; (e) Ultrastructure: collagen-rich domains (mineralized fibrils, light areas) and collagen-free domains (extrafibrillar space, dark areas); (f) Molecular level: hydroxyapatite crystals; (g) Molecular level: collagen molecules	20
1.2	Light micrographs of vascular and lacunar porosity in human femur bone: (a) Longitudinal section (100 times magnification); (b) Transversal section (25 times magnification). The images were taken with a Zeiss Imager Z1m light microscope, after polishing the bone samples in preparation for the nanoindentation campaign in Chapter 3	22
1.3	Hierarchical micromechanical model for stiffness homogenization of cortical bone (Morin and Hellmich, 2014): (a) Representative Volume Element (RVE) of molecular collagen; (b) RVE of mineralized fibril; (c) RVE of extrafibrillar space; (d) RVE of extracellular bone matrix – bone ultrastructure; (e) RVE of extravascular bone matrix; (f) RVE of cortical bone	26
1.4	Bone remodeling cells and biochemical factors: an overview of the most important relationships; OBU – uncommitted osteoblast precursors; OBp – committed osteoblast precursors; OBA – active osteoblasts; BLc – bone lining cells; OCY – osteocytes; OCu – uncommitted osteoclast precursors; OCp – committed osteoclast precursors; OCa – active osteoclasts	30
1.5	Bone’s mechanical usage windows after Frost (1992)	33
1.6	(Bi)linear increase of relative endocortical bone formation rate in rats, plotted based on experimental data from Turner et al. (1994a,b, 1995) and Turner (1998)	35

1.7	BTE scaffolds made of the ceramic material baghdadite, tested in Chapter 5 for the mechanical properties of both the macroscopic scaffold structure and the intact baghdadite material at microscopic scale	37
1.8	Model of mechanical usage windows in terms of number of cycles and peak strain magnitude, after Turner and Akhter (1999), for a constant frequency $f = 2 \text{ Hz}$	39
1.9	Graph of the function inside the absolute value in the integral on the right-hand side of Eq. (1.10), necessary for solving the integral on the left-hand side of the respective equation	40
2.1	Hierarchical organization of bone showing the various pore spaces discernible at different observation scales: (a) X-ray image of the proximal part of a human femur; (b) midshaft cross section A-A, showing the cortical shell; (c) left: scanning electron microscopy (SEM), and right: light microscopy images of cortical bone microstructure, showing an osteon with vascular and lacunar pores; (d) computed tomography (CT) image of trabecular bone; (e) a photomicrograph of a single trabecula showing the composition of trabecular bone with vascular and lacunar pores; (f) SEM image of an osteocyte and canaliculi	46
2.2	Micromechanical representation of bone tissue; the microstructure is composed of extravascular bone matrix and vascular pores with diameter d_{vas} , $\mathcal{L}_{\text{bone}} \gg \ell_{\text{macro}} \gg d_{\text{vas}}$; these pores host bone-forming and -resorbing cells at various differentiation stages, stimulated by the vascular pore pressure p_{vas} , as well as by the biochemical factors that act upon them; active osteoblasts and osteoclasts are responsible for forming and resorbing extravascular bone matrix, respectively; the extravascular matrix is composed of extracellular matrix and lacunar pores with diameter d_{lac} , $\ell_{\text{exvas}} \gg d_{\text{lac}}$; these pores host osteocytes, that are stimulated by the lacunar pore pressure p_{lac} , and produce SCLR, which travels to the vascular pore space, where it acts on osteoblast precursor proliferation	49

2.3	(a) Comparison of the model-predicted change in extravascular bone matrix volume fraction, f_{bm} , in the mouse tibia, following compressive loading for 16 days, with the experimental results of Sugiyama et al. (2012); (b) Model simulation of the evolution of the change in f_{bm} over 16 days, loaded with the peak strain values of Sugiyama et al. (2012); (c) Evolution of the mechanical stimulus, normalized with the steady state mechanical stimulus, for a case of disuse (black lines) and one of overuse (blue lines) from the mouse studies in Figure 2.3(b); (d) Evolutions of the vascular active osteoblast and active osteoclast concentrations, normalized with their initial vascular concentrations, for a case of disuse (black lines) and one of overuse (blue lines) from the mouse studies in Figure 2.3(b)	57
2.4	Comparison of model-predicted extravascular bone matrix volume fraction decrease in tibiae of rats with tail-suspension after 6 and 16 days, with experimental data from Laib et al. (2000): dark grey bar – experimental data; light grey bar – model-predicted disuse-related change in f_{bm} , with the same model parameters as in the case of the mouse, see Section 2.4.1	59
2.5	Simulation of decreasing extravascular bone matrix volume fraction arising from spaceflight-induced disuse lasting for 180 days	60
2.6	Parameter studies: Dependence of the relative decrease of the bone matrix volume fraction after 10 days of disuse (black graph) and 100 days of disuse (grey graph) on the resorption factor $k_{\text{OCa}}^{\text{res}}$ and inhibition parameter κ , for (a) cortical bone, with an initial bone matrix volume fraction $f_{\text{bm,ini}} = 0.95$; (b) trabecular bone, with an initial bone matrix volume fraction $f_{\text{bm,ini}} = 0.2$; Dependence of the relative increase in bone matrix volume fraction after 10 days of overuse (black graph) and 100 days of overuse (grey graph) on the formation factor $k_{\text{OBa}}^{\text{form}}$ and anabolic strength parameter $\lambda_{\text{OBp}}^{\text{vas}}$, for (c) cortical bone; (d) trabecular bone; Dependence of the relative increase in bone matrix volume fraction after 10 days of overuse (black graph) and 100 days of overuse (grey graph) on the anabolic strength parameters $\lambda_{\text{OBp}}^{\text{vas}}$ and $\lambda_{\text{WNT/SCLR}}^{\text{vas}}$, for (e) cortical bone; (f) trabecular bone	62
2.7	Effects of five years of disuse, followed by five years of steady-state loading, in aging and non-aging bone: (a) full 10 year time span; (b) zoom into region around five years; (c) zoom in on the last year . . .	63
2.8	(a) Disuse and (b) Overuse simulation in trabecular and cortical bone with and without osteocytes, over a period of ten years	65

3.1	Scheme of sample extraction locations with anatomical and mechanical axes: Blocks were extracted from the right femur of two donors (Donor ID 269 or 275). One sample was extracted from each anatomical location (medial – M; lateral – L; anterior – A; posterior – P) and for each donor two samples were tested by nanoindentation (269-L, 269-P; 275-M, 275-P), first in the proximal-distal (Pr-D or longitudinal) direction; the sample was then rotated and tested either in the mediolateral (M-L) or anteroposterior (A-P) direction, both corresponding to the mechanical tangential direction. In each direction, three zones relative to the bone marrow were tested: endosteal (white), intracortical (light gray), and periosteal (dark gray)	85
3.2	Results of the nanoindentation tests in the longitudinal direction of bone (mean \pm SD): The mean elastic modulus [GPa] obtained by simple averaging characterizes both damaged and undamaged material phases, while the modulus obtained as a mean of the last of n Gaussian distributions characterizes only the undamaged material phase. The deconvolution of the data from samples marked with * resulted in the best fit with only one distribution	89
3.3	1200 nanoindentation tests performed in the longitudinal direction of bone: (a) Histogram of the experimental data for the 400 tests performed in the endosteal zone, and the nine theoretical distributions fitted by means of deconvolution; (b) Histogram of the experimental data for the 400 tests performed in the intracortical zone, and the three fitted distributions; (c) Histogram of the experimental data for the 400 tests performed in the periosteal zone, and the four fitted distributions	90
3.4	SEM image taken during nanoindentation tests in the longitudinal direction, showing cracks in the grid of indents	91
3.5	Results of the nanoindentation tests in the anteroposterior and mediolateral directions of bone (mean \pm SD), both corresponding to the mechanical tangential direction: The mean elastic modulus [GPa] obtained by simple averaging characterizes both damaged and undamaged material phases, while the modulus obtained as a mean of the last of n Gaussian distributions characterizes only the undamaged material phase. The deconvolution of the data of samples marked with * resulted in the best fit with only one distribution	92

3.6	1200 nanoindentation tests performed in the tangential direction of bone: (a) Histogram of the experimental data for the 600 tests performed in the anteroposterior direction, and the two theoretical distributions fitted by means of deconvolution; (b) Histogram of the experimental data for the 600 tests performed in the mediolateral direction, and the fitted distribution	93
4.1	(a) Light micrograph of the surface of Sample 1 (120 min of fine polishing with a 1 μm diamond suspension on a cloth); (b) Light micrograph of the surface of Sample 4 (300 min of fine polishing with a 1 μm diamond suspension on a cloth); the two surfaces show no significant optical differences; (c) A surface topography image of the indented area of Sample 1 generated in the SPM mode for roughness determination, with visible indentation marks	105
4.2	Typical load-displacement curve of non-damaged extracellular bovine bone matrix, delivering, according to Eq. (4.2) and (4.3), an elastic modulus of $E_s = 30.53 \text{ GPa}$ at 250 nm maximal displacement	106
4.3	Probability distribution functions (normalized histogram) of experimental values of elastic moduli obtained by nanoindentation and fitting of the data by means of the sum of five Gaussian distributions, four of them representing damaged material and the last one representing intact extracellular bone matrix	107
4.4	SEM image taken during nanoindentation tests, showing cracks and holes inside the grid of indents	109
5.1	Porosity-stiffness relation for porous baghdadite scaffolds, from optimizing micromechanics model response (Fritsch et al., 2013) for length measuring, weighing, and ultrasonic test results of Table 5.4 and 5.5 (experimental values are discriminated per sample set in the lower inset); this optimization provides elastic properties of pure (dense) baghdadite, and the stiffness increases with decreasing porosity	123
5.2	Histogram of elastic moduli obtained from nanoindentation measurements and representation through contribution of five material phases, the stiffest of which is pure (non-damaged) baghdadite	124
5.3	Experimental CDF obtained by nanoindentation, and the five theoretical Gaussian CDFs obtained by deconvolution according to the statistical nanoindentation method of Constantinides et al. (2006) and Constantinides and Ulm (2007)	125

5.4	Typical load-displacement curve of a non-damaged single crystal of the baghdadite scaffolds, with an obtained elastic modulus of $E_s^{NI} = 124.7$ GPa at 10 mN maximal load	126
5.5	Nanoindentation size effect in baghdadite scaffolds: Young's modulus E_s as a function of indentation depth; experimental results are discriminated for the four investigated load levels	128
5.6	(a) SEM image showing the macropores (black) of the baghdadite scaffolds, with beam- and shell-type structural elements in between (reproduced from (Roohani-Esfahani et al., 2012)); (b) SEM image showing one structural element surrounded by macroporous space; on the surface of the structural element, micropores are seen in black; (c) High resolution SEM image of the baghdadite crystals	129
5.7	(a) Light micrograph of polished sample surface, as prepared for nanoindentation (resin-filled macropores appear black), and (b) zoomed-out Scanning Electron Micrograph of crystalline strut surface; triangles indicate in (a) maximum indentation size; and in (b) mean and minimum indentation sizes	132
5.8	Poroelasticity of porous baghdadite scaffolds: (a) Biot coefficient as a function of porosity; (b) Biot modulus as a function of porosity . . .	135
6.1	Typical load-displacement curves of different polymers used for coating the scaffolds	147
6.2	SEM imgs of (a) uncoated, (b) PHBV coated, (c) gelatin coated, (d) crosslinked gelatin coated, (e) alginate coated, and (f) crosslinked alginate coated Bioglass [®] -based scaffolds	148

List of Tables

2.1	Performed simulations and parameters related to mechanical stimulus, namely steady-state compressive peak strain $-\overline{E^{\text{peak}}}$; steady-state mechanical stimulus related to vascular pressure $\overline{p_{\text{vas}}^{\text{peak}}}$; steady-state mechanical stimulus related to lacunar pressure $\overline{p_{\text{lac}}^{\text{peak}}}$; peak compressive strain range during the simulation $-E^{\text{peak}}$; ratios between steady-state and simulation-related mechanical stimuli, $(\overline{p_{\text{vas}}^{\text{peak}}})/(\overline{p_{\text{vas}}^{\text{peak}}})$ and $(\overline{p_{\text{lac}}^{\text{peak}}})/(\overline{p_{\text{lac}}^{\text{peak}}})$, entering mechanosensitivity Eqs. (2.16) and (2.18); values of $(\overline{p_{\text{vas}}^{\text{peak}}})/(\overline{p_{\text{vas}}^{\text{peak}}})$ and $(\overline{p_{\text{lac}}^{\text{peak}}})/(\overline{p_{\text{lac}}^{\text{peak}}})$ lower than 1 relate to disuse, whereas values higher than 1 relate to overuse	67
2.2	Overview of the values of parameters used as direct input in the model	78
3.1	Summary of the tested samples, the anatomical locations of their extraction, tested anatomical (mechanical) directions and zones, with corresponding number of nanoindentation tests performed	86
4.1	Polishing protocol for sample preparation	101
4.2	Results for different numbers of distributions used to fit the experimental data: mean value of Young's modulus for the distribution corresponding to intact bone material (E_{BT}); standard deviation (σ_{BT}); coefficient of determination (R^2); relative error (e_{rel})	107
5.1	Coefficients a^* and b^* defining linear relation (5.9) between Poisson's ratio of single crystals, ν_s , and polynomial coefficients A_ν , B_ν , C_ν , D_ν and E_ν in porosity-Poisson's ratio relation (5.8)	117
5.2	Polishing protocol with machine PM5 Logitech (Scotland)	118
5.3	Number of nanoindentation measurements per sample and per load .	118
5.4	Weight, dimensions, mass density, and porosity of tested baghdadite samples	121
5.5	Results of ultrasonic tests on baghdadite samples: time of flight t_f , height h_s , wave velocity v , wavelength λ , mass density ρ , and normal stiffness component C_{1111}^{exp}	122

5.6	Porosity and stiffness per sample set: mean values and standard deviations	124
5.7	Superposition results of N_{Gau} Gaussian distributions fitted to the experimental CDF which was obtained from 1750 nanoindentation measurements of baghdadite substrate; values of Young's modulus E_s^{NI} , weighting factor f_j , and the goodness of fit measurements refer to the rightmost distribution	125
5.8	Mean value of indentation depth per load	133
6.1	Density of used polymers and sintered Bioglass [®]	146
6.2	Elastic modulus of different polymers used for coating scaffolds . . .	147
6.3	Characteristics of uncoated and polymer coated Bioglass [®] -based scaffolds: mass (m), diameter (D), height (h), mass density (ρ), and porosity (p)	148
6.4	Time of flight (Δt), signal velocity (v), and wavelength (λ) of the transmitted signal in uncoated and polymer coated Bioglass [®] -based scaffolds	149
6.5	Calculation of the normal stiffness tensor component of overall scaffolds from ultrasonic pulses with 0.1 MHz frequency, with F_1 according to Eq. (6.6)	150
6.6	Volume fraction of pores (f_{pore}), Bioglass [®] (f_{Bioglass}), and polymer coating (f_{polymer}) in the scaffolds	153

Introduction

1.1 Bone structure

Bone is one of the most versatile biomaterials and a complex living tissue, with numerous functions: not only does the skeleton provide a framework for muscle attachment and protection of the internal organs, but bone also plays a major role in the formation of blood cells (hematopoiesis) and in mineral storage, and it is considered an important element of the immune system.

Bone is a hierarchically built material, revealing different elements and compositions at different length scales, from trabecular or cortical structures at the macroscopic level, to collagen fibrils and hydroxyapatite crystals at the nanoscale. The accurate description of the organizational levels of this structure plays a major role in understanding the mechanical, biological and functional properties of the tissue. The following five levels of the hierarchical organization of bone can be distinguished at different length scales (Katz et al., 1984; Weiner and Wagner, 1998), as shown in Figure 1.1, and shall be considered in the current work:

- The **macrostructural** level, on an observation scale from several mm to several cm, on which the size, shape and type of bone (cortical or trabecular) are described, see Figure 1.1(a) and (b);
- The **microstructural** level, on an observation scale of several hundreds of μm to several mm, on which osteons – cylindrical bone units surrounding vascular pores – or trabecular struts can be observed in case of cortical or trabecular bone, respectively (Figure 1.1(c) and (d));
- The **ultrastructural** level, on an observation scale of several μm , represented by the material building up osteons and trabeculae, see Figure 1.1(e);
- **Collagen-rich** and **collagen-free** domains can be identified within the ultra-

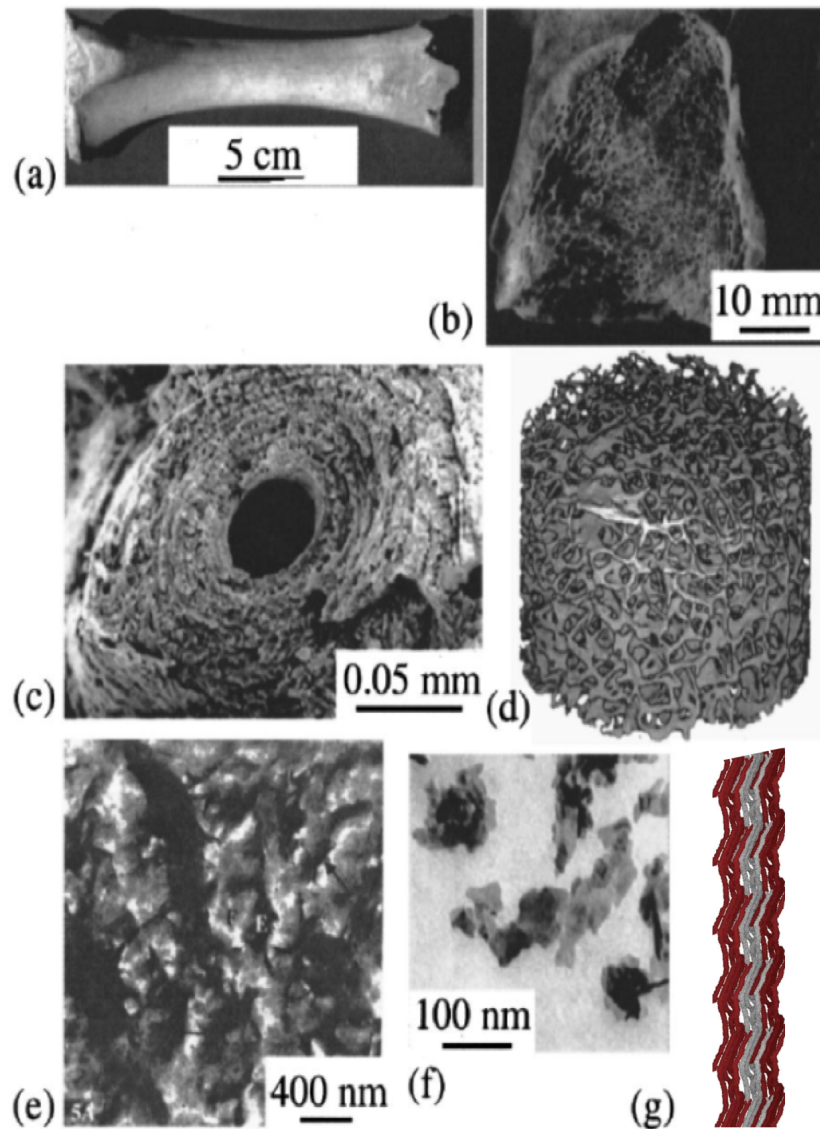


Figure 1.1: Hierarchical levels of structural organization of the human long bone, reproduced from Hellmich et al. (2004a) and (Fritsch et al., 2009b): (a) Macrostructure: whole bone; (b) Macrostructure: section through long bone; (c) Microstructure: osteons in cortical bone; (d) Microstructure: trabecular struts; (e) Ultrastructure: collagen-rich domains (mineralized fibrils, light areas) and collagen-free domains (extrafibrillar space, dark areas); (f) Molecular level: hydroxyapatite crystals; (g) Molecular level: collagen molecules

structure, at the scale of several hundreds of nanometers, see light and dark areas in Figure 1.1(e), respectively. The former represent mineralized fibrils, while the latter represent an extrafibrillar mineral foam or the extrafibrillar

space (Fritsch and Hellmich, 2007);

- The **molecular** level, on which the elementary components of bone can be distinguished, namely: (i) Hydroxyapatite (HA; $\text{Ca}_{10}[\text{PO}_4]_6[\text{OH}]_2$), organized as plate- or needle-shaped mineral crystals with a typical thickness of 1–5 nm and length of 25–50 nm (Weiner and Wagner, 1998) (Figure 1.1(f)); (ii) Collagen, appearing as long, cylindrical molecules with a diameter of about 1.2 nm and a length of about 300 nm (Lees, 1987), self-assembled in staggered stacks (fibrils) with characteristic diameters of 50–500 nm (Cusack and Miller, 1979; Miller, 1984; Lees et al., 1990, 1994; Probst and Lees, 1996; Weiner et al., 1997; Rho et al., 1998; Weiner and Wagner, 1998) (Figure 1.1(g)); (iii) Other organic components, such as lipids or proteoglycans (Urist et al., 1983; Hunter et al., 1996); and (iv) water.

1.2 Bone porosity

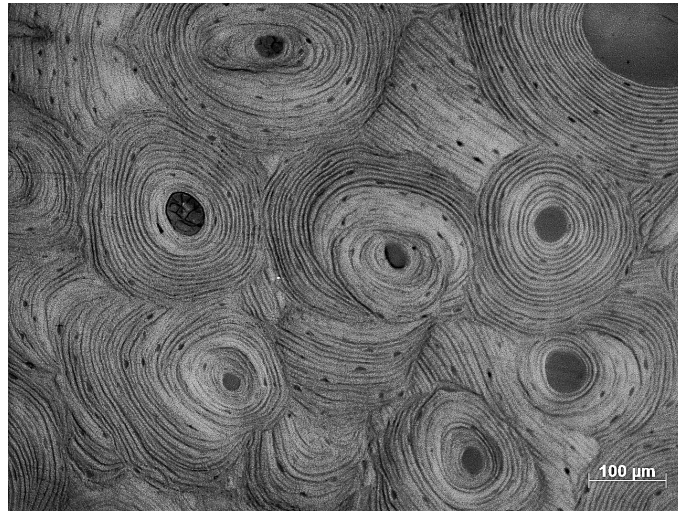
Bone has a complex network of canals, vascular pores, lacunae and canaliculi; taken together, the surface of all these forms of porosity is 100 times larger than the combined inner and outer surface of mature cortical bone (Buckwalter et al., 1995a). The formation of this porosity is a result of the bone modeling and remodeling processes, described in more detail in Chapter 1.4. Through modeling, bones are formed, with their primary porosity, which develops into primary osteons; through remodeling, secondary osteons are built by resorption and circumferential deposition of new bone lamellae in the resulting resorption spaces.

The following forms of bone porosity, visible in longitudinal and transverse cross-section in the light micrographs of Figure 1.2, are relevant for the current work:

- The **vascular pores**, with characteristic diameters of 10–100 μm , host blood vessels, lymphatic vessels and occasionally nerves, as well as remodeling-related bone cells (Buckwalter et al., 1995a), and form a branching structure. The main branches, which run longitudinally through the bone cortex, are often called Haversian canals, and they are connected with each other by obliquely running Volkmann canals;
- The **lacunar pores** have typical diameters of the order of 0.1–1 μm (Gardinier et al., 2010), and each of them hosts an osteocyte, which, in turn, is connected with its neighbouring osteocytes via small channels called **canaliculi**. The latter, with typical diameters between 100–500 nm and length of 35 μm , extend radially from the vascular pore in an apparently regular striped pattern with an interval of 125 nm (Reilly et al., 2001), and contain cell processes of osteocytes.

Especially in the rather dense cortical bone, where diffusion of nutrients from the blood vessels is limited, cells depend on the canaliculi for delivery of such nutrients (Buckwalter et al., 1995a).

(a)



(b)

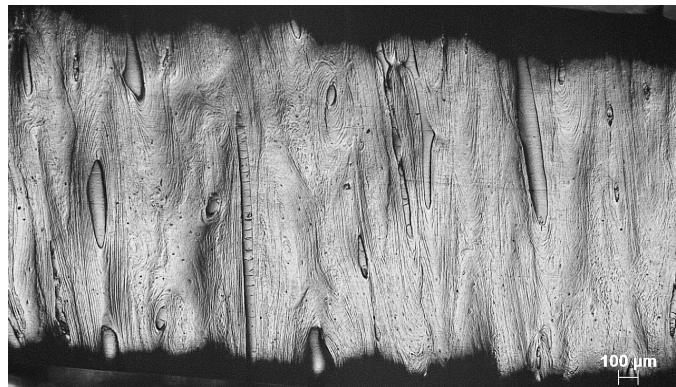


Figure 1.2: Light micrographs of vascular and lacunar porosity in human femur bone: (a) Longitudinal section (100 times magnification); (b) Transversal section (25 times magnification). The images were taken with a Zeiss Imager Z1m light microscope, after polishing the bone samples in preparation for the nanoindentation campaign in Chapter 3

The vascular porosity can be determined using methods such as Archimede's method for density measurement, porosimetry, microradiographs or microCT (Cooper et al., 2003). The values of the vascular porosity for animal cortical bone range from 3 % under normal conditions to 35 % in case of disease or drug treatment (see Fritsch and Hellmich (2007) for a collection of values gathered from literature, for different

species). In humans, Sietsema (1995) reports average cortical porosities of 4.2% and 5% under physiological conditions in two control groups of healthy subjects, as compared with subjects with different diseases, for which this value can be as high as 14%; while Cooper et al. (2007) show that the vascular porosity increases with the age of the individual and may reach up to 35% at age 90. In trabecular bone, the vascular or inter-trabecular porosities range between 50% and 90% (Buckwalter et al., 1995b). This porosity increases with age due to a decrease in the bone volume fraction (BV/TV), trabecular thickness and number, or an increase in trabecular separation (Chen et al., 2010).

The lacunar porosity at the level of the bone matrix without vascular pores (or extravascular matrix) has been shown to amount to about 10% (Tai et al., 2008), and to decrease with age. This happens as a consequence of increased osteocyte apoptosis in older subjects, and a subsequent hypermineralization of the osteocyte lacunae, which leads to occlusion of this porosity (Busse et al., 2010).

Generally, the porosity of a material has a large influence on its mechanical properties, as revealed by the relationship between the stiffness and porosity of the bone replacement material baghdadite in the experimental study in Chapter 5. This is also the case for bone, if we consider that mechanical properties of the bone matrix such as Young's modulus (dealt with in Chapters 3 and 4) are much larger than those of the macroscopic material, including porosity. Additionally, the network of canals and lacunae in bone form a space where macroscopic deformation by mechanical loads causes an increase in the pore fluid pressures, shown in Chapter 2 to have the potential of regulating mechanobiological processes in bone, such as (re)modeling.

1.3 Bone elasticity

1.3.1 Young's modulus

For bone, Young's modulus of elasticity is one of the most important mechanical properties, as it provides information about the behaviour of the material's structures under physiological or less physiological loading conditions (Turner and Burr, 1993). Young's modulus defines a relationship between stresses applied to a material sample and the strains they cause, and it is related to the portion of elastic energy stored in the investigated material, which is fully recovered in form of efficient mechanical work upon sample unloading.

Considering this latter, thermodynamical approach to understanding the elastic modulus (Salençon, 2001), it becomes clear that this quantity should be derived from the unloading rather than the loading curve during loading-unloading mechanical tests. However, many authors report elastic moduli obtained from the "linear

portion” of the loading stress-strain curve (Keller, 1994; Vuola et al., 1998; Chu et al., 2002; Charles-Harris et al., 2007), and these moduli might actually also contain information on inelastic, most probably plastic, deformation events. On the other hand, the unloading curve has been known to deliver “true” Young’s moduli, and for this reason it has also been applied in the evaluation of nanoindentation tests over the past two decades.

The nanoindentation technique, a method made famous by the work of Oliver and Pharr (1992), has been used in the present work to determine Young’s modulus of human femur bone (Chapter 3), of bovine femur bone (Chapter 4) and of bone replacement materials (Chapters 5 and 6). Alternatively, ultrasonic testing has also been used herein for determination of the elasticity of the bone replacement materials baghdadite (Chapter 5) and Bioglass[®] (Chapter 6). Although this method delivers one component of the stiffness tensor of the material (rather than Young’s modulus), e.g., the normal component C_{1111} in case of longitudinal waves, for isotropic linear elastic materials the corresponding elastic modulus E can be derived from the straightforward relationship

$$C_{1111} = \frac{E \times (1 - \nu)}{(1 + \nu) \times (1 - 2\nu)}, \quad (1.1)$$

ν being Poisson’s ratio of the respective material. In case of a non-isotropic linear elastic material, if all the components of the 6×6 stiffness tensor \mathbb{C} are known, then the following formulae allow for derivation of Young’s modulus in direction i without knowledge of Poisson’s ratio:

$$\mathbb{D} = \mathbb{C}^{-1} \quad \text{and} \quad E_i = \frac{1}{D_{iiii}}, \quad i \in \{1, 2, 3\}, \quad (1.2)$$

where \mathbb{D} is called the compliance matrix of the material. Theoretical concepts for the nanoindentation and ultrasound methods for elasticity measurement are detailed in the corresponding chapters.

1.3.2 Stiffness homogenization

As mentioned in Chapter 1.1, bone reveals different material components and structures depending on the considered length scale, and therefore the characterization of its mechanical properties always needs to be defined length-scale specific. Research into continuum micromechanics of bone has led to the establishment of a way to predict the stiffness tensor of bone material at different length scales from the material’s hierarchical microstructure and composition (Hellmich and Ulm, 2002; Hellmich et al., 2004a; Fritsch and Hellmich, 2007) and, recently, a 6-step homogenization model based on the bone microstructure presented in Chapter 1.1 has been

developed (Morin and Hellmich, 2014). At each length scale, the model is based on the description of a Representative Volume Element (RVE) – a subvolume of material, statistically representative for the latter, that is smaller than the macroscopic structural dimensions, yet sufficiently large to contain enough information on the microstructure, i.e. to include a large number of the material’s microheterogeneities (Zaoui, 2002). These relationships need to fulfil the so-called separation of scales condition, explained in more detail in Chapters 2, 5, and 6.

The homogenization model and the RVEs defined at each length scale, as illustrated in Figure 1.3, can be summarized as follows:

- a) The RVE “wet collagen” is composed of the phase intermolecular space embedded as cylindrical inclusions in a matrix of crosslinked collagen molecules (Figure 1.3a);
- b) The RVE “fibril” is composed of the mixed phases hydroxyapatite, with a spherical shape, and the collagen from a), of cylindrical shape (Figure 1.3b);
- c) The RVE “extrafibrillar space” is composed of the mixed phases hydroxyapatite and intercrystalline space, of cylindrical and spherical shape, respectively (Figure 1.3c);
- d) The RVE “extracellular bone matrix” is composed of the mixed cylindrical-shaped phases collagen fibrils from b) and extrafibrillar space from c) (Figure 1.3d);
- e) The RVE “extravascular bone matrix” is composed of the extracellular matrix from d) with spherical inclusions of lacunar pores (Figure 1.3e);
- f) The RVE “cortical or trabecular bone” is composed of the extravascular matrix from e) with cylindrical inclusions of vascular pores (Figure 1.3f).

The estimation of the homogenized stiffness of the corresponding RVE follows from the morphological and compositional information of the constitutive phases, by applying the Eshelby matrix-inclusion problem (Eshelby, 1957):

$$\mathbb{C}^{\text{hom}} = \sum_r f_r \mathbb{C}_r : [\mathbb{I} + \mathbb{P}_r^0 : (\mathbb{C}_r - \mathbb{C}^0)]^{-1} : \left\{ \sum_s f_s [\mathbb{I} + \mathbb{P}_s^0 : (\mathbb{C}_s - \mathbb{C}^0)]^{-1} \right\}^{-1}, \quad (1.3)$$

where \mathbb{C}_r is the stiffness of phase r , f_r its volume fraction, “:” represents the tensorial operation double contraction, \mathbb{I} the fourth-order unity tensor, and \mathbb{P}_r^0 the fourth-order Hill tensor, accounting for phase morphology. The latter depends on the shape of the inclusion (in terms of aspect and slenderness ratios), as well as on \mathbb{C}^0 – the stiffness of the embedding matrix, revealing information on the interaction between

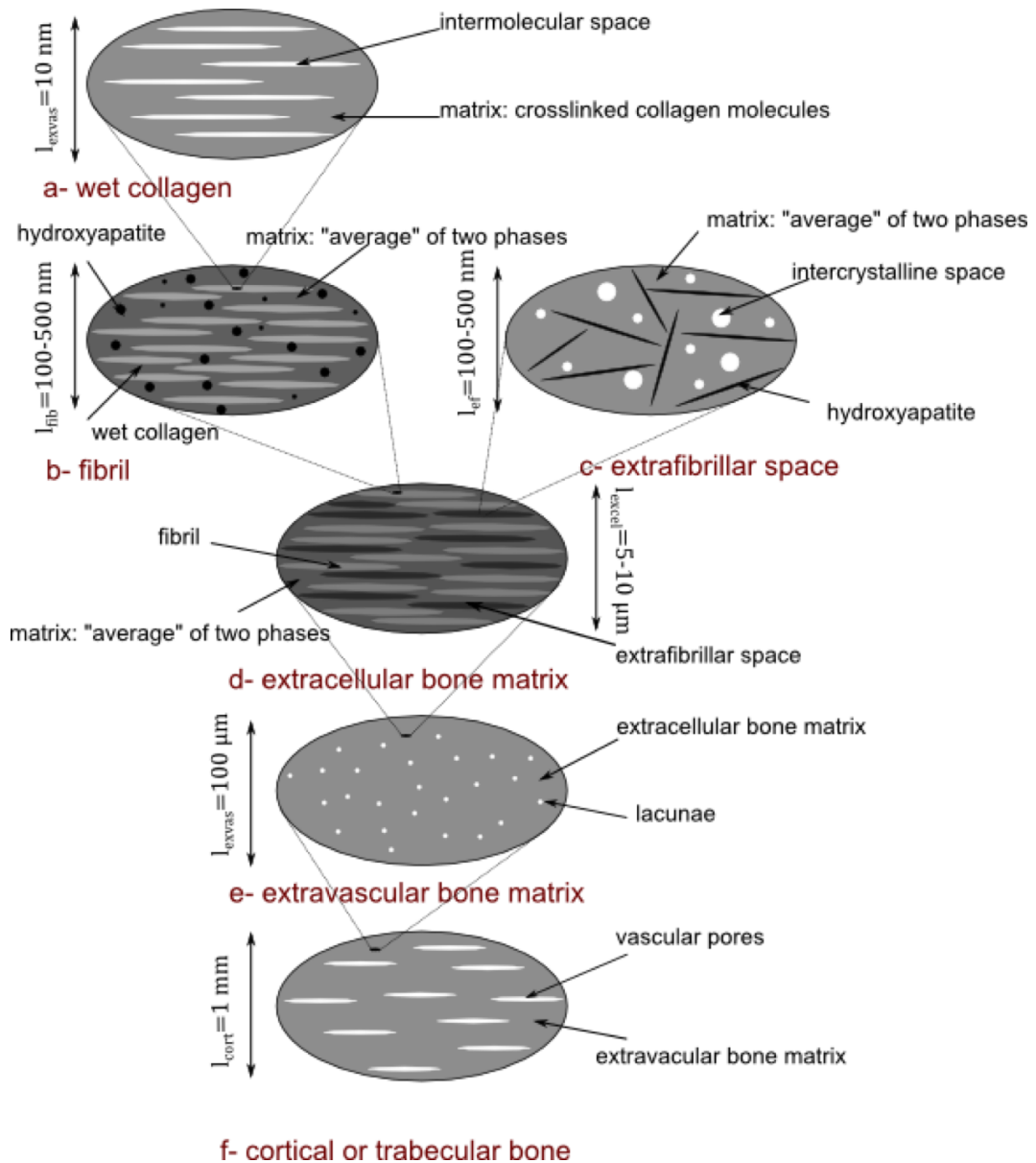


Figure 1.3: Hierarchical micromechanical model for stiffness homogenization of cortical bone (Morin and Hellmich, 2014): (a) Representative Volume Element (RVE) of molecular collagen; (b) RVE of mineralized fibril; (c) RVE of extrafibrillar space; (d) RVE of extracellular bone matrix – bone ultrastructure; (e) RVE of extravascular bone matrix; (f) RVE of cortical bone

the phases. If the material RVE is represented by a matrix with inclusions (composite material), as is the case for RVEs “wet collagen”, “extravascular bone matrix” and “cortical or trabecular bone” above, then \mathbb{C}^0 is the matrix stiffness, $\mathbb{C}^0 = \mathbb{c}_r$ with $r = m$, and a Mori-Tanaka homogenization scheme is applied (Mori and Tanaka, 1973). If the material RVE is best represented as a polycrystal, i.e., there is an intimate mixing of phases, as for RVEs “fibril”, “extrafibrillar space” and “extracellular bone matrix”, then \mathbb{C}^0 is the homogenized stiffness itself, $\mathbb{C}^0 = \mathbb{C}^{\text{hom}}$, and the homogenization follows a self-consistent scheme (Hershey, 1954; Hill, 1963).

By applying this homogenization technique starting from the level of wet collagen in Figure 1.3, and up-scaling to the next length scale, the homogenized stiffness of the macroscopic piece of cortical or trabecular bone can be step-wise estimated.

1.4 Bone adaptation and mechanobiology

One of the most fascinating properties of bone is the mechanism by which its architecture is modulated and optimized. Before 1892, this property was thought to be “determined by magic or God” and thus not accessible to human understanding (Frost, 1998); afterwards, Wolff (1892) showed that bone has the ability to adapt its structure and composition to the mechanical loads it is subjected to. Later on, Frost (1964b) introduced the “mechanostat”, a concept explaining bone adaptation to mechanical loads, and went beyond acknowledging this adaptation ability of bone, to describing it from a mechanical, physiological, and biological point of view.

According to the famous work of Frost, bone has two mechanisms by which skeletal formation or tissue renewal may be achieved (Frost, 1992). The first one is bone modeling, the second is remodeling, and both shall be shortly presented in the following subchapters.

1.4.1 Bone modeling

Bone modeling occurs mostly during growth, and consists of changes in the shape, size, strength, anatomy or position in tissue space of bone cross-sections, so as to optimize bone geometry while the organ grows. This is achieved either by bone-forming cells (osteoblasts) in “formation drifts”, that deposit bone, or by osteoclasts, that resorb bone in “resorption drifts” – i.e., according to Frost, in bone modeling, formation and resorption may both occur, but uncoupled and not at the same location.

After reaching skeletal maturity, bone modeling happens relatively rarely, and it takes the form of modulation of the bone architecture and mass when the mechanical loading conditions change dramatically. Then, it is rather trabecular bone being modeled, where resorption or formation may lead to thinning or thickening of the

trabeculae, respectively. In cortical bone, formation and resorption occur mostly endocortically and periosteally, but not on Haversian surfaces. Cancellous bone responds faster to changes in mechanical loads than cortical bone; therefore, in the case of e.g., disuse, resorption of trabeculae might be seen before an increase of cortical porosity (Buckwalter et al., 1995a).

Many studies have shown bone formation, i.e., modeling due to an increased mechanical environment, illustrated through e.g., increase in trabecular BV/TV (bone volume/total volume) and trabecular number, as well as thickening of trabeculae in sheep femura (Rubin et al., 2002a,b) following one year of low magnitude, high frequency vibration treatment; increased cortical bone area in tibiae of athletes subjected to various exercises involving ground impact (Nikander et al., 2010), or in tibiae and radii of female weightlifters (Heinonen et al., 2002); increased strength in rat radius following daily compressive loading (Robling et al., 2002); periosteal new bone formation in rats following ulna loading (Hsieh and Turner, 2001); endocortical new bone formation in rat tibia following mechanical bending (Turner et al., 1994b). Some of these results, along with others, were used as experimental validation of the model presented in Chapter 2.

However, it seems that, during high mechanical loading, resorption drifts are not completely “off” in terms of Frost, but simply the probability of bone resorption is much lower than that of formation, while in the case of very reduced mechanical loading the opposite is the case (Schulte et al., 2013). Therefore, it may be that even in bone modeling, formation and resorption take place simultaneously, but one of them takes over and dominates the other, depending on the mechanical environment.

1.4.2 Bone remodeling

The second mechanism described by Frost is bone remodeling, a process occurring throughout the whole life of vertebrates, which involves simultaneous or coupled bone resorption and formation. This is achieved by “teams” of bone-forming and bone-resorbing cells working together in the vascular space, collectively called Basic Multicellular Units (BMUs) – the primary functional units for bone remodeling (Frost, 1964a). New stem cells are constantly provided to the BMU by a capillary inside the unit, growing at the same rate as the latter progresses, and these cells differentiate to active osteoclasts and osteoblasts which attach to the vascular pore walls once the remodeling is initiated (Buenzli et al., 2011). The front region of a BMU is lined with osteoclasts which excavate tunnels typically 250–300 μm in diameter in the bone matrix (Robling et al., 2006), while the back region is made up of osteoblasts, which deposit unmineralized bone matrix or osteoid in order to fill these cavities. When deposition is stopped, a Haversian canal is left in the center of the

newly formed (“secondary”) osteon.

In the case of healthy bone, resorption and formation are balanced, meaning the amount of old bone removed and new bone rebuilt in the remodeling cycle are equal. In disease states, however, bone balance can vary. For instance, osteoporotic patients have a negative bone balance, i.e., more bone is resorbed than is replaced by the BMUs, leading to an increase in bone porosity and a higher risk of fragility fractures.

1.4.3 Bone cells and biochemical factors

The bone modeling and remodeling processes are accomplished by osteoblasts and osteoclasts at various levels of differentiation, see Figure 1.4, distinguishable by morphology, as well by the level-specific set of markers they express.

Although some authors have reported as many as seven stages of osteoblast differentiation (Aubin, 1998), literature generally accepts the following stages for these mononucleated bone-forming cells:

- **Uncommitted osteoblast precursors**, representing mesenchymal stem cells which have the potential to develop into osteoblasts at a later stage, once they are stimulated to differentiate through release of various growth factors. They have an irregular shape and reside in the bone canals, endosteum, periosteum, bone marrow or blood (Buckwalter et al., 1995a);
- **Committed osteoblast precursors**, progenitor cells restricted to osteoblast development;
- **Active osteoblasts**, mature cells responsible for bone formation via synthesis and secretion of bone organic matrix. They line the surface of trabeculae or the inner walls of vascular pores, and have a rounded, oval form;
- **Bone lining cells**, resting or “old”, inactive osteoblasts that become flat or pancake-shaped after ceasing their activity. They lie directly against the bone matrix, contain gap junction connections to osteocytes and osteoblasts, and have been shown to respond to mechanical stimuli *in vivo* (Robling et al., 2006). Additionally, they regulate passage of calcium into and out of the bone, and respond to hormones such as PTH by secreting special enzymes that activate osteoclasts;
- **Osteocytes**, terminally differentiated osteoblasts residing in the bone lacunae, ellipsoidal in shape, and thought to respond to mechanical load via their cell bodies, dendritic processes or bending of cilia (Bonewald, 2011).

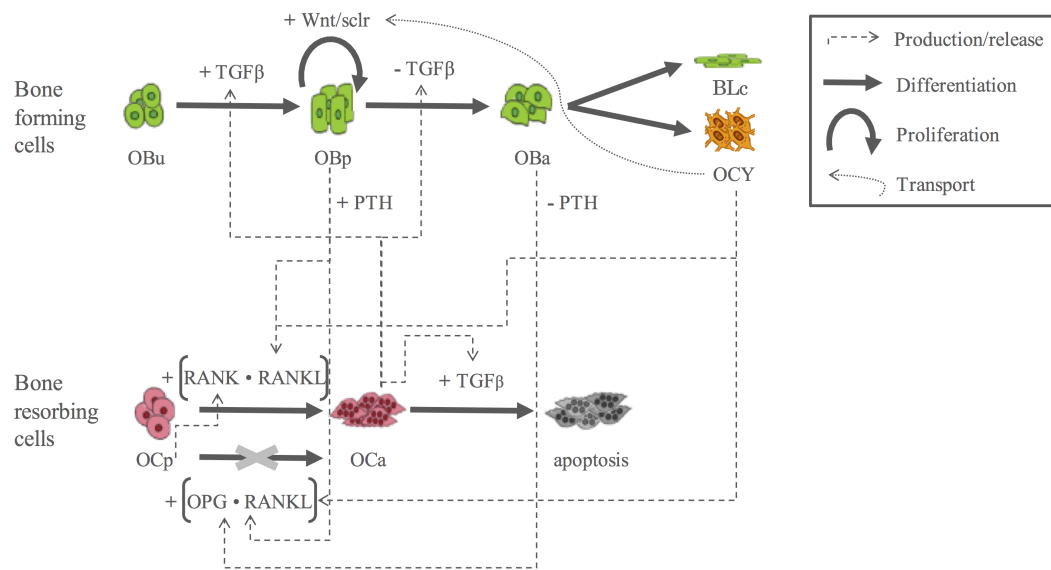


Figure 1.4: Bone remodeling cells and biochemical factors: an overview of the most important relationships; OBU – uncommitted osteoblast precursors; OBp – committed osteoblast precursors; OBa – active osteoblasts; BLc – bone lining cells; OCY – osteocytes; OCu – uncommitted osteoclast precursors; OCp – committed osteoclast precursors; OCa – active osteoclasts

It is noteworthy that the latter type of cells, osteocytes, are thought to play the most important role in bone (re)modeling. Representing 90–95% of all cells in adult bone, they are the longest lived of all of them (Bonewald, 2011), and have long processes that branch through canaliculi, thus forming a dense network, through which they communicate with each other and with other bone cells. As they support both osteoblast and osteoclast differentiation to the active cells initiating bone formation and resorption, osteocytes are sometimes considered the sole “orchestrators” of bone remodeling (Bonewald, 2011; O’Brien et al., 2013; Bellido, 2014). On the one hand, they express sclerostin, an antagonist of the Wnt/ β -catenin pathway, the latter promoting osteoblastic proliferation and differentiation. Mechanical loading reduces sclerostin expression and, thus, releases the osteoblast inhibition, leading to increased osteoblast activity via osteocytes (Robling et al., 2006; Bonewald, 2011). On the other hand, both healthy and dying osteocytes can recruit osteoclasts at the site of bone remodeling by sending signals of bone resorption (Bonewald, 2011).

Osteoclasts are multinucleated bone-resorbing cells, having three to twenty nuclei (Buckwalter et al., 1995a), with the following developmental stages, as reported by Roodman (1999):

- **Uncommitted osteoclast precursors**, hematopoietic stem cells which may be found in the bone marrow or in the circulating blood;

- **Committed osteoclast precursors**, more differentiated cells committed to the osteoclast lineage;
- **Active osteoclasts**, mature cells responsible for bone resorption. With their ruffled border, they attach themselves to the surface of the bone, dissolving the bone matrix and releasing bone mineral into the extracellular space.

The biochemical regulatory mechanisms for bone remodeling are very complex, but the main factors involved, depicted in Figure 1.4 together with the above-mentioned cell differentiation stages and the relationships between them, are the following:

- **Transforming growth factor β** , abbreviated to **TGF β** , is released by osteoclasts during bone resorption (Bonewald and Dallas, 1994) or secreted by osteocytes (Heino et al., 2002). This factor promotes differentiation of uncommitted osteoblast progenitor cells to committed osteoblast precursors, inhibits the further differentiation of osteoblast precursor cells to active osteoblasts, and promotes active osteoclast apoptosis (Bonewald and Dallas, 1994; Mundy et al., 1996; Greenfield et al., 1999; Roodman, 1999; Alliston et al., 2001);
- **Receptor activator of nuclear factor kappa-B (RANK)** is expressed at the surface of osteoclast progenitor cells and mature osteoclasts (Nakagawa et al., 1998; Kartsogiannis et al., 1999). Binding of RANK to its ligand, **RANKL**, expressed by osteoblast progenitors and, to a very large extent, also by osteocytes (Nakashima et al., 2011), up-regulates differentiation of osteoclast precursor cells to active osteoclasts (Boyce and Xing, 2008);
- **Osteoprotegerin (OPG)** is a protein secreted by active osteoblasts (Boyce and Xing, 2008) but also osteocytes (Bellido, 2014). It is known to act as a decoy ligand, also binding to RANKL, thereby preventing the RANK-RANKL binding (Martin, 2004) and, consequently, down-regulating differentiation of osteoclast precursor cells to active osteoclasts (Lacey et al., 1998; Nakagawa et al., 1998);
- **Parathyroid hormone (PTH)** up-regulates the maximum number of RANKL molecules and inhibits production of OPG, thus indirectly activating osteoclast precursor differentiation (Kroll, 2000);
- **Sclerostin**, produced by osteocytes in the lacunar pore space, is transported via canaliculi to the vascular pore space, where it acts on Wnt, thus indirectly regulating osteoblast precursor proliferation (Westendorf et al., 2004; Gaur et al., 2005).

The RANK-RANKL-OPG signalling pathway has a major influence on three main biological systems (Theoleyre et al., 2004): (i) the vascular system, (ii) the immune system, and (iii) the osteoarticular (bone) system. Nevertheless, studies have shown this triad to also play a role in nephrology (Klejna et al., 2009), or heart failure (Ueland et al., 2005). It was hypothesized that the expression of RANKL in cells of very diverse origins (lymphocytes, monocytes, endothelial cells, mammary epithelial cells, etc.) may influence cell survival and participate in the control of apoptosis, an essential process in such events as embryonic development, normal cell turnover, metamorphosis, and hormone-induced tissue involution (Kartsogiannis et al., 1999). The RANK-RANKL-OPG triad can, therefore, be considered a “universal” tuning mechanism *in vivo*, the equilibrium of its components ensuring the good functioning of the systems in which it is involved.

In the context of the bone system, the discovery of this triad was essential for the understanding of the regulatory mechanisms of bone remodeling. The equilibrium of the three factors is essential for a balance between bone resorption and formation: decreased expression of OPG can lead to excessive osteoclast activity and, therefore, to excessive resorption and osteoporosis, while excessive production of OPG can inhibit resorption to such an extent that it leads to osteopetrosis (Simonet et al., 1997).

1.4.4 The mechanical usage windows of bone

One of the main ideas of Frost’s “mechanostat” is that, in the process of bone adaptation, the peak mechanical strains influence and guide the activity of non-mechanical factors such as cells, cell-cell interactions, biochemical factors, hormones, DNA, RNA etc. (Frost, 1998). Particularly, there are certain strain thresholds and strain intervals that activate or de-activate these non-mechanical elements, and regulate how and where they act.

Frost postulated that bone’s biologic responses to mechanical stimuli may be divided into four windows, depending on the peak strains acting on the organ (Frost, 1992). The latter are defined in relation to bone’s fracture strain (a measure of its ultimate strength), considered to be $25000 \mu\epsilon$ (microstrains), corresponding to a deformation of 2.5%. These windows, shown in Figure 1.5, with their corresponding thresholds or MES (minimum effective strain), can be described as follows:

- The **disuse window**, between approximately $50 - 100 \mu\epsilon$, with a remodeling threshold MES_r , is characterized by increased disuse-induced bone remodeling and resorption, as is the case e.g., in spaceflight or prolonged bedrest. As this strain range is well below the physiological one, the bone biology “seems

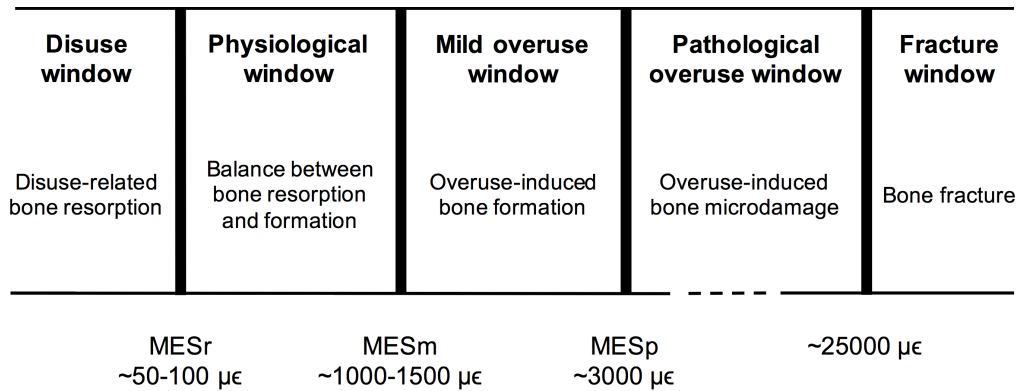


Figure 1.5: Bone’s mechanical usage windows after Frost (1992)

to perceive too much bone for its mechanical usage so it makes remodeling remove the excess bone” (Frost, 1992);

- The **adapted window**, in a range of approximately 100–1500 $\mu\epsilon$, corresponds to every day, physiological loading for healthy adult mammals, implies no increase or decrease in bone mass, and maintains a balance between resorption and formation. This is the range for which bone is adapted to its mechanical stimuli and does not need to change its architecture;
- The **mild overuse window**, between 1500–3000 $\mu\epsilon$, with a modeling threshold MESm of about 1500 $\mu\epsilon$, is typical for increased mechanical stimuli that do not yet cause damage, but may lead to bone modeling, reshaping, and increased bone formation;
- The **pathological overuse window**, with loading exceeding the threshold MESp of 3000 $\mu\epsilon$, is characterized by increased microdamage formation and, in extreme cases, microdamage accumulation that may lead to bone failure.

Although many authors agree with the general concept of Frost’s mechanostat and with the values of the above described mechanical usage windows, some have falsified the theory that a bone adapted window or “lazy zone” exists (Rubin and Lanyon, 1985; Sugiyama et al., 2012; Schulte et al., 2013). Moreover, some showed experimentally that rat or mouse bone has a modeling threshold of about 1000 $\mu\epsilon$, above which increased bone formation occurs, but that below this value bone is resorbed (Rubin and Lanyon, 1985; Sugiyama et al., 2012). More rarely, no significant change in bone mass was shown below 1000 $\mu\epsilon$, leaving open the question of the existence of an adapted window (Turner et al., 1994b).

1.4.5 Mechanical stimulus

It has been often confirmed experimentally, in the line of Frost, that the peak strain to which a piece of bone is subjected can drive bone adaptation (Rubin and Lanyon, 1985; Frost, 1992; Hsieh et al., 2001; Brodt and Silva, 2010). However, other experiments revealed that bone formation is influenced, besides peak strains, by such factors as strain frequency (Turner et al., 1994a; Hsieh and Turner, 2001; Rubin et al., 2001; Judex et al., 2007), number of loading cycles (Umemura et al., 1997), strain rate (Mosley and Lanyon, 1982; Frost, 1992; Forwood and Turner, 1995), duration and amplitude of the dynamic portion of applied loads (Forwood and Turner, 1995), strain gradients (Frost, 1992), or novelty of the stimulus (Skerry and Lanyon, 1995).

During the endeavours to define a mechanical stimulus driving bone adaptation/remodeling in Chapter 2, that potentially incorporates all or some of the above factors, based on a formulation presented by Turner and Akhter (1999) it was initially hypothesized that this stimulus could be the *change* in energy throughout the bone loading history. After several calculations, presented in detail in Chapter 1.6, it was found that the energy change depends on the *square* of the peak strain, while many experiments have shown that bone formation increases *linearly* with mechanical stimulus (Rubin and Lanyon, 1985; Turner et al., 1994a; Sugiyama et al., 2012).

In-depth studies by Charles Turner and colleagues have identified peak strain and strain frequency as the essential factors driving bone formation, leading to the definition of the mechanical stimulus as the product of these parameters (Turner, 1998; Turner and Akhter, 1999). Figure 1.6 shows a (bi)linear increase in the relative endocortical bone formation rate of rat tibia with a mechanical stimulus defined as above, plotted from data obtained from several experiments (Turner et al., 1994a,b, 1995; Turner, 1998). While the number of loading cycles may also play an important role, increasing numbers of cycles were shown to give diminishing returns with respect to bone adaptation (Rubin and Lanyon, 1984; Umemura et al., 1997).

For these reasons, instead of the change in energy, the quantity peak strain \times frequency was further investigated herein as a potential candidate for the mechanical stimulus involved in bone (re)modeling, according to the studies of Turner. Scheiner et al. (2016) have shown that bone cellular activity can be driven by the pressures experienced by the cells. Therefore, these (peak) pressures, arising from certain values of the peak strain, multiplied with the peak strain frequency, were chosen as a mechanical stimulus driving bone remodeling in the model presented in Chapter 2.

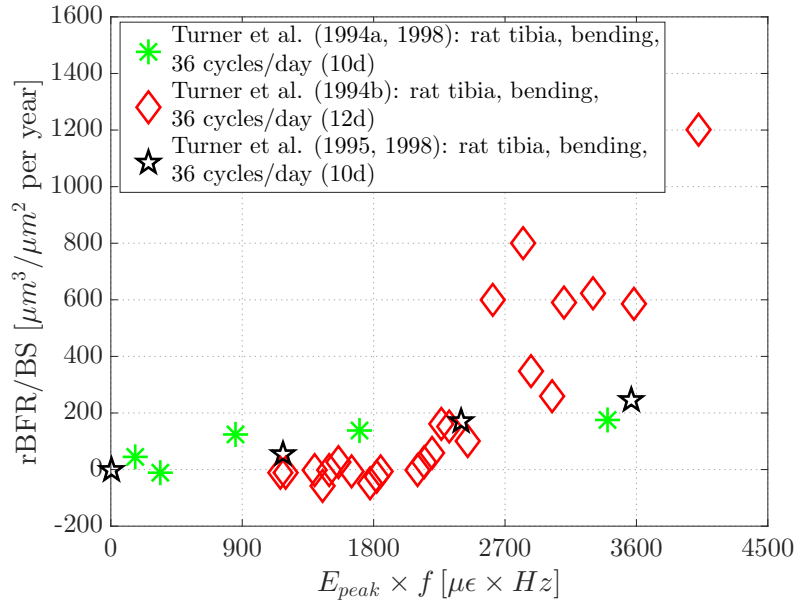


Figure 1.6: (Bi)linear increase of relative endocortical bone formation rate in rats, plotted based on experimental data from Turner et al. (1994a,b, 1995) and Turner (1998)

1.4.6 Mathematical modeling of bone (re)modeling

An imbalance between bone resorption and bone formation can significantly affect the load-carrying capacity of the tissue, and understanding the complex remodeling process can provide insights into treatments of several bone disorders and conditions. For this reason, much effort has been put into explaining and, ultimately, modeling this process mathematically.

In Chapter 2, a mathematical model for simulation of bone remodeling is presented, derived from a previously published modeling strategy (Scheiner et al., 2013, 2014), which, as a novelty, describes the processes occurring at the level of the vascular and lacunar pores. For the first time, the length-scale specificity of all quantities is considered in the model, biochemical factors and cells being both quantified in terms of vascular concentrations. Mechanical strains are quantified in terms of hydrostatic pore pressures, estimated by means of the continuum micromechanics representation of bone presented in Chapter 1.3.2 and a recently developed multiscale poromechanics model (Scheiner et al., 2016), and the mechanical stimulus is defined as specified in Chapter 1.4.5. Besides osteocytes, mechanically stimulated by the lacunar pore pressure, the mechanosensing capabilities of osteoblast precursors, mechanically stimulated by the vascular pore pressure, are also investigated.

1.5 Bone replacement materials

Regenerative medicine and, in particular, tissue engineering, have drawn much attention in research over the past few years. These fields are particularly attractive as they do not focus on just healing or replacing damaged tissue, but on achieving this by stimulating the body's own repair mechanisms. One of the most popular fields for application of regenerative medicine is orthopaedics, particularly bone tissue engineering (BTE). The latter involves implantation of bone cells or stem cells that later develop into bone cells at the damaged bone site, in order to promote regeneration and healing of the tissue. For implantation, the cells are cultivated on a scaffold – a 3D porous support structure fabricated with materials that exhibit high surface reactivity in physiological fluids, thus leading to the formation of strong bonds to the bone tissue.

A BTE scaffold should act as a template that allows cells to attach, proliferate, differentiate and organize themselves into normal, healthy bone as the scaffold degrades and is replaced by cell-derived tissue function. The design of the scaffold requires special attention, as it needs to immitate the bimodal porosity of bone, and the pore size and pore interconnectivity should be tailored to promote osteogenesis (Karageorgiou and Kaplan, 2005): on the one hand, larger pores ($> 300 \mu\text{m}$) are required for enhanced new bone formation, greater bone ingrowth and formation of capillaries; on the other hand, microporosity ($\sim 2 - 10 \mu\text{m}$, $< 50 \mu\text{m}$) is essential for immediate protein and cell adhesion, cell migration and osteointegration. Additionally, high permeability is also of great importance: a porosity higher than 90 % and pore diameters smaller than $500 \mu\text{m}$ are essential for cell seeding, tissue ingrowth and vascularization, as well as for nutrient delivery and waste removal (Gerhardt and Boccaccini, 2010). However, the mechanical properties of scaffolds decrease significantly with porosity, thus a compromise must be reached in scaffold design.

Ideally, the mechanical properties of a BTE scaffold – particularly its stiffness – should match those of the surrounding bone tissue, in order to ensure proper load transfer. A mismatch between Young's modulus of the bone and that of the scaffold or implant results in the bone being insufficiently loaded. The latter effect, called stress shielding, eventually leads to bone resorption (Ryan et al., 2006), which, in excess, may determine failure of the implant. Huiskes et al. (1992) have shown that the amount of bone resorption around the stem of a titanium hip implant is equally affected by implant stiffness and initial bone stiffness.

In Chapters 5 and 6, the mechanical properties of the ceramic materials for bone scaffold production baghdadite and Bioglass[®] are investigated. In the case of baghdadite, scaffolds seeded with bone cells have shown good biological properties *in*

vivo, but research on their mechanical properties are scarce. In Chapter 5, Young's modulus of the intact baghdadite material was determined by nanoindentation, and compared with results from ultrasonic tests on macroscopic, cylindrically-shaped scaffolds, shown in Figure 1.7. In the case of Bioglass[®], mechanical properties have been measured before, and the study in Chapter 6 investigates the possibilities of enhancing the stiffness of this material by coating it with various types of polymers.

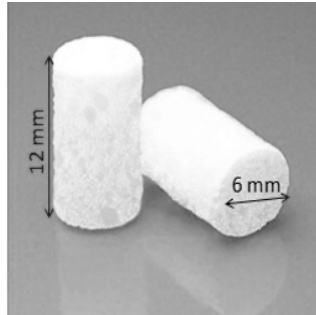


Figure 1.7: BTE scaffolds made of the ceramic material baghdadite, tested in Chapter 5 for the mechanical properties of both the macroscopic scaffold structure and the intact baghdadite material at microscopic scale

1.6 Appendix: Energy considerations for bone adaptation

The driving stimulus for bone adaptation to mechanical loads seems to be more than just the strain magnitude, i.e., a quantity that can take into account strain magnitude, as well as strain frequency, rate, and number of cycles. Based on a formulation presented by Turner and Akhter (1999), it was hypothesized that the stimulus that drives bone adaptation is the *change* in energy throughout the bone loading history.

The curves of Turner and Akhter

Starting from Frost's mechanical usage windows (Frost, 1992), Turner and Akhter (1999) have expanded the theory of bone adaptation, considering that the loading stimulus driving this adaptation depends on more quantities than just the peak strain magnitude, E^{peak} . Based on studies showing that an increasing number of loading cycles gives diminishing returns with respect to bone formation (Rubin and Lanyon, 1984; Umemura et al., 1997), they introduced a logarithmic dependence of the loading stimulus on the number of cycles N ; and based on evidence that the loading frequency f also plays a role (Turner et al., 1994a,b), they defined the daily

loading stimulus S as

$$S = \log(1 + N)E^{\text{peak}}f. \quad (1.4)$$

Turner et al. (1994a) showed that for $f = 2$ Hz and $N = 36$ cycles/day, the threshold for bone formation in rat tibia was $E^{\text{peak}} = 1050 \mu\epsilon$. Inserting these values in Eq. (1.4), the threshold daily loading stimulus for bone formation is

$$S_{\text{formation}} = \log(1 + N)E^{\text{peak}}f = \log(1 + 36) \times 1050 \times 2 = 3293. \quad (1.5)$$

Therefore, any combination of E^{peak} , N and f for which $S > 3293$ leads to bone formation. The authors have, in an analogous way, defined a threshold for bone resorption, considering $E^{\text{peak}} = 200 \mu\epsilon$, $N = 100$ cycles/day and keeping $f = 2$ Hz (values inspired by Frost's mechanostat presented in Chapter 1.4.4), which results in $S_{\text{resorption}} = 801.73$. Any S below this value leads to bone resorption, while values of S between $S_{\text{resorption}}$ and $S_{\text{formation}}$ are in the "physiological window" and do not result in changes in bone mass.

Keeping the frequency constant, $f = 2$ Hz, Turner and Akther have plotted the curve in Eq. (1.5) representing the threshold for bone formation, $S = S_{\text{formation}} = 3293$, as well as the resorption curve mentioned above; between the two curves there is the so-called "physiological window" or lazy zone, see Figure 1.8. The hypothesis was that, along the curve that represents the threshold for bone formation (solid line), the change in energy is constant, i.e., it is this change in energy that is actually the threshold stimulus for bone formation which, once surpassed (values in the "mild overuse window"), leads to bone formation.

Energy change formulation for the bone formation curve of Turner and Akther

For a fixed value of the frequency, $f = 2$ Hz, the peak strain in the longitudinal direction 33 as a function of number of daily loading cycles was first defined, according to Eq. (1.4) and (1.5) as

$$E_{33}^{\text{peak}} = \frac{3293}{\log(1 + N)f}. \quad (1.6)$$

For $N = 1$, $E_{33}^{\text{peak}} = 5469.6 \mu\epsilon$. Then, the strain history in direction 33 was considered to be a positive sinus wave with amplitude E_{33}^{peak} , starting from 0 (hence the phase shift with -0.125):

$$E_{33} = \frac{E_{33}^{\text{peak}}}{2} + \frac{E_{33}^{\text{peak}}}{2} \sin(2\pi f(t - 0.125)). \quad (1.7)$$

Considering that, except E_{33} , all other strain tensor components are zero, the energy Ψ reads as

$$\Psi = \frac{1}{2}C_{\text{hom},33}E_{33}^2 = \frac{(E_{33}^{\text{peak}})^2 C_{\text{hom},33}}{8} [1 + \sin(2\pi f(t - 0.125))]^2, \quad (1.8)$$

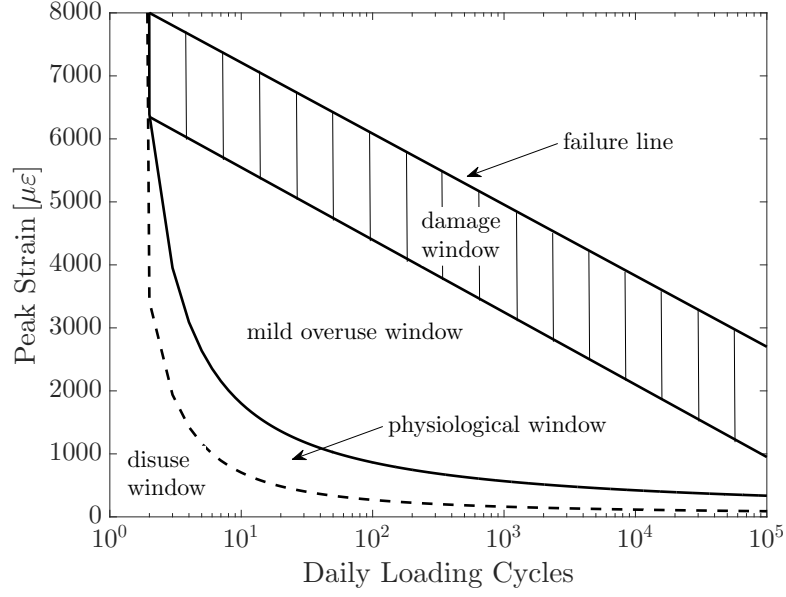


Figure 1.8: Model of mechanical usage windows in terms of number of cycles and peak strain magnitude, after Turner and Akhter (1999), for a constant frequency $f = 2 \text{ Hz}$

with $C_{\text{hom},33}$ as component 3333 of the homogenized bone stiffness tensor, equal to 23 GPa for undrained conditions, according to the values of $C_{\text{macro}}^{\text{lac,vas-u}}$ in the bone remodeling model in Chapter 2. Then, the derivative of the energy reads as

$$\begin{aligned} \frac{d\Psi}{dt} &= E_{33} C_{\text{hom},33} \frac{dE_{33}}{dt} \\ &= \frac{(E_{33}^{\text{peak}})^2 C_{\text{hom},33} \pi f}{2} \cos(2\pi f(t - 0.125)) [1 + \sin(2\pi f(t - 0.125))]. \end{aligned} \quad (1.9)$$

The total, *absolute* change in energy for one cycle is the integral of the absolute value of the above quantity, from 0 to $t = N/f = 0.5 \text{ s}$:

$$\begin{aligned} \int_0^{0.5} \left| \frac{d\Psi}{dt} \right| dt &= \frac{(E_{33}^{\text{peak}})^2 C_{\text{hom},33} \pi f}{2} \\ &\quad \int_0^{0.5} \left| \cos(2\pi f(t - 0.125)) [1 + \sin(2\pi f(t - 0.125))] \right| dt. \end{aligned} \quad (1.10)$$

The function inside the absolute value above takes both negative and positive values between 0 and 0.5, therefore the integral has to be solved on separate intervals. However, since the plot of the function is symmetric (see Figure 1.9), the integral

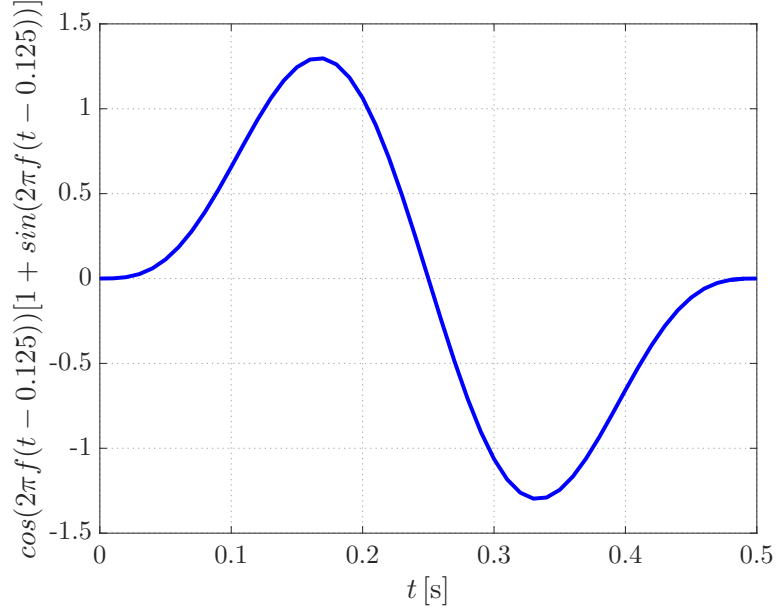


Figure 1.9: Graph of the function inside the absolute value in the integral on the right-hand side of Eq. (1.10), necessary for solving the integral on the left-hand side of the respective equation

may simply be solved on half of the interval and the result multiplied by 2:

$$\int_0^{0.5} \left| \frac{d\Psi}{dt} \right| dt = (E_{33}^{\text{peak}})^2 C_{\text{hom},33} \pi f \int_0^{0.25} \left| \cos(2\pi f(t - 0.125)) [1 + \sin(2\pi f(t - 0.125))] \right| dt, \quad (1.11)$$

and, using

$$\int \sin(ax) \cos(ax) dx = \frac{1}{4ax} \sin^2(ax), \quad (1.12)$$

we obtain

$$\begin{aligned} \int_0^{0.5} \left| \frac{d\Psi}{dt} \right| dt &= \frac{(E_{33}^{\text{peak}})^2 C_{\text{hom},33}}{4} [2\sin(2\pi f(t - 0.125)) + \sin^2(2\pi f(t - 0.125))] \Big|_0^{0.25} \\ &= \frac{(E_{33}^{\text{peak}})^2 C_{\text{hom},33}}{4} [2(1 + 1) + (1 - 1)] \\ &= (E_{33}^{\text{peak}})^2 C_{\text{hom},33}, \end{aligned} \quad (1.13)$$

with $f = 2$. For N cycles, the change in energy reads

$$\int_0^{N/2} \left| \frac{d\Psi}{dt} \right| dt = N (E_{33}^{\text{peak}})^2 C_{\text{hom},33}. \quad (1.14)$$

Generalized energy change formulation

In order to obtain a generalized formula for the above absolute change in energy, with any E^{peak} , N and f , the strain history needs to be re-defined with a general phase shift, depending on f :

$$E_{33} = \frac{E_{33}^{\text{peak}}}{2} + \frac{E_{33}^{\text{peak}}}{2} \sin(2\pi f(t - \frac{1}{4f})). \quad (1.15)$$

The total, *absolute* change in energy then reads

$$\begin{aligned} \int_0^{N/f} \left| \frac{d\Psi}{dt} \right| dt &= \frac{(E_{33}^{\text{peak}})^2 C_{\text{hom},33} \pi f}{2} \\ &\int_0^{N/f} \left| \cos(2\pi f(t - \frac{1}{4f})) [1 + \sin(2\pi f(t - \frac{1}{4f}))] \right| dt \\ &= \frac{(E_{33}^{\text{peak}})^2 C_{\text{hom},33} \pi f}{2} 2N \\ &\int_0^{N/2Nf} \left| \cos(2\pi f(t - \frac{1}{4f})) [1 + \sin(2\pi f(t - \frac{1}{4f}))] \right| dt \\ &= \frac{N(E_{33}^{\text{peak}})^2 C_{\text{hom},33}}{4} \\ &[2\sin(2\pi f(t - \frac{1}{4f})) + \sin^2(2\pi f(t - \frac{1}{4f}))] \Big|_0^{1/2f} \\ &= \frac{N(E_{33}^{\text{peak}})^2 C_{\text{hom},33}}{4} [2(1 + 1) + (1 - 1)] \\ &= N(E_{33}^{\text{peak}})^2 C_{\text{hom},33}. \end{aligned} \quad (1.16)$$

Conclusions

The absolute change in energy for any values of E^{peak} , N and f , depends on the square of the peak strain, while many experiments have shown that bone formation increases *linearly* with peak strain magnitude (Rubin and Lanyon, 1985; Turner et al., 1994a; Sugiyama et al., 2012), implying that, if a mechanical stimulus formulation were to include the peak strain, the latter should appear at the power 1. Moreover, the change in energy is not constant along the bone formation curve in Figure 1.8, as hypothesized. This energy change is, therefore, not an appropriate candidate for the mechanical stimulus driving bone formation.

Chapter 2

Multiscale systems biology of bone, accounting for pore space-specific mechanosensation

Authored by

Maria-Ioana Pastrama, Stefan Scheiner, Peter Pivonka, and Christian Hellmich

In preparation for submission to *Bone*

While bone tissue is a hierarchically organized material, mathematical formulations of bone remodeling are often defined on the level of a millimeter-sized representative volume element (RVE), “smeared” over all types of bone microstructures seen at lower observation scales. Thus, there is no explicit consideration of the fact that the biological cells and biochemical factors driving bone remodeling are actually located in differently sized pore spaces: active osteoblasts and osteoclasts can be found in the vascular pores, whereas the lacunar pores host osteocytes – bone cells originating from former osteoblasts which were then “buried” in newly deposited extracellular bone matrix. We here propose a mathematical description which considers size and shape of the pore spaces where the biological and biochemical events take place. In particular, a previously published systems biology formulation, accounting for biochemical regulatory mechanisms such as the RANK-RANKL-OPG pathway, is cast into a multiscale framework coupled to a poromicromechanical model. The latter gives access to the vascular and lacunar pore pressures arising from macroscopic loading. Extensive experimental data on the biological consequences of this loading strongly propose that the aforementioned pore

pressures, together with the loading frequency, are essential drivers of bone remodeling. The novel approach presented here allows for satisfactory simulation of the evolution of the bone systems under various experimental loading conditions, and for different species; including scenarios such as mechanical disuse of human bone, or remodeling in osteocyte-free fish bone.

Collaboration

This paper results from the extension of a bone remodeling model initially conceived by Stefan Scheiner and Peter Pivonka, and previously published together with Christian Hellmich. Maria-Ioana Pastrama extended the model through a precise introduction of the pore spaces where the bone remodeling-related cell and biochemical processes take place, the quantification of the mechanical stimuli in terms of pore pressures, and model validation with a variety of experimental data. She improved and optimized some computational aspects of the initial code, adapted it to make the aforementioned changes, ran simulations, performed extensive literature research and wrote the initial paper draft. All of these activities qualify her for first authorship. Stefan Scheiner assisted both in code-related issues and in correcting the first draft, conceived the research idea together with Christian Hellmich and Peter Pivonka, and all three contributed to giving feedback on the draft.

2.1 Introduction

It is well known that in vertebrates bone takes on a number of vital roles, including provision of the skeleton's load-carrying capacity. For this purpose, it is essential that the microstructural integrity of the bone tissue is continuously maintained. The mechanism concerned with this important task is bone remodeling, involving numerous biochemically and mechanically stimulated processes, in concert leading to removal of bone tissue by cells called osteoclasts, and to concurrent addition of bone tissue by cells called osteoblasts, while a third cell type, osteocytes, has been identified as bone remodeling "conductor" (Buckwalter et al., 1995b; Martin et al., 1998; Theoleyre et al., 2004; Robling et al., 2008; Ozcivici et al., 2010; Bonewald, 2011). Under normal physiological conditions, the activities of osteoclasts and osteoblasts are finely tuned, and the volumes of removed and added bone tissue are the same. However, disturbance of this balance (caused e.g., by bone disorders or a changed mechanical loading regime) can lead to changes in the bone composition (Vico and Alexandre, 1992; Manolagas, 2000; Martin and Shapiro, 2007); in the worst case,

the load-carrying capacity becomes significantly impaired (Chavassieux et al., 2007; Brennan et al., 2012; Kazakia et al., 2014).

In order to quantify the effects of diseases and changes of the mechanical loading in predictive fashion, great efforts have been made in terms of computational simulation of bone remodeling. Today's golden standard is set by approaches considering the bone remodeling processes to be predominantly driven by mechanical loading. In most cases, large-scale Finite Element simulations comprise mechanical feedback algorithms with the strain energy density as remodeling stimulus (Huiskes et al., 1987; Carter et al., 1989; van Rietbergen et al., 1993; Huiskes et al., 2000; Doblaré and García, 2002; Badilatti et al., 2016). Recently, the computational efficiency of such purely numerical models has been greatly improved through semi-analytical approaches inspired by continuum micromechanics (Colloca et al., 2014a,b). From a fundamentally different viewpoint, Lemaire et al. (2004) introduced a systems biology approach based on cell populations, by formulating chemical kinetics laws for chemical concentrations of biological cells and biochemical factors, modeling in this way the RANK-RANKL-OPG pathway. These concentrations were defined on millimeter-sized volumes encompassing both (and not differentiating between) the pore spaces hosting biological cells and substances, and the solid extracellular bone matrix in-between. Refinements of this model approach concerned introduction of the temporal change in bone matrix volume as a model output (Pivonka et al., 2008, 2010, 2012). More recently, the latter approaches have been combined with poromicromechanics, which allowed for downscaling of the macroscopic loading to the level of the extravascular matrix hosting the mechanically sensitive osteocytes, and for consideration of this matrix's strain energy density as mechanical stimulus entering the aforementioned kinetics laws (Scheiner et al., 2013, 2014, 2016).

However, until now, despite the improvements achieved over the past years, to the best of the authors' knowledge, a comprehensive multiscale modeling framework for bone remodeling, explicitly taking into account the different characteristic lengths at which the underlying processes and mechanisms take place, does not exist. More precisely, none of the modeling approaches has taken into consideration the exact spaces *within* a representative volume element (RVE) where bone remodeling takes place. Both bone-forming and -resorbing cells at various differentiation stages are located in the vascular pores, where they are activated or inhibited by biochemical factors to initiate the remodeling process; at this stage, they are attached to the pore walls and work in basic multicellular units (BMUs), resorbing old and forming new bone (Frost, 1964a; Buenzli et al., 2011). Osteocytes reside in the lacunar pore space and release biochemical factors such as sclerostin (SCLR); the latter gets transported to the vascular pore space, and there it upregulates osteoblast precursor proliferation

via WNT (Westendorf et al., 2004; Gaur et al., 2005). As concerns mechanical stimuli, it is well known that oscillating hydrostatic pressure in the order of tens of kPa activates a variety of different biological cells, including bone cells (Klein-Nulend et al., 1995; Brighton et al., 1996; Vergne et al., 1996; Nagatomi et al., 2001, 2002, 2003; Gardinier et al., 2009), and Scheiner et al. (2016) have recently shown that pressures of this order of magnitude indeed may occur in the lacunar and vascular pore spaces of bone under physiologically relevant loading.

Explicit mathematical consideration of these aspects is the focus of the present paper, by providing a multiscale systems biology approach complemented by poro-micromechanics. This novel approach features consideration of cell and biochemical factor concentrations at the pore fluid level where these cells and factors actually occur, it takes into account concentration changes arising from pore volume changes, as well as mechanical stimuli directly at the level of biological cells. This paper is organized as follows: First, we elaborate, in Section 2.2, on the mechanobiological and biochemical processes involved in bone remodeling, and on the different length scales where they occur. This review is then translated into a new mathematical framework, described in Section 2.3 and Appendix C. Numerical evaluation of the resulting mathematical model allows then for studying various loading scenarios. In particular, the focus is on replication of *in vivo* data obtained in experimental studies dealing with the effects of different mechanical loading regimes on the corresponding evolution of the bone composition, see Section 2.4. After further elucidating the model behavior by means of parameter studies, in Section 2.5, its potentials and limitations are discussed in Section 2.6.

2.2 Multiscale organization of bone remodeling

Bone is a complex, hierarchically organized, biological material, whose constantly occurring metabolism is governed by processes and mechanisms taking place in its various pore spaces. The latter exhibit characteristic lengths spanning several orders of magnitude, see Figure 2.1.

The largest pore space in bone is formed by the blood vessel-hosting vascular pores, with characteristic diameters of approximately 50 to 80×10^{-6} m (Martin, 1984; Cooper et al., 2003; Wang and Ni, 2003; Cooper et al., 2007). In cortical bone, the vascular pores occur in form of a branching structure (Cooper et al., 2003), with the main branches (often referred to as Haversian canals) running longitudinally through the bone cortex, see Figure 2.1(b), and the smaller, less frequently occurring branches (often referred to as Volkmann canals) connecting the Haversian canals. The vascular porosity in cortical bone typically amounts, depending on the bone type and on the

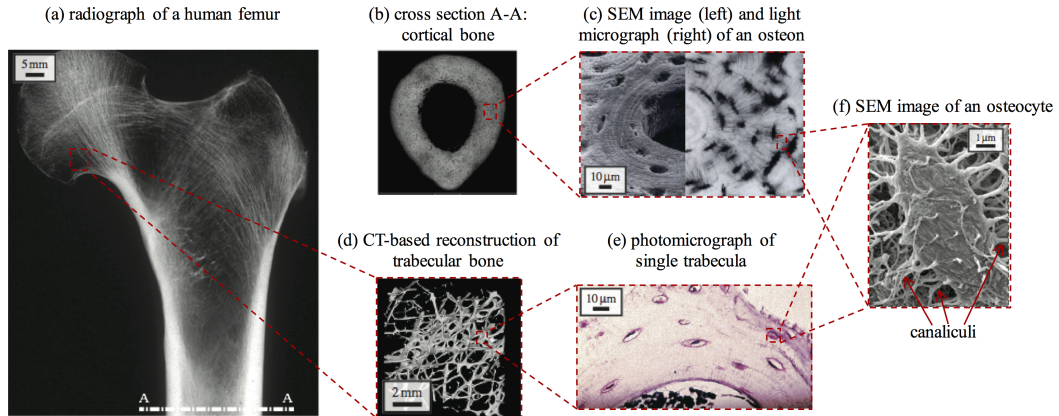


Figure 2.1: Hierarchical organization of bone showing the various pore spaces discernible at different observation scales: (a) X-ray image of the proximal part of a human femur; (b) midshaft cross section A-A, showing the cortical shell; (c) left: scanning electron microscopy (SEM), and right: light microscopy images of cortical bone microstructure, showing an osteon with vascular and lacunar pores; (d) computed tomography (CT) image of trabecular bone; (e) a photomicrograph of a single trabecula showing the composition of trabecular bone with vascular and lacunar pores; (f) SEM image of an osteocyte and canaliculi

anatomical location, from 3% under normal physiological conditions to 35% in case of disease or drug treatment (Sietsema, 1995; Fritsch and Hellmich, 2007; Cardoso et al., 2013). In trabecular bone, the morphology of the vascular pore spaces differs significantly as compared to cortical bone. Namely, extravascular bone appears in form of struts or plates, called trabeculae, and between the trabeculae the vascular pores occur in interpenetrating fashion, see Figure 2.1(d), at porosities of 50 to 90% of the total bone volume (Fuchs et al., 2009). Most of the factors needed for initiating or maintaining bone remodeling events are actually provided through the vascular pores. This includes mesenchymal stem cells, from which osteoblasts originate, and hematopoietic stem cells, from which osteoclasts originate (Buckwalter et al., 1995a). Furthermore, within the vascular pores, the progenitors of osteoblasts and osteoclasts may differentiate (over a sequence of developmental stages) into mature bone cells, which actively form new or resorb old bone (Aubin, 1998; Roodman, 1999).

Moreover, the vascular pore fluid also contains a multitude of biochemical factors influencing the progress of bone remodeling events (or even rendering them possible), as highlighted by several review articles, see e.g., (Buckwalter et al., 1995b; Theoleyre et al., 2004; Boyce and Xing, 2008; Silva and Branco, 2011). We consider the following as key factors (in terms of bone remodeling regulation):

- Transforming growth factor β ($TGF\beta$) is released by osteoclasts during bone resorption (Bonewald and Dallas, 1994), and acts upon osteoblasts and os-

teoclasts in different ways: while promoting differentiation of uncommitted osteoblast progenitor cells (Erlebacher et al., 1998; Janssens et al., 2005), it inhibits the differentiation of osteoblast precursor cells (Bonewald and Dallas, 1994; Mundy et al., 1996; Erlebacher et al., 1998; Alliston et al., 2001; Janssens et al., 2005), and activates osteoclast apoptosis (Greenfield et al., 1999; Roodman, 1999; Fuller et al., 2000).

- Receptor activator of nuclear factor kappa-B (RANK) is expressed at the surface of osteoclast progenitor cells and mature osteoclasts (Nakagawa et al., 1998; Kartsogiannis et al., 1999). Binding of RANK to its ligand, known as RANKL, the latter being expressed either by osteoblast progenitors or osteocytes (Nakashima et al., 2011), upregulates differentiation of osteoclast precursor cells to active osteoclasts (Boyce and Xing, 2008).
- Osteoprotegerin (OPG) is expressed by active osteoblasts (Boyce and Xing, 2008). It is known to act as a decoy ligand, also binding to RANKL, thereby preventing the RANK-RANKL binding (Martin, 2004) and, consequently, downregulating differentiation of osteoclast precursor cells to active osteoclasts (Lacey et al., 1998; Nakagawa et al., 1998).
- Parathyroid hormone (PTH) upregulates the maximum number of RANKL molecules and represses production of OPG, thus indirectly activating osteoclast precursor differentiation (Kroll, 2000).
- Sclerostin (SCLR), produced by osteocytes in the lacunar pore space, is an antagonist of the WNT β -catenin pathway, the latter promoting osteoblastic proliferation and differentiation. Sclerostin travels from the lacunar to the vascular pore space, where it acts on the so-called wingless gene (WNT), thus indirectly regulating osteoblast precursor proliferation (Westendorf et al., 2004; Gaur et al., 2005).

The extravascular bone matrix hosts another class of pore space, namely the lacunar pores, see Figures 2.1(c), (e), and (f), with a characteristic length of approximately 10×10^{-6} m (Buckwalter et al., 1995a; Martin et al., 1998) and a pore volume fraction within extravascular bone of roughly 10 % (Buckwalter et al., 1995a; Tai et al., 2008). Each lacunar pore hosts an osteocyte, i.e., the cell which is believed to be *the* mechanosensor of bone (Bonewald, 2011). Two specific mechanisms appear to be particularly important in this context: (i) increased mechanical loading promotes nitric oxide (NO) production by the osteocytes (Pitsillides et al., 1995; Mullender et al., 2004), and NO is known to decrease the RANKL/OPG ratio expressed on bone marrow stromal cells (Fan et al., 2004; Wang et al., 2004), resulting in an

overall inhibition of RANKL through mechanical stimuli; (ii) increased mechanical loading induces reduced SCLR levels (Tatsumi et al., 2007; Robling et al., 2008).

It is an important feature of the lacunae that they form a dense network; the lacunae are connected by so-called canaliculi. They exhibit diameters of typically 100 to 500×10^{-9} m and 35×10^{-6} m length (Reilly et al., 2001), and they contain junctions of the osteocyte cell processes (Buckwalter et al., 1995a; Reilly et al., 2001; Robling et al., 2006), see Figure 2.1(f).

One further key aspect of bone remodeling is the regulatory influence of the mechanical loading. Applied macroscopically (e.g., via physical exercise or simply the dead weight), the mechanical loading is somehow transferred to specific cells or specific biochemical factors, e.g., reiterating from above, by a decrease in the production of RANKL, and, hence, a decreased amount of the RANK-RANKL complex, which eventually leads to a downregulation of osteoclast precursor differentiation. Furthermore, it could be shown that mechanical loading upregulates the proliferation of osteoblast precursors (Jones et al., 1991; Kaspar et al., 2002), which could be explained by the above-mentioned decrease in the amount of SCLR, which leads to a removal of the WNT β -catenin inhibition. The exact stimulus relating mechanical loading and biochemical activities has remained a matter of intensive debate. Recently, it could be shown that for a wide range of physiologically meaningful mechanical loading conditions, cells (and other biochemical factors) are subjected to significant hydrostatic pressures in response to macroscopically applied loading (Scheiner et al., 2016). Remarkably, pressures of such magnitude (typically 13 to 69 kPa, as revealed through *in vitro* tests) were shown to influence the activities of the cells and biochemical factors driving bone remodeling, see e.g. (Klein-Nulend et al., 1995; Brighton et al., 1996; Vergne et al., 1996; Nagatomi et al., 2001, 2002, 2003; Gardinier et al., 2009).

2.3 Mathematical model combining multiscale systems biology with poromicromechanics

2.3.1 Model representation of bone tissue

For mathematical modeling of the various mechanobiological and biochemical processes as described in Section 2.2, we consider a three-scale representation of bone tissue, as seen in Figure 2.2:

Firstly, a macroscopic representative volume element (RVE) of cortical or trabecular bone is chosen in the line of earlier work (Hellmich et al., 2004b; Hellmich and Ulm, 2005; Fritsch et al., 2009b; Grimal et al., 2011; Scheiner et al., 2016). This RVE is composed of an extravascular bone matrix, into which cylindrical vascular pores, aligned with the main anatomical axis, are embedded. Notably, the vascular

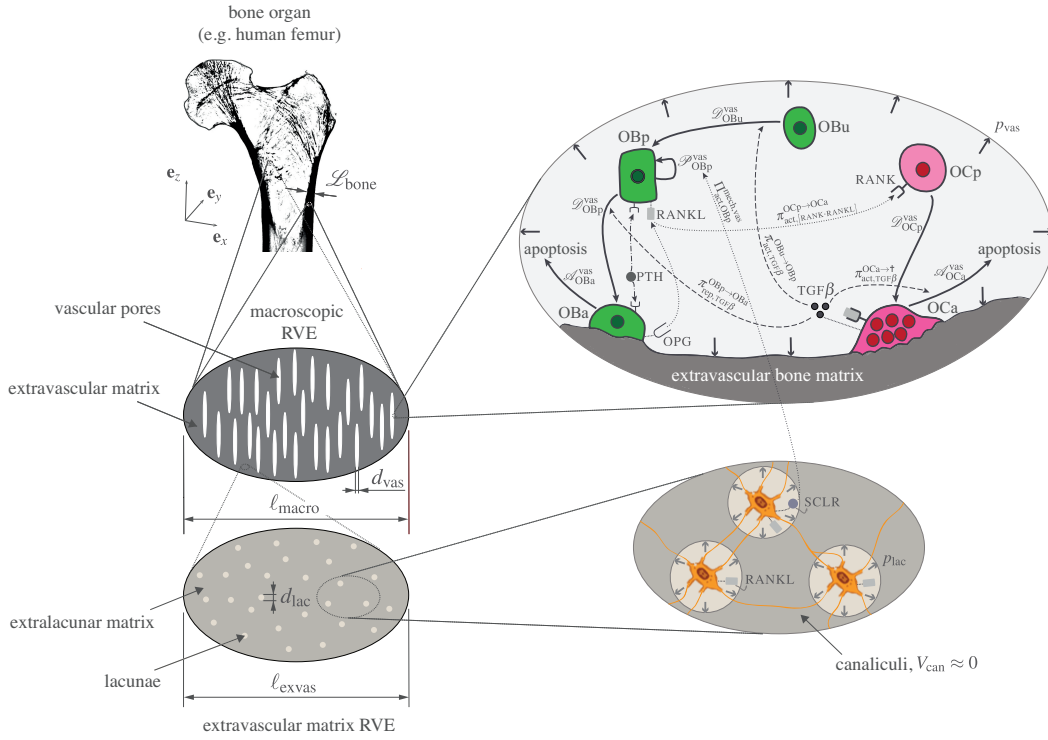


Figure 2.2: Micromechanical representation of bone tissue; the microstructure is composed of extravascular bone matrix and vascular pores with diameter d_{vas} , $\mathcal{L}_{\text{bone}} \gg l_{\text{macro}} \gg d_{\text{vas}}$; these pores host bone-forming and -resorbing cells at various differentiation stages, stimulated by the vascular pore pressure p_{vas} , as well as by the biochemical factors that act upon them; active osteoblasts and osteoclasts are responsible for forming and resorbing extravascular bone matrix, respectively; the extravascular matrix is composed of extracellular matrix and lacunar pores with diameter d_{lac} , $l_{\text{exvas}} \gg d_{\text{lac}}$; these pores host osteocytes, that are stimulated by the lacunar pore pressure p_{lac} , and produce SCLR, which travels to the vascular pore space, where it acts on osteoblast precursor proliferation

pores either represent Haversian canals (if the RVE contains cortical bone) or intertrabecular pore space (if the RVE contains trabecular bone), containing cells of the osteoblastic and osteoclastic lineages, and the biochemical factors affecting the activities and behaviour of these cells; in our model, these factors are RANK, RANKL, OPG, PTH, WNT, and SCLR.

Secondly, zooming into extravascular bone shows that one hierarchical level below (approximately spherical) osteocyte-containing lacunar pores are embedded in a matrix of extralacunar bone. The latter contains extralacunar bone matrix and canalicular pores; since the volume of the latter is negligibly small, this additional resolution step is omitted here.

From a mechanical point of view, such model representation of bone tissue fulfills

the so-called “separation of scales”-requirement, thereby allowing for application of continuum poromicromechanics (Hill, 1963, 1965; Suquet, 1997; Zaoui, 1997, 2002), for estimation of the vascular and lacunar pore pressures in response to macroscopically applied mechanical loading, see Appendix B.

2.3.2 Introduction of pore space-specific concentrations

Let us assume that a specific species i is present in pore space j , and that the amount of this species, denoted as N_i , is quantified in mole. Dividing N_i by the volume of the pore space, V_j , yields the respective molar concentration (Atkins, 1998), simply referred to as “concentration” from here on,

$$C_i^j = \frac{N_i}{V_j}. \quad (2.1)$$

Such a concentration is different from those which are standardly used in systems biology models for bone (Lemaire et al., 2004; Pivonka et al., 2008, 2010, 2012). There, the concentrations per millimeter-sized volume of “macroscopic bone material” are considered. The latter concentrations, denoted in the following by C_i^{macro} , are associated with the former pore space-specific concentration through

$$C_i^{\text{macro}} = \frac{N_i}{V_{\text{macro}}} = C_i^j f_j, \quad (2.2)$$

with f_j being the volume fraction of the pore space j with respect to the macroscopic RVE of bone,

$$f_j = \frac{V_j}{V_{\text{macro}}}. \quad (2.3)$$

We are now interested in temporal evolutions of such concentrations. Mathematically, they are expressed as the differentiation of C_i^j with respect to the time t , yielding

$$\frac{dC_i^j}{dt} = \frac{d}{dt} \left(\frac{N_i}{V_j} \right) = \frac{1}{V_j} \frac{dN_i}{dt} - \frac{N_i}{(V_j)^2} \frac{dV_j}{dt}. \quad (2.4)$$

Eq. (2.4) expresses that a change of the concentration of species i , quantified in the pore space j , can occur (i) due to a change in the amount of this species (see the first term on the right-hand side), and (ii) due to a change of the pore space volume (see the second term on the right-hand side). Eqs. (2.2) and (2.3) now allow for re-writing Eq. (2.4) in the format

$$\frac{dC_i^j}{dt} = \frac{1}{f_j} \frac{dC_i^{\text{macro}}}{dt} - \frac{C_i^j}{f_j} \frac{df_j}{dt} = \frac{1}{f_j} \left(\frac{1}{V_{\text{macro}}} \frac{dN_i}{dt} - C_i^j \frac{df_j}{dt} \right). \quad (2.5)$$

In other words, the concentration change of species i in pore space j is not only driven by the production (or degradation) of substance i , but also by the change in

size of that pore space where the substance i actually resides. This effect was neglected in earlier bone systems biology approaches, so that these approaches, strictly speaking, qualify for small porosity changes only. It is an original aspect of the present contribution that we explicitly consider the effect of pore space evolutions on the concentrations of substances residing in these pores; namely, concentrations of cells and factors increase upon pore space reduction and *vice versa*.

2.3.3 Cell evolution in changing vascular pore space

The concentration evolution relation given by Eq. (2.5) is now applied to the cell populations in the vascular pore space, starting with the osteoblast lineage. The number of osteoblast precursors increases due to differentiation of uncommitted osteoblast progenitor cells, proportional to the maximum differentiation rate $\mathcal{D}_{\text{OBu}}^{\text{vas}}$, and to the Hill-type activation function $\pi_{\text{act,TGF}\beta}^{\text{OBu}\rightarrow\text{OBp}}$, which considers the promotion of cell differentiation through TGF β ; see Eq. (2.12) in Section 2.3.4. Also, osteoblast precursors proliferate upon mechanical stimulation, as quantified through the mechanical activator function $\Pi_{\text{act,OBp}}^{\text{mech,vas}}$, Eq. (2.16). Furthermore, the number of osteoblast precursors decreases due to differentiation of osteoblast precursors to active osteoblasts (with maximum rate $\mathcal{D}_{\text{OBp}}^{\text{vas}}$); this differentiation is repressed by TGF β , a mechanism quantified through $\pi_{\text{rep,TGF}\beta}^{\text{OBp}\rightarrow\text{OBa}}$, see Eq. (2.13). All these effects can be expressed mathematically through

$$\begin{aligned} \frac{dN_{\text{OBp}}}{dt} = & \mathcal{D}_{\text{OBu}}^{\text{vas}} \pi_{\text{act,TGF}\beta}^{\text{OBu}\rightarrow\text{OBp}} N_{\text{OBu}} + \mathcal{P}_{\text{OBp}}^{\text{vas}} \Pi_{\text{act,OBp}}^{\text{mech,vas}} N_{\text{OBp}} \\ & - \mathcal{D}_{\text{OBp}}^{\text{vas}} \pi_{\text{rep,TGF}\beta}^{\text{OBp}\rightarrow\text{OBa}} N_{\text{OBp}}. \end{aligned} \quad (2.6)$$

Insertion of this relation into Eq. (2.5), specified for the vascular pore space and osteoblast precursors, i.e., for $j = \text{vas}$ and $i = \text{OBp}$, yields

$$\begin{aligned} \frac{dC_{\text{OBp}}^{\text{vas}}}{dt} = & \mathcal{D}_{\text{OBu}}^{\text{vas}} \pi_{\text{act,TGF}\beta}^{\text{OBu}\rightarrow\text{OBp}} C_{\text{OBu}}^{\text{vas}} + \mathcal{P}_{\text{OBp}}^{\text{vas}} \Pi_{\text{act,OBp}}^{\text{mech,vas}} C_{\text{OBp}}^{\text{vas}} \\ & - \mathcal{D}_{\text{OBp}}^{\text{vas}} \pi_{\text{rep,TGF}\beta}^{\text{OBp}\rightarrow\text{OBa}} C_{\text{OBp}}^{\text{vas}} - \frac{C_{\text{OBp}}^{\text{vas}}}{f_{\text{vas}}} \frac{df_{\text{vas}}}{dt}. \end{aligned} \quad (2.7)$$

Hence, osteoblast precursor concentration change results not only from cell number change, considered by the first three terms right of the equal sign in Eq. (2.7), but also from the vascular porosity change, considered by the last term right of the equal sign in Eq. (2.7).

Analogously, the concentration of active osteoblasts in the vascular pore space, $C_{\text{OBa}}^{\text{vas}}$, follows from another differential equation:

$$\frac{dC_{\text{OBa}}^{\text{vas}}}{dt} = \mathcal{D}_{\text{OBp}}^{\text{vas}} \pi_{\text{rep,TGF}\beta}^{\text{OBp}\rightarrow\text{OBa}} C_{\text{OBp}}^{\text{vas}} - \mathcal{A}_{\text{OBa}}^{\text{vas}} C_{\text{OBa}}^{\text{vas}} - \frac{C_{\text{OBa}}^{\text{vas}}}{f_{\text{vas}}} \frac{df_{\text{vas}}}{dt}, \quad (2.8)$$

i.e., C_{OBa}^{vas} is considered to increase due to differentiation of osteoblast precursors (inhibited by $TGF\beta$, as previously described); and to decrease with active osteoblast apoptosis (with apoptosis rate \mathcal{A}_{OBa}^{vas}), as well as due to the increase of the vascular porosity.

Finally, the vascular concentration of active osteoclasts, C_{OCa}^{vas} , evolves according to

$$\frac{dC_{OCa}^{vas}}{dt} = \mathcal{D}_{OCp}^{vas} \pi_{act, [RANK \cdot RANKL]}^{OCp \rightarrow OCa} C_{OCp}^{vas} - \mathcal{A}_{OCa}^{vas} \pi_{act, TGF\beta}^{OCa \rightarrow \dagger} C_{OCa}^{vas} - \frac{C_{OCa}^{vas}}{f_{vas}} \frac{df_{vas}}{dt}. \quad (2.9)$$

Eq. (2.9) expresses that C_{OCa}^{vas} increases with differentiation of osteoclast precursors (with maximum differentiation rate \mathcal{D}_{OCp}^{vas}), promoted by the binding of RANK to RANKL. The latter promotion mechanism is quantified by activator function $\pi_{act, [RANK \cdot RANKL]}^{OCp \rightarrow OCa}$, see Eq. (2.17) in Section 2.3.6. Additionally, C_{OCa}^{vas} decreases due to active osteoclast apoptosis, with maximum rate \mathcal{A}_{OCa}^{vas} , and promoted by $TGF\beta$ via activator function $\pi_{act, TGF\beta}^{OCa \rightarrow \dagger}$, see Eq. (2.14). Finally, similarly to the other vascular concentrations, compare Eqs. (2.7)–(2.8), C_{OCa}^{vas} is reduced due to the increase of the vascular porosity.

Resorption and formation of bone matrix is accomplished by active osteoclasts and active osteoblasts located in the vascular pore space. Thus, the change of extravascular bone volume, or, conversely, of vascular pore space, is driven by

$$\frac{dV_{vas}}{dt} = -\frac{dV_{exvas}}{dt} = \left(\frac{dV_{vas}}{dt} \right)_{res} - \left(\frac{dV_{vas}}{dt} \right)_{form} = N_{OCa} k_{OCa}^{res} - N_{OBa} k_{OBa}^{form} \quad (2.10)$$

where $(dV_{vas}/dt)_{res}$ is the volumetric change of the vascular pore space due to bone resorption, $(dV_{vas}/dt)_{form}$ is the volumetric change of the vascular pore space due to bone formation, N_{OCa} is the number of active osteoclasts (in moles), N_{OBa} is the number of active osteoblasts (in moles), k_{OCa}^{res} is the (constant) amount of bone volume resorbed by one mole of active osteoclasts, and k_{OBa}^{form} is the (constant) amount of bone volume resorbed by one mole of active osteoblasts. When dividing both sides of Eq. (2.10) by V_{macro} , we obtain

$$\frac{df_{vas}}{dt} = C_{OCa}^{macro} k_{OCa}^{res} - C_{OBa}^{macro} k_{OBa}^{form} = f_{vas} (C_{OCa}^{vas} k_{OCa}^{res} - C_{OBa}^{vas} k_{OBa}^{form}). \quad (2.11)$$

2.3.4 Effects of $TGF\beta$ on osteoblast differentiation and osteoclast apoptosis

Differentiation of osteoblast progenitors to osteoblast precursor cells is promoted by the presence of $TGF\beta$ (Erlebacher et al., 1998; Janssens et al., 2005). Mathematically, this is considered by means of activator function $\pi_{act, TGF\beta}^{OBu \rightarrow OBp}$. Following previous

works (Lemaire et al., 2004; Pivonka et al., 2008; Scheiner et al., 2013), $\pi_{\text{act,TGF}\beta}^{\text{OBu}\rightarrow\text{OBp}}$ is defined as a so-called Hill-type function (Alon, 2007), thus

$$\pi_{\text{act,TGF}\beta}^{\text{OBu}\rightarrow\text{OBp}} = \frac{C_{\text{TGF}\beta}^{\text{vas}}}{K_{\text{act,TGF}\beta}^{\text{OBu}\rightarrow\text{OBp,vas}} + C_{\text{TGF}\beta}^{\text{vas}}}, \quad (2.12)$$

where $C_{\text{TGF}\beta}^{\text{vas}}$ is the concentration of TGF β in the vascular pore space, see Appendix C for details, and $K_{\text{act,TGF}\beta}^{\text{OBu}\rightarrow\text{OBp,vas}}$ is the activation coefficient of osteoblast progenitor differentiation.

Furthermore, differentiation of osteoblast precursors to active osteoblasts is inhibited by the presence of TGF β (Bonewald and Dallas, 1994; Mundy et al., 1996; Erlebacher et al., 1998; Alliston et al., 2001; Janssens et al., 2005). This is mathematically considered by means of the repression function $\pi_{\text{rep,TGF}\beta}^{\text{OBp}\rightarrow\text{OBa}}$, defined as

$$\pi_{\text{rep,TGF}\beta}^{\text{OBp}\rightarrow\text{OBa}} = \frac{K_{\text{rep,TGF}\beta}^{\text{OBp}\rightarrow\text{OBa}}}{K_{\text{rep,TGF}\beta}^{\text{OBp}\rightarrow\text{OBa,vas}} + C_{\text{TGF}\beta}^{\text{vas}}}, \quad (2.13)$$

with $K_{\text{rep,TGF}\beta}^{\text{OBp}\rightarrow\text{OBa,vas}}$ as the repression coefficient of osteoblast precursor differentiation by TGF β .

TGF β also affects the availability of active osteoclasts. In particular, the apoptosis of active osteoclasts is promoted by TGF β (Greenfield et al., 1999; Roodman, 1999; Fuller et al., 2000), and this is expressed mathematically by the activator function $\pi_{\text{act,TGF}\beta}^{\text{OCa}\rightarrow\uparrow}$, defined as the Hill-type function

$$\pi_{\text{act,TGF}\beta}^{\text{OCa}\rightarrow\uparrow} = \frac{C_{\text{TGF}\beta}^{\text{vas}}}{K_{\text{act,TGF}\beta}^{\text{OCa}\rightarrow\uparrow,\text{vas}} + C_{\text{TGF}\beta}^{\text{vas}}}, \quad (2.14)$$

with $K_{\text{act,TGF}\beta}^{\text{OCa}\rightarrow\uparrow,\text{vas}}$ as the activation coefficient of active osteoclast apoptosis by TGF β .

2.3.5 Mechanical stimulation of osteoblast precursor proliferation

Considering a comprehensive basis of experimental data from mechanobiological investigations (Rubin and Lanyon, 1984, 1985; Rubin and McLeod, 1994; Turner et al., 1994a,b, 1995; Umemura et al., 1997), Turner and coworkers (Turner, 1998; Turner and Akhter, 1999) identified the product of the frequency f and the peak amplitude E^{peak} of the (axial normal) macroscopic strain as the key mechanical stimulus driving bone adaptation. Thereby, the macroscopic strain state is typically related to uniaxial stress, and therefore to a strain tensor of the format

$$\mathbf{E}_{\text{macro}} = E^{\text{peak}} \mathbf{e}_z \otimes \mathbf{e}_z + \nu_{\text{macro}}^{\text{lac,vas-u}} E^{\text{peak}} (\mathbf{e}_x \otimes \mathbf{e}_x + \mathbf{e}_y \otimes \mathbf{e}_y), \quad (2.15)$$

with $\nu_{\text{macro}}^{\text{lac,vas-u}}$ standing for Poisson's ratio related to the undrained homogenized stiffness tensor $\mathbf{C}_{\text{macro}}^{\text{lac,vas-u}}$ given in Eq. (2.25).

Physiologically relevant oscillating strains often entail undrained conditions in the vascular and lacunar pore spaces of bone, as evidenced by Scheiner et al. (2016) using a comprehensive experimental basis comprising relaxation/consolidation tests (Gardinier et al., 2009), measured loading patterns related to typical physiological activities (Bergmann et al., 1993; Mikić and Carter, 1995; Burr et al., 1996; Kutzner et al., 2010), and oscillating pore pressure magnitudes which have been repeatedly shown to stimulate biological cells (Klein-Nulend et al., 1995; Brighton et al., 1996; Vergne et al., 1996; Nagatomi et al., 2001, 2002, 2003). In addition, it is remarkable that under such undrained conditions, the components of the macroscopic strain tensor (such as E^{peak}) are multi-linearly related to the pore pressures, see Eq. (2.19) to (2.25). This multi-linear relationship allows for downscaling the aforementioned relevant macroscopic stimulus found by Turner (1998) and Turner and Akhter (1999) down to the level of the immediate mechanical environment of the biological cells; and in this sense, strongly suggests the product of frequency f and peak amplitude of pore pressure p^{peak} , i.e., $p^{\text{peak}}f$, as a particularly relevant choice for a mechanical stimulus.

In particular, two types of cells are stimulated by oscillating pore pressure: the osteocytes residing in the lacunar pores, reacting to a stimulus proportional to $p_{\text{lac}}^{\text{peak}}f$, and the osteoblast precursors, cells which reside in the vascular space, thereby reacting to a stimulus proportional to $p_{\text{vas}}^{\text{peak}}f$, in terms of differentiating into osteoblasts producing new bone tissue (the measure Turner (1998) and Turner and Akhter (1999) took as obvious marker for ongoing bone adaptation). As concerns the osteocytes, populating the extravascular bone matrix space at a concentration of $C_{\text{OCY}}^{\text{exvas}}$, mechanical stimulation triggers the WNT/SCLR pathway: Upon mechanical stimulation, osteocytes produce SCLR, which is transported through the canaliculi from the lacunar to the vascular pore space. There, it acts on WNT, and the latter upregulates preosteoblast proliferation.

These types of mechanically stimulated preosteoblast proliferation are mathematically expressed by specifying the function $\Pi_{\text{act,OBp}}^{\text{mech,vas}}$ occurring in Eq. (2.7) as

$$\begin{aligned} \Pi_{\text{act,OBp}}^{\text{mech,vas}} = \hat{\Pi}_{\text{act,OBp}}^{\text{mech,vas}} & \left[1 + \lambda_{\text{OBp}}^{\text{vas}} \left(\frac{p_{\text{vas}}^{\text{peak}}f}{p_{\text{vas}}^{\text{peak}}f} - 1 \right) \right. \\ & \left. + \lambda_{\text{WNT/SCLR}}^{\text{vas}} C_{\text{OCY}}^{\text{exvas}} \frac{1 - f_{\text{vas}}}{f_{\text{vas}}} \left(\frac{p_{\text{lac}}^{\text{peak}}f}{p_{\text{lac}}^{\text{peak}}f} - 1 \right) \right] \leq 1. \end{aligned} \quad (2.16)$$

By definition, the maximum value of $\Pi_{\text{act,OBp}}^{\text{mech,vas}}$ is 1, and it is reached when the mechanical stimulus is sufficiently larger than the threshold value, $(p^{\text{peak}}f) > (\overline{p^{\text{peak}}f})$. At the threshold value of the mechanical stimulus, $(p^{\text{peak}}f) = (\overline{p^{\text{peak}}f})$, $\Pi_{\text{act,OBp}}^{\text{mech,vas}}$ reaches its minimum, $\hat{\Pi}_{\text{act,OBp}}^{\text{mech,vas}}$, only above which increased proliferation is activated.

The term $(1 - f_{\text{vas}})/f_{\text{vas}}$ reflects the concentration changes due to transport of SCLR from the extravascular to the vascular compartments of bone (this transport process is quasi-instantaneous with respect to the overall bone adaptation process).

2.3.6 Mechanical inhibition of osteoclast precursor differentiation

Differentiation of osteoclast precursors is promoted by the binding of RANK to RANKL (Boyce and Xing, 2008), and quantified by activator function $\pi_{\text{act},[\text{RANK}\cdot\text{RANKL}]}^{\text{OCp}\rightarrow\text{OCa}}$, reading as

$$\pi_{\text{act},[\text{RANK}\cdot\text{RANKL}]}^{\text{OCp}\rightarrow\text{OCa}} = \frac{C_{[\text{RANK}\cdot\text{RANKL}]}^{\text{vas}}}{K_{\text{act},[\text{RANK}\cdot\text{RANKL}]}^{\text{OCp}\rightarrow\text{OCa,vas}} + C_{[\text{RANK}\cdot\text{RANKL}]}^{\text{vas}}}. \quad (2.17)$$

In the above equation, $K_{\text{act},[\text{RANK}\cdot\text{RANKL}]}^{\text{OCp}\rightarrow\text{OCa,vas}}$ is the activation coefficient related to osteoclast precursor differentiation due to RANK-RANKL binding, and $C_{[\text{RANK}\cdot\text{RANKL}]}^{\text{vas}}$ is the concentration of the respective complex in the vascular space.

Definition of $C_{[\text{RANK}\cdot\text{RANKL}]}^{\text{vas}}$ is dealt with in detail in Appendix C. Importantly, one of the quantities on which $C_{[\text{RANK}\cdot\text{RANKL}]}^{\text{vas}}$ depends, i.e., the production of concentration of RANKL, is also driven mechanically; decreasing mechanical loading leads to increasing production of RANKL (Henriksen et al., 2003). In order to include this effect in our model, we introduce a mechanically induced RANKL production term $P_{\text{RANKL}}^{\text{mech,vas}}$. Taking into account that both osteoblast precursors and osteocytes produce RANKL (Nakashima et al., 2011), $P_{\text{RANKL}}^{\text{mech,vas}}$ is defined as follows:

$$P_{\text{RANKL}}^{\text{mech,vas}} = \kappa \left[C_{\text{OBp}}^{\text{vas}} \left(1 - \frac{p_{\text{vas}}^{\text{peak}_f}}{p_{\text{vas}}^{\text{peak}_f}} \right) + C_{\text{OCY}}^{\text{exvas}} \frac{1 - f_{\text{vas}}}{f_{\text{vas}}} \left(1 - \frac{p_{\text{lac}}^{\text{peak}_f}}{p_{\text{lac}}^{\text{peak}_f}} \right) \right] \geq 0, \quad (2.18)$$

with κ as the (mechanically governed) inhibition parameter for RANKL production, which we assume to be identical for both osteoblast precursors and osteocytes.

2.4 Model calibration and validation

2.4.1 Simulation of bone formation and bone resorption occurring upon loading of mouse tibiae

First, we consider the experimental study of Sugiyama et al. (2012), who subjected mouse tibiae to axial compression, at a frequency of 0.1 Hz, for 40 cycles per day, over a period of 16 days. Thereby, the magnitude of the applied compressive force was varied from 0 to 14 N, resulting in peak compressive strains ranging from 0 to 2600×10^{-6} , see Figure 2.3(a). A linear fit of the experimental data points

shows that at a peak strain of $E^{\text{peak}} = -1056 \times 10^{-6}$ bone volume is neither gained nor lost; thus, we consider this strain value as a kind of reference or steady state-value $\overline{E^{\text{peak}}}$, corresponding, via our poromicromechanical model, see Appendix B, to $\overline{p_{\text{vas}}^{\text{peak}} \mathfrak{f}} = 23.3 \text{ kPa/s}$ and $\overline{p_{\text{lac}}^{\text{peak}} \mathfrak{f}} = 144.1 \text{ kPa/s}$.

Then, we simulate mechanical load cases aiming at replication of the experimentally recorded relation between change of bone volume and peak strains. Considering an initial vascular porosity of trabecular bone of $f_{\text{vas,ini}} = 0.8$, relating to an initial extravascular bone matrix volume fraction f_{bm} (often called BV/TV in the context of morphometric measurements) of $f_{\text{bm,ini}} = 1 - f_{\text{vas,ini}} = 0.2$, as shown in literature for the proximal metaphyseal mouse tibia (Fritton et al., 2005), a lacunar porosity of $f_{\text{lac,ini}}^{\text{exas}} = 0.1$ (Buckwalter et al., 1995a; Tai et al., 2008), and an osteocyte concentration of $C_{\text{OCY}}^{\text{exas}} = 5.928 \times 10^{-2} \text{ pM}$, according to the osteocyte density in rat tibia reported by Mader et al. (2013), allowed us to back-calculate the mechanoregulatory parameters $\lambda_{\text{OBp}}^{\text{vas}}$, $\lambda_{\text{WNT/SCLR}}^{\text{vas}}$, see Eq. (2.16), and κ , see Eq. (2.18), as $\lambda_{\text{OBp}}^{\text{vas}} = 2$, $\lambda_{\text{WNT/SCLR}}^{\text{vas}} = 100 \text{ pM}^{-1}$, and $\kappa = 3.5 \times 10^4 \text{ day}^{-1}$; for the remaining model parameters, see Appendix D. Thereby, the bone resorption and formation rates were set to $k_{\text{OCa}}^{\text{res}} = 20 \text{ (pM} \cdot \text{day)}^{-1}$ and $k_{\text{OBa}}^{\text{form}} = 4 \text{ (pM} \cdot \text{day)}^{-1}$. Comparing the resulting bone change after 16 days, see Figure 2.3(b), with the corresponding experimental data shows a remarkably good agreement, corroborating the adequacy of our model, see Figure 2.3(a).

For the sake of illustrating of how our model works, it is furthermore instructive to elucidate the mechanisms that lead to the evolutions of the bone volume fraction when prescribing disuse and overuse load cases. For this purpose, we consider two of the load cases of Sugiyama et al. (2012), starting with the one leading to a peak strain of $E^{\text{peak}} = -700 \times 10^{-6}$, thus $|E^{\text{peak}}| < |\overline{E^{\text{peak}}}|$. Initializing this load case at $t = 0$ leads to an instantaneous decrease of the mechanical stimuli considered in our model, see Figure 2.3(c). Several mechanoregulation-related consequences follow: On the one hand, the mechanically induced production of RANKL is promoted, see Eq. (2.18), leading to a significant increase of osteoclast precursor differentiation, and a significant increase of the concentration of active osteoclasts, see the black dashed line in Figure 2.3(d). On the other hand, due to cell concentration changes following the change of f_{vas} , the concentration of active osteoblasts slightly decreases, see the black solid line in Figure 2.3(d). As a consequence, bone loss, i.e., the decrease of the volume fraction of extravascular bone matrix, f_{bm} , is initiated, see the green dashed line in Figure 2.3(b). Over time, the change of the bone composition implies that the mechanical stimuli again reach steady states. Thereby, it is remarkable that $\overline{p_{\text{lac}}^{\text{peak}} \mathfrak{f}}$ apparently approaches $\overline{p_{\text{lac}}^{\text{peak}} \mathfrak{f}}$ faster than $\overline{p_{\text{vas}}^{\text{peak}} \mathfrak{f}}$ approaches $\overline{p_{\text{vas}}^{\text{peak}} \mathfrak{f}}$, see Figure 2.3(c). As for the related concentrations of active osteoblasts and osteoclasts, it

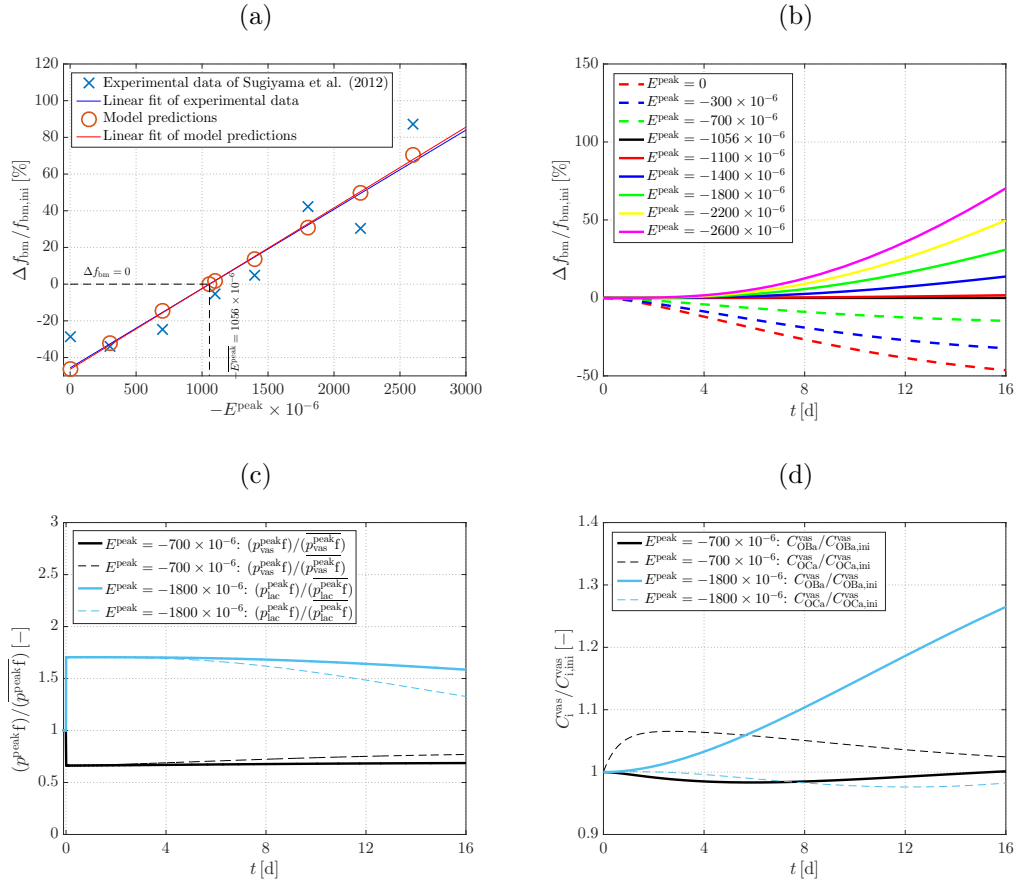


Figure 2.3: (a) Comparison of the model-predicted change in extravascular bone matrix volume fraction, f_{bm} , in the mouse tibia, following compressive loading for 16 days, with the experimental results of Sugiyama et al. (2012); (b) Model simulation of the evolution of the change in f_{bm} over 16 days, loaded with the peak strain values of Sugiyama et al. (2012); (c) Evolution of the mechanical stimulus, normalized with the steady state mechanical stimulus, for a case of disuse (black lines) and one of overuse (blue lines) from the mouse studies in Figure 2.3(b); (d) Evolutions of the vascular active osteoblast and active osteoclast concentrations, normalized with their initial vascular concentrations, for a case of disuse (black lines) and one of overuse (blue lines) from the mouse studies in Figure 2.3(b)

can be observed that, after the initial, disuse-related changes, both osteoblast and osteoclast concentrations converge towards steady states, see the two black lines in Figure 2.3(d).

Secondly, we consider the load case of Sugiyama et al. (2012) leading to a peak strain of $E^{\text{peak}} = -1800 \times 10^{-6}$, thus $|E^{\text{peak}}| > |\overline{E^{\text{peak}}}|$. Initializing this load case at $t = 0$ leads to an instantaneous increase of the mechanical stimuli considered in our model, see Figure 2.3(c). The mechanically-induced osteoblast precursor proliferation is promoted via Eq. (2.16), leading to a significant increase of the concentration of active osteoblasts, see the blue solid line in Figure 2.3(d). Additionally, due to the change of f_{vas} , the concentration of the active osteoclasts slightly increases after an initial decrease, see the blue dashed line in Figure 2.3(d). As a consequence, bone gain, i.e., the increase of the volume fraction of extravascular bone matrix, f_{bm} , is initiated, see the green solid line in Figure 2.3(b). Again, $\overline{p_{\text{lac}}^{\text{peak}}}$ apparently approaches $\overline{p_{\text{lac}}^{\text{peak}}}$ faster than $\overline{p_{\text{vas}}^{\text{peak}}}$ approaches $\overline{p_{\text{vas}}^{\text{peak}}}$, see Figure 2.3(c). It can be observed that after the initial, overuse-related changes, both active osteoblast and active osteoclast concentrations continue to increase, see the two black lines in Figure 2.3(d), and a steady state is not yet reached in the given time frame.

2.4.2 Independent model check: simulation of bone resorption in tibiae of tail-suspended rats

Next, we check whether our model is capable of reproducing experimental data collected from the proximal tibiae of tail-suspended rats, considering for this purpose the experiments of Laib et al. (2000). We assume that the mechanical sensitivity and cell activities between mice and rats are comparable, thus we borrow the values of $\overline{p_{\text{vas}}^{\text{peak}}}$, $\overline{p_{\text{lac}}^{\text{peak}}}$, and κ , as well as $k_{\text{OCa}}^{\text{res}}$ and $k_{\text{OBa}}^{\text{form}}$ from the back-analysis described in Section 2.4.1. Furthermore, we assume, for simplicity, that tail-suspension actually induces a complete removal of mechanical loading on the hindlimb, i.e., in our model the mechanical loading is set to zero. Comparing then the model-predicted bone loss with the experimentally recorded values shows that after six days the difference between model and experiment amounts to 10.85%, and after 16 days this difference is 10.16%, see Figure 2.4. Hence, without any data fitting, we arrived at remarkably good agreements between model predictions and corresponding experimental results.

2.4.3 Simulation of bone resorption resulting from exposure to microgravity

Exposure to microgravity (as it occurs e.g., in spaceflight) implies a reduced mechanical loading leading to significant bone loss. For studying this effect quantitatively, we consider cortical bone, with $f_{\text{bm,ini}} = 0.95$. We consider that the mechanical

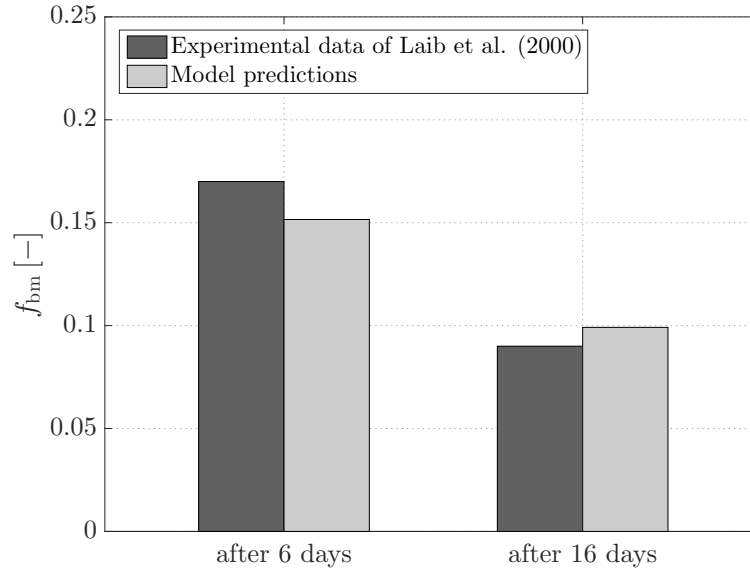


Figure 2.4: Comparison of model-predicted extravascular bone matrix volume fraction decrease in tibiae of rats with tail-suspension after 6 and 16 days, with experimental data from Laib et al. (2000): dark grey bar – experimental data; light grey bar – model-predicted disuse-related change in f_{bm} , with the same model parameters as in the case of the mouse, see Section 2.4.1

stimulus in steady state relates to walking under normal terrestrial conditions. According to Burr et al. (1996), walking induces peak strains of -500×10^{-6} , while the load frequency is 2 Hz, which can be “translated”, by means of our poromicromechanical model, into $p_{\text{vas}}^{\text{peak}} \mathbf{f} = 406.5 \text{ kPa/s}$ and $p_{\text{lac}}^{\text{peak}} \mathbf{f} = 1694.5 \text{ kPa/s}$. In microgravity conditions, we assume peak strains of -5×10^{-6} and a loading frequency of 30 Hz to arise from muscle contractions as the only source of mechanical loading (Fritton et al., 2000; Rubin et al., 2001). Furthermore, we consider an osteocyte density of $C_{\text{OCY}}^{\text{exvas}} = 7.705 \times 10^{-2} \text{ pM}$, according to the values reported for women of various ages by Metz et al. (2003), as well as a bone resorption rate of $k_{\text{OCa}}^{\text{res}} = 2 \text{ (pM} \cdot \text{day)}^{-1}$, a bone formation rate of $k_{\text{OBa}}^{\text{form}} = 0.4 \text{ (pM} \cdot \text{day)}^{-1}$, and $\kappa = 5 \times 10^4 \text{ day}^{-1}$.

Evaluating our model in terms of the bone loss over time, see Figure 2.5, shows again satisfying agreement with corresponding experimental data. According to Vico et al. (2000), the loss of bone mineral density after being exposed to microgravity for 6 months amounted to 2.5% in the distal radius and 4.3% in the distal tibia – corresponding to a bone loss rate of 0.42%/month (distal radius) and 0.72%/month (distal tibia). Our model predicts a bone loss of 4.36% in 180 days, or a bone loss rate of 0.73%/month, a value very close to the experimental results for distal tibia.

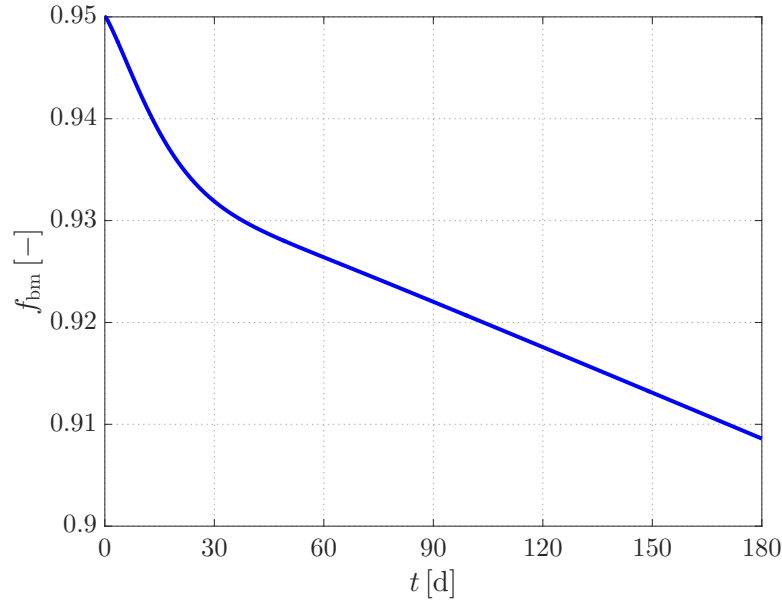


Figure 2.5: Simulation of decreasing extravascular bone matrix volume fraction arising from spaceflight-induced disuse lasting for 180 days

2.5 Parameter studies

2.5.1 Study of mechanoregulatory model features

In order to show how our model responds to variations of the mechanoregulatory parameters, we perform disuse and overuse simulations, based on $\overline{E^{\text{peak}}} = -500 \times 10^{-6}$, and with disuse simulated through prescribing $E^{\text{peak}} = 0.9\overline{E^{\text{peak}}}$, while for the overuse load case $E^{\text{peak}} = 1.1\overline{E^{\text{peak}}}$. For all simulations, the load frequency was set to 2 Hz. For the mechanoregulatory parameters, the following ranges were considered: $\lambda_{\text{OBp}}^{\text{vas}}$ was varied between 0.1 and 0.5, $\lambda_{\text{WNT/SCLR}}^{\text{vas}}$ was varied between 0.1 and 0.5 pM^{-1} , and κ was varied between 1×10^5 and $5 \times 10^5 \text{ day}^{-1}$. Furthermore, in order to also study the consequences of varying cell effectivities, the bone formation rate $k_{\text{OBa}}^{\text{form}}$ was varied between 0.2 and 0.8 $(\text{pM} \cdot \text{day})^{-1}$, and the bone resorption rate $k_{\text{OCa}}^{\text{res}}$ was varied between 1 and 4 $(\text{pM} \cdot \text{day})^{-1}$. In order to study the different behaviors of cortical and trabecular bone, we have considered both types of bone, with $f_{\text{bm,ini}} = 0.95$ for cortical bone, and $f_{\text{bm,ini}} = 0.2$ for trabecular bone. For ensuring good comparability of the results, we consider in the following the relative change of the extravascular bone volume fraction at specific points in time, $(f_{\text{bm}}(t) - f_{\text{bm,ini}})/f_{\text{bm,ini}} = \Delta f_{\text{bm}}(t)/f_{\text{bm,ini}}$, namely at $t = 10 \text{ d}$ and at $t = 100 \text{ d}$, with $t = 0$ being the point of initialization of the respective load cases.

It turns out that for disuse loading both κ and $k_{\text{OCa}}^{\text{res}}$ affect the amount of bone loss

significantly, see Figure 2.6(a) and (b), particularly after 100 days. Furthermore, the influences of κ and k_{OCa}^{res} on the bone loss are non-linear, with these non-linearities being more pronounced at 100 days. Comparing Figures 2.6(a) and (b) shows that in trabecular bone the relative bone loss is much higher than in cortical bone. The overuse simulations are evaluated in two ways: First, the influences of the bone formation rate, k_{OBa}^{form} , and of the anabolic strength parameter related to the osteoblast precursors, λ_{OBp}^{vas} , on the bone gain are shown. After 100 days, the increase of the extravascular bone matrix volume fraction is again significantly non-linear, for both cortical and trabecular bone, see Figures 2.6(c) and (d), while after 10 days, the observed bone gain is quite small and apparently only weakly influenced by k_{OBa}^{form} and λ_{OBp}^{vas} . This indicates that the effect of increased osteoblast proliferation is kind of time-delayed with respect to overuse initialization. Secondly, both λ_{OBp}^{vas} and $\lambda_{WNT/SCLR}^{vas}$ are varied, in order to study the effects of independently perturbed anabolic sensitivities of osteoblasts and osteocytes. Again, after 10 days, bone gain is apparently weakly influenced by variations of λ_{OBp}^{vas} and $\lambda_{WNT/SCLR}^{vas}$. After 100 days, the relative bone gain is much more pronounced for both cortical and trabecular bone, see Figures 2.6(e) and (f), while the relative bone gain is much higher for trabecular bone. Also, it is remarkable that for trabecular bone the influence of λ_{OBp}^{vas} is negligible, while for cortical bone both parameters are actually effective in terms of influencing bone gain due to overuse.

2.5.2 Effects of temporary disuse in aging bone

It is well known that the bone porosities change in the course of aging; the vascular porosity increases, while the lacunar porosity decreases. In particular, Cooper et al. (2007) have shown that the inverse of the cortical porosity decreases linearly, with $d[(f_{vas})^{-1}]/dt = -0.43\%^{-1}/\text{year}$, leading to an exponential increase of f_{vas} . On the other hand, according to Busse et al. (2010), $d(f_{lac}^{exvas})/dt = -5 \times 10^{-4}/\text{year}$. Since these porosity changes imply respective changes of the hydrostatic pressures occurring in response to a certain mechanical loading applied macroscopically, the question arises how aging influences the effects of a changed mechanical environment. For addressing this issue, we consider cortical bone, with $f_{vas,ini} = 0.05$ and $f_{lac,ini}^{exvas} = 0.1$. The anabolic strength parameters were set to $\lambda_{OBp}^{vas} = 0.5$ and $\lambda_{WNT/SCLR}^{vas} = 130 \text{ pM}^{-1}$, while all other model parameters were set as described in Section 2.4.3, and the same disuse loading as defined in Section 2.5.1 was prescribed. After initialization, the disuse loading was maintained for five years, after which the loading returned to the original magnitude.

Assuming that the number of lacunar pores reaches its maximum at an age of 18 years, and that, at the same age, vascular porosity starts to increase (Cooper et al.,

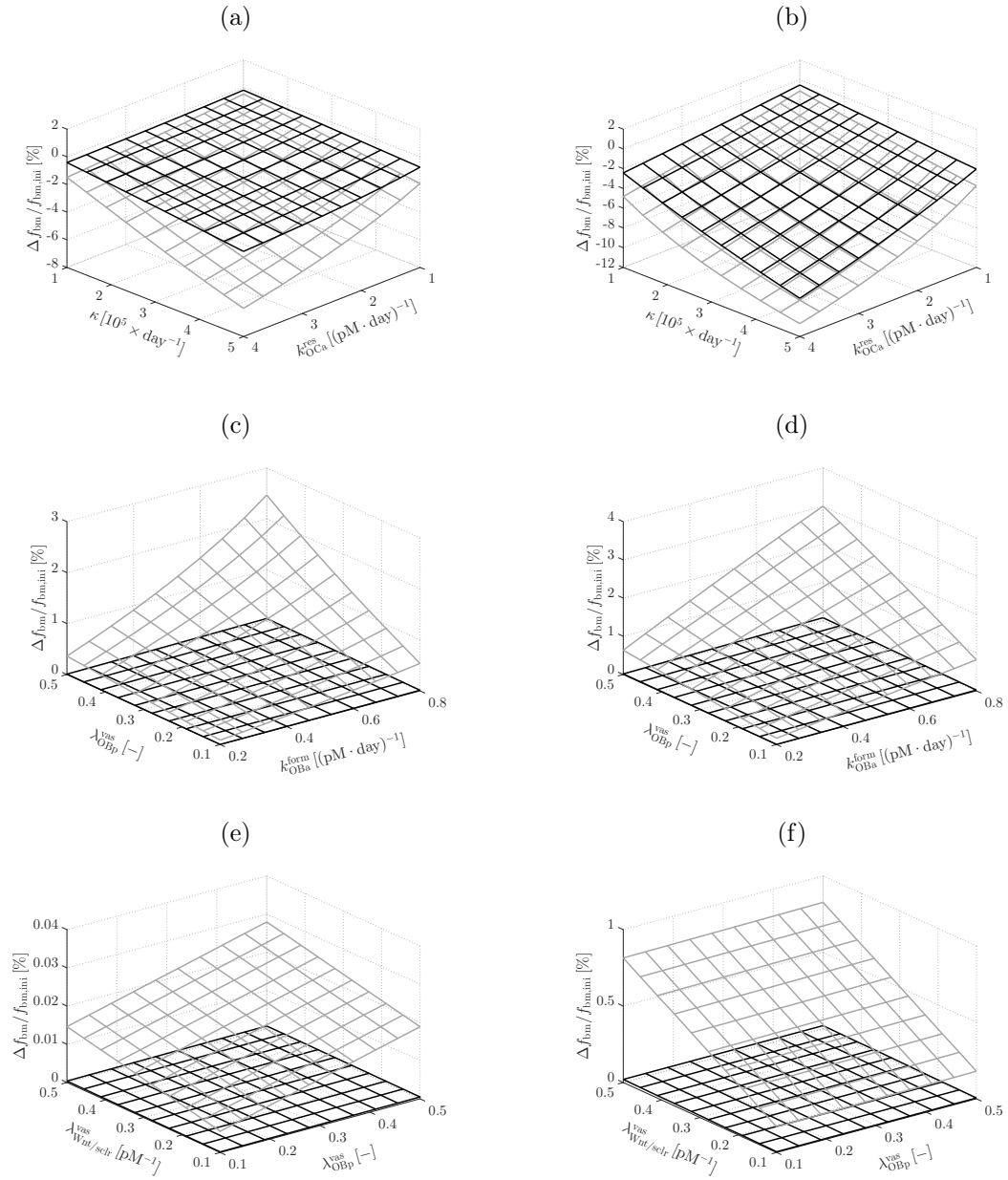


Figure 2.6: Parameter studies: Dependence of the relative decrease of the bone matrix volume fraction after 10 days of disuse (black graph) and 100 days of disuse (grey graph) on the resorption factor k_{OCa}^{res} and inhibition parameter κ , for (a) cortical bone, with an initial bone matrix volume fraction $f_{bm,ini} = 0.95$; (b) trabecular bone, with an initial bone matrix volume fraction $f_{bm,ini} = 0.2$; Dependence of the relative increase in bone matrix volume fraction after 10 days of overuse (black graph) and 100 days of overuse (grey graph) on the formation factor k_{OBa}^{form} and anabolic strength parameter λ_{OBp}^{vas} , for (c) cortical bone; (d) trabecular bone; Dependence of the relative increase in bone matrix volume fraction after 10 days of overuse (black graph) and 100 days of overuse (grey graph) on the anabolic strength parameters $\lambda_{Wnt/sclr}^{vas}$ and λ_{OBp}^{vas} , for (e) cortical bone; (f) trabecular bone

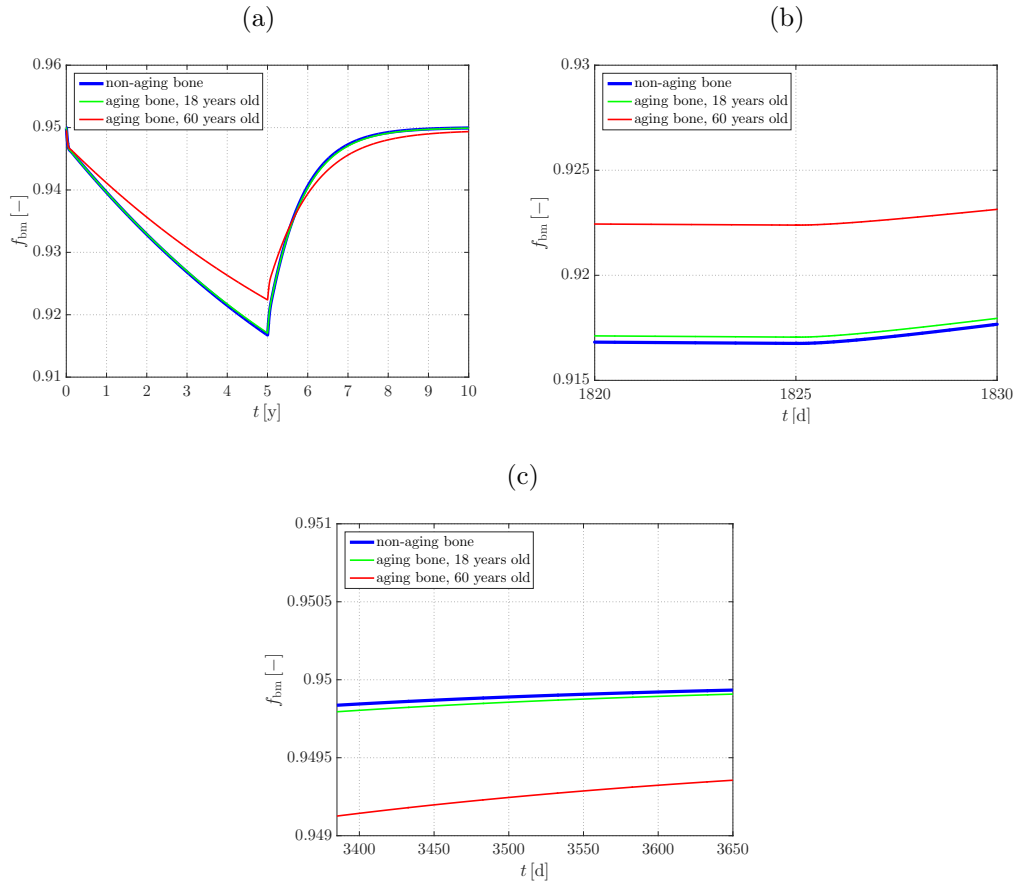


Figure 2.7: Effects of five years of disuse, followed by five years of steady-state loading, in aging and non-aging bone: (a) full 10 year time span; (b) zoom into region around five years; (c) zoom in on the last year

2007), simulations have been performed for non-aging bone, for aging bone, i.e., bone with increasing vascular porosity and decreasing lacunar porosity at 18 years of age, and for aging bone at 60 years of age, see Figure 2.7. Figure 2.7(a) shows that, with aging, there is a delay in the bone adaptation to mechanical loading, characterized by a slower decrease of f_{bm} with disuse, and that this effect is much more pronounced in bone that is already old than in rather young bone, compare red and green lines. The same effect can be seen during re-loading after five years of disuse, see Figure 2.7(b): there is a decelerated increase of f_{bm} , which is much more pronounced for 60-year old than for 18-year old bone, see red and green lines.

Thus, due to aging, at the end of the 10 years simulated, the bone composition reaches a lower value than in the case of non-aging bone, compare blue with green and red lines in Figure 2.7(c). Once again, the effect is much more pronounced in older bone. This suggests that, with aging, the restoration of the original bone composition

after temporary disuse is slower, and delayed compared to non-aging bone. However, these simulations also show that the effects of aging-related porosity changes on the responsiveness of bone remodeling changes in the mechanical environment are of minor importance. Thus, other mechanisms, such as osteocyte apoptosis, are required to obtain the significantly impaired mechanosensitivity of senescent bone (Wong et al., 1987; Dunstan et al., 1990, 1993; Jilka et al., 2013; Jilka and O'Brien, 2016).

2.5.3 Mechanoresponsiveness without osteocytes – example of fish bone

It is well known that some fish are acellular or anosteocytic (Weiss and Watabe, 1979; Glowacki et al., 1986). Nevertheless, the bones of such fish do actually still adapt to loads; e.g., Shahar and Dean (2013) and Atkins et al. (2014) report on the ability for local damage repair in the rostrum bone of billfishes, and Meyer (1987); Huysseune et al. (1994); Hegrenes (2001); Witten and Huysseune (2010) and Muschick et al. (2011) report on the adaptation of jaw trabecular bone in chichlids. On the one hand, this confirms our modeling strategy concerning the consideration of both osteoblasts and osteocytes as mechanosensitive cells (given that apparently osteocytes are not the only mechanosensing cells in bone). On the other hand, the aforementioned findings have motivated us to perform simulations for bone tissue without osteocytes; this may be also relevant for certain bone pathologies because of which osteocytes are partially or even completely absent. For this purpose, we consider both cortical bone (with $f_{\text{bm,ini}} = 0.95$) and trabecular bone (with $f_{\text{bm,ini}} = 0.2$); all model parameters were chosen as described in Section 2.5.2, except for $\lambda_{\text{OBP}}^{\text{vas}}$, changed to 0.05 and $\lambda_{\text{WNT/SCLR}}^{\text{vas}} = 2.49 \text{ pM}^{-1}$. Both disuse and overuse simulations are carried out (again as described in Section 2.5.2), for bone with and for bone without osteocytes.

Figure 2.8(a) shows the evolution of the bone matrix volume fraction with disuse, with osteocytes present and not present. Interestingly, when not considering osteocytes in cortical bone, f_{bm} changes very little with disuse loading, as shown by the black dashed line. However, in the case of trabecular bone, anosteocytic bone is able to follow the decrease of f_{bm} over time, see blue dashed line, similar to the osteocytic case. Moreover, the decrease seems to be even accelerated in the case of bone without osteocytes, thus confirming the mechanosensing capabilities of osteoblast precursors.

When not considering osteocytes in cortical bone, f_{bm} changes very little also with overuse loading, as shown by the black dashed line in Figure 2.8(b). The contribution of osteoblast precursors and osteocytes to the mechanically-induced osteoblast proliferation in Eq. (2.16) was considered in the model to be proportional to the respective cells' *macroscopic* concentrations. In cortical bone, due to the large

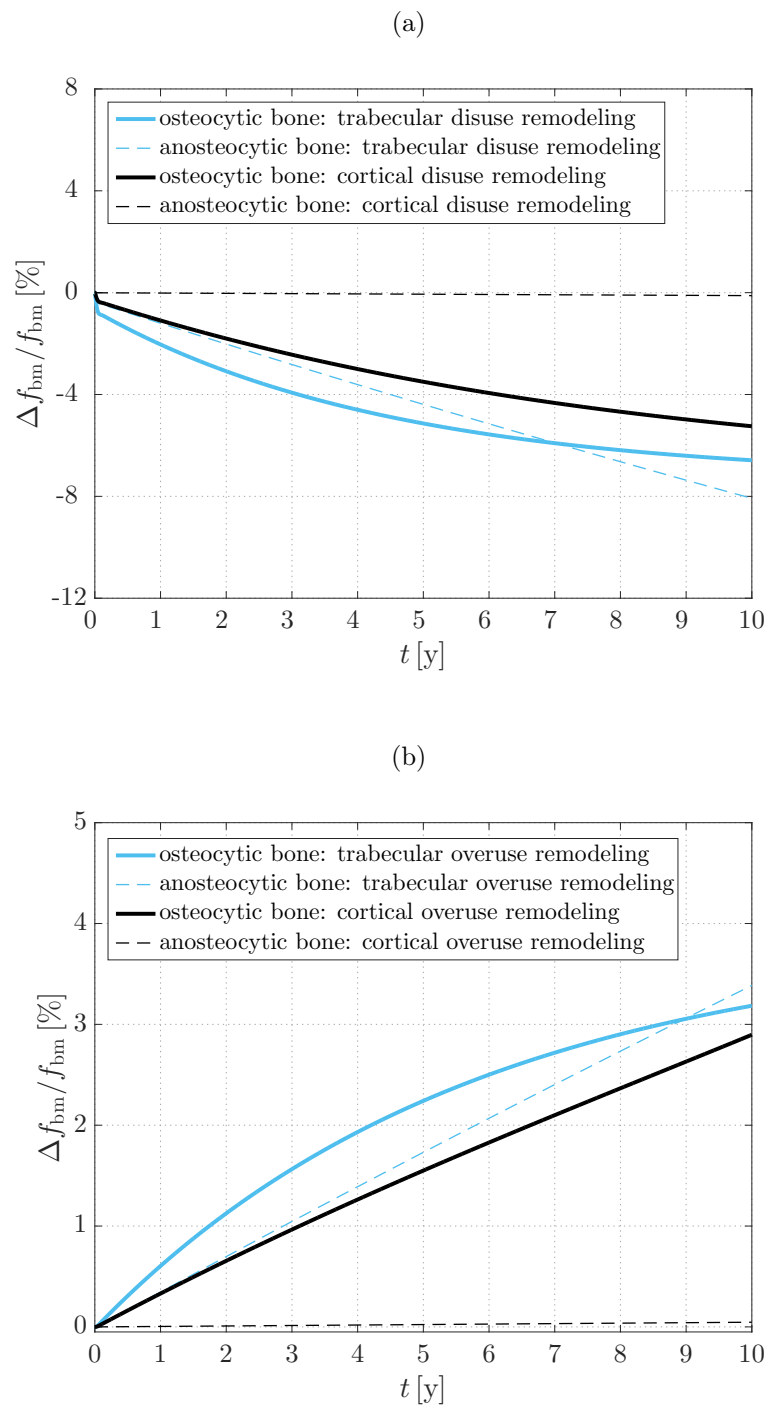


Figure 2.8: (a) Disuse and (b) Overuse simulation in trabecular and cortical bone with and without osteocytes, over a period of ten years

volume fraction of bone matrix in which osteocytes are embedded, these cells have a much higher macroscopic concentration than osteoblast precursors. As such, the contribution of osteocytes to the mechanically-induced bone formation via osteoblast precursor proliferation is quite large. The osteoblast precursors may indeed take over the mechanosensing with overuse in cortical bone, but they are not able to make up for this large contribution. On the other hand, in trabecular bone with no osteocytes, see blue dotted line in Figure 2.8(b), there is still a significant increase in f_{bm} with overuse, even more accelerated than in the case of osteocytic trabecular bone. Osteocytes have a much lower contribution to the mechanosensing process due to their relatively low macroscopic concentration, stemming from the low volume fraction of the trabecular bone matrix. Thus, even without them, osteoblast precursors are still able to stimulate bone formation with increased mechanical loading.

2.6 Discussion

In this paper, a mathematical model of bone remodeling is presented, based on coupling a multiscale systems biology model with a multiscale bone mechanics model. This way, for the very first time, all mechanisms eventually driving bone remodeling can be considered on the respectively relevant length scale. The adequacy of the derived model formulation has been confirmed by a number of simulations, dealing with disuse and/or overuse scenarios to which mice, rats, and humans were subjected, see Sections 2.4.1 to 2.4.3 – consistently, model predictions nicely agree with corresponding experimental data.

Remarkably, most of the involved model parameters were held constant throughout all simulations. However, the parameters governing the mechanobiology of bone remodeling, as well as the eventual activities of active osteoblasts and osteoclasts had to be varied species-specifically, see Table 2.1. It is furthermore interesting to consider the trends of the aforementioned parameters. It appears that in our model the activities of osteoblasts and osteoclasts, quantified through the formation and resorption factors, must be highest for mice, and lowest for humans. This finding is perfectly confirmed by a large number of previous works, showing that the bone (mechano)biology of small animals is much more responsive to changes in their biochemical and mechanical environments than this is the case for large animals (Vico and Alexandre, 1992; Checa et al., 2011; Borgiani et al., 2015).

This variation provides also incentives for future model extensions and refinements. Explicitly taking into account the mechanisms that eventually lead to the species-specificity is certainly a desirable (yet challenging) goal.

Table 2.1: Performed simulations and parameters related to mechanical stimulus, namely steady-state compressive peak strain $-\overline{E}^{\text{peak}}$; steady-state mechanical stimulus related to vascular pressure $p_{\text{vas}}^{\text{peak}}$; steady-state mechanical stimulus related to lacunar pressure $p_{\text{lac}}^{\text{peak}}$; peak compressive strain range during the simulation $-\overline{E}^{\text{peak}}$; ratios between steady-state and simulation-related mechanical stimuli, $(p_{\text{vas}}^{\text{peak}})/(\overline{p_{\text{vas}}^{\text{peak}}})$ and $(p_{\text{lac}}^{\text{peak}})/(\overline{p_{\text{lac}}^{\text{peak}}})$, entering mechanosensitivity Eqs. (2.16) and (2.18); values of $(p_{\text{vas}}^{\text{peak}})/(\overline{p_{\text{vas}}^{\text{peak}}})$ and $(p_{\text{lac}}^{\text{peak}})/(\overline{p_{\text{lac}}^{\text{peak}}})$ lower than 1 relate to disuse, whereas values higher than 1 relate to overuse

Species	$-\overline{E}^{\text{peak}}$ $\times 10^{-6}$	$\overline{p_{\text{vas}}^{\text{peak}}}$ [kPa/s]	$\overline{p_{\text{lac}}^{\text{peak}}}$ [kPa/s]	$-\overline{E}^{\text{peak}}$ $\times 10^{-6}$	$\frac{p_{\text{vas}}^{\text{peak}}}{\overline{p_{\text{vas}}^{\text{peak}}}}$ [-]	$\frac{p_{\text{lac}}^{\text{peak}}}{\overline{p_{\text{lac}}^{\text{peak}}}}$ [-]
Mouse (disuse)	1056.03	23.30	144.09	0.026 – 819.47	$2.47 \times$ $10^{-5} - 0.66$	$2.47 \times$ $10^{-5} - 0.66$
Mouse (overuse)	1056.03	23.30	144.09	1081.29 – 2600.33	1.04 – 2.46	1.03 – 2.46
Rat (disuse)	1056.03	22.42	143.68	0.027 – 0.052	(2.59 – $2.91) \times 10^{-5}$	(2.59 – $4.81) \times 10^{-5}$
Human (disuse)	501.35	406.50	169.65	5.01 – 5.24	0.150 – 0.162	0.150 – 0.154

2.7 Acknowledgements

Financial support by the European Research Council (ERC), in the framework of the project *Multiscale poromicromechanics of bone materials, with links to biology and medicine* (project number FP7–257023), is gratefully acknowledged.

2.8 Appendix A: Abbreviations and nomenclature

OBa	active osteoblasts
OBp	committed osteoblast precursors
OBu	uncommitted osteoblast precursors
OCa	active osteoclasts
OCp	committed osteoclast precursors
OCY	osteocytes
$\alpha_{\text{TGF}\beta}^{\text{exas}}$	amount of TGF β in one dm ³ of extravascular bone
$\beta_{\text{RANKL}}^{\text{exas(OCY)}}$	extravascular RANKL production by OCY
$\beta_{\text{RANKL}}^{\text{vas(OBp)}}$	vascular RANKL production by OBp
$\beta_{\text{RANKL}}^{\text{vas(OCY)}}$	vascular RANKL production by OCY
$\beta_{\text{PTH}}^{\text{vas}}$	vascular intrinsic PTH production

$\kappa_{\text{OBp}} = \kappa_{\text{OCY}} = \kappa$	inhibition parameters that allow for tuning of the sensitivity of RANKL production by OBps and OCYs, respectively, to reduced mechanical loading
$\lambda_{\text{OBp}}^{\text{vas}}$	“anabolic strength parameter” for sensitivity of OBp to increased mechanical loading
$\lambda_{\text{WNT/SCLR}}^{\text{vas}}$	“anabolic strength parameter” for sensitivity of OCY to increased mechanical loading through the WNT/SCLR pathway
$\pi_{\text{rep,TGF}\beta}^{\text{OBp}\rightarrow\text{OBa}}$	repression function of OBp differentiation by TGF β
$\pi_{\text{act,TGF}\beta}^{\text{OBu}\rightarrow\text{OBp}}$	activation function of OBU differentiation by TGF β
$\pi_{\text{act,TGF}\beta}^{\text{OCa}\rightarrow\uparrow}$	activation function of OCa apoptosis by TGF β
$\pi_{\text{act,[RANK}\cdot\text{RANKL}]}$	activation function of OCp differentiation by RANKL-RANK binding
$\pi_{\text{act,PTH}}^{\text{maxRANKL}}$	activation function of RANKL production by OBp through PTH
$\pi_{\text{rep,PTH}}^{\text{OPG/OBa}}$	repression function of OPG production by OBa through PTH
$\Pi_{\text{act,OBp}}^{\text{mech,vas}}$	mechanically-induced OBp proliferation
$\hat{\Pi}_{\text{act,OBp}}^{\text{mech,vas}}$	steady state value of the mechanically-induced OBp proliferation
ρ_{RANK}	density of RANK receptors per OCp
Σ_{macro}	macroscopic stress tensor
$\mathbf{b}_{\text{macro}}^{\text{lac}}$	lacunar pore space-specific Biot tensor
$\mathbf{b}_{\text{macro}}^{\text{vas}}$	vascular pore space-specific Biot tensor
$(\mathbf{B}_{\text{macro}}^{\text{lac}})_{\text{lac,vas-u}}$	second-order Skempton tensor related to lacunar pores
$(\mathbf{B}_{\text{macro}}^{\text{vas}})_{\text{lac,vas-u}}$	second-order Skempton tensor related to vascular pores
$\mathbf{C}_{\text{macro}}$	homogenized stiffness tensor of the macroscopic RVE
$\mathbf{C}_{\text{macro}}^{\text{lac,vas-u}}$	homogenized stiffness tensor of the macroscopic RVE, considering both lacunar and vascular pores undrained
$\mathbf{E}_{\text{macro}}$	macroscopic strain tensor
$A_{\text{OBa}}^{\text{vas}}$	apoptosis rate of OBa
$A_{\text{OCa}}^{\text{vas}}$	maximum apoptosis rate of OCa
$D_{\text{OBp}}^{\text{vas}}$	maximum differentiation rate of OBp
$D_{\text{OBu}}^{\text{vas}}$	maximum differentiation rate of OBU
$D_{\text{OCp}}^{\text{vas}}$	maximum differentiation rate of OCp
$\mathcal{P}_{\text{OBp}}^{\text{vas}}$	maximum proliferation rate of OBp
$C_{\text{OBa}}^{\text{macro}}$	macroscopic OBa concentration
$C_{\text{OCa}}^{\text{macro}}$	macroscopic OCa concentration
$C_{\text{OBa}}^{\text{vas}}$	vascular OBa concentration
$C_{\text{OBp}}^{\text{vas}}$	vascular OBp concentration

$C_{\text{OBu}}^{\text{vas}}$	vascular OBU concentration
$C_{\text{OCa}}^{\text{vas}}$	vascular OCa concentration
$C_{\text{OCp}}^{\text{vas}}$	vascular OCp concentration
$C_{\text{OCY}}^{\text{exvas}}$	extravascular OCY concentration
$C_{\text{OPG}}^{\text{vas}}$	vascular concentration of OPG
$C_{\text{OPG,max}}^{\text{vas}}$	maximum vascular concentration of OPG
$C_{\text{PTH}}^{\text{vas}}$	vascular concentration of PTH
$C_{\text{RANK}}^{\text{vas}}$	vascular concentration of RANK
$C_{\text{RANKL}}^{\text{vas}}$	vascular concentration of RANKL
$C_{\text{RANKL,max}}^{\text{vas}}$	maximum vascular concentration of RANKL
$C_{\text{RANKL,tot}}^{\text{vas}}$	total vascular concentration of RANKL
$C_{\text{TGF}\beta}^{\text{vas}}$	vascular concentration of TGF β
$C_{[\text{OPG}\cdot\text{RANKL}]}^{\text{vas}}$	vascular concentration of the OPG-RANKL complex
$C_{[\text{RANK}\cdot\text{RANKL}]}^{\text{vas}}$	vascular concentration of the RANK-RANKL complex
$D_{\text{OPG}}^{\text{vas}}$	vascular degradation rate of OPG
$D_{\text{PTH}}^{\text{vas}}$	vascular degradation rate of PTH
$D_{\text{RANKL}}^{\text{vas}}$	vascular degradation rate of RANKL
$D_{\text{TGF}\beta}^{\text{vas}}$	vascular degradation rate of TGF β
E^{peak}	peak compressive strain during simulations
$\overline{E^{\text{peak}}}$	peak compressive steady state strain during simulations
$K_{\text{rep,TGF}\beta}^{\text{OBp}\rightarrow\text{OBa,vas}}$	repression coefficient of OBp differentiation by TGF β
$K_{\text{act,TGF}\beta}^{\text{OBu}\rightarrow\text{OBp,vas}}$	activation coefficient of OBU differentiation by TGF β
$K_{\text{act,TGF}\beta}^{\text{OCa}\rightarrow\text{t,vas}}$	activation coefficient of OCa apoptosis by TGF β
$K_{\text{act,[RANK}\cdot\text{RANKL}]}^{\text{OCp}\rightarrow\text{OCa,vas}}$	activation coefficient of OCp differentiation by RANK-RANKL binding
$K_{\text{act,PTH}}^{\text{maxRANKL/OBp,vas}}$	activation coefficient of RANKL production by OBp through PTH
$K_{\text{rep,PTH}}^{\text{OPG/OBa,vas}}$	repression coefficient of OPG production by OBa through PTH
$K_{\text{a,[OPG}\cdot\text{RANKL}]}^{\text{vas}}$	association binding constant between OPG-RANKL
$K_{\text{a,[RANK}\cdot\text{RANKL}]}^{\text{vas}}$	association binding constant between RANK-RANKL
M_{macro}^i	modulus-type quantity defined by Coussy for porosity i , $i \in \{\text{vas, lac}\}$
$N_{\text{macro}}^{i,j}$	Biot modulus considering the effect of the pressure in pore space j on the porosity change of pore space i in the macroscopic RVE, $i, j \in \{\text{vas, lac}\}$
N_{OBp}	macroscopic quantity of OBp in mol
N_{OBu}	macroscopic quantity of OBU in mol
$P_{\text{OPG,e}}^{\text{vas}}$	endogeneous vascular production of OPG

$P_{\text{RANKL}}^{\text{mech,vas}}$	mechanically-induced, additional vascular production of RANKL
$P_{\text{RANKL}}^{\text{vas}}$	total vascular production of RANKL
$P_{\text{RANKL,d}}^{\text{vas}}$	external (dosage) vascular production of RANKL
$P_{\text{RANKL,e}}^{\text{vas}}$	endogeneous vascular production of RANKL
V_{exvas}	total volume of the extravascular bone matrix
V_{macro}	volume of the microscopic RVE
V_{vas}	total volume of the vascular pore spaces
f	frequency of the mechanical stimulus
f_{bm}	extravascular bone matrix volume fraction (or BV/TV)
$f_{\text{bm,ini}}$	initial extravascular bone matrix volume fraction (or BV/TV)
$f_{\text{lac}}^{\text{exvas}}$	extravascular lacunar pore volume fraction
$f_{\text{lac,ini}}^{\text{exvas}}$	initial extravascular lacunar pore volume fraction
f_{vas}	vascular pore volume fraction
$f_{\text{vas,ini}}$	initial vascular pore volume fraction
$k_{\text{OBa}}^{\text{form}}$	bone formation factor by OBa
$k_{\text{OCa}}^{\text{res}}$	bone resorption factor by OCa
k_i	bulk modulus of the fluid in pore space i , $i \in \{\text{vas, lac}\}$
$n_{\text{OPG/OBa}}$	quantity of OPG per OBa
$n_{\text{RANKL/OBp}}$	maximum number of RANKL receptors per OBp
$p_{\text{lac}}^{\text{peak}}$	peak amplitude of the lacunar pore pressure
$p_{\text{vas}}^{\text{peak}}$	peak amplitude of the vascular pore pressure
$\frac{p_{\text{lac}}^{\text{peak}}}{f}$	steady state mechanical stimulus related to lacunar porosity
$\frac{p_{\text{vas}}^{\text{peak}}}{f}$	steady state mechanical stimulus related to vascular porosity

2.9 Appendix B: Poromicromechanics model

A multiscale modeling approach for bone as a multiporous material has recently been developed (Morin and Hellmich, 2014; Scheiner et al., 2016), which takes into account the hydrostatic pressure building up in the vascular and lacunar pore spaces, as a result of macroscopically applied loading. The macroscopic stress Σ_{macro} is linearly related to the macroscopic strain $\mathbf{E}_{\text{macro}}$, both acting homogeneously at the boundary of the RVE, as well as to the pore pressures acting in the vascular and lacunar pores, p_{vas} and p_{lac} (Dormieux et al., 2006; Hellmich et al., 2009; Pichler and Hellmich, 2010):

$$\Sigma_{\text{macro}} = \mathbf{C}_{\text{macro}} : \mathbf{E}_{\text{macro}} - \mathbf{b}_{\text{macro}}^{\text{vas}} p_{\text{vas}} - \mathbf{b}_{\text{macro}}^{\text{lac}} p_{\text{lac}}, \quad (2.19)$$

with $\mathbf{C}_{\text{macro}}$ as the macroscopic cortical stiffness tensor, and $\mathbf{b}_{\text{macro}}^{\text{vas}}$ and $\mathbf{b}_{\text{macro}}^{\text{lac}}$ the pore-space specific Biot tensors, which describe the additional macroscopic stress

arising as a consequence of the pressure in the two considered pore spaces. The latter three terms are derived from a homogenization scheme over the macroscopic RVE, as described in more detail by Morin and Hellmich (2014). In this work, a material is understood as a macrohomogeneous, but microheterogeneous body filling an RVE with characteristic length ℓ_{RVE} . Thereby, $\ell_{\text{RVE}} \gg d_{\text{RVE}}$, d_{RVE} representing the characteristic length of inhomogeneities within the RVE, and the “ \gg ”-sign typically refers to a factor of two to three (Drugan and Willis, 1996). On the other hand, $\ell_{\text{RVE}} \ll \{\mathcal{L}, \mathcal{P}\}$, \mathcal{L} representing the characteristic length of the geometry and \mathcal{P} representing the characteristic length of the loading of a structure built up by the material defined on the RVE. In this context, the “ \ll ”-sign typically refers to a factor of five to ten (Kohlhauser and Hellmich, 2013).

In general, the microstructure within one RVE is so complicated that it cannot be described in complete detail. Therefore, quasi-homogeneous subdomains with known physical properties are reasonably chosen. They are called material phases, typically comprising solid and pore phases. The homogenized (upscaled) poroelastic behavior of the material on the observation scale of the RVE can then be estimated from the elastic behavior of the material phases, their volume fractions within the RVE, their characteristic shapes, and their interactions. If a single phase exhibits a heterogeneous microstructure itself, its mechanical behavior can be estimated by introduction of an RVE within this phase, with dimensions $\ell_{\text{RVE},2} \leq d_{\text{RVE}}$, comprising again smaller phases with characteristic length $d_{\text{RVE},2} \ll \ell_{\text{RVE},2}$, and so on. This leads to a multistep homogenization scheme.

In the case of *undrained* lacunar and vascular pores, where the pores are fluid-filled and the fluid does not move, the pore pressures read (Scheiner et al., 2016):

$$p_{\text{vas}} = -(\mathbf{B}_{\text{macro}}^{\text{vas}})_{\text{lac,vas-u}} : \boldsymbol{\Sigma}_{\text{macro}} \quad (2.20)$$

and

$$p_{\text{lac}} = -(\mathbf{B}_{\text{macro}}^{\text{lac}})_{\text{lac,vas-u}} : \boldsymbol{\Sigma}_{\text{macro}}, \quad (2.21)$$

with the second-order Skempton tensors $(\mathbf{B}_{\text{macro}}^{\text{vas}})_{\text{lac,vas-u}}$ and $(\mathbf{B}_{\text{macro}}^{\text{lac}})_{\text{lac,vas-u}}$ explicit as

$$\begin{aligned} (\mathbf{B}_{\text{macro}}^{\text{vas}})_{\text{lac,vas-u}} &= \frac{M_{\text{macro}}^{\text{vas}} N_{\text{macro}}^{\text{lac,vas}}}{(N_{\text{macro}}^{\text{lac,vas}})^2 - M_{\text{macro}}^{\text{lac}} M_{\text{macro}}^{\text{vas}}} \\ &\times (\mathbf{b}_{\text{macro}}^{\text{lac}} M_{\text{macro}}^{\text{lac}} + \mathbf{b}_{\text{macro}}^{\text{vas}} N_{\text{macro}}^{\text{lac,vas}}) : (\mathbf{C}_{\text{macro}}^{\text{lac,vas-u}})^{-1} \end{aligned} \quad (2.22)$$

and

$$\begin{aligned} (\mathbf{B}_{\text{macro}}^{\text{lac}})_{\text{lac,vas-u}} &= \frac{M_{\text{macro}}^{\text{lac}} N_{\text{macro}}^{\text{lac,vas}}}{(N_{\text{macro}}^{\text{lac,vas}})^2 - M_{\text{macro}}^{\text{lac}} M_{\text{macro}}^{\text{vas}}} \\ &\times (\mathbf{b}_{\text{macro}}^{\text{vas}} M_{\text{macro}}^{\text{vas}} + \mathbf{b}_{\text{macro}}^{\text{lac}} N_{\text{macro}}^{\text{lac,vas}}) : (\mathbf{C}_{\text{macro}}^{\text{lac,vas-u}})^{-1}. \end{aligned} \quad (2.23)$$

M_{macro}^i is a modulus-type quantity, defined by Coussy (2004) as

$$\frac{1}{M_{\text{macro}}^i} = \frac{f_i}{k_i} + \frac{1}{N_{\text{macro}}^{i,i}}, \quad i \in \{\text{lac}, \text{vas}\}, \quad (2.24)$$

f_i being the corresponding volume fraction of the porosity, k_i the bulk modulus of the fluid in the pore space i , approximated with that of water, $k_{\text{vas}} = k_{\text{lac}} = 2.3$ kPa, and $N_{\text{macro}}^{i,j}$ the Biot moduli, which consider the effect of the pressure in pore space j on the porosity change of pore space i in the macroscopic RVE. Finally, $\mathbf{C}_{\text{macro}}^{\text{lac,vas-u}}$ is the undrained homogenized stiffness tensor of the RVE, taking into consideration both undrained lacunar and undrained vascular pores; it links the macroscopic strains multi-linearly to the macroscopic stresses, and it reads as (Scheiner et al., 2016)

$$\begin{aligned} \mathbf{C}_{\text{macro}}^{\text{lac,vas-u}} = & \mathbf{C}_{\text{macro}} + \mathbf{b}_{\text{macro}}^{\text{lac}} \otimes \left[\frac{M_{\text{macro}}^{\text{lac}} N_{\text{macro}}^{\text{lac,vas}}}{(N_{\text{macro}}^{\text{lac,vas}})^2 - M_{\text{macro}}^{\text{lac}} M_{\text{macro}}^{\text{vas}}} \right. \\ & \times \left. (\mathbf{b}_{\text{macro}}^{\text{vas}} M_{\text{macro}}^{\text{vas}} + \mathbf{b}_{\text{macro}}^{\text{lac}} N_{\text{macro}}^{\text{lac,vas}}) \right] \\ & + \mathbf{b}_{\text{macro}}^{\text{vas}} \otimes \left[\frac{M_{\text{macro}}^{\text{vas}} N_{\text{macro}}^{\text{lac,vas}}}{(N_{\text{macro}}^{\text{lac,vas}})^2 - M_{\text{macro}}^{\text{lac}} M_{\text{macro}}^{\text{vas}}} \right. \\ & \times \left. (\mathbf{b}_{\text{macro}}^{\text{lac}} M_{\text{macro}}^{\text{lac}} + \mathbf{b}_{\text{macro}}^{\text{vas}} N_{\text{macro}}^{\text{lac,vas}}) \right]. \end{aligned} \quad (2.25)$$

For a specific prescribed macroscopic mechanical loading, the aforementioned model gives access to the vascular and lacunar pore pressures, which, together with the loading frequency, act as mechanical stimuli driving two mechanoregulatory processes: the proliferation of osteoblast precursors due to increased mechanical loading, see Eq. (2.16); and the extra production of RANKL due to decreased mechanical loading, see Eq. (2.18).

2.10 Appendix C: Mass kinetics equations and definition of vascular concentrations of biochemical factors

The mathematical functions describing the dependencies within the RANK-RANKL-OPG signalling pathway are based on the occurrence of the three factors, quantified through their vascular concentrations, which unfold their effects upon binding to specific molecules, acting either as receptor or ligand. Receptors are parts of cells, featuring an extracellular domain to which external ligands can bind, causing a cell reaction (Lauffenburger and Linderman, 1993). The binding of the ligand RANKL to its receptors RANK and OPG can be symbolically represented as follows:



with $L = \text{RANKL}$ and $R = \{\text{RANK}, \text{OPG}\}$, $R \cdot L$ the complex resulted from binding, k^f the forward and k^r the reverse reaction rates of the binding process between receptor and ligand.

Considering the model used by Scheiner et al. (2013), but including a novel term which takes into account the influence of the vascular porosity change, analogous to Eq. (2.5), the kinetics of receptor-ligand reactions can be given in the form:

$$\begin{aligned} \frac{dC_R^{\text{vas}}}{dt_{\text{fast}}} = & -k_{[R \cdot L]}^{f, \text{vas}}(t_{\text{fast}})C_R^{\text{vas}}(t_{\text{fast}})C_L^{\text{vas}}(t_{\text{fast}}) + k_{[R \cdot L]}^{r, \text{vas}}(t_{\text{fast}})C_{[R \cdot L]}^{\text{vas}}(t_{\text{fast}}) \\ & + S_R^{\text{vas}}(t_{\text{fast}}) - \frac{C_R^{\text{vas}}}{f_{\text{vas}}} \frac{df_{\text{vas}}}{dt_{\text{slow}}} \end{aligned} \quad (2.27)$$

$$\begin{aligned} \frac{dC_L^{\text{vas}}}{dt_{\text{fast}}} = & -k_{[R \cdot L]}^{f, \text{vas}}(t_{\text{fast}})C_R^{\text{vas}}(t_{\text{fast}})C_L^{\text{vas}}(t_{\text{fast}}) + k_{[R \cdot L]}^{r, \text{vas}}(t_{\text{fast}})C_{[R \cdot L]}^{\text{vas}}(t_{\text{fast}}) \\ & + S_L^{\text{vas}}(t_{\text{fast}}) - \frac{C_L^{\text{vas}}}{f_{\text{vas}}} \frac{df_{\text{vas}}}{dt_{\text{slow}}} \end{aligned} \quad (2.28)$$

$$\begin{aligned} \frac{dC_{[R \cdot L]}^{\text{vas}}}{dt_{\text{fast}}} = & k_{[R \cdot L]}^{f, \text{vas}}(t_{\text{fast}})C_R^{\text{vas}}(t_{\text{fast}})C_L^{\text{vas}}(t_{\text{fast}}) - k_{[R \cdot L]}^{r, \text{vas}}(t_{\text{fast}})C_{[R \cdot L]}^{\text{vas}}(t_{\text{fast}}) \\ & - \frac{C_{[R \cdot L]}^{\text{vas}}}{f_{\text{vas}}} \frac{df_{\text{vas}}}{dt_{\text{slow}}}, \end{aligned} \quad (2.29)$$

where C_R^{vas} , C_L^{vas} , and $C_{[R \cdot L]}^{\text{vas}}$ are the concentrations of receptor, ligand, and receptor-ligand complex, $k_{[R \cdot L]}^{f, \text{vas}}$ and $k_{[R \cdot L]}^{r, \text{vas}}$ are the forward and reverse reaction rates for the binding of receptor and ligand, and S_R^{vas} and S_L^{vas} are sink/source terms (including production and degradation processes) related to receptor and ligand; all quantities are given with respect to the vascular pore space. Notably, these kinetics equations can be easily extended to the case where several receptors and ligands react with each other.

In the above equations, two time frames are included:

- t_{fast} , referring to processes taking place on a time scale of seconds to minutes, namely the change in the receptor and ligand concentrations, receptor-ligand binding and de-binding, and source-sink dynamics, and
- t_{slow} , referring to processes taking place on a time scale of days to weeks, namely the change in vascular porosity. It takes approximately 20 days to initiate and increase the diameter of the resorption cavity by the osteoclasts (Fuchs et al., 2009).

On a ‘‘fast’’ time scale, $t_{\text{slow}} \rightarrow \infty$, the vascular porosity change becomes negli-

gible, therefore the differential equations above become

$$\begin{aligned} \frac{dC_R^{\text{vas}}}{dt_{\text{fast}}} = & -k_{[R.L]}^{\text{f,vas}}(t_{\text{fast}})C_R^{\text{vas}}(t_{\text{fast}})C_L^{\text{vas}}(t_{\text{fast}}) + k_{[R.L]}^{\text{r,vas}}(t_{\text{fast}})C_{[R.L]}^{\text{vas}}(t_{\text{fast}}) \\ & + S_R^{\text{vas}}(t_{\text{fast}}) \end{aligned} \quad (2.30)$$

$$\begin{aligned} \frac{dC_L^{\text{vas}}}{dt_{\text{fast}}} = & -k_{[R.L]}^{\text{f,vas}}(t_{\text{fast}})C_R^{\text{vas}}(t_{\text{fast}})C_L^{\text{vas}}(t_{\text{fast}}) + k_{[R.L]}^{\text{r,vas}}(t_{\text{fast}})C_{[R.L]}^{\text{vas}}(t_{\text{fast}}) \\ & + S_L^{\text{vas}}(t_{\text{fast}}) \end{aligned} \quad (2.31)$$

$$\frac{dC_{[R.L]}^{\text{vas}}}{dt_{\text{fast}}} = k_{[R.L]}^{\text{f,vas}}(t_{\text{fast}})C_R^{\text{vas}}(t_{\text{fast}})C_L^{\text{vas}}(t_{\text{fast}}) - k_{[R.L]}^{\text{r,vas}}(t_{\text{fast}})C_{[R.L]}^{\text{vas}}(t_{\text{fast}}). \quad (2.32)$$

On a “slow” time scale, for $t_{\text{fast}} \rightarrow 0$, a steady state is reached, where the input/output of the system in the change of receptor and ligand concentrations is equal to 0, which implies for Eqs. (2.30) and (2.31)

$$-k_{[R.L]}^{\text{f,vas}}C_R^{\text{vas}}C_L^{\text{vas}} + k_{[R.L]}^{\text{r,vas}}C_{[R.L]}^{\text{vas}} + S_j^{\text{vas}} = 0. \quad (2.33)$$

The same assumption for Eq. (2.32) delivers

$$-k_{[R.L]}^{\text{f,vas}}C_R^{\text{vas}}C_L^{\text{vas}} + k_{[R.L]}^{\text{r,vas}}C_{[R.L]}^{\text{vas}} = 0, \quad (2.34)$$

and combining Eqs. (2.33) and (2.34) results in

$$S_j^{\text{vas}} = 0, \quad (2.35)$$

with index j representing either a receptor or a ligand. Considering that these source/sink terms include endogenous production, external feeding (dosage), and degradation, Eq. (2.35) can be further specified to

$$P_{j,e}^{\text{vas}} + P_{j,d}^{\text{vas}} - D_j^{\text{vas}}C_{j,\text{tot}}^{\text{vas}} = 0, \quad (2.36)$$

where $P_{j,e}^{\text{vas}}$, $j = \{R, L\}$ are the endogenous production rates of receptors and ligands, $P_{j,d}^{\text{vas}}$ the respective dosage rates, while D_j^{vas} are the respective degradation rates and $C_{j,\text{tot}}^{\text{vas}}$ is the total concentration of j .

Concentration of $\text{TGF}\beta$ in the vascular pore space

The production of $\text{TGF}\beta$ has been defined previously (Pivonka et al., 2008; Scheiner et al., 2013), based on the consideration that $\text{TGF}\beta$ gain occurs solely due to its release from the bone matrix in the course of bone resorption, and reads

$$C_{\text{TGF}\beta}^{\text{vas}} = \frac{\alpha_{\text{TGF}\beta}^{\text{exvas}}C_{\text{OCa}}^{\text{vas}}k_{\text{OCa}}^{\text{res}}}{D_{\text{TGF}\beta}^{\text{vas}}}, \quad (2.37)$$

with $\alpha_{\text{TGF}\beta}^{\text{exvas}}$ in pM as a constant factor quantifying how much $\text{TGF}\beta$ (given in mol) is contained in one dm^3 of extravascular bone matrix, $C_{\text{OCa}}^{\text{vas}}$ the vascular concentration of active osteoclasts, $k_{\text{OCa}}^{\text{res}}$ the resorption coefficient of extravascular bone matrix, and $D_{\text{TGF}\beta}^{\text{vas}}$ the degradation rate of $\text{TGF}\beta$ in $(\text{day})^{-1}$.

Concentration of RANK in the vascular pore space

We assume that the concentration of RANK, produced by osteoclast precursors (Nakagawa et al., 1998; Kartsogiannis et al., 1999), follows from a constant number of receptors per preosteoclast,

$$C_{\text{RANK}}^{\text{vas}} = \rho_{\text{RANK}} C_{\text{OCp}}^{\text{vas}}, \quad (2.38)$$

with ρ_{RANK} being the density of receptors per cell, and $C_{\text{OCp}}^{\text{vas}}$ the vascular concentration of osteoclast precursors.

Concentration of PTH in the vascular pore space

The vascular concentration of PTH follows from Eq. (2.36), considering no external production ($P_{\text{PTH,d}}^{\text{vas}} = 0$):

$$C_{\text{PTH}}^{\text{vas}} = \frac{\beta_{\text{PTH}}^{\text{vas}}}{D_{\text{PTH}}^{\text{vas}}}, \quad (2.39)$$

with intrinsic PTH production rate $\beta_{\text{PTH}}^{\text{vas}}$ and degradation rate $D_{\text{PTH}}^{\text{vas}}$.

Concentration of OPG in the vascular pore space

Considering that OPG is produced by active osteoblasts (Boyce and Xing, 2008), the endogenous OPG production is herein defined as

$$P_{\text{OPG,e}}^{\text{vas}} = n_{\text{OPG/OBa}} C_{\text{OBa}}^{\text{vas}} \pi_{\text{rep,PTH}}^{\text{OPG/OBa}} \left(1 - \frac{C_{\text{OPG}}^{\text{vas}}}{C_{\text{OPG,max}}^{\text{vas}}} \right), \quad (2.40)$$

where $n_{\text{OPG/OBa}}$ is a proportionality factor quantifying how much of this protein can be synthesized per active osteoblast, and $C_{\text{OPG,max}}^{\text{vas}}$ is the maximum concentration of OPG. The inhibition of OPG production by PTH (Kroll, 2000) is mathematically expressed by the repression function $\pi_{\text{rep,PTH}}^{\text{OPG/OBa}}$, explicitied as

$$\pi_{\text{rep,PTH}}^{\text{OPG/OBa}} = \frac{K_{\text{rep,PTH}}^{\text{-OPG/OBa,vas}}}{K_{\text{rep,PTH}}^{\text{-OPG/OBa,vas}} + C_{\text{PTH}}^{\text{vas}}}, \quad (2.41)$$

with the repression coefficient $K_{\text{rep,PTH}}^{\text{OPG/OBa,vas}}$.

Then, insertion of Eq. (2.40) into Eq. (2.36) and consideration of the external OPG production to be 0, $P_{\text{OPG,d}}^{\text{vas}} = 0$, gives access to $C_{\text{OPG}}^{\text{vas}}$, through

$$C_{\text{OPG}}^{\text{vas}} = C_{\text{OPG,max}}^{\text{vas}} \frac{n_{\text{OPG/OBa}} C_{\text{OBa}}^{\text{vas}} \pi_{\text{rep,PTH}}^{\text{OPG/OBa}}}{n_{\text{OPG/OBa}} C_{\text{OBa}}^{\text{vas}} \pi_{\text{rep,PTH}}^{\text{OPG/OBa}} + D_{\text{OPG}}^{\text{vas}} C_{\text{OPG,max}}^{\text{vas}}}, \quad (2.42)$$

with OPG degradation rate $D_{\text{OPG}}^{\text{vas}}$.

Concentration of RANKL in the vascular pore space

The total production of the RANK ligand, RANKL, is the sum of the endogeneous and external productions of this factor, namely

$$\begin{aligned} P_{\text{RANKL}}^{\text{vas}} &= P_{\text{RANKL,e}}^{\text{vas}} + P_{\text{RANKL,d}}^{\text{vas}} \\ &= \beta_{\text{RANKL}}^{\text{vas(OBp)}} \left(1 - \frac{C_{\text{RANKL,tot}}^{\text{vas}}}{C_{\text{RANKL,max}}^{\text{vas}}} \right) + \beta_{\text{RANKL}}^{\text{vas(OCY)}} + P_{\text{RANKL,d}}^{\text{vas}}, \end{aligned} \quad (2.43)$$

where $\beta_{\text{RANKL}}^{\text{vas(OBp)}}$ is the intrinsic production of RANKL by osteoblast precursors in the vascular pore space, $C_{\text{RANKL,tot}}^{\text{vas}}$ is the total vascular concentration of RANKL, $C_{\text{RANKL,max}}^{\text{vas}}$ is the maximum vascular concentration of RANKL, and $\beta_{\text{RANKL}}^{\text{vas(OCY)}}$ considers the (baseline) intrinsic production of RANKL by osteocytes that is transported from the extravascular to the vascular space,

$$\beta_{\text{RANKL}}^{\text{vas(OCY)}} = \beta_{\text{RANKL}}^{\text{exvas(OCY)}} \frac{1 - f_{\text{vas}}}{f_{\text{vas}}}, \quad (2.44)$$

with $\beta_{\text{RANKL}}^{\text{exvas(OCY)}}$ proportional to the extravascular osteocyte concentration $C_{\text{OCY}}^{\text{exvas}}$.

The total concentration of RANKL includes not only the “free” RANKL, but also the bound one, as it exists in receptor-ligand complexes. Taking into account that RANKL can bind to both RANK and OPG, its total concentration reads as

$$\begin{aligned} C_{\text{RANKL,tot}}^{\text{vas}} &= C_{\text{RANKL}}^{\text{vas}} + C_{[\text{OPG}\cdot\text{RANKL}]}^{\text{vas}} + C_{[\text{RANK}\cdot\text{RANKL}]}^{\text{vas}} \\ &= C_{\text{RANKL}}^{\text{vas}} \left(1 + K_{\text{a},[\text{OPG}\cdot\text{RANKL}]}^{\text{vas}} C_{\text{OPG}}^{\text{vas}} + K_{\text{a},[\text{RANK}\cdot\text{RANKL}]}^{\text{vas}} C_{\text{RANK}}^{\text{vas}} \right), \end{aligned} \quad (2.45)$$

with $K_{\text{a},[\text{OPG}\cdot\text{RANKL}]}^{\text{vas}}$ and $K_{\text{a},[\text{RANK}\cdot\text{RANKL}]}^{\text{vas}}$ as the respective association binding constants.

Inserting Eqs. (2.43)–(2.45) into Eq. (2.36) allows then to derive the vascular concentration of RANKL

$$\begin{aligned} C_{\text{RANKL}}^{\text{vas}} &= C_{\text{RANKL,max}}^{\text{vas}} \left(\beta_{\text{RANKL}}^{\text{vas(OBp)}} + \beta_{\text{RANKL}}^{\text{exvas(OCY)}} \frac{1 - f_{\text{vas}}}{f_{\text{vas}}} + P_{\text{RANKL,d}}^{\text{vas}} \right) \\ &\quad \times \left(\beta_{\text{RANKL}}^{\text{vas(OBp)}} + D_{\text{RANKL}}^{\text{vas}} C_{\text{RANKL,max}}^{\text{vas}} \right)^{-1} \\ &\quad \times \left(1 + K_{\text{a},[\text{OPG}\cdot\text{RANKL}]}^{\text{vas}} C_{\text{OPG}}^{\text{vas}} + K_{\text{a},[\text{RANK}\cdot\text{RANKL}]}^{\text{vas}} C_{\text{RANK}}^{\text{vas}} \right)^{-1}. \end{aligned} \quad (2.46)$$

The maximum RANKL concentration, $C_{\text{RANKL,max}}^{\text{vas}}$, is governed by the concentration of osteoblast precursors that produce RANKL, as well as by the influence of PTH, which promotes the production of RANKL (Kroll, 2000). The latter activation is considered via the activation function $\pi_{\text{act,PTH}}^{\text{maxRANKL}}$,

$$\pi_{\text{act,PTH}}^{\text{maxRANKL}} = \frac{C_{\text{PTH}}^{\text{vas}}}{K_{\text{act,PTH}}^{\text{maxRANKL/OBp,vas}} + C_{\text{PTH}}^{\text{vas}}}, \quad (2.47)$$

where $K_{\text{act,PTH}}^{\text{maxRANKL,vas}}$ is the respective activation coefficient, and $C_{\text{PTH}}^{\text{vas}}$ is determined according to Eq. (2.39). The maximum concentration of RANKL then reads:

$$C_{\text{RANKL,max}}^{\text{vas}} = n_{\text{RANKL/OBp}} C_{\text{OBp}}^{\text{vas}} \pi_{\text{act,PTH}}^{\text{maxRANKL}}, \quad (2.48)$$

with $n_{\text{RANKL/OBp}}$ as the maximum number of RANKL receptors per osteoblast precursor.

Concentration of the RANK-RANKL complex in the vascular pore space

Finally, the vascular concentration of the RANK-RANKL complex reads as

$$C_{[\text{RANK}\cdot\text{RANKL}]}^{\text{vas}} = C_{\text{RANK}}^{\text{vas}} C_{\text{RANKL}}^{\text{vas}} K_{\text{a},[\text{RANK}\cdot\text{RANKL}]}^{\text{vas}}, \quad (2.49)$$

and governs the activation function of osteoclast differentiation, Eq. (2.17).

2.11 Appendix D: Parameter values

Table 2.2: Overview of the values of parameters used as direct input in the model

Parameter	Description	Unit	Value
$\frac{\alpha_{\text{TCF}\beta}^{\text{ex vas}} K_{\text{OCa}}^{\text{res}}}{D_{\text{TCF}\beta}^{\text{vas}}}$	production of TGF β / degradation rate of TGF β	–	1
$\beta_{\text{PTH}}^{\text{vas}}$	vascular intrinsic PTH production	pM/day	5000
$\hat{\Pi}_{\text{act,OBp}}^{\text{mech,vas}}$	steady state value of mechanically-induced OBp proliferation	–	0.155
ρ_{RANK}	density of RANK receptors per OCa	–	10000
$A_{\text{OBa}}^{\text{vas}}$	apoptosis rate of OBa	1/day	0.2111
$A_{\text{OCa}}^{\text{vas}}$	maximum apoptosis rate of OCa	1/day	5.6487
$D_{\text{OBp}}^{\text{vas}}$	maximum differentiation rate of OBp	1/day	0.1657
$D_{\text{OBu}}^{\text{vas}} C_{\text{OBu, ini}}^{\text{vas}}$	maximum differentiation rate of OBU \times initial vascular OBU concentration	pM/day	0.0126
$D_{\text{OCp}}^{\text{vas}}$	maximum differentiation rate of OCp	1/day	2.1000
$P_{\text{OBp}}^{\text{vas}}$	maximum proliferation rate of OBp	1/d	0.0680
$C_{\text{OBa, ini}}^{\text{vas}}$	initial vascular OBa concentration	pM	0.0100
$C_{\text{OBp, ini}}^{\text{vas}}$	initial vascular OBp concentration	pM	0.0200
$C_{\text{OCa, ini}}^{\text{vas}}$	initial vascular OCa concentration	pM	0.0020
$C_{\text{OCp, ini}}^{\text{vas}}$	initial vascular OCp concentration	pM	0.0200
$C_{\text{OPG, max}}^{\text{vas}}$	maximum vascular concentration of OPG	pM	4×10^9
$D_{\text{OPG}}^{\text{vas}}$	vascular degradation rate of OPG	1/day	0.3500
$D_{\text{PTH}}^{\text{vas}}$	vascular degradation rate of PTH	1/day	86
$D_{\text{RANKL}}^{\text{vas}}$	vascular degradation rate of RANKL	1/day	10.1325
$K_{\text{rep, TGF}\beta}^{\text{OBp} \rightarrow \text{OBa, vas}}$	repression coefficient of OBp differentiation by TGF β	pM	0.0035
$K_{\text{act, TGF}\beta}^{\text{OBu} \rightarrow \text{OBp, vas}}$	activation coefficient of OBU differentiation by TGF β	pM	0.0113
$K_{\text{act, TGF}\beta}^{\text{OCa} \rightarrow \dagger, \text{vas}}$	activation coefficient of OCa apoptosis by TGF β	pM	0.0113
$K_{\text{act, [RANK-RANKL]}}^{\text{OCp} \rightarrow \text{OCa, vas}}$	activation coefficient of OCp differentiation by RANK-RANKL binding	pM	113.5944
$K_{\text{act, PTH}}^{\text{maxRANKL/OBp, vas}}$	activation coefficient of RANKL production by OBp through PTH	pM	3000
$K_{\text{rep, PTH}}^{\text{OPG/OBa, vas}}$	repression coefficient of OPG production by OBa through PTH	pM	4.4516
$K_{\text{a, [OPG-RANKL]}}^{\text{vas}}$	association binding constant between OPG-RANKL	1/pM	5×10^{-5}
$K_{\text{a, [RANK-RANKL]}}^{\text{vas}}$	association binding constant between RANK-RANKL	1/pM	0.0017
$n_{\text{OPG/OBa}}$	quantity of OPG per OBa	1/day	1.6249×10^8
$n_{\text{RANKL/OBp}}$	maximum number of RANKL receptors per OBp	1/day	2.7035×10^6

Chapter 3

Spatial variation of longitudinal and transverse elastic properties in mid femur cortical cross sections, as assessed by statistical nanoindentation

Authored by

Maria-Ioana Pastrama, Romane Blanchard, John Clement, Peter Pivonka, and Christian Hellmich

In preparation for submission to *Journal of Bone and Mineral Research*

The elasticity of human bone tissue varies with anatomical location, due to several factors such as remodeling activity, tissue mineralization or load bearing. In the present study, the elastic modulus of extracellular bone matrix was investigated site-specifically throughout the human femoral cortex, thereby discriminating mediolateral, anteroposterior, and proximal-distal orientations; as well as endosteal, intracortical, and periosteal regions. The elastic modulus was obtained by means of a statistical nanoindentation-based method, which, coupled with an evolutionary algorithm, can distinguish between damaged and undamaged material phases. The underlying assumption that damage is caused by pre-existing or newly formed microcracks was checked by Scanning Electron Microscope (SEM) imaging. The results confirmed the known anisotropy of bone, namely that the material is stiffer in the proximal-distal or longitudinal direction than in the anteroposterior or mediolateral directions,

the latter two corresponding here to the mechanical tangential direction. Moreover, in the longitudinal direction, bone seems to be stiffer at the endosteum than at the periosteum, probably due to the aging-related increased resorption activity and the resulting trabecularization of cortical bone. The results also showed that bone is stiffer in the anteroposterior than in the mediolateral directions, the former being aligned with the neutral bending axis of the femur and, thus, undergoing less remodeling and being more mineralized. Finally, the statistical nanoindentation method showed a higher degree of damage on the longitudinal than on the anteroposterior and mediolateral surfaces, which may be explained by the preferential direction for crack propagation along the mineralized collagen fibrils in bone.

Collaboration

This paper is the result of a collaboration with St. Vincent's Department of Surgery at The University of Melbourne, and the Melbourne Dental School in Australia. Romane Blanchard and Peter Pivonka came up with the research question. Romane Blanchard performed the cutting and color coding of the samples obtained from the Melbourne Femur Collection, with the help of John Clement. In Vienna, Maria-Ioana Pastrama prepared the received samples and tested them by means of nanoindentation. She also performed the statistical analysis of the results and the deconvolution of the experimental data by means of the evolutionary strategy, prepared the necessary images, and wrote a first draft of the paper, activities qualifying her for first authorship. The revision of the manuscript content was performed by all authors involved, with John Clement, Peter Pivonka, and Christian Hellmich approving it in its final version.

3.1 Introduction

Bone is a living tissue that undergoes continuous modeling and remodeling throughout life. Age-related changes of this tissue have been associated with increased bone fracture risk. The majority of studies on age-related changes in human bone have focused on either morphological changes (Dequeker et al., 1971; Black et al., 1974), or on changes in modeling and remodeling rates to quantify bone loss (Riggs et al., 1982). The mechanical properties of bone are, nevertheless, influenced by a variety of material and structural properties, such as, among others, concentration of mineral in the matrix and amount of porosity. While several methods are available to measure bone tissue mineralization and porosity, one cannot directly infer from these

properties the respective mechanical properties of the material. It is known that the local elastic modulus varies within a particular bone region (at a scale of hundreds of microns), e.g., osteons are less mineralized and softer than the interstitial bone (Zysset et al., 1999; Hoffer et al., 2005; Gupta et al., 2006), and experimental data on bone stiffness at particular sites (such as, for example, the iliac crest) are widely available. However, the spatial stiffness distribution across entire bone structures (such as whole mid femur or femoral neck cross sections), which determines the structural behaviour of whole bones, has been only sparsely investigated.

The objective of this paper is to fill this knowledge gap, and determine the stiffness at the micrometer scale of the extracellular matrix of cortical bone, throughout different plane sections through the midshaft of a human femur; thereby discriminating mediolateral, anteroposterior, and proximal-distal orientations; as well as endosteal, intracortical, and periosteal regions. The motivation for this study was to gain a deeper understanding of the spatial variation of bone mechanical properties, their relation with modeling and remodeling events, and potential associations with mechanical loading.

Through the processes of modeling and remodeling, packets of bone (e.g., osteons in the cortex) are constantly being laid down and turned over. As newly formed bone accumulates mineral with time, the most recently deposited tissue will generally be less mineralized than that deposited months or years earlier. On the one hand, it has been shown that regions with high turnover (such as the endosteal regions), containing many newly formed osteons, will generally display lower average mineralization than areas of low turnover (such as the periosteal regions). In particular, Boivin and Meunier (2002) have shown that an increase in bone remodeling (coupled formation and resorption) leads to an increase of bone multicellular unit (BMU) birthrate and, consequently, to younger bone material and a decrease in tissue mineral density (TMD), related to a lower probability of completing secondary mineralization (Ruffoni et al., 2007, 2008; Bala et al., 2013). Thereby, the kinetics of mineralization exhibits two (temporal) phases: (i) a fast primary phase lasting about 5 to 10 days, during which collagen fibrils are deposited onto previously remodeled surfaces and mineralize until they reach about 70 % of the maximum mineral content (Bala et al., 2010); and (ii) a slow secondary phase, consisting of a gradual maturation of the mineral component, which may take up to several years, with a large fraction completed after one year (Marotti et al., 1972; Meunier and Boivin, 1997). On the other hand, it has also been proposed that the observed trabecularization of cortical bone in endosteal regions with aging is related to increased resorption-only modeling activities (Simmons et al., 1991). Thus, depending on the mode of action, together with a conceptual model of bone mineralization, endosteal bone would be

either less or more mineralized compared to periosteal bone. Here we test the latter hypothesis, i.e., that endosteal bone is more mineralized compared to periosteal bone, due to increased resorption activity in endosteal regions.

Throughout these mineralization processes, the current tissue mineralization degree (TMD) has been associated with the mechanical properties at the bone tissue level (Currey et al., 1996; Follet et al., 2004; Currey, 2006); and the underlying micromechanical reasons have been revealed by means of experimentally validated multiscale models of bone stiffness and strength (Fritsch and Hellmich, 2007; Fritsch et al., 2009b; Morin and Hellmich, 2014). The issue stays tricky though, as small increases in mineralization lead to relatively large increases in bone strength (Vose and Kubala, 1959), while at approximately 66% mineralization, increases in mineral will lead to brittleness and a reduction in strength (Currey, 1969a; Bonfield and Clark, 1973).

An important factor influencing femoral bone remodeling is the mechanical loading of the human femur, leading to bending deformations and, consequently, inducing spatially varying stresses and strains in the cross section of the midshaft. The latter variation in strain stimuli may induce a spatial dependency of bone remodeling. Associations between mechanical loading and variations of vascular porosity in human cortical femur sections have shown that bone loss occurs where bone strain is least, i.e., along the neutral axis of bending. This axis is closely aligned with the anteroposterior bending axis and continues to shift closer to the latter with age, as the femur midshaft approaches circularity, resulting in greater resorption and, therefore, increased porosity at this region (Feik et al., 2000; Thomas et al., 2005, 2006). Given the aforementioned correlations between increased resorption and tissue mineralization, one would also expect higher tissue mineralization in the neutral axis; however, studies correlating the average degree of mineralization of cortical extracellular matrix with the prevailing mechanical loading of that cortex have shown mixed results. It was found that, in human femora, regions of the bone primarily loaded in tension had lower mineralization density due to a higher number of forming osteons (Portigliatti Barbos et al., 1983). By contrast, other studies found that, in the horse radius, the cortex experiencing predominantly higher tensile strains demonstrated a higher mineralization density and a lower remodeling rate than the one experiencing predominantly compressive strains (Riggs et al., 1993).

In order to elucidate the interactions of predominant loading patterns and potentially corresponding tissue elasticity variations, nanoindentation is the method of choice, allowing us to measure the elastic material properties at the extracellular scale of bone and other mineralized tissues (i.e., on the order of 5–10 μm) (Rho, 1996; Turner et al., 1999; Zysset et al., 1999; Hoffer et al., 2000a, 2005; Gupta et al.,

2006; Franzoso and Zysset, 2009; Reisinger et al., 2011). However, classical evaluations based on nanoindentation data averaging typically deliver elasticity values lower than those obtained, at the same scale, with the non-destructive ultrasonic technique (Lees et al., 1979; Lees, 1982; Lees et al., 1996; Malandrino et al., 2012; Morin and Hellmich, 2014). This may be due to the presence of microcracks which, as structural units, are not considered in the Oliver-Pharr halfspace solution (Oliver and Pharr, 1992), which is standardly used for nanoindentation evaluation. This idea has been confirmed by mechanical tests on focused ion beam-produced bovine bone pillars at the single micron-scale, i.e., at a scale well below the occurrence of microcracks: These tests provided stiffness values which were fully consistent with values stemming from ultrasonic tests (Luczynski et al., 2015). Therefore, we herein do not only resort to classical statistical methods applied to the nanoindentation raw data (including simple averaging, as alluded to before), but we also apply a recently proposed and validated deconvolution method (Kariem et al., 2015; Furin et al., 2016) to subsets of data, so as to discriminate between truly elastic properties derived from indentation processes taking place far from microcracks, and moduli associated to indents in the immediate vicinity of microcracks.

To summarize, the primary objective of the current study is twofold: (i) to determine whether bone stiffness in endosteal regions is higher than in periosteal regions; implying that endosteal regions, due to increased resorption activities, are more mineralized; and (ii) to check if the local stiffness patterns in loaded areas are different to those regions near the neutral axis characterized by low mechanical loading. More specifically, these aspects were investigated herein through quantification of the elastic modulus of the undamaged human femoral bone matrix at different anatomical locations, in different directions, and at different positions with respect to the bone marrow.

3.2 Materials and methods

3.2.1 Sample preparation

The samples were prepared from bones collected in 1990-1993 and 1998 at the Melbourne Femur Collection, assembled from material obtained from the Victorian Institute of Forensic Medicine. The donors, a 38- and a 28-year old female, are known to be free of blood-borne disease. From each donor, an approximately 0.5 cm thick section was removed from the mid-shaft of the right femur, cleaned of adhering soft tissue, coarsely dehydrated in a series of graded alcohols under occasional ultrasonication and vacuum, and then refluxed for 7-14 days in a 50:50 heptane-isopropanol mixture. The bone sections were then transferred through two 12-hour changes of

100% methanol, soaked in two one-hour long changes of xylene, both under occasional ultrasonication and vacuum, and embedded in poly-methyl-methacrylate (PMMA) according to a previously described procedure (Boyde et al., 1984).

3.2.2 Cutting protocol

For each bone section, the linea aspera (LA), the ridge of roughened surface on the posterior surface, was identified visually, and the center of the endocortical surface was measured. The anteroposterior (A-P) axis was drawn by connecting the LA and this point. Then an orthogonal line to the anteroposterior axis, going through the center point, was designated as the mediolateral (M-L) axis. From each donor, coded 269 and 275, respectively, bone samples were cut along the two axes by means of a low speed saw (IsoMet 1000, Buehler) with a diamond cut-off wheel M1D10 (Streuers), resulting in four 2-mm wide match stick-like samples per donor, one from each anatomical location: medial (M), lateral (L), anterior (A), posterior (P). The samples were then named using the number of the donor, followed by the anatomical location, and the proximal, posterior and medial planes were colored with permanent markers so as to color-code three different anatomical directions. From the eight samples, four were tested by nanoindentation, two from each donor, namely 269-L, 269-P, 275-M and 275-P, see Figure 3.1 for a representation of the sample extraction locations. First, the samples were indented in the proximal-distal direction, corresponding to the mechanical longitudinal direction; then they were rotated and tested again transversally, either in the anteroposterior or mediolateral directions, both corresponding to the mechanical tangential direction. Additionally, each sample was divided into three thirds and, in each direction, tests were done in each third, corresponding to the three zones relative to the bone center (endosteal, intracortical, periosteal), see Table 3.1 for an overview and description of the samples and number of tests.

3.2.3 Polishing protocol for nanoindentation

The four samples were glued onto metal holders and polished with a polishing machine (PM5, Logitech, Scotland) in order to provide smooth, i.e., low-roughness, surfaces for nanoindentation. The polishing protocol included a 3-minute rough polishing step with paper particle size of $18.3\ \mu\text{m}$ at 10 rpm (rotations per minute), in order to ensure that the top of each sample was completely parallel to the bottom; and a second finishing step, in which the samples were finely polished for 120 min at 20 rpm with a napped cloth impregnated with $1\ \mu\text{m}$, high performance, polycrystalline diamond spray (DP-Spray P). It has been previously shown that polishing samples for a longer period of time with only one size of diamond particles increases

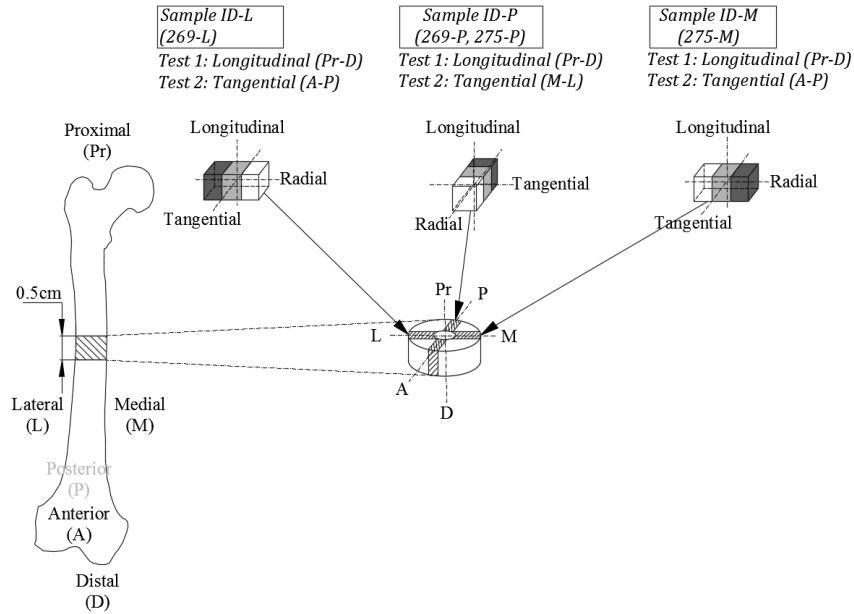


Figure 3.1: Scheme of sample extraction locations with anatomical and mechanical axes: Blocks were extracted from the right femur of two donors (Donor ID 269 or 275). One sample was extracted from each anatomical location (medial – M; lateral – L; anterior – A; posterior – P) and for each donor two samples were tested by nanoindentation (269-L, 269-P; 275-M, 275-P), first in the proximal-distal (Pr-D or longitudinal) direction; the sample was then rotated and tested either in the mediolateral (M-L) or anteroposterior (A-P) direction, both corresponding to the mechanical tangential direction. In each direction, three zones relative to the bone marrow were tested: endosteal (white), intracortical (light gray), and periosteal (dark gray)

the repeatability of the procedure (Miller et al., 2008), but that diamond polishing for longer than 120 min does not significantly improve the quality of the surface any further (Furin et al., 2016).

For testing in the tangential direction, the samples were unglued from the holders with the help of ultrasonication in distilled water, rotated, then glued again with the corresponding plane facing upwards, and the polishing procedure described above was repeated.

3.2.4 Nanoindentation

In order to determine direction-specific elastic properties of the bone samples, nanoindentation tests were performed using a Berkovich diamond tip in a TriboIndenter nanoindenting system (Hysitron Inc., Minneapolis, MN, USA). According to a previously published protocol for bone testing (Reisinger et al., 2011), a maximum indentation depth of 250 nm was prescribed, with a loading and unloading rate of

Table 3.1: Summary of the tested samples, the anatomical locations of their extraction, tested anatomical (mechanical) directions and zones, with corresponding number of nanoindentation tests performed

Donor ID	Sample	Anatomical location	Tested direction	Tested zones (no of tests)
269	269-L	Lateral	Proximal-distal (Longitudinal)	Endosteal (100) Intracortical (100) Periosteal (100)
			Anteroposterior (Tangential)	Endosteal (100) Intracortical (100) Periosteal (100)
	269-P	Posterior	Proximal-distal (Longitudinal)	Endosteal (100) Intracortical (100) Periosteal (100)
			Mediolateral (Tangential)	Endosteal (100) Intracortical (100) Periosteal (100)
275	275-M	Medial	Proximal-distal (Longitudinal)	Endosteal (100) Intracortical (100) Periosteal (100)
			Anteroposterior (Tangential)	Endosteal (100) Intracortical (100) Periosteal (100)
	275-P	Posterior	Proximal-distal (Longitudinal)	Endosteal (100) Intracortical (100) Periosteal (100)
			Mediolateral (Tangential)	Endosteal (100) Intracortical (100) Periosteal (100)

40 nm/s and a holding time of 20 s. In the longitudinal direction, for each of the four samples, a grid of 10×10 indents with 10 μm spacing was defined in each of the three zones relative to the bone center (endosteal, intracortical, periosteal), resulting in altogether 300 tests per sample and 1200 indents per direction (longitudinal and tangential). In the tangential direction, this resulted in 600 indents in the anteroposterior and mediolateral directions each. The nanoindentation tests delivered the reduced modulus of the samples, E_r , which takes into account both the elastic properties of the sample, E_s (here the extracellular bone tissue), and those of the indenter tip, E_t . The measurements were then evaluated according to the method of Oliver

and Pharr (1992), where the modulus of the sample can be calculated from the reduced modulus as

$$E_s = \frac{(1 - \nu_s^2)}{\frac{1}{E_r} - \frac{(1 - \nu_t^2)}{E_t}}, \quad (3.1)$$

considering Poisson's ratio of the extracellular bone matrix, $\nu_s = 0.3$ (van Rietbergen et al., 1995), and Poisson's ratio and the elastic modulus of the diamond indenter tip, $\nu_t = 0.07$ and $E_t = 1141$ GPa, respectively (Oliver and Pharr, 1992).

The values thus obtained for Young's modulus of the extracellular bone matrix were then evaluated site-specifically. For each of the tested zones (see Table 3.1), two types of evaluation were applied: Either the elastic modulus values were averaged, or a method reminiscent of statistical nanoindentation (Constantinides et al., 2006; Ulm et al., 2007) was employed. This method allows for identification of different material phases according to their different properties. In case of the herein tested extracellular human femoral bone matrix, the phases are to be understood as damaged and non-damaged material, i.e., the evaluation is based on the assumption that nanoindentation testing may induce damage in the material – or the material may be pre-damaged e.g., due to pre-existing microcracks. In order to discriminate between phases as described above, the data for the values of E_s were fitted by a superposition of n Gaussian Cumulative Distribution Functions (CDFs), following an algorithm described previously. From the n Gaussian distributions that best fit the experimental data, only one represented the intact, non-damaged material (Kariem et al., 2015; Furin et al., 2016); namely the one with the largest mean value. This mean value was considered as the (average, zone-specific) elastic modulus of undamaged human femoral extracellular bone tissue, while all other $n - 1$ Gaussian CDFs represented material damaged to varying extents.

3.2.5 Scanning electron microscopy

In the longitudinal direction, a preliminary number of nanoindentation tests (PI85 Picoindenter, Hysitron Inc., Minneapolis, MN, USA) in a scanning electron microscopy (SEM) environment (FEI Quanta 200 FEG, Oregon, USA) was done on other samples than those presented in Table 3.1, with the purpose of imaging microcracks. The same displacement-controlled protocol was used as described in the previous section. Samples were silver sputtered and imaged with an accelerating voltage of 10 kV.

3.2.6 Statistical tests

All statistical tests were performed with the open access software SOFA Statistics. For the study of differences between sample groups, non-parametric Mann-Whitney U tests were performed, due to deviations from normal distributions and differences between standard deviations of the groups. A p value < 0.05 was considered significant. No outliers were removed, due to the underlying assumption of the deconvolution algorithm, namely that higher or lower values of the elastic modulus E_s correspond to less or more damaged material, respectively.

3.3 Results

3.3.1 Longitudinal direction

The results of the nanoindentation tests for all the samples in the longitudinal direction are presented in Figure 3.2. The results are given both as simple mean \pm standard deviation, showing the elastic properties of combined undamaged and damaged material phases; and as mean \pm standard deviation of the last of the n Gaussian distributions resulted from fitting the experimental data as described above, showing only the elastic properties of the undamaged extracellular human femoral bone matrix. For all individual samples the difference between the endosteal and periosteal zones was statistically significant, $E_{\text{long, endost}} > E_{\text{long, periost}}$ ($p < 0.001$). For one sample (269-P) $E_{\text{long, endost}} = E_{\text{long, intracort}}$ ($p = 0.336$), for another (275-M) $E_{\text{long, periost}} = E_{\text{long, intracort}}$ ($p = 0.355$), while for the remaining two $E_{\text{long, endost}} > E_{\text{long, intracort}} > E_{\text{long, periost}}$. Applying the deconvolution algorithm to the endosteal results from all the four samples tested in the longitudinal plane resulted in an average modulus of the undamaged bone material $\bar{E}_{\text{long, endost}} = 29.342 \pm 0.746$ GPa (nine distributions, depicted in Figure 3.3(a)), while $\bar{E}_{\text{long, intracort}}$ was 26.237 ± 1.932 GPa (three distributions, depicted in Figure 3.3(b)), and $\bar{E}_{\text{long, periost}}$ amounted to 24.665 ± 1.626 GPa (four distributions, depicted in Figure 3.3(c)). Figure 3.4 shows an image taken during indentation of a sample from a different batch in an SEM environment (275-L, periosteal), with visible cracks in the indentation grid.

3.3.2 Tangential direction

The results of the nanoindentation tests for all the samples in the anteroposterior and mediolateral directions are presented in Figure 3.5. The results are given both as simple mean \pm standard deviation, showing the elastic properties of both damaged and undamaged material phases; and as mean \pm standard deviation of the last of the n Gaussian distributions resulted from fitting the experimental data as described

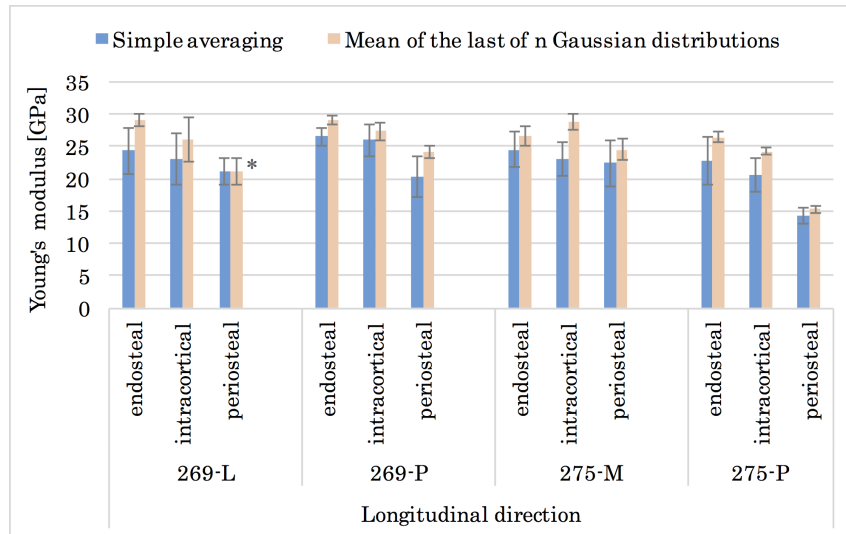
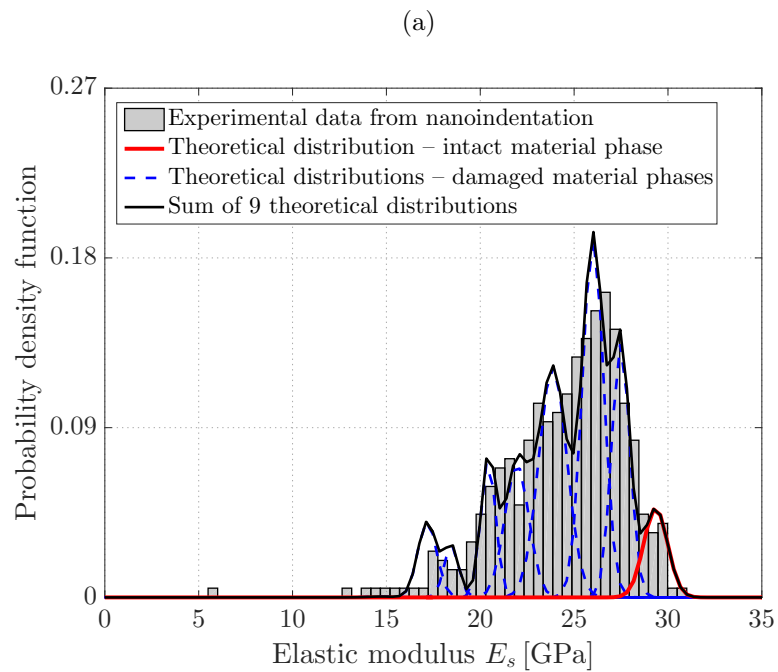


Figure 3.2: Results of the nanoindentation tests in the longitudinal direction of bone (mean \pm SD): The mean elastic modulus [GPa] obtained by simple averaging characterizes both damaged and undamaged material phases, while the modulus obtained as a mean of the last of n Gaussian distributions characterizes only the undamaged material phase. The deconvolution of the data from samples marked with * resulted in the best fit with only one distribution



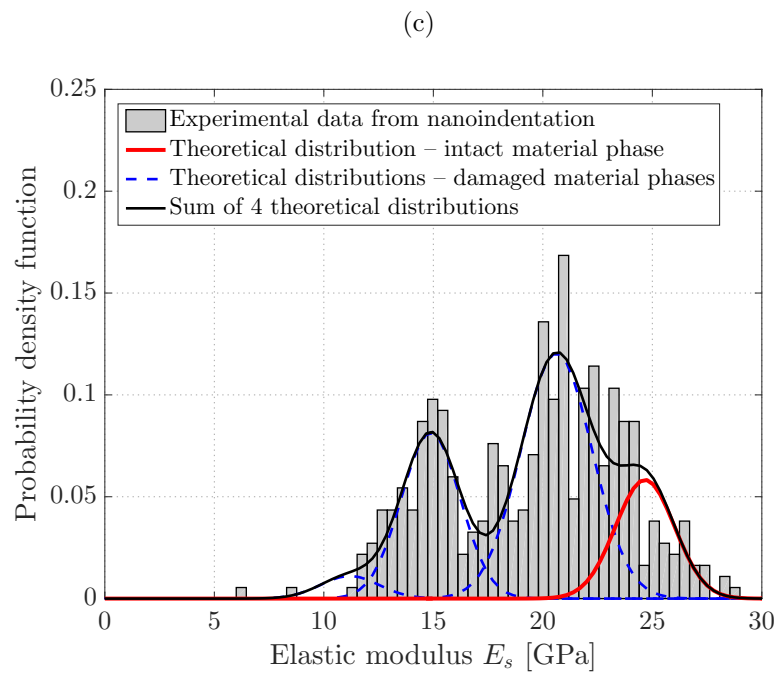
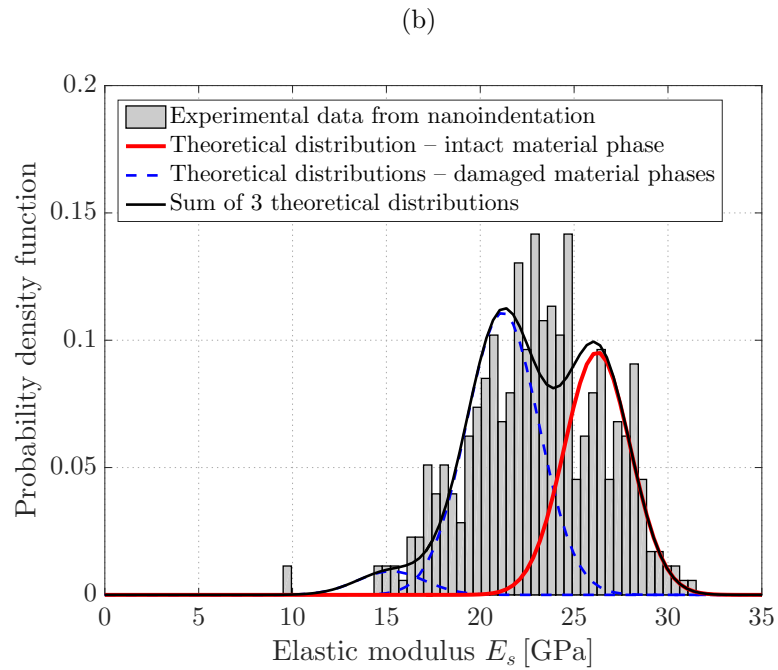


Figure 3.3: 1200 nanoindentation tests performed in the longitudinal direction of bone: (a) Histogram of the experimental data for the 400 tests performed in the endosteal zone, and the nine theoretical distributions fitted by means of deconvolution; (b) Histogram of the experimental data for the 400 tests performed in the intracortical zone, and the three fitted distributions; (c) Histogram of the experimental data for the 400 tests performed in the periosteal zone, and the four fitted distributions

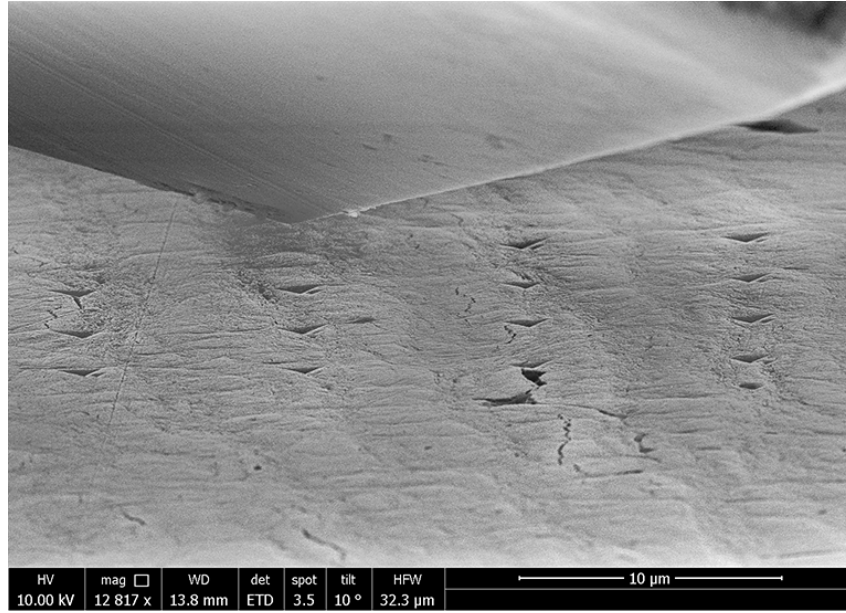


Figure 3.4: SEM image taken during nanoindentation tests in the longitudinal direction, showing cracks in the grid of indents

above, showing only the elastic properties of the undamaged extracellular human femoral bone matrix. The comparison between the data in the longitudinal and the tangential direction showed that the extracellular bone matrix was stiffer in the longitudinal direction than both in the anteroposterior and mediolateral directions ($p < 0.001$). A Mann-Whitney test comparing the 600 test results in the anteroposterior direction with the 600 in the mediolateral direction showed that the material was stiffer in the anteroposterior direction, $E_{\text{anteropost}} > E_{\text{mediolat}}$ ($p < 0.001$). Grouping all 600 test results for each anatomical direction together and applying the deconvolution algorithm as described above resulted in the average undamaged elastic moduli $\bar{E}_{\text{anteropost}} = 23.395 \pm 1.953$ GPa (two distributions, see Figure 3.6(a)) and $\bar{E}_{\text{mediolat}} = 19.966 \pm 3.108$ GPa (one distribution, see Figure 3.6(b)). As regards the differences between the three zones relative to the bone center, no clear trend was noticed in the tangential direction, with the endosteal zone being in some cases stiffer, in some less stiff than the periosteal one.

3.4 Discussion

The present study was undertaken to explore whether mechanical properties in the femoral midshaft cross section vary with spatial position, and if the latter could be associated with modeling and remodeling activities in cortical bone and the prevailing loading pattern. We used statistical nanoindentation at different spatial locations in

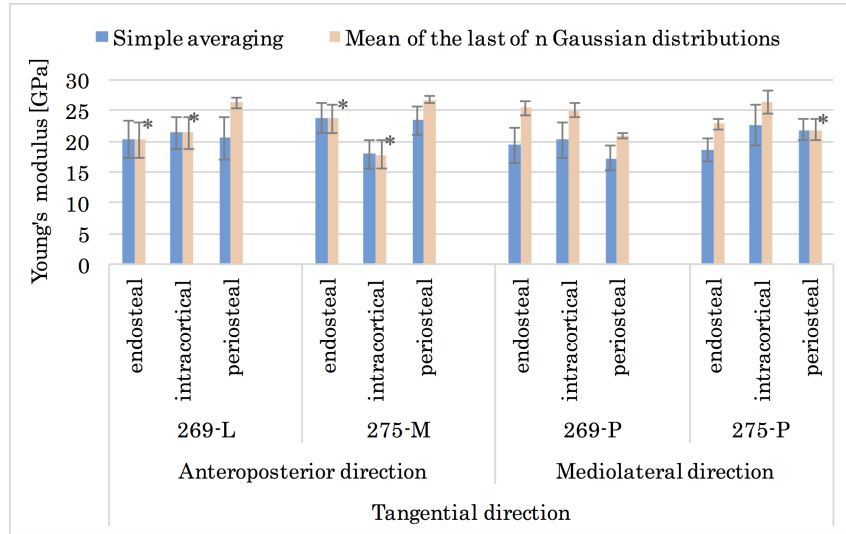


Figure 3.5: Results of the nanoindentation tests in the anteroposterior and mediolateral directions of bone (mean \pm SD), both corresponding to the mechanical tangential direction: The mean elastic modulus [GPa] obtained by simple averaging characterizes both damaged and undamaged material phases, while the modulus obtained as a mean of the last of n Gaussian distributions characterizes only the undamaged material phase. The deconvolution of the data of samples marked with * resulted in the best fit with only one distribution

whole human femoral cross sections, giving access to the local mechanical properties at identical cortical sites at the micrometer level.

Elastic modulus values obtained in literature from nanoindentation for dry, human femur samples, and with a similar preparation protocol as ours, range from 19.47 GPa (Hoffler et al., 2000a) to 24.66 ± 2.71 GPa (Franzoso and Zysset, 2009) in the longitudinal direction, and from 16.58 ± 0.32 GPa (Turner et al., 1999) to 17.28 ± 1.89 GPa in the tangential direction (Franzoso and Zysset, 2009). Values reported for wet or re-hydrated samples are lower than the above, as bone softens with increasing degree of hydration; the elasticity difference between dry and wet bone was reported to amount up to about 22 % (Hoffler et al., 2005). We note that material testing by means of nanoindentation was shown to deliver elasticity values lower than those obtained with ultrasonic testing, and this proves to be the case also for human bone tissue. For instance, Van Buskirk et al. (1981) obtained values of 26.5 GPa for the longitudinal and 19.4 GPa for the tangential elastic modulus of the extracellular matrix of dried human femur, using data of Yoon and Katz (1976a,b) from ultrasound tests with 5 MHz transducer frequency.

The values of the (dry) extracellular bone matrix elasticity for human femur reported in the current work, by means of statistical nanoindentation, are close to

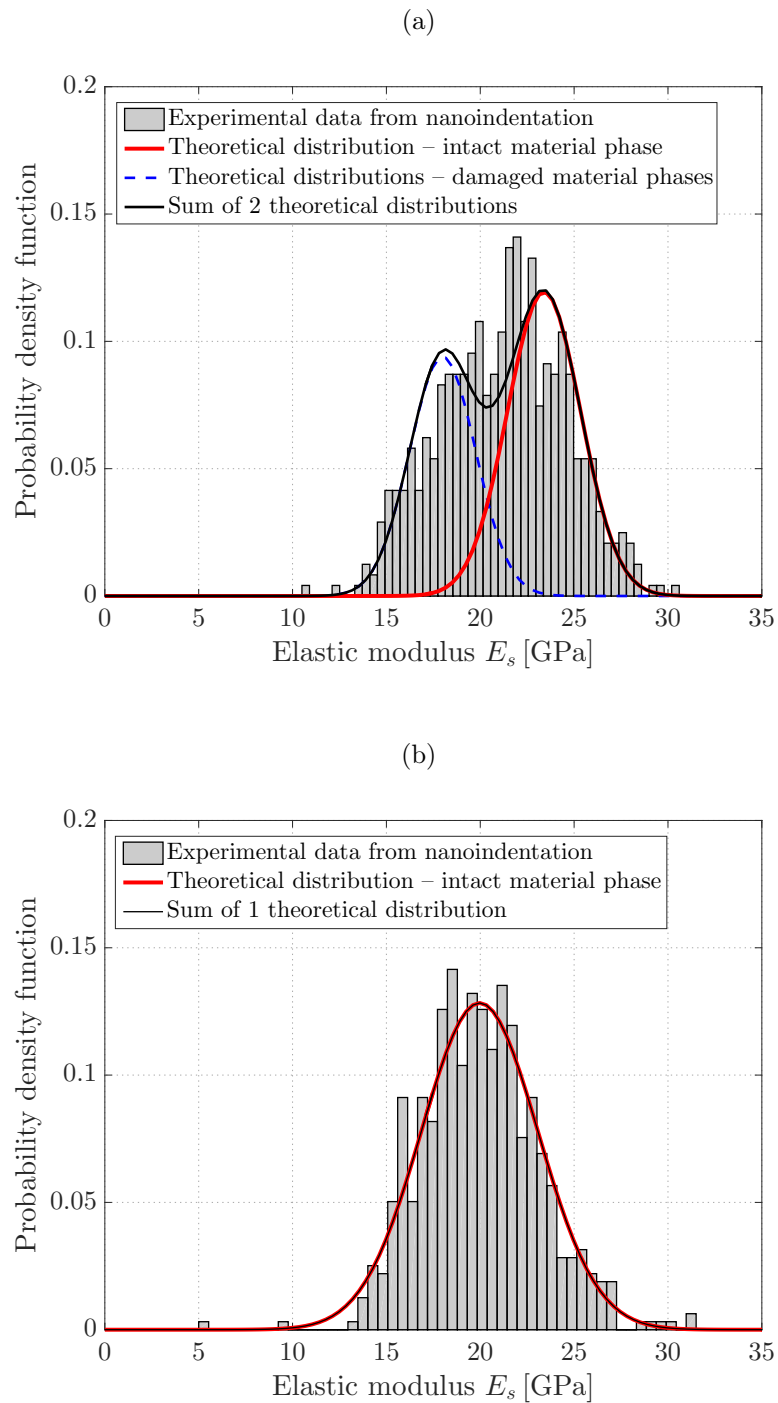


Figure 3.6: 1200 nanoindentation tests performed in the tangential direction of bone: (a) Histogram of the experimental data for the 600 tests performed in the antero-posterior direction, and the two theoretical distributions fitted by means of deconvolution; (b) Histogram of the experimental data for the 600 tests performed in the mediolateral direction, and the fitted distribution

those obtained from ultrasonic experiments by Van Buskirk et al. (1981), with the elastic modulus in the longitudinal direction as the average of the three zones, endosteal, intracortical, periosteal, $\bar{E}_{\text{long}} = 26.748$ GPa. In the tangential direction, considering an average of the anteroposterior and mediolateral stiffnesses, we obtain $\bar{E}_{\text{tang}} = 21.680$ GPa, a value approximately 10% higher than that reported by Van Buskirk et al. (1981).

3.4.1 Difference between endosteal and periosteal bone stiffness

Our major hypothesis was that endosteal regions of cortical bone undergo modeling-related bone resorption during aging. The latter is due to increased osteoclast activity at the endosteal surface close to the bone marrow, which supplies abundant osteoclast precursor cells. Furthermore, endosteal bone regions are characterized by higher specific surface available for cell attachment and modeling/remodeling, compared to intracortical and periosteal regions (Buckwalter and Cooper, 1987). This ultimately leads to trabecularization of the cortex. Increased resorption modeling would then lead to (i) more mature bone, i.e., higher mineralization and, consequently, a stiffer bone matrix in endosteal regions; and (ii) a lower probability of microdamage removal and, therefore, higher damage in the endosteal area. Our results confirm this hypothesis: the periosteal regions are less stiff than the endosteal and mid-cortical regions; and there are more phases related to damage in the endosteal regions compared to the periosteal regions in the longitudinal direction, see Figure 3.3. These results are in agreement with studies showing that, in rat humeri and femora, under normal conditions, the majority of microcracks *in vivo* (84%) accumulates at the endosteal surface (O'Brien et al., 2005a), and that the volume fraction of microdamage is correlated with the maximum strain applied to the specimen (Fazzalari et al., 1998). On the other hand, they contradict studies showing no difference in elasticity between the endosteal, intracortical, and periosteal zones in dry human femoral bone (Rho et al., 2002).

While differences in modeling resorption and remodeling activity in endosteal and periosteal regions may explain the differences in the observed stiffness values, variation of the elastic modulus of bone may also be related to different levels of mineralization (Currey, 1969a,b; Katz, 1971; Oyen, 2006), differences in collagen fibril orientation (Franzoso and Zysset, 2009; Reisinger et al., 2011), and differences in collagen crosslinking within the different structural units during bone development (Willems et al., 2011).

3.4.2 Difference in bone stiffness between the anteroposterior and mediolateral directions

The significant differences found between the samples tested in the anteroposterior and the mediolateral direction confirm our hypothesis that the lack of mechanical stimulation near the neutral axis, closely aligning with the anteroposterior bending axis of the cross section, leads to a decrease of remodeling and, therefore, to a larger mineralized area and stiffer material in this direction.

3.4.3 Difference in bone stiffness between the longitudinal and tangential directions

Bone has been regarded as a transversely isotropic or orthotropic material. In the latter case, most authors agree that $E_{\text{longitudinal}} > E_{\text{tangential}} > E_{\text{radial}}$ (Van Buskirk et al., 1981; Rho, 1996; Espinoza Orías et al., 2009; Franzoso and Zysset, 2009), while in the former case, where no difference was found between the tangential and radial stiffness, it has been shown that $E_{\text{longitudinal}} > E_{\text{tangential}}$ (Reilly and Burstein, 1975; Yoon and Katz, 1976b; Ashman et al., 1984; Katz et al., 1984; Turner et al., 1999). Testing the variation of stiffness in tangential and radial direction was out of scope of this work. However, we confirmed the latter relationship, i.e., the extracellular bone matrix is stiffer in the longitudinal than in the tangential direction.

Overall, the properties of microstructural components of cortical bone in the tangential direction were lower than those in the longitudinal direction. These observations are consistent with other studies addressing bone anisotropy using nanoindentation (Fan et al., 2002; Rho et al., 2002; Franzoso and Zysset, 2009; Reisinger et al., 2011).

3.4.4 Difference in extent of damage in the longitudinal and tangential directions

An interesting finding of the current study is related to differences in the way experimental data in the longitudinal and tangential directions were fitted with a number of distributions by means of deconvolution. As shown in Figures 3.2 and 3.5, tests on more samples in the tangential direction resulted in the best fit with one distribution, compared with those in the longitudinal direction. This suggests that, in the longitudinal direction, for all but one sample, nanoindentation tests deliver elasticity data related to one undamaged and several damaged phases. In the tangential direction, on the other hand, the single distribution fitting the nanoindentation results for many of the samples suggests the existence of only one, undamaged, but no damaged phases. This can be explained by the cracks in bone lying predominantly in planes

comprising the longitudinal axis (Burr and Martin, 1993; O'Brien et al., 2000). Accordingly, the statistical probability of indenting in a crack or creating propagating cracks by indenting is lower on the anteroposterior and mediolateral surfaces than on the longitudinal ones, which may well explain the higher degree of damage detected on the latter.

Moreover, it was shown that osteonal boundaries in bone cross sections (on longitudinal surfaces) may act as barriers for microcrack propagation (Boyce et al., 1998), as long as the cracks have a certain length; but cracks over $300\ \mu\text{m}$ were reported to be able to penetrate osteons (O'Brien et al., 2005b). The collagen fiber-bone mineral relationship plays a key role in minimizing the formation of such larger detrimental microcracks, while encouraging the formation of numerous small cracks whose propagation does not lead to failure (Schaffler et al., 1994). Additionally, as many as to 87% of the microcracks were reported to appear in the interstitial tissue regions, the more mineralized bone material composed of osteonal and other lamellar bone fragments, which is also the oldest bone, therefore accumulating the greatest number of loading cycles and damage (Schaffler et al., 1995; Boyce et al., 1998; Mohsin et al., 2006). Considering the fact that, in the current work, the testing locations were chosen so that they are sufficiently far away from a Haversian canal, and the grid size was $90 \times 90\ \mu\text{m}^2$, most of the test results in the longitudinal direction relate to interstitial tissue, which explains also the extensive amount of damaged phases on the respective surfaces.

Regarding the origin of microcracks, we could not assess visually in the SEM how many stemmed from nanoindentation testing and how many had previously existed at the testing locations; however, microcrack formation studies in macroscopically tested bone have shown that pre-existing microcracks are fewer and generally shorter in comparison to those formed as a consequence of testing (O'Brien et al., 2005b; Mohsin et al., 2006).

3.5 Acknowledgements

The authors would like to acknowledge the kind, expert assistance of Dr. Tim Spelman in the statistical analysis of this project, and the assistance of David Thomas in the handling of the samples. MIP acknowledges a travel stipend of TU Wien for a research stay at the University of Melbourne. The ongoing cooperation between TU Wien and the University of Melbourne was facilitated through COST action MP 1005, NAMABIO. MIP and CH acknowledge financial support through the project ERC-StG-2010 MICROBONE, #257032. RB acknowledges the financial support of the Regional Partnership Program of the Canadian Institutes of Health Research.

Chapter 4

A new nanoindentation protocol for identifying the elasticity of undamaged extracellular bone tissue

Authored by Irina Furin, Maria-Ioana Pastrama, Hawraa Kariem, Krzysztof W. Luczynski, Olaf Lahayne, and Christian Hellmich
Published in *MRS Advances*, 1(11): 693–704, 2016

While the quest for understanding and even mimicking biological tissue has propelled, over the last decades, more and more experimental activities at the micro and nanoscales, the appropriate evaluation and interpretation of respective test results has remained a formidable challenge. As a contribution to tackling this challenge, we here describe a new method for identifying, from nanoindentation, the elasticity of the undamaged extracellular bone matrix. The underlying premise is that the tested bovine bone sample is either initially damaged (i.e., exhibits microcracks *a priori*) or that such microcracks are actually induced by the nanoindentation process itself, or both. Then, (very many) indentations may relate to either an intact material phase (which is located sufficiently far away from microcracks), or to differently strongly damaged material phases. Corresponding elastic phase properties are identified from the statistical evaluation of the measured indentation moduli, through representation of their histogram as a weighted sum of Gaussian distribution functions. The resulting undamaged elastic modulus of bovine femoral extracellular

bone matrix amounts to 31 GPa, a value agreeing strikingly well both with direct quasi-static modulus tests performed on SEM-FIB-produced micropillars (Luczynski et al., 2015), and with the predictions of a widely validated micromechanics model (Morin and Hellmich, 2014). Further confidence is gained through observing typical indentation imprints under Scanning Electron Microscopy (SEM), which actually confirms the existence of the two types of microcracks as described above.

Collaboration

This paper is the result of the masters' thesis of Irina Furin, who prepared the bone samples, carried out the nanoindentation campaign together with Maria-Ioana Pastrama, and processed the experimental results. The author of this thesis also performed supervision work of the master student and wrote most of the paper body, activities clearly indicating her as the second author of the paper. Hawraa Kariem provided support with the computational aspects of the deconvolution strategy, Krzysztof W. Luczynski was of great help in issues regarding sample preparation, while Olaf Lahayne conducted the machine training for the nanoindenter. Christian Hellmich conceived the research idea, provided constant supervision and manuscript feedback, and approved the paper for submission.

4.1 Introduction

Ever since the famous paper of Oliver and Pharr (Oliver and Pharr, 1992), indentation techniques have re-gained a very prominent role in material characterization, by extending their application to smaller and smaller scales, and coining a new term for these developments: nanoindentation. Originally applied to materials such as fused silica, soda-lime glass, or single crystals of aluminum, tungsten, quartz, and sapphire, the method was, soon thereafter, extended to biological materials such as bone (Rho et al., 1997, 1999; Zysset et al., 1999; Hengsberger et al., 2002; Rho et al., 2002). These applications were motivated, according to Rho et al. (1997), by the wish to measure the “intrinsic” elastic properties of several of the microstructural components of bone. In this context, “intrinsic” refers to the properties of bone tissue or extracellular bone matrix, which is defined at the scale of several to several tens of microns; rather than to those of a macroscopic (typically millimeter-sized) sample of cortical or trabecular bone. The aforementioned references revealed important new insight into these “intrinsic” bone properties. On the one hand, this insight concerned heterogeneity of bone tissue properties at different (small) observation scales; e.g., it was found that the bone tissue elastic properties of vertebrae are much smaller than

those of tibiae; that tibial osteonal regions are softer than interstitial ones (Rho et al., 1997); and that human femoral trabecular bone tissue is softer than cortical bone tissue (Zysset et al., 1999). On the other hand, such tests revealed that bone tissue properties are, on average, independent of adult tissue age (Rho et al., 2002; Hoffer et al., 2000b; Feng and Jasiuk, 2011; Wolfram et al., 2010); that bone tissue behaves not only instantaneously elastic, but also in a delayed fashion, i.e., viscoelastically; and that the latter properties depend critically on the hydration state of the material (Bembey et al., 2006).

Hence, while the method was very successful in terms of evidencing local differences in varying aspects of material behavior (exactly as the pioneers of the method had actually hoped for), the reconciliation of the quantitative values it provided with those of other methods delivering elastic properties, such as ultrasonic and quasi-static mechanical testing, turned out as challenging: In more detail, applying ultrasonic signals in the MHz frequency regime to bone samples results in the propagation of waves the wavelengths of which are typically less than one millimeter (Ashman et al., 1984; Lees et al., 1979, 1983); and according to the separation of scales principle in continuum (micro-) mechanics (Zaoui, 2002; Drugan and Willis, 1996) and the continuum theory of elastic waves (Fedorov, 1968), the aforementioned wavelengths need to be much larger than the characteristic material volume (also called representative volume element) whose elastic properties are characterized by the ultrasonic waves (Kohlhauser and Hellmich, 2013). Accordingly, MHz-regime-related ultrasonic tests reveal the elastic properties at the bone tissue scale (i.e., that of a material volume with several microns characteristic length), averaged over the size of the ultrasonically tested sample (Fritsch and Hellmich, 2007; Vuong and Hellmich, 2011).

However, such ultrasonically determined elastic stiffness values are, as a rule, consistently larger than those obtained (on average) from nanoindentation campaigns (Malandrino et al., 2012). Additionally, the same discrepancy was very recently found in the context of unloading mechanical tests on SEM FIB-produced micropillars (Luczynski et al., 2015), again delivering results in line with ultrasonic tests, but stiffer than those obtained from nanoindentation.

This discrepancy motivates the present study, aiming at an improved nanoindentation protocol that may indeed deliver results which are consistent with the aforementioned well-established and well-understood methods for elasticity determination, namely ultrasonic tests and unloading mechanical tests. Our proposition is that the aforementioned discrepancy may stem from bone microcracks measuring several to several tens of micrometers (Schaffler et al., 1994; Wenzel et al., 1996; O'Brien et al., 2000; Chapurlat et al., 2007), which may be – to some extent – ini-

tially present close to the indentation sites, but may be also actively induced by the indentation process itself. The basis for this proposition is that bone tissue is known to behave plastically at the level of several microns, as revealed by nanoindentation test imprints studied in the context of plasticity theory for nanogranular materials (Tai et al., 2006), by advanced micromechanics theories validated through various biochemical and biomechanical experiments (Fritsch et al., 2009b), and by mechanical tests of single micrometer-sized micropillars (Luczynski et al., 2015; Schwiedrzik et al., 2014); while it shows a quasi-brittle behavior at the scale of tens to hundreds of micrometers (Ritchie, 2011).

Accordingly, we here target at distinguishing tests conducted sufficiently far from microcracks *and* not inducing any neighbouring cracking events, hence fulfilling more appropriately the conditions needed for nanoindentation evaluation as proposed by Oliver and Pharr in 1992, from tests triggering such events or conducted close to microcracks. Therefore, we take inspiration from the so-called statistical or grid nanoindentation technique developed in the late 2000s (Constantinides and Ulm, 2007; Ulm et al., 2007; Vandamme and Ulm, 2009), where a statistical evaluation of very many indentation results allows for assignment of subgroups of these results to different chemical material phases present in a highly microheterogeneous material; and basically extend this idea from purely chemical differences between phases, to different degrees of mechanical *damage* present in the phases, or in other words, to indents differently close to crack-type defects. Thereby, our interest focuses exclusively on the one undamaged phase, and on its elastic properties.

The corresponding experimental and data evaluation steps are given in greater detail in the Materials and Methods section, and the corresponding results for the elasticity of the undamaged phase are then compared to tests giving direct access to this elasticity, namely to micropillar tests, and to ultrasonic tests in combination with advanced micromechanical theories (Morin and Hellmich, 2014). This comparison is further discussed in the Discussion section, which concludes the paper.

4.2 Materials and methods

4.2.1 Sample preparation

A diamond saw (Isomet, Buehler, USA) was used to cut four plane-parallel cortical bone samples normal to the longitudinal bone axis, under constant distilled water irrigation. These samples, obtained from an 18-month old bovine femur, had a thickness of 3.5 mm, and measured roughly 10×12 mm in the two other directions. They were glued onto glass slides and polished with a polishing machine (PM5, Logitech, Scotland), in order to provide smooth, i.e., low roughness surfaces. Thereby, the

Table 4.1: Polishing protocol for sample preparation

Sample	Particle size of sandpaper [μm]	Polishing time [min]	Plate speed [rpm]
1	18.3	3	10
	1 (diamond suspension on a cloth)	120	20
2	18.3	3	10
	1 (diamond suspension on a cloth)	180	20
3	18.3	3	10
	1 (diamond suspension on a cloth)	240	20
4	18.3	3	10
	1 (diamond suspension on a cloth)	300	20

polishing machine was operated in the “sweeping arm” mode – the polishing paper underwent a rotational movement, while the sample holder with the sample was not only rotating, but also translating – with 10 sweeps/minute. Between the preparation steps, the samples were kept in a freezer at -20°C , in order to preserve their mechanical properties (Linde and Sorensen, 1993; Nazarian et al., 2009; Fölsch et al., 2012).

In the first polishing step, all four samples were polished with coarse polishing paper (particle size $18.3\ \mu\text{m}$) for 3 min, in order to ensure that the top of each sample is completely parallel to the bottom, and an even surface without any tilt is provided. In the second polishing step the samples were finely polished, according to a previously published protocol (Miller et al., 2008), with a napped cloth impregnated with $1\ \mu\text{m}$, high performance, polycrystalline diamond spray (DP-Spray P), for different amounts of time (see Table 4.1 for details), so as to achieve a minimized roughness. In fact, the use of only one size of diamond particles for longer periods of time (rather than different sizes used over shorter times) increased the repeatability of the procedure until sample finishing. Differently long polished sample surfaces were compared, both visually in a light microscope (Zeiss Imager Z1m), and by means of scanning probe microscopy in the course of surface roughness measurements, as described in the next section.

4.2.2 Roughness determination

The roughnesses of Sample 1 (120 min of $1\ \mu\text{m}$ polishing) and of Sample 4 (300 min of $1\ \mu\text{m}$ polishing) were measured by means of the scanning probe microscopy (SPM) mode of a TriboIndenter system (Hysitron Inc., Minneapolis, MN, USA). This resulted in two topographic images measuring $15 \times 15\ \mu\text{m}^2$, with approximately 60 nm pixel size.

The root-mean-squared average roughness (RMS) of the surface, R_q , was calculated as

$$R_q = \sqrt{\frac{1}{P^2} \sum_{m=1}^P \sum_{n=1}^P z_{mn}^2}, \quad (4.1)$$

where P denotes the number of pixels along the edges of the scanned area, and z_{mn} is the distance height at position (m, n) from the mean plane of the scanned surface (Miller et al., 2008).

4.2.3 Nanoindentation

In order to check the undamaged elasticity of cortical bovine bone, nanoindentation tests were performed on the four prepared samples, using a Berkovich diamond tip attached to a TriboIndenter nanoindenting system (Hysitron Inc., Minneapolis, MN, USA). According to a previously published protocol for bone testing (Reisinger et al., 2011), a maximum indentation depth of 250 nm was prescribed, at a rate of 40 nm/s, then fixed for 20 s, before the substrate was again fully unloaded, at the same displacement rate. On each sample a grid of 12×12 indents with 5 μm spacing was defined, resulting in altogether 576 indentations. The measurements were evaluated according to the method of Oliver and Pharr (1992), where the reduced modulus E_r results from the initial slope S of the unloading portion in the load-displacement diagram, according to

$$E_r = \frac{S\sqrt{\Pi}}{2\sqrt{A}}. \quad (4.2)$$

In Eq. (4.2), A stands for the projected area of the elastic indentation contact. Then, E_r gives access to the elastic modulus of the substrate (here the extracellular bone tissue) E_s ,

$$E_s = \frac{(1 - \nu_s^2)}{\frac{1}{E_r} - \frac{(1 - \nu_t^2)}{E_t}}, \quad (4.3)$$

based on knowledge of Poisson's ratio of the extracellular bone matrix, $\nu_s = 0.3$ (van Rietbergen et al., 1995), as well as of Poisson's ratio and the elastic modulus of the diamond indenter tip, amounting to $\nu_t = 0.07$ and $E_t = 1141$ GPa.

The $N_E = 576$ test results for the value of the elastic modulus $E_{s,i}, i = 1, \dots, N_E$ were evaluated considering the potential (initial or penetration-induced) presence of microcracks close to the performed indents, effecting the values obtained from Eq. (4.2)–(4.3), which are actually resting on half-space theory for homogeneous (crack-free) solid domains. In order to discriminate “damaged” from “non-damaged” halfspaces characterized by nanoindentation, the concept of statistical or grid nanoindentation (Constantinides et al., 2006; Constantinides and Ulm, 2007; Ulm et al.,

2007) was adopted and modified, in the line of Kariem et al. (2015): The data for the values of E_s were fitted by N_{Gau} Gaussian Cumulative Distribution Functions (CDFs) with weighting factors f_j , $\sum_j^{N_{\text{Gau}}} f_j = 1$, out of which only one represented the intact, undamaged material; namely the one with the largest mean value. The latter is considered as the (average) elastic modulus of undamaged (extracellular) bone tissue. All other Gaussian CDFs represent material damaged to varying extents. This fitting process was repeated for several numbers of phases, and it can be written in mathematical detail as follows: Each one of the N_{Gau} Gaussian CDFs is written in standard form as

$$F_j^{\text{model}}(E_s; \mu_j, \sigma_j) = \frac{1}{\sigma_j \sqrt{2\pi}} \int_{-\infty}^{E_s} \exp\left(\frac{-(u - \mu_j)^2}{2\sigma_j^2}\right) du. \quad (4.4)$$

The weighted sum of these distributions is then

$$F_E^{\text{model}}(E_s) = \sum_{j=1}^{N_{\text{Gau}}} f_j F_j^{\text{model}}(E_s; \mu_j, \sigma_j). \quad (4.5)$$

Next, the CDF representing the (sorted) experimental data from nanoindentation, $E_{s,i}$, $i = 1, \dots, N_E$, is constructed according to

$$F_E^{\text{exp}}(E_{s,i}) = \frac{i}{N_E} - \frac{1}{2N_E}, \quad (4.6)$$

with $i \in [1, N_E]$, $N_E = 576$ indentations. An optimal fit of the experimental CDF through the superposition of N_{Gau} Gaussian CDFs with mean values μ and standard deviations σ was obtained through the following minimization problem:

$$\varepsilon = \sum_{i=1}^{N_E} [F_E^{\text{model}}(E_{s,i}) - F_E^{\text{exp}}(E_{s,i})]^2 \rightarrow \min. \quad (4.7)$$

The minimization procedure (4.7) was realized by means of an evolutionary algorithm that started with a set of approximated CDF parameters (mean μ_j , standard deviation σ_j , and weighting factor f_j), and, through several so-called ‘‘mutation cycles’’, converged towards the optimal parameters μ_j and σ_j , which, for a chosen number N_{Gau} of phases, provide the minimum given in Eq. (4.7). The algorithm was stopped based on a criterion involving the coefficient of determination, reading as

$$R^2 = 1 - \frac{\sum_{i=1}^{N_E} [F_E^{\text{model}}(E_{s,i}) - F_E^{\text{exp}}(E_{s,i})]^2}{\sum_{i=1}^{N_E} \left[F_E^{\text{exp}}(E_{s,i}) - \frac{1}{N_E} \sum_{k=1}^{N_E} F_E^{\text{exp}}(E_{s,k}) \right]^2}. \quad (4.8)$$

The chosen criterion was inspired by the deliberations of Weicker (2007), and reads as

$$0.00009 > \text{abs} \left[R_l^2 - \left(\frac{1}{1000} \sum_{l=1000}^i R_l^2 \right) \right] \quad \text{AND} \quad R^2 > 0.98, \quad (4.9)$$

with l as the number of mutation cycles; i.e., once the attained coefficient of determination is larger than 0.98 and different by not more than 0.00009 from those attained in the last 1000 mutations, the algorithm is stopped.

In order to finally select the optimal number of Gaussian CDFs, $N_{\text{Gau}} = N_{\text{opt}}$, for each superposition of Gaussian cumulative distribution functions, the relative error between experimental and model CDF was determined according to

$$e_{\text{rel}} = 100 \times \frac{1}{\max(E_{s,i}) - \min(E_{s,i})} \int_{\max(E_{s,i})}^{\min(E_{s,i})} [F_E^{\text{model}}(E_{s,i}) - F_E^{\text{exp}}(E_{s,i})] dE, \quad (4.10)$$

with $\max(E_{s,i})$ and $\min(E_{s,i})$ as the maximum and minimum values of Young's modulus obtained from nanoindentation tests, respectively, their difference representing the total range of experimental values, while the integral on the right hand side of the equation represents the difference between the $E_{s,i}$ -specific values of the model CDF (based on N_{Gau} Gaussians) and of the experimental CDFs. The number of Gaussian distributions N_{opt} that best fit the experimental data was chosen to be that which resulted in the minimum relative error e_{rel} . The corresponding mean value μ_0 is regarded as the undamaged bone tissue modulus, $\mu_0 = E_{\text{BT}}$.

4.3 Results

4.3.1 Microscopic surface investigation and roughness measurements

The initial, coarse polishing of the specimens mainly resulted in milling off enough material so as to correct a potential tilt of the sample; this left scratch-type traces on the surface, and reduced the sample thickness by approximately 0.5 mm. Subsequent polishing with the 1 μm diamond suspension clearly revealed, under light microscopic magnifications, the finer bone microstructures, see Figure 4.1(a) and (b); all bone samples exhibited a transitional state between plexiform (lamellar) and haversian (osteonal) bone structures, common for young growing beef: stacks of long, parallel lamellae separated by vascular spaces, with osteons in between (Katz et al., 1984; Locke, 2004). No optical differences between samples subjected to different polishing times could be found, see Figure 4.1(a) and (b) for a comparison of the surfaces of Samples 1 and 4, polished with 1 μm diamond suspension for 120 and for 300 min, respectively.

The roughness measurements delivered an average RMS roughness of 11.61 nm for Sample 1, and of 9.12 nm for Sample 4. These results confirm that the different polishing times did not result in significantly different RMS roughnesses of the respective samples. In fact, the maximum indentation depth (250 nm) was more than

one order of magnitude larger than the average roughness, thus ensuring that the latter does not influence the results of the nanoindentation tests (Bobji and Biswas, 1998). The SPM-detected surface topography of Sample 1 with visible indentation marks is shown in Figure 4.1(c).

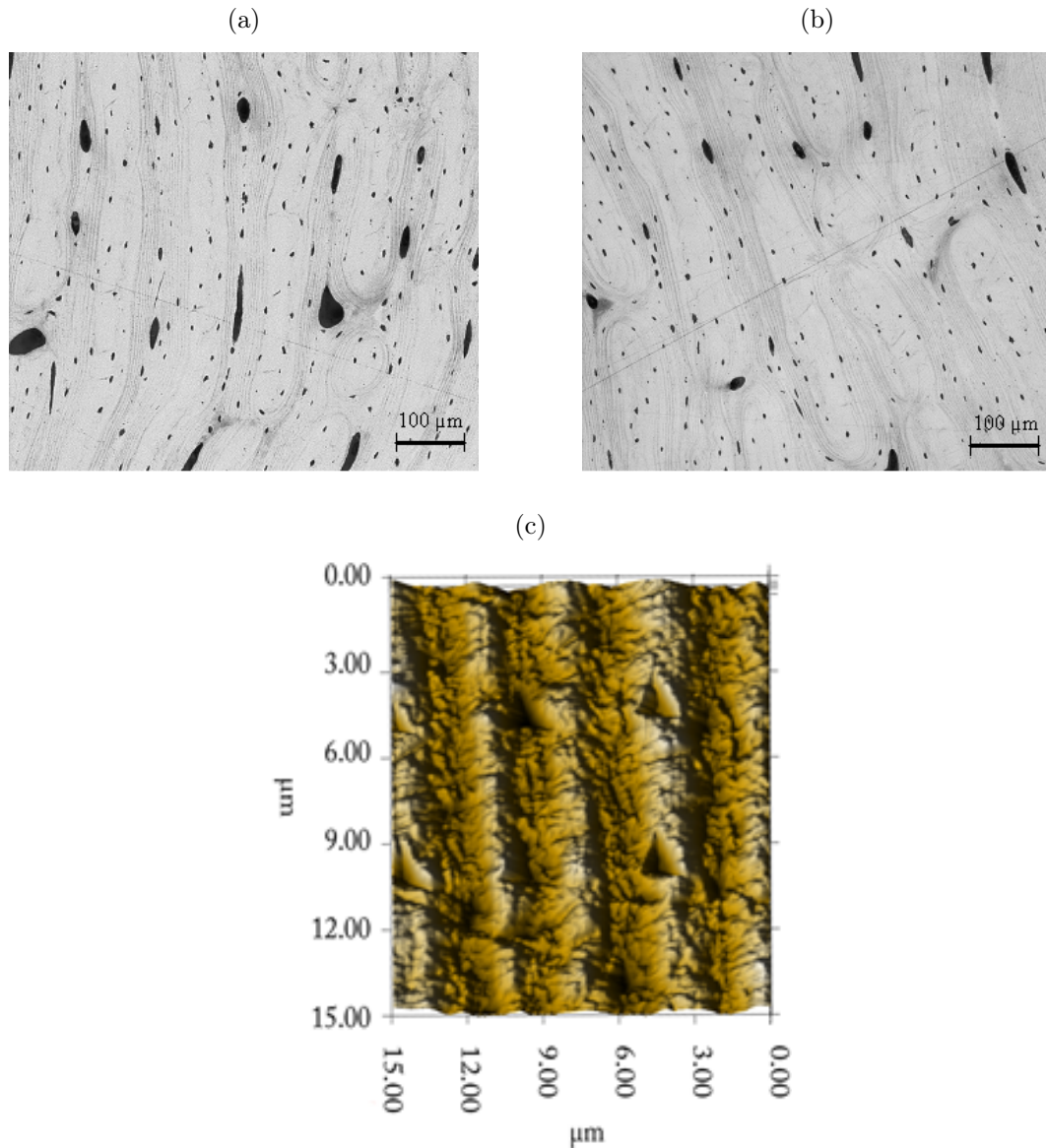


Figure 4.1: (a) Light micrograph of the surface of Sample 1 (120 min of fine polishing with a 1 μm diamond suspension on a cloth); (b) Light micrograph of the surface of Sample 4 (300 min of fine polishing with a 1 μm diamond suspension on a cloth); the two surfaces show no significant optical differences; (c) A surface topography image of the indented area of Sample 1 generated in the SPM mode for roughness determination, with visible indentation marks

4.3.2 Undamaged elastic modulus of bovine bone

A typical load-displacement curve for undamaged bone material is shown in Figure 4.2. According to the optimization procedure given by Eq. (4.4) – (4.10), all $N_E = 576$ experimentally determined elastic modulus data were fitted with a number N_{Gau} of distributions varying from 1 to 10. The best fit, that minimized the relative error e_{rel} between the experimental and the summed model CDF, as given through Eq. (4.10), to 0.62 % (see Table 4.2), was obtained for $N_{\text{opt}} = 5$ Gaussian distributions, of which four are considered to represent damaged material phases, and one corresponds to the intact material; the mean value of the elastic modulus of the latter being the highest of all and thus representing Young’s modulus of the undamaged, intact bovine bone material. This modulus amounts to $E_{\text{BT}} = 31.4 \pm 2.5$ GPa.

The experimental, as well as the single and summed Gaussian probability distribution functions (or normalized histograms) corresponding to the CDFs of the elastic modulus are shown in Figure 4.3.

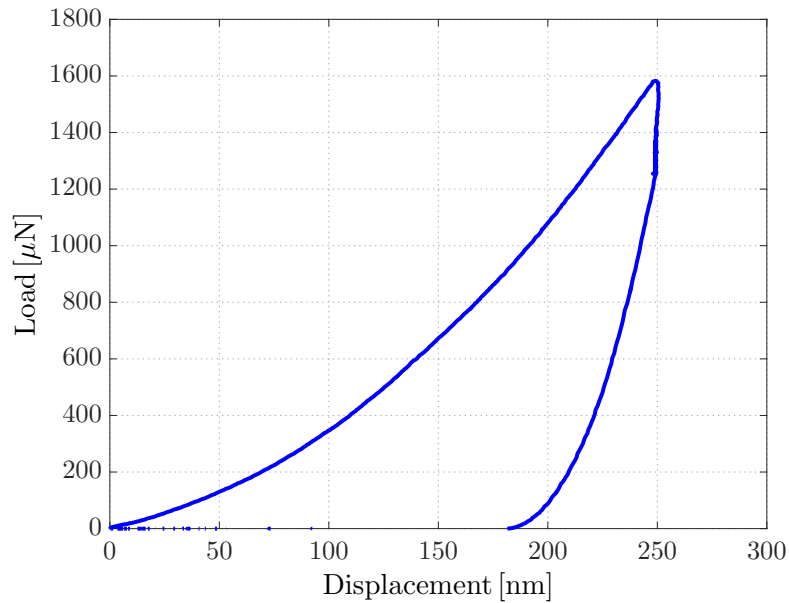


Figure 4.2: Typical load-displacement curve of non-damaged extracellular bovine bone matrix, delivering, according to Eq. (4.2) and (4.3), an elastic modulus of $E_s = 30.53$ GPa at 250 nm maximal displacement

4.4 Discussion

We presented here a new method for identification of the undamaged elastic modulus of a solid phase within a (partially) microcracked medium tested through nanoin-

Table 4.2: Results for different numbers of distributions used to fit the experimental data: mean value of Young's modulus for the distribution corresponding to intact bone material (E_{BT}); standard deviation (σ_{BT}); coefficient of determination (R^2); relative error (e_{rel})

Number of distributions	E_{BT} [GPa]	σ_{BT}	R^2	e_{rel} [%]
1	24.6651	9.1864	0.8891	13.7157
2	28.0215	5.7494	0.9833	3.8431
3	29.7854	3.0053	0.9935	2.0848
4	30.8070	2.4301	0.9957	1.1774
5	31.3892	2.4858	0.9967	0.6221
6	31.9549	2.0082	0.9949	0.6587
7	32.2018	1.9942	0.9943	0.6326
8	32.4607	1.9967	0.9932	0.6786
9	32.7463	1.9947	0.9928	0.7211
10	33.8508	0.9211	0.9899	3.3354

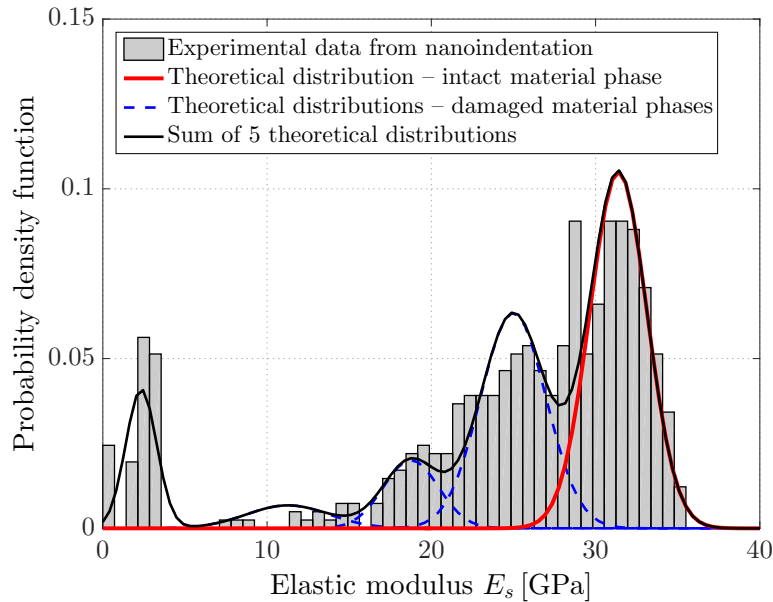


Figure 4.3: Probability distribution functions (normalized histogram) of experimental values of elastic moduli obtained by nanoindentation and fitting of the data by means of the sum of five Gaussian distributions, four of them representing damaged material and the last one representing intact extracellular bone matrix

dentation. Therefore, very many indents were performed on bovine bone samples, and the corresponding histogram of elastic moduli was represented in terms of the weighted sum of Gaussian distribution functions. This representation turned out as very precise, so that the different Gaussians could be interpreted as reflecting the elastic behavior of differently stiff material phases, the stiffest of which would be the undamaged matrix phase, the others referring to different levels of mechanical damage. It is interesting to compare our result for the undamaged phase, $E_{BT} = 31.4 \pm 2.5$ GPa, to independent, alternative experimental results concerning extracellular bovine bone matrix. In fact, on the very same type of bone, unloading quasi-static tests on SEM-FIB-produced micropillars with only one micron side length and a couple of micrometers height (Luczynski et al., 2015) revealed a strikingly similar value, amounting to 29.9 ± 2 GPa.

Furthermore, our results can be compared to the predictions of advanced micromechanical material modeling of bone (Morin and Hellmich, 2014): Feeding the composition and hierarchical interaction rules documented in the aforementioned paper with the bone tissue mass density reported as 2.044 ± 0.43 g/cc (Lees et al., 1979), yields an axial elastic modulus of bone tissue amounting to 30.1 GPa, again in virtually perfect agreement with the outcome of our new experimental method. Coincidentally, this micromechanics model predicts the corresponding axial Poisson ratio as 0.3, thus fully confirming the choice used in the second section of the present paper (van Rietbergen et al., 1995).

Finally, the underlying idea of microcracks, either positioned at different distances from the indents (and therefore affecting the result stemming from Oliver and Pharr's half-space problem), or directly emanating from the indents, indicating direct sample damaging by the very indentation process itself, can be checked through observation of indentation processes in a scanning electron microscope (SEM). A preliminary small number of tests using the same protocol as described above was made with a PI85 nanoindenter (Hysitron Inc., Minneapolis, MN, USA) mounted in an SEM (FEI Quanta 200 FEG, Oregon, USA). Secondary electron images obtained using an Everhart-Thornley Detector (ETD) with an accelerating voltage of 10 kV revealed indeed the existence of the aforementioned types of cracks, see Figure 4.4.

4.5 Acknowledgements

Financial support through project ERC-StG-2010 MICROBONE, #257032, is gratefully acknowledged. The authors are also grateful for the support of Jelena Zivkovic, in the course of the preliminary SEM-nanoindentation tests. Her stay at TU Wien was made possible through a scholarship of KMM-VIN.

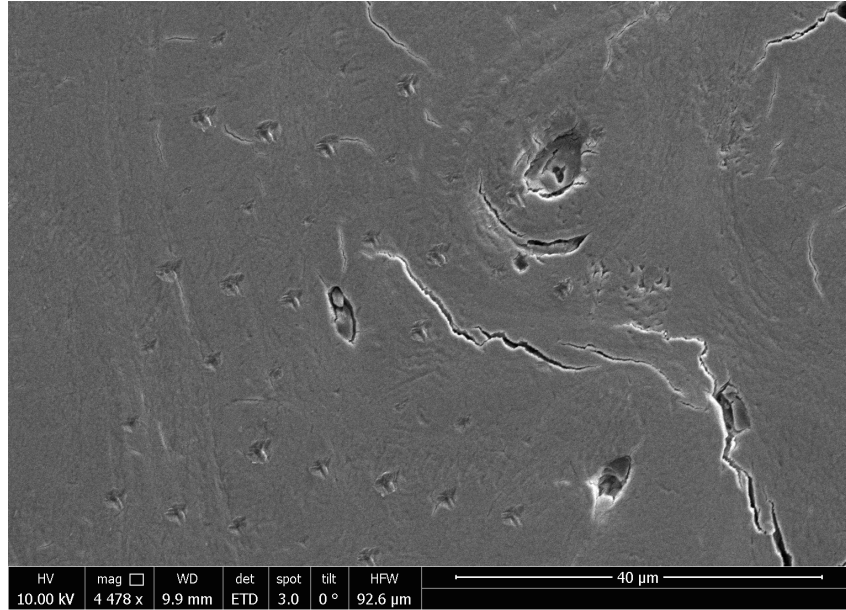


Figure 4.4: SEM image taken during nanoindentation tests, showing cracks and holes inside the grid of indents

4.6 Appendix: Abbreviations and nomenclature

A	projected area of the elastic indentation contact
CDF	cumulative distribution function
e_{rel}	relative error
$E_{\text{BT}} = \mu_0$	elastic modulus of undamaged, intact extracellular bone tissue material
E_r	reduced elastic modulus
E_s	elastic modulus of the tested substrate (i.e., damaged or undamaged extracellular bone matrix)
$E_{s,i}$	i^{th} experimental value of E_s , as determined by nanoindentation
E_t	elastic modulus of the indenter tip
f_j	weighting factor of the Gaussian cumulative distribution function (CDF) related to material phase j
F_E^{exp}	CDF of elastic modulus of extracellular bone matrix, determined from nanoindentation experiments
F_E^{model}	CDF of elastic modulus of extracellular bone matrix, modeled as weighted sum of Gaussian CDFs
F_j^{model}	Gaussian CDF of elastic modulus of j^{th} phase of extracellular bone matrix

FIB	focused ion beam
i	index numbering of the performed indentations $i \in [1, N_E]$
l	number of mutation cycles in evolutionary strategy
m	index in topographic image (from SPM-based roughness measurement)
n	index in topographic image (from SPM-based roughness measurement)
N_E	total number of performed indentations for elastic modulus determination
N_{Gau}	total number of Gaussian CDFs
N_{opt}	optimal number of Gaussian CDFs
P	number of pixels along the edges of the area scanned for roughness determination
R^2	coefficient of determination
R_q	root-mean-squared (RMS) roughness of the surface
S	contact stiffness, defined as the initial slope of the unloading branch of a load-displacement diagram obtained from a nanoindentation test
SEM	scanning electron microscopy
SPM	scanning probe microscopy
u	integration variable in CDF
z_{mn}	SPM-derived distance from mean plane, at pixel with position (m, n)
ε	sum of squares of residuals
μ_j	mean value of elastic modulus related to material phase j
ν_t	Poisson's ratio of the indenter tip
ν_s	Poisson's ratio of the tested substrate (i.e., extracellular bone matrix)
σ_j	standard deviation of elastic modulus related to material phase j

Micro-poro-elasticity of baghdadite-based bone tissue engineering scaffolds: A unifying approach based on ultrasonics, nanoindentation, and homogenization theory

Authored by Hawraa Kariem, Maria-Ioana Pastrama, Seyed Iman Roohani-Esfahani, Peter Pivonka, Hala Zreiqat, and Christian Hellmich

Published in *Materials Science and Engineering C*, 46: 553–564, 2015

Microstructure-elasticity relations for bone tissue engineering scaffolds are key to rational biomaterial design. As a contribution thereto, we here report comprehensive length measuring, weighing, and ultrasonic tests at 0.1 MHz frequency on porous baghdadite ($\text{Ca}_3\text{ZrSi}_2\text{O}_9$) scaffolds. The resulting porosity-stiffness relations further confirm a formerly detected, micromechanically explained, general relationship for a great variety of different polycrystals, which also allows for estimating the zero-porosity case, i.e., Young's modulus and Poisson's ratio of pure (dense) baghdadite. These estimates were impressively confirmed by a physically and statistically independent nanoindentation campaign comprising 1750 indents. Consequently, we can present a remarkably complete picture of porous

baghdadite elasticity across a wide range of porosities, and, thanks to the micromechanical understanding, reaching out beyond classical elasticity, towards poroelastic properties, quantifying the effect of pore pressure on the material system behavior.

Collaboration

This paper results from a collaboration between the Institute for Mechanics of Materials and Structures of TU Wien, the Australian Institute for Musculoskeletal Science at the University of Melbourne, and the Biomaterials and Tissue Engineering Research Unit at The University of Sydney, Australia. The scaffolds were produced by Seyed Iman Roohani-Esfahani under the supervision of Hala Zreiqat. In the course of her masters' thesis, Hawraa Kariem carried out the nanoindentation and ultrasound tests together with Maria-Ioana Pastrama, and conceived the evolutionary algorithm for the deconvolution of the nanoindentation data. Besides her experimental and supervision work, as well as support in planning the nanoindentation campaign, the author of this thesis contributed to documentation and manuscript writing, activities which qualify her as the second author of this paper. Peter Pivonka and Christian Hellmich conceived the reasearch direction, provided final feedback for the manuscript, and approval for submission.

5.1 Introduction

With an estimated 2.2 million yearly bone graft procedures for the treatment of critical size defects, bone is the second-most implanted material after blood (Lewandrowski et al., 2000). Despite considerable progress over the years, the current gold standard, autografting (Calori et al., 2011), where bone from the patient is transplanted from one place to another, is limited by the amount of bone available, and may imply pre-and post-operative complications and morbidity, as well as the risk of infection (Goulet et al., 1997). The current clinical alternative, allografting, where cadaveric or synthetic bone is implanted, carries the risk of viral disease transmission, immunogenicity, and nonunion (Moore et al., 2001). This has motivated, for more than two decades, research in the field of bone tissue engineering (Langer and Vacanti, 1993; Hutmacher, 2000; Griffith and Naughton, 2002; Hollister, 2005), aiming at repairing damaged bone and restoring its functions (Bala et al., 2011) with the help of biocompatible materials cultivated with cells and corresponding growth factors (Khanna et al., 2012). For this purpose, the scaffolds have to be designed in a way to provide sufficient porosity for good vascular and tissue ingrowth, while not overly compromising the overall mechanical properties of the implant, i.e., its

stiffness and strength. This design process, involving also the biological properties of the implant material, turns out as very complex, and implies many design parameters whose interplay is extremely challenging to decipher in a classical “trial-and-error” procedure, requiring a multitude of *in vitro* and *in vivo* experiments. This challenging situation has given rise to the wish for rational, computer-aided design of biomaterials, regarding not only biological and cell transport aspects, but also mechanics.

The present paper will concentrate on the latter aspect, thereby not being restricted to the measurement of some mechanical properties, but to a micromechanics theory-based understanding of an entire class of ceramic biomaterials, supported by a new set of experimental data making the aforementioned understanding feasible. More precisely, we will develop the micromechanics of porous baghdadite scaffolds (Ramaswamy et al., 2008) – these materials showed an *in vivo* osteoconductivity in critically sized defects induced into rabbit radius bones, which exceeds that of other scaffold types (Roohani-Esfahani et al., 2012). These developments will be described in the remainder of the present paper, which is organized as follows: porosity and ultrasonic test protocols together with their theoretical foundations will be dealt with in Section 5.2.1. For a deeper understanding of the resulting porosity-elasticity relations, Section 5.2.2 will cover a micromechanics formulation valid for a multitude of porous polycrystals, as developed in recent years (Fritsch et al., 2006, 2009a, 2013), and its application to the newly collected experimental data. This will give access to the elastic properties of pure (dense) baghdadite. The methods section is then completed by a nanoindentation campaign allowing for an independent check of the elasticity of pure baghdadite, as described in Section 5.2.3. The results of our comprehensive and consistent experimental-theoretical-computational multiscale mechanics approach to baghdadite scaffolds for bone tissue engineering are presented in Section 5.3, and further discussed in Section 5.4, in particular with respect to important theoretical and experimental features which allow for this consistent, unified view on the investigated bone biomaterial class.

5.2 Materials and methods

5.2.1 Weighing and ultrasonic tests, for porosity and elasticity determination

Combining the sol-gel method for powder production with the polymer sponge replication method for the final scaffold processing (Roohani-Esfahani et al., 2012), cylindrically shaped porous baghdadite samples of nominally 12 mm height and 6 mm diameter were made, and categorized with decreasing nominal porosities, into sample

sets A to D. Their precise dimensions of height and diameter were measured by means of a digital sliding caliper, and these dimensions were used to compute the cylindrical volume V of each of the samples. Then, their mass m was weighed, giving access to the samples' mass density through

$$\rho = \frac{m}{V}. \quad (5.1)$$

Additional consideration of the (real) mass density of pure (dense) baghdadite, $\rho_{\text{solid}} = 3.48 \text{ g} \cdot \text{cm}^{-3}$ (Al-Hermezi et al., 1986), allows for computation of the scaffold porosity as

$$\phi^{\text{exp}} = 1 - \frac{\rho}{\rho_{\text{solid}}}. \quad (5.2)$$

Thereafter, ultrasonic tests were performed in the pulse transmission mode, by means of a device consisting of a pulser receiver (5077PR, OlympusNDT), an oscilloscope (WaveRunner 62Xi, Lecroy, USA), and ultrasonic transducers. Following the protocol of Kohlhauser et al. (2009) and Kohlhauser and Hellmich (2013) the pulser unit was set to emit an electrical square pulse up to 400 V. The piezoelectric elements inside the ultrasonic transducers transformed the electrical signals of a frequency f into corresponding mechanical signals, when operating in the sending mode, or they transformed mechanical signals back into electrical ones, when functioning as a receiver. Honey was used as a coupling medium. The time of flight t_f of the ultrasonic wave through the sample was accessed by the oscilloscope, and the travel distance through the specimen was equivalent to the scaffold's height h_s . These quantities provide direct access to the wave velocity v through

$$v = \frac{h_s}{t_f}. \quad (5.3)$$

According to the theory of plane waves in a 3D solid (Carcione, 2007), the wave velocity gives access to the stiffness of the tested sample. The current study is restricted to longitudinal waves, where the directions of "particle" displacement and of the wave propagation are parallel – in this case, the wave velocity gives access to the normal component C_{1111}^{exp} of the stiffness tensor, through

$$C_{1111}^{\text{exp}} = \rho \times v^2. \quad (5.4)$$

What still needs to be specified is the size at which the aforementioned "particle" is defined. In continuum (micro)mechanics (Zaoui, 2002), such a "particle" is called material volume or representative volume element (RVE), with a characteristic length l_{RVE} being considerably larger than the inhomogeneities d within the RVE, and the RVE being subjected to homogeneous stress and strain states. Consequently, the

characteristic length l_{RVE} needs to be much smaller than the scale of the characteristic loading of the medium, here the wavelength λ , which follows from wave velocity v and frequency f as

$$\lambda = \frac{v}{f}. \quad (5.5)$$

The aforementioned separation of length scales reads mathematically as

$$d \ll l_{\text{RVE}} \ll \lambda. \quad (5.6)$$

Accordingly, ultrasonic waves with wavelength λ detect the stiffness of a material with characteristic length l_{RVE} . More precisely, the “ \ll ” signs in Eq. (5.6) need to refer to a ratio of $d/\lambda \leq 0.03$, in order to access the normal stiffness component C_{1111} of the tested material with inhomogeneity size d , as was experimentally quantified by Kohlhauser and Hellmich (2013). As for the aforementioned baghdadite samples, the inhomogeneity size relates to the pore diameters, amounting to about 500 μm , as accessed by scanning electron microscopy (Roohani-Esfahani et al., 2012). Thereby, the sample needs to be always representative of the material (i.e., it needs to consist of at least one entire RVE of the latter), so that $(h_s, d_s) \geq l_{\text{RVE}}$. Hence, the required scale separation between RVE length and wavelength λ might well accommodate wavelengths which are much larger than the sample, while precisely delivering the elastic properties of the material making up the sample. In order to check different options for the determination of C_{1111}^{exp} according to Eq. (5.4), while considering scale separation conditions (5.6), the samples were sonified with a frequency of 0.1 MHz.

5.2.2 Polycrystal micromechanics – elastic properties of pure (dense) baghdadite

The porosity-stiffness relations determined experimentally according to Section 5.2.1 were then evaluated within the framework of continuum micromechanics (or random homogenization (Zaoui, 2002; Dormieux et al., 2006)) of porous polycrystals, developed in recent years for RVEs consisting of one porous phase and infinitely many, disc- or needle-shaped crystal phases oriented in different space directions (Fritsch et al., 2006, 2009a, 2013). More specifically, a large number of porosity and stiffness data from different isotropic materials, such as hydroxyapatite (De With et al., 1981; Gilmore and Katz, 1982; Liu, 1998; Charrière et al., 2001), bioactive glass-ceramics (CEL2) (Malasoma et al., 2008), gypsum (Ali and Singh, 1975; Phani, 1986; Tazawa, 1998; Meille, 2001; Çolak, 2006; Sanahuja et al., 2010), various piezoelectric ceramics (Craciun et al., 1998), alumina (Coble and Kingery, 1956; Pabst et al., 2004, 2006), zirconia (Pabst et al., 2006), as well as silica and nitride carbides (Haglung and Hunter, 1973; Díaz and Hampshire, 2004; Reynaud et al., 2005) could be integrated

into only two crystal shape- (i.e., needle or disc-) specific scaling relations for the (homogenized) elastic modulus of polycrystals. Both relations can be approximated by a power function reading as (Fritsch et al., 2013)

$$\frac{E^{\text{hom}}}{E_s} \cong B_E(1 - \phi)^{C_E}, \quad (5.7)$$

with E^{hom} as Young's modulus of the overall porous polycrystal, E_s as Young's modulus of the single crystal, and B_E and C_E as crystal shape-specific coefficients. Earlier obtained images (Roohani-Esfahani et al., 2012) suggest the baghdadite crystals to be disc-shaped, with corresponding coefficients $B_E = 0.9867$ and $C_E = 2.053$ (Fritsch et al., 2013), and overall Poisson's ratio which only depends on that of the single crystals, ν_s , and on the porosity ϕ , following a polynomial approximation

$$\nu^{\text{hom}} = A_\nu(1 - \phi)^4 + B_\nu(1 - \phi)^3 + C_\nu(1 - \phi)^2 + D_\nu(1 - \phi) + E_\nu, \quad (5.8)$$

with the coefficients fulfilling a linear relation of the format

$$q = a^*\nu_s + b^*, \quad \text{with } q = A_\nu, B_\nu, C_\nu, D_\nu, E_\nu, \quad (5.9)$$

see Table 5.1 for values of a^* and b^* . Young's modulus and Poisson's ratio give access to the stiffness component C_{1111} , whereby E_s and ν_s follow the scaling relations in Eqs. (5.7) and (5.8), so that

$$C_{1111}^{\text{hom}} = \frac{E^{\text{hom}}(E_s, \phi) \times [1 - \nu^{\text{hom}}(\nu_s, \phi)]}{[1 + \nu^{\text{hom}}(\nu_s, \phi)] \times [1 - 2\nu^{\text{hom}}(\nu_s, \phi)]}. \quad (5.10)$$

Minimizing the mean absolute error between the micromechanics-based stiffness expression (5.10) evaluated for experimentally determined porosities ϕ_i^{exp} , and corresponding experimentally determined stiffness values $C_{1111}^{\text{exp},i}$,

$$\sum_i \left| C_{1111}^{\text{hom}}(\phi_i^{\text{exp}}, E_s, \nu_s) - C_{1111}^{\text{exp},i} \right| \rightarrow \min, \quad (5.11)$$

provides an estimate for the elastic properties of pure (dense) baghdadite.

5.2.3 Nanoindentation

In order to provide a check for the estimated properties of pure baghdadite, according to Section 5.2.2, from experimentally determined porosity-stiffness relations and polycrystal micromechanics, a nanoindentation campaign comprising 1750 indents was performed. For this purpose, one sample was chosen from each of the sample sets A to D. Following the protocol reported by Hum et al. (2013), these samples were then embedded in resin (Epofix, Struers, Denmark), and held for 10 min in a

Table 5.1: Coefficients a^* and b^* defining linear relation (5.9) between Poisson's ratio of single crystals, ν_s , and polynomial coefficients A_ν , B_ν , C_ν , D_ν and E_ν in porosity-Poisson's ratio relation (5.8)

q	a^*	b^*
A_ν	-1.0521	0.2197
B_ν	2.2684	-0.4645
C_ν	-0.8121	0.1662
D_ν	0.3602	-0.0718
E_ν	0.2394	0.1496

vacuum chamber to eliminate air bubbles, before being dried for 48 h. Afterwards, the embedded samples were cut into 2 mm thick sections by means of a water-cooled low speed saw (IsoMet, Buehler), and glued onto object slides. This enabled subsequent polishing, first through a polishing machine (PM5, Logitech, Scotland) with increasingly fine sandpaper, and, eventually, with a napped cloth impregnated with 3 μm small diamond grains, see Table 5.2 for details of the polishing protocol. Due to their high porosity, the samples from set A displayed very limited solid surfaces for testing. Therefore, two scaffolds from this set were prepared for nanoindentation, in order to allow for a sufficient number of measurements. The nanoindentation tests (Nano Hardness Tester, CSM, Switzerland) were performed with a Berkovich tip in the load-controlled mode. The loading-unloading rate was set at 30 mN/min, the holding time was 10 s, and four different maximum loads were used: 10, 15, 20 and 30 mN. The specific measurement details are given in Table 5.3. Although two scaffolds from set A were prepared for indentation, there was still not enough surface for performing as many measurements as on samples from the other sets. Thus, no tests with a maximum load of 30 mN were performed on sample set A.

The 1750 measurements were evaluated according to the method of Oliver and Pharr (1992), which states that the elastic unloading stiffness S is defined as the slope of the unloading curve during the initial stages of unloading. The relationship between the stiffness S , the contact area A , and the reduced elastic modulus E_r is given by

$$S = \frac{2}{\sqrt{\pi}} E_r \sqrt{A}. \quad (5.12)$$

The reduced modulus E_r takes into account that elastic displacements occur in both the substrate – here a dense (pure) baghdadite crystal with elastic modulus E_s and Poisson's ratio ν_s – and in the Berkovich indenter, with elastic modulus E_t and Poisson's ratio ν_t :

$$\frac{1}{E_r} = \frac{(1 - \nu_t^2)}{E_t} + \frac{(1 - \nu_s^2)}{E_s}. \quad (5.13)$$

Table 5.2: Polishing protocol with machine PM5 Logitech (Scotland)

Step	Particle size of sandpaper [μm]	Polishing time [min]	Type of arm movement	Plate speed [rpm]
1	6.5	3	Sweeping	18
2	2.5	5	Sweeping	25

Table 5.3: Number of nanoindentation measurements per sample and per load

Sample	Porosity [%]	Maximum load [mN]	Measurements
A2	94	10	22
		10	56
A8		15	39
		20	33
B8	85	10	50
		15	50
		20	50
		30	50
C3	81	10	50
		15	50
		20	50
		30	50
D1	66	10	300
		15	300
		20	300
		30	300

The elastic properties of the diamond indenter are known and considered in the indentation software: $E_t = 1141$ GPa and $\nu_t = 0.07$ (Oliver and Pharr, 1992; CSM, 2008). Hence, combination of Eqs. (5.12) and (5.13) allows for expressing Young's modulus of pure baghdadite as a function of the unloading stiffness S , and of E_t , ν_t , and ν_s :

$$E_s = \frac{(1 - \nu_s^2) \frac{S\sqrt{\Pi}}{2\sqrt{A}} E_t}{E_t - (1 - \nu_t^2) \frac{S\sqrt{\Pi}}{2\sqrt{A}}}, \quad (5.14)$$

where the value for ν_s is adopted from the results corresponding to Section 5.2.2.

The analysis of 1750 values for E_s according to Eq. (5.14) follows the concept of the statistical or grid nanoindentation method (Constantinides et al., 2006; Constantinides and Ulm, 2007; Ulm et al., 2007). This method is based on the statistical analysis of a large number of indentation-derived values of a mechanical property

such as Young's modulus E_s . In more detail, the measured data are first used to generate the experimental Cumulative Distribution Function (CDF): The number of indentations N_E and the sorted values of elastic modulus $E_{s,i}$ deliver the N_E points $F_E^{\text{exp}}(E_{s,i})$ of the experimental CDF,

$$F_E^{\text{exp}}(E_{s,i}) = \frac{i}{N_E} - \frac{1}{2N_E}, \quad (5.15)$$

with $i \in [1, N_E]$, $N_E = 1750$ denoting the number of indentations. The key premise of the statistical indentation method is then to approximate the experimental CDF by the superposition of several CDFs related to the individual material phases making up the substrate which is subjected to grid nanoindentation. While earlier applications of the method discriminated the material phases according to their different chemical natures (Constantinides et al., 2006; Constantinides and Ulm, 2007; Ulm et al., 2007), we here consider different mechanical properties arising from changes induced in the substrate material through the indentation testing itself: The loads to which the substrate is subjected are likely to sometimes induce cracking (or damage) of the material, a phenomenon which is known to occur also in the context of nanoindentation of bone with a protocol similar to ours, see e.g., (Malandrino et al., 2012). This implies that at least two material phases are expected in the tested substrate: (i) intact baghdadite, and (ii) one damaged phase (or several different damaged phases related to different crack sizes or densities, representing somehow the "fractal" nature of cracking).

We represent the mechanical effect of each of the phases by means of a Gaussian (cumulative) distribution

$$F_j^{\text{model}}(E_s; \mu_j, \sigma_j) = \frac{1}{\sigma_j \sqrt{2\pi}} \int_{-\infty}^{E_s} \exp\left(-\frac{(u - \mu_j)^2}{2\sigma_j^2}\right) du, \quad (5.16)$$

with the mean value μ_j and standard deviation σ_j of each phase, the weighted sum of these distributions being

$$F_E^{\text{model}}(E_s) = \sum_{j=1}^{N_{\text{Gau}}} f_j F_j^{\text{model}}(E_s; \mu_j, \sigma_j). \quad (5.17)$$

We then fit the experimental CDF by N_{Gau} model CDFs with weighting factors (or volume fractions) f_j , $\sum_j^{N_{\text{Gau}}} f_j = 1$, through minimization of the following error:

$$\varepsilon = \sum_{i=1}^{N_E} [F_E^{\text{model}}(E_{s,i}) - F_E^{\text{exp}}(E_{s,i})]^2 \rightarrow \min. \quad (5.18)$$

The minimization procedure itself is performed by an evolutionary strategy, as described in the Appendix. We realize this optimization procedure for different numbers

of phases, we check whether the number of chosen phases, $N_{\text{Gau}} \geq 2$, has an effect on the mean value of the rightmost CDF (relating to Young's modulus of pure, intact baghdadite $\max(\mu_j) = E_s^{\text{NI}}$), and whether the latter agrees with that obtained according to Section 5.2.2. The goodness of the fit with N_{Gau} distributions is quantified through the coefficient of determination R^2 , and through the relative error e_{rel} in % which is defined as

$$e_{\text{rel}} = 100 \times \sum_{i=1}^{N_E} \left[1 - \frac{F_E^{\text{model}}(E_{s,i})}{F_E^{\text{exp}}(E_{s,i})} \right]. \quad (5.19)$$

5.3 Results

5.3.1 Porosity and elasticity determination

The porosity of the baghdadite samples ranged between 66 % and 94 %, see Table 5.4 for sample-specific details. The corresponding normal stiffness components C_{1111}^{exp} ranged from 0.43 to 17.27 GPa, see Table 5.5. These stiffness components monotonously decrease with increasing porosity, see Table 5.6 and Figure 5.1. The corresponding wavelengths according to Eq. (5.5) with $f = 0.1$ MHz and v as reported in Table 5.5, ranged from 1.40 to 3.88 cm, hence, they fulfill the separation of scales requirement given in Eq. (5.6) for $d = 500$ μm , and, correspondingly, the derived stiffness values ranging from 0.43 to 17.27 GPa indeed refer to the overall porous baghdadite scaffold material.

5.3.2 Elastic properties of pure (dense) baghdadite

The aforementioned stiffness-porosity relation can be very well predicted by the micromechanics model of Eqs. (5.7) – (5.10): The optimization procedure (5.11) resulted in a fit characterized by a relative error of -4.12 % and a coefficient of determination of 0.98, see Figure 5.1. The corresponding elastic properties of pure (dense) baghdadite amounted to $E_s^{US} = 126$ GPa and $\nu_s^{US} = 0.29$. Their reliability is expressed through a comparison with the 1750 results from the nanoindentation campaign, depicted in the form of a (normalized) histogram in Figure 5.2. They are optimally represented by a superposition of five Gaussian distribution functions, relating to a relative error amounting to only $e_{\text{rel}} = 0.006$ %, and a correlation coefficient of $R^2 = 0.99$, see Table 5.7. It is clearly seen in this table that, for up to five Gaussian distributions, the relative error decreases and the coefficient of determination increases with increasing numbers of distributions, while again higher errors and lower coefficients of determination are encountered for six and more distributions. Consequently, the fit with five distributions is the best one for the nanoindentation results, as it both

Table 5.4: Weight, dimensions, mass density, and porosity of tested baghdadite samples

Sample	m [g]	h_s [cm]	d_s [cm]	V [cm ³]	ρ [g · cm ⁻³]	ϕ [%]
A1	0.108	1.27	0.656	0.431	0.251	93
A2	0.077	1.24	0.598	0.347	0.222	94
A3	0.127	1.20	0.625	0.369	0.344	90
A4	0.108	1.26	0.611	0.370	0.292	92
A5	0.111	1.29	0.627	0.399	0.278	92
A6	0.103	1.17	0.670	0.411	0.251	93
A7	0.132	1.27	0.616	0.379	0.348	90
A8	0.076	1.19	0.607	0.344	0.221	94
B1	0.142	1.30	0.603	0.372	0.382	89
B2	0.154	1.27	0.652	0.425	0.363	90
B3	0.151	1.26	0.638	0.404	0.374	89
B4	0.142	1.34	0.620	0.407	0.349	90
B5	0.195	1.36	0.617	0.409	0.477	86
B6	0.134	1.20	0.630	0.374	0.358	90
B7	0.146	1.27	0.630	0.396	0.368	89
B8	0.211	1.34	0.628	0.416	0.507	85
B9	0.133	1.24	0.637	0.397	0.335	90
B10	0.197	1.34	0.649	0.446	0.441	87
B11	0.126	1.21	0.633	0.381	0.330	91
C1	0.24	1.26	0.628	0.393	0.611	82
C2	0.244	1.32	0.608	0.385	0.634	82
C3	0.274	1.21	0.656	0.409	0.669	81
C4	0.236	1.31	0.642	0.427	0.553	84
C5	0.274	1.26	0.681	0.461	0.595	83
C6	0.282	1.28	0.618	0.386	0.731	79
C7	0.215	1.16	0.618	0.349	0.616	82
C8	0.267	1.30	0.664	0.450	0.593	83
C9	0.219	1.29	0.637	0.414	0.529	85
C10	0.221	1.28	0.645	0.418	0.528	85
D1	0.520	1.34	0.657	0.457	1.138	67
D2	0.484	1.25	0.656	0.423	1.144	67
D3	0.456	1.24	0.641	0.402	1.134	67
D4	0.508	1.33	0.662	0.458	1.110	68
D5	0.453	1.24	0.649	0.412	1.100	68
D6	0.430	1.17	0.675	0.420	1.024	71
D7	0.419	1.20	0.675	0.432	0.969	72
D8	0.504	1.23	0.659	0.422	1.195	66

Table 5.5: Results of ultrasonic tests on baghdadite samples: time of flight t_f , height h_s , wave velocity v , wavelength λ , mass density ρ , and normal stiffness component C_{1111}^{exp}

Sample	t_f [s] Measured	h_s [cm]	v [km/s] Eq. (5.3)	λ [cm] Eq. (5.5)	ρ [g · cm ⁻³] Eq. (5.1)	C_{1111}^{exp} [GPa] Eq. (5.4)
A1	5.89×10^{-6}	1.27	2.16	2.16	0.251	1.17
A2	8.84×10^{-6}	1.23	1.40	1.40	0.222	0.43
A3	6.95×10^{-6}	1.20	1.73	1.73	0.344	1.03
A4	6.72×10^{-6}	1.26	1.88	1.88	0.292	1.03
A5	6.36×10^{-6}	1.29	2.03	2.03	0.278	1.15
A6	6.36×10^{-6}	1.16	1.83	1.83	0.251	0.84
A7	5.92×10^{-6}	1.27	2.15	2.15	0.348	1.61
A8	7.45×10^{-6}	1.19	1.60	1.60	0.221	0.56
B1	6.46×10^{-6}	1.30	2.01	2.01	0.382	1.55
B2	5.61×10^{-6}	1.27	2.26	2.26	0.363	1.86
B3	5.77×10^{-6}	1.26	2.19	2.19	0.374	1.79
B4	5.35×10^{-6}	1.34	2.52	2.52	0.349	2.21
B5	5.60×10^{-6}	1.36	2.44	2.44	0.477	2.84
B6	5.74×10^{-6}	1.20	2.09	2.09	0.358	1.56
B7	5.51×10^{-6}	1.27	2.30	2.30	0.368	1.96
B8	5.85×10^{-6}	1.34	2.30	2.30	0.507	2.67
B9	5.45×10^{-6}	1.24	2.29	2.29	0.335	1.75
B10	5.54×10^{-6}	1.34	2.43	2.43	0.441	2.62
B11	6.58×10^{-6}	1.21	1.84	1.84	0.330	1.12
C1	4.74×10^{-6}	1.26	2.67	2.67	0.611	4.36
C2	4.83×10^{-6}	1.32	2.74	2.74	0.634	4.76
C3	4.03×10^{-6}	1.21	3.00	3.00	0.669	6.02
C4	5.63×10^{-6}	1.31	2.34	2.34	0.553	3.03
C5	4.95×10^{-6}	1.26	2.55	2.55	0.595	3.87
C6	4.87×10^{-6}	1.28	2.64	2.64	0.731	5.09
C7	5.12×10^{-6}	1.16	2.27	2.27	0.616	3.18
C8	5.59×10^{-6}	1.30	2.32	2.32	0.593	3.20
C9	5.62×10^{-6}	1.29	2.31	2.31	0.529	2.82
C10	5.05×10^{-6}	1.28	2.53	2.53	0.528	3.39
D1	3.69×10^{-6}	1.34	3.65	3.65	1.138	15.13
D2	3.28×10^{-6}	1.25	3.81	3.81	1.144	16.57
D3	3.36×10^{-6}	1.24	3.70	3.70	1.134	15.53
D4	3.54×10^{-6}	1.33	3.76	3.76	1.110	15.65
D5	3.26×10^{-6}	1.24	3.82	3.82	1.100	16.04
D6	3.66×10^{-6}	1.17	3.20	3.20	1.024	10.48
D7	3.11×10^{-6}	1.20	3.88	3.88	0.969	14.61
D8	3.25×10^{-6}	1.23	3.80	3.80	1.195	17.27

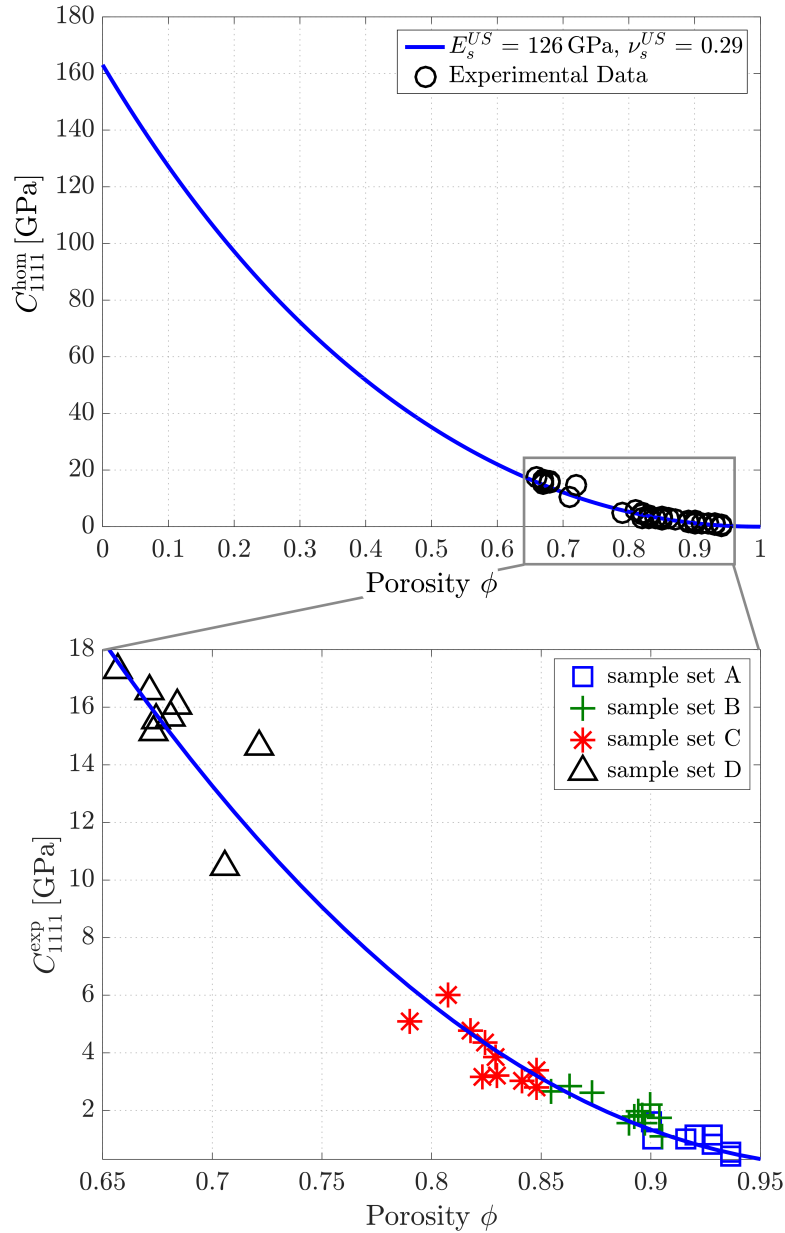


Figure 5.1: Porosity-stiffness relation for porous baghdadite scaffolds, from optimizing micromechanics model response (Fritsch et al., 2013) for length measuring, weighing, and ultrasonic test results of Table 5.4 and 5.5 (experimental values are discriminated per sample set in the lower inset); this optimization provides elastic properties of pure (dense) baghdadite, and the stiffness increases with decreasing porosity

Table 5.6: Porosity and stiffness per sample set: mean values and standard deviations

Sample set	ϕ [%]	C_{1111}^{exp} [GPa]
A	92 ± 1	0.98 ± 0.34
B	89 ± 2	1.99 ± 0.51
C	83 ± 2	3.97 ± 1.00
D	68 ± 2	15.16 ± 1.93

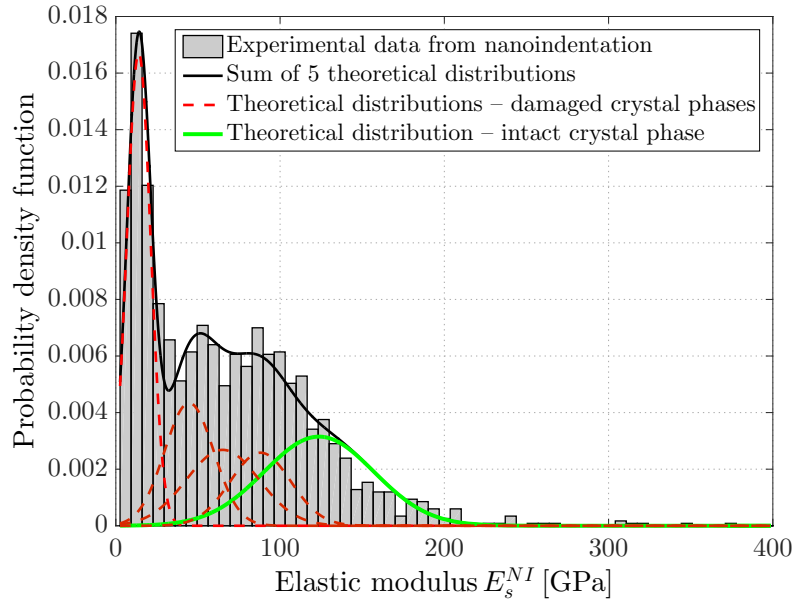


Figure 5.2: Histogram of elastic moduli obtained from nanoindentation measurements and representation through contribution of five material phases, the stiffest of which is pure (non-damaged) baghdadite

minimizes the relative error and maximizes the coefficient of determination. Accordingly, the corresponding black solid line in Figure 5.2 very accurately follows the trend given by the histogram columns, and an even more impressive, almost perfect match between experimental and theoretical CDFs is observed in Figure 5.3. The right most Gaussian distribution relates to the non-damaged baghdadite, i.e., to the state of the solid scaffold material also expected in ultrasonically tested scaffolds. Indeed, its mean value of $E_s^{NI} = 124$ GPa agrees almost perfectly with $E_s^{US} = 126$ GPa obtained from the micromechanical evaluation of the ultrasonic tests. An example of a typical load-displacement curve corresponding to a nanoindented non-damaged baghdadite crystal is depicted in Figure 5.4.

Table 5.7: Superposition results of N_{Gau} Gaussian distributions fitted to the experimental CDF which was obtained from 1750 nanoindentation measurements of baghdadite substrate; values of Young's modulus E_s^{NI} , weighting factor f_j , and the goodness of fit measurements refer to the rightmost distribution

Number of distributions	E_s^{NI} [GPa]	f_j [%]	R^2	e_{rel} [%]
2	124.2	37.52	0.8821	-27.810
3	127.4	26.99	0.9547	8.780
4	122.5	27.97	0.9917	2.130
5	123.7	26.38	0.9993	0.006
6	127.2	32.76	0.9941	-1.530
7	126.6	24.67	0.9531	-3.724
8	125.6	23.65	0.9682	-1.634
9	125.9	21.85	0.9854	-1.373
10	126.0	20.15	0.9569	-2.921

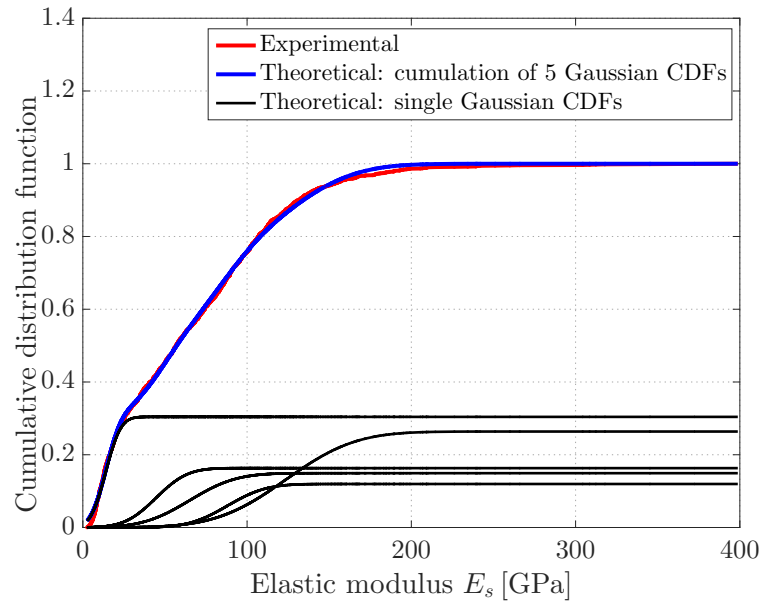


Figure 5.3: Experimental CDF obtained by nanoindentation, and the five theoretical Gaussian CDFs obtained by deconvolution according to the statistical nanoindentation method of Constantinides et al. (2006) and Constantinides and Ulm (2007)

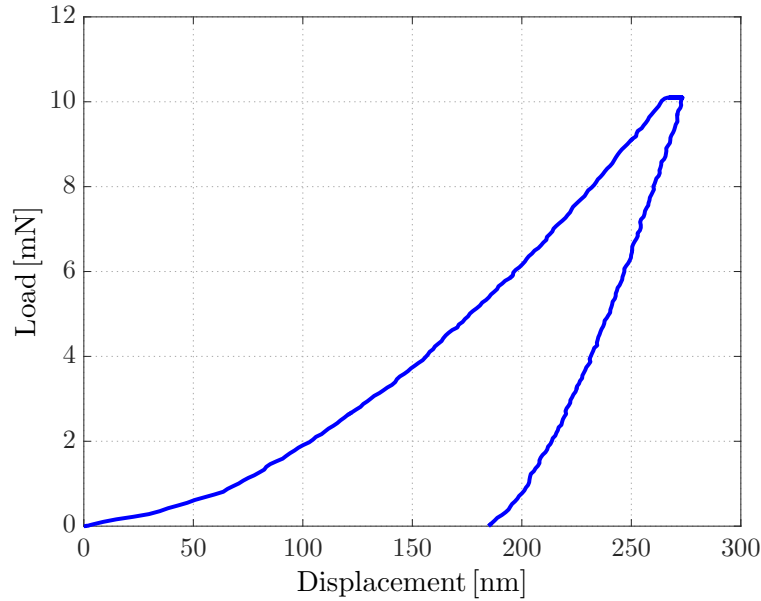


Figure 5.4: Typical load-displacement curve of a non-damaged single crystal of the baghdadite scaffolds, with an obtained elastic modulus of $E_s^{NI} = 124.7$ GPa at 10 mN maximal load

5.4 Discussion

While the current state-of-the-art in mechanical characterization of biomaterials is defined by the measurement of a few selected mechanical properties in mostly standardized mechanical testing devices, we here go a step forward, towards a unified understanding of the mechanical functioning of an entire material class – porous scaffolds for bone tissue engineering made of baghdadite – which itself turned out to be part of yet a larger material class encompassing numerous different porous (glass-) ceramic systems. In more detail, continuum micromechanics was used as a versatile theoretical and computational framework, allowing for deriving structure-property relations in the form of elasticity functions with the porosity as an argument, these functions being experimentally validated by various physically and statistically independent experiments, namely weighing, ultrasound, and nanoindentation tests. It is not the first time that such tests have been performed on biomaterials (although mechanical testing of baghdadite appears quite rarely in literature), but the consistent emergence of just one overall picture of scaffold behavior arising from all the different tests is indeed considered as something original and remarkable (the only direct relation which can be made between our newly determined Young’s modulus value of pure baghdadite, $E_s^{NI} = 124$ GPa, and data reported in the literature con-

cerns very recent bending tests on low porosity baghdadite scaffolds (Schuhmacher et al., 2014), revealing modulus values between 82 and 120 GPa).

The aforementioned consistency of our new results critically depends on careful evaluation of experimental data, taking into account important theoretical concepts underlying the used experimental devices. In this context, the following features of our evaluation method are particularly noteworthy:

- While the sample dimensions qualify them as fairly “thick” beams, and classical mechanical tests when driven in unloading mode (Luczynski et al., 2013) would certainly deliver Young’s modulus E of the tested material, it is important to remember that ultrasonic tests in most of the cases deliver the normal stiffness component C_{1111} , rather than Young’s modulus. Actually, the tested beams need to be extremely slender to allow for an extensional wave to propagate along a beam-type sample, and systematic studies (Kohlhauser and Hellmich, 2013) have shown that as long as

$$A \log \left(\frac{d_s}{h_s} \right) + B \log \left(\frac{h_s}{\lambda} \right) \leq 1, \quad (5.20)$$

with $A = -1.426$ and $B = -0.530$, bulk wave propagation related to a 3D solid with normal stiffness C_{1111} occurs. For all the tests reported in the present paper, the left-hand side of Eq. (5.20) ranged from 0.45 to 0.67, therefore all the samples behaved as 3D solids.

- Given the fact that ultrasonic tests deliver C_{1111} rather than E , they cannot be simply compared to some more or less empirical relation concerning Young’s modulus, but they need to be related to a more complete description of the material behavior. In the present case, this description was provided by continuum micromechanics, which delivered the full elasticity tensor. In the case of isotropic materials, as encountered here, the elasticity tensor can be expressed in terms of Young’s modulus and Poisson’s ratio, the latter two defining, therefore, also the stiffness component C_{1111} .
- Another critical issue with ultrasonic tests is the choice of a suitable frequency – once the corresponding wavelength does not fulfill the separation-of-scales criteria (5.6) anymore (a case not encountered here), the velocity of the ultrasonic wave is not related to the components of the elasticity tensor, i.e., ultrasound cannot be used for elasticity characterization of biomaterials anymore.
- The probably most remarkable feature of the present evaluation as compared to earlier scientific endeavors is the use and application-specific adaptation of the statistical nanoindentation method. Rather than averaging over the results

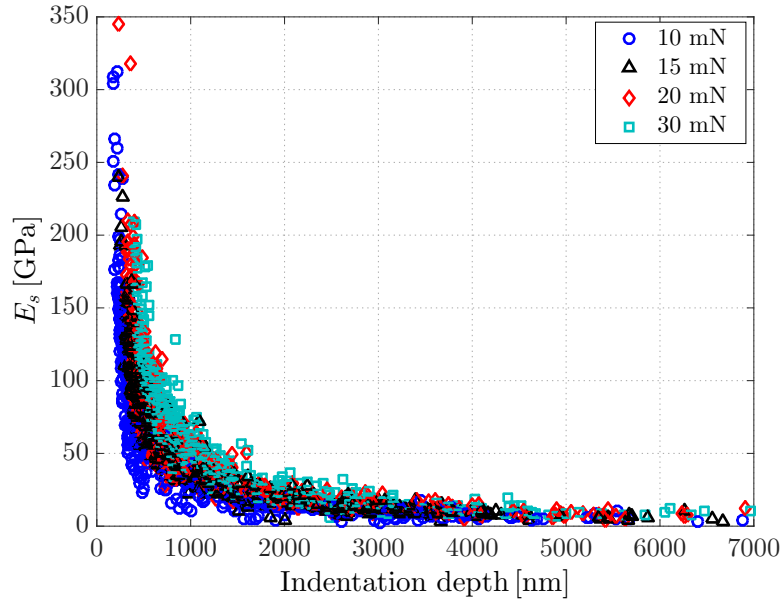


Figure 5.5: Nanoindentation size effect in baghdadite scaffolds: Young's modulus E_s as a function of indentation depth; experimental results are discriminated for the four investigated load levels

of a few tests, or checking nanoindentation size effect laws (Nix and Gao, 1998) – see Figure 5.5 for a corresponding evaluation of our nanoindentation results – which could not have provided access to the elasticity of pure (intact) baghdadite, we identified the indented substrate as being composed of one intact crystal phase and several mechanically damaged phases. This provided elastic properties which were absolutely in line with those obtained from the micromechanics-based ultrasound evaluation.

Our use of micromechanics, ultrasound, and nanoindentation relates to several aspects and issues discussed in the open literature in recent years, and the following paragraphs highlight the most important of these issues.

5.4.1 Simple, but sufficient microelastic representation of porous baghdadite

It is noteworthy that the aforementioned successful elastic property identification rested on a relatively simple micromechanics model, which was approximated through Eq. (5.7), introducing just one porosity, encompassing all spaces in the material volume, except those of the dense baghdadite crystals with a mass density of $3.48 \text{ g} \cdot \text{cm}^{-3}$. However, when more closely observing scanning electron images of the tested samples, see Figure 5.6(a), it becomes directly obvious that the material actually ex-

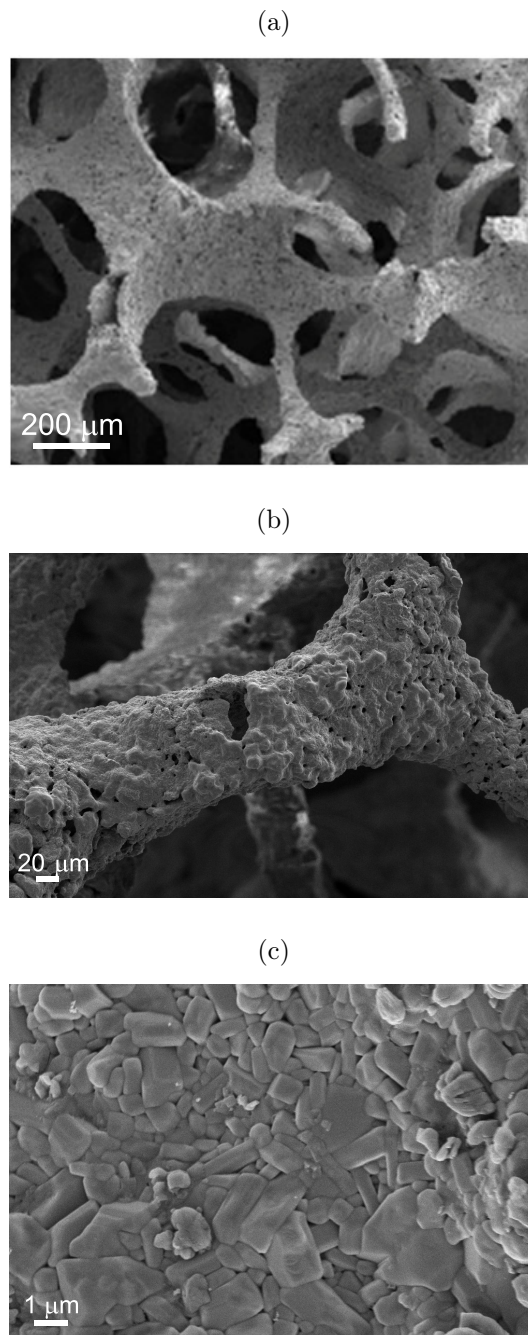


Figure 5.6: (a) SEM image showing the macropores (black) of the baghdadite scaffolds, with beam- and shell-type structural elements in between (reproduced from (Roohani-Esfahani et al., 2012)); (b) SEM image showing one structural element surrounded by macroporous space; on the surface of the structural element, micropores are seen in black; (c) High resolution SEM image of the baghdadite crystals

hibits two porosity types, one with a characteristic size of 500 μm (see Figure 5.6(a)), and another one with just a few microns characteristic size (see Figure 5.6(b)). The larger pores are fully interconnected, with solid structures in between. The latter exhibit beam- and shell-type morphologies. Zooming into the aforementioned structural elements reveals intriguing microstructures, where more disc-type, platy crystals are interconnected, so as to form a porous polycrystal (see Figure 5.6(c)). The micromechanical model approximated by Eq. (5.7) integrates both porosities into one “total porosity”, being related to the sum of both pore spaces divided by the total volume of the overall several millimeter-sized RVE of the investigated bio-material. From a theoretical viewpoint, this is clearly admissible, since both pore spaces exhibit lineal dimensions which are much smaller than the RVE size, and similar mechanical properties (namely, a vanishing stiffness), so that they can be seen as just one material phase. The same holds for the solid crystals in the micrometer range: they all show comparable shapes (disc-type) and elastic properties (that of pure baghdadite), and therefore qualify as material phase in the framework of continuum micromechanics.

The question on whether this quite simple micromechanical representation of the investigated (double-porous) material system is actually admissible can only be answered through an experimental campaign: The results presented in this paper constitute indeed an impressive affirmative answer to this question. This is perhaps surprising at the first glance, but not so much at the second one, since porous baghdadite, after the present investigation, falls into a vast class of porous polycrystals given in (Fritsch et al., 2013), which were all very well characterizable through Eq. (5.7). In this context, it is noteworthy that the used micromechanics model, falling into the class of “self-consistent” models, can well represent stiffnesses of materials over the entire porosity range from 0 to 100 %. This is due to the consideration of non-spherical phases, with aspect ratios going to the limit cases of “zero” or “infinity”, respectively (Fritsch et al., 2006; Pichler et al., 2009), and this needs to be distinguished from the situation encountered with the very first self-consistent models, which were based exclusively on spherical phases (Hershey, 1954; Fritsch et al., 2006): These original models predict vanishing stiffness for a porosity larger than 50 %.

5.4.2 Separation of scales, wavelength, and ultrasonic sample size

Elastic properties are defined on so-called representative volume elements (RVEs). The latter are characterized by homogeneous boundary conditions, e.g., by boundary displacements which are related to homogeneous strains (Hashin, 1983). In order to allow for such homogeneous loading conditions of the RVE, the strain fields to

which the structure built up by the RVEs is subjected need to be characterized by a phenomenological length (Auriault et al., 2009),

$$\mathcal{L}_\epsilon = \frac{\|\epsilon\|}{\|\nabla\epsilon\|}, \quad (5.21)$$

which is considerably larger than the RVE,

$$\mathcal{L}_\epsilon \gg l_{\text{RVE}}. \quad (5.22)$$

In Eq. (5.21), $\|\cdot\|$ refers to the norm of the tensorial object (\cdot), and the nabla-operator ∇ denotes derivatives with respect to space (spatial gradients). In addition, the RVE needs to be much larger than the characteristic inhomogeneity size d within the RVE, see Eq. (5.6). Targeting, in the latter context, at a few percent (around 3%) elastic homogenization error requires the RVE to be just three times larger than the inhomogeneity size (Drugan and Willis, 1996) - i.e., $l_{\text{RVE}} \sim 1.5 \text{ mm}$ in our case. On the other hand, ultrasonic characterization with a similar precision typically requires the wavelength to be at least five times larger than the RVE-size (Kohlhauser et al., 2009; Scheiner et al., 2009), implying, in our case, wavelengths of at least 7.5 mm, a requirement clearly overfulfilled in all the ultrasonic tests performed herein. Accordingly, also the difference between the two independently determined Young's moduli for pure baghdadite is only slightly more than 1%. Moreover, except for the "loading or phenomenological length scale" $\lambda = \mathcal{L}_\epsilon$, no other quantity of a similar length scale enters the analysis described in the present paper. However, if one used the material properties derived here, so as to design larger constructs of porous baghdadite for large bone defect regeneration, then a structural length scale of corresponding implants $\mathcal{L}_s \gg l_{\text{RVE}}$ would need to come into play, as well.

5.4.3 Nanoindentation: size effects, damage, and creep

It is instructive to relate the size effect shown in Figure 5.5 to the microstructure appearing at the scale of corresponding indented areas, see Figure 5.7. The three triangles indicated there refer to the maximum, the mean and the minimum projected indentation area A , a quantity which, for a perfect Berkovich indenter (Oliver and Pharr, 1992), is related to the indentation depth h_c by

$$A(h_c) = 24.5h_c^2. \quad (5.23)$$

Also, this illustration confirms our result, given in Table 5.7 and Figure 5.2, that only the smallest indentation sizes are related to the properties of the single crystals, while all others characterize crystal clusters with micropores and probably indentation-induced cracks in between. Accordingly, our "damaged phases" are, in fact, microporous materials (with rather small microporosity), characterized by different degrees

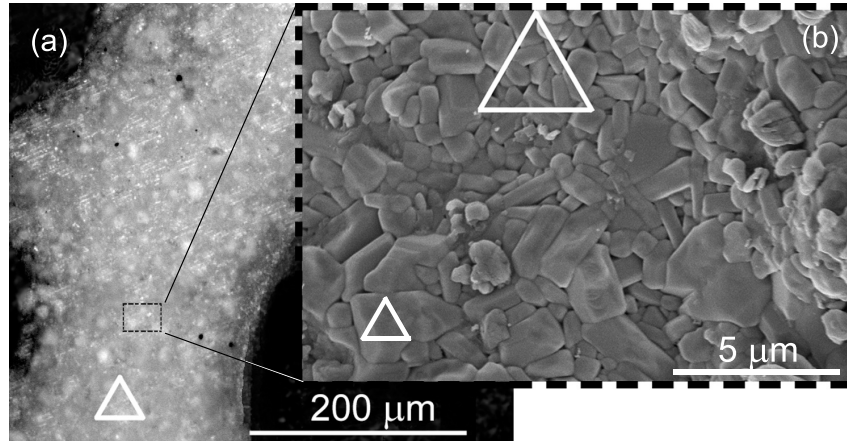


Figure 5.7: (a) Light micrograph of polished sample surface, as prepared for nanoindentation (resin-filled macropores appear black), and (b) zoomed-out Scanning Electron Micrograph of crystalline strut surface; triangles indicate in (a) maximum indentation size; and in (b) mean and minimum indentation sizes

of damage, i.e., by different (and rather substantial) microcrack densities. The latter microporosity is also probable to be (at least partially) filled by the resin used for sample preparation.

As for the indentation protocol, the holding time was introduced in order to allow for creep of the material before unloading, thus eliminating any effect of creep in the determination of Young's modulus from the unloading curve. The characteristic time of creep τ_{creep} was obtained from an exponential fitting of the relationship between the creep displacement rate occurred during the holding time, \dot{u}_{creep} , and the time t :

$$\dot{u}_{\text{creep}} = u_0 \exp\left(-\frac{t}{\tau_{\text{creep}}}\right), \quad (5.24)$$

where u_0 is a constant. For the nanoindentation results referring to the pure (undamaged) baghdadite phase, the characteristic creep time amounted to $\tau_{\text{creep}} = 2.3$ s; since 2.3 s is much less than the holding time of 10 s, we do not expect this (rather fast) creep to bias the values obtained for Young's modulus related to elasticity only.

Another important issue with nanoindentation testing is the potential dependence of the obtained results on the chosen load level; often increased load levels are related to reduced on average measured elastic moduli (Khanna et al., 2009). Our rationale was not so much to reproduce this effect (which we mainly attribute to the increased damaging of the material when indenting it too strongly), but we rather targeted at finding a reasonable loading range, where at least part of the indentation campaign would be related to intact crystal characterization. In fact, the indentation loads between 10 mN and 30 mN allowed us to have loads which were high enough for reaching indentation depths beyond the roughness of the surface, and, at the same

time, low enough for still obtaining results relating to non-damaged crystals (Bobko and Ulm, 2008). Interestingly, the mean indentation depths showed no clear trend with respect to the chosen levels of 10, 15, 20 or 30 mN (see Table 5.8). This is consistent with the size effect relation of Figure 5.5, being also independent of the chosen load level.

Table 5.8: Mean value of indentation depth per load

Load [mN]	10	15	20	30
Depth [nm]	1152	1407	1371	1458

5.4.4 Anisotropy effects of single baghdadite crystals

Baghdadite is a monoclinic-prismatic crystal, and therefore, in principle, anisotropic. We are not aware of any direct measurements of the full elasticity tensor of baghdadite, nor of its determination from molecular or atomistic computations. However, such data are known for other members of the monoclinic-prismatic crystal class, such as wadsleyite. The latter material was experimentally characterized by means of Brillouin light scattering (Sawamoto et al., 1984) and its mechanical properties were computationally derived from a plane-wave pseudopotential method (Kiefer et al., 2001). These methods show wadsleyite to be approximately transversely isotropic with out-of-plane Young's modulus of $E_0 = 221$ GPa, and transverse Young's modulus of around $E_T \sim 330$ GPa. Hence, the moduli in different directions vary by about $\sim 30\%$, a number which could also be relevant for baghdadite. As regards nanoindentation, both the lower out-of-plane and the higher in-plane elastic moduli may be detected, or any value between these two extremes, depending on the crystal orientation with respect to the indentation direction. Therefore, to one and the same phase (differently oriented though), many different nanoindentation-derived moduli are related, and this is exactly what we consider through our statistical distribution of moduli depicted in Figure 5.2. More precisely, an increased difference between out-of-plane modulus and in-plane modulus would be reflected by a wider probability distribution function assigned to the respective formally isotropic phase. In this sense, the widths of all statistical distribution functions related to our differently strongly damaged phases, depicted in Figure 5.2, may partially reflect the actually anisotropic nature of the tested crystals. These distribution functions also exhibit expected values, and the expected value of the undamaged phase is Young's modulus E_s which we have been referring to throughout the present contribution. In particular, we have introduced an isotropic crystal phase exhibiting exactly this elastic modulus, so as to arrive at homogenized properties of the porous polycrystal by

means of Eq. (5.7). The admissibility of this approximation (namely using average isotropic rather than transversely isotropic crystal properties, so as to still arrive at relevant homogenized properties of porous polycrystals) has been shown theoretically and computationally for the case of hydroxyapatite polycrystals (Fritsch et al., 2006).

5.4.5 Perspectives

The herein introduced and validated micromechanics model of porous baghdadite allows for prediction of mechanical properties well beyond elasticity: In continuum micromechanics, an RVE may not only be subjected to stresses and strains at its outer boundary, but also to a pore pressure acting within the pore space. Hence, once the upscaling from the single crystal elasticity to the overall porous polycrystal is achieved, also the key poroelastic properties are known (Fritsch et al., 2013; Dormieux et al., 2006). They are: (i) the Biot coefficient quantifying the stress arising at the undeformed boundary of the RVE, from internal pore pressure (see Figure 5.8(a)), and (ii) the Biot modulus quantifying the porosity change within an RVE whose boundary is undeformed, again arising from pore pressure (see Figure 5.8(b)). Equipped with this information, the elastic deformation arising from any external or internal stress states acting, under physiological conditions, on implanted porous baghdadite scaffolds can be determined. This is considered as a firm basis for computer-aided design or safety assessment of such scaffolds. In order to complete the latter, our current research activities are directed towards strength upscaling, based on the already achieved success for biomaterials such as hydroxyapatite (Fritsch et al., 2006, 2009a, 2013), glass-ceramics (Malasoma et al., 2008), or titanium (Müllner et al., 2008).

5.5 Acknowledgements

Maria-Ioana Pastrama and Christian Hellmich were financially supported by the European Research Council (ERC), through project ERC-StG-2010 MICROBONE, #257032. The work of Hala Zreiqat and Peter Pivonka was supported by the Australian Research Council (ARC) for linkage project funding (LP0991099).

5.6 Appendix: Evolutionary algorithm

The evolutionary strategy (Jaindl et al., 2009) considers starting parameters for Gaussian distributions, namely, mean value μ_0^g , variance s_0^g , and weighting factor

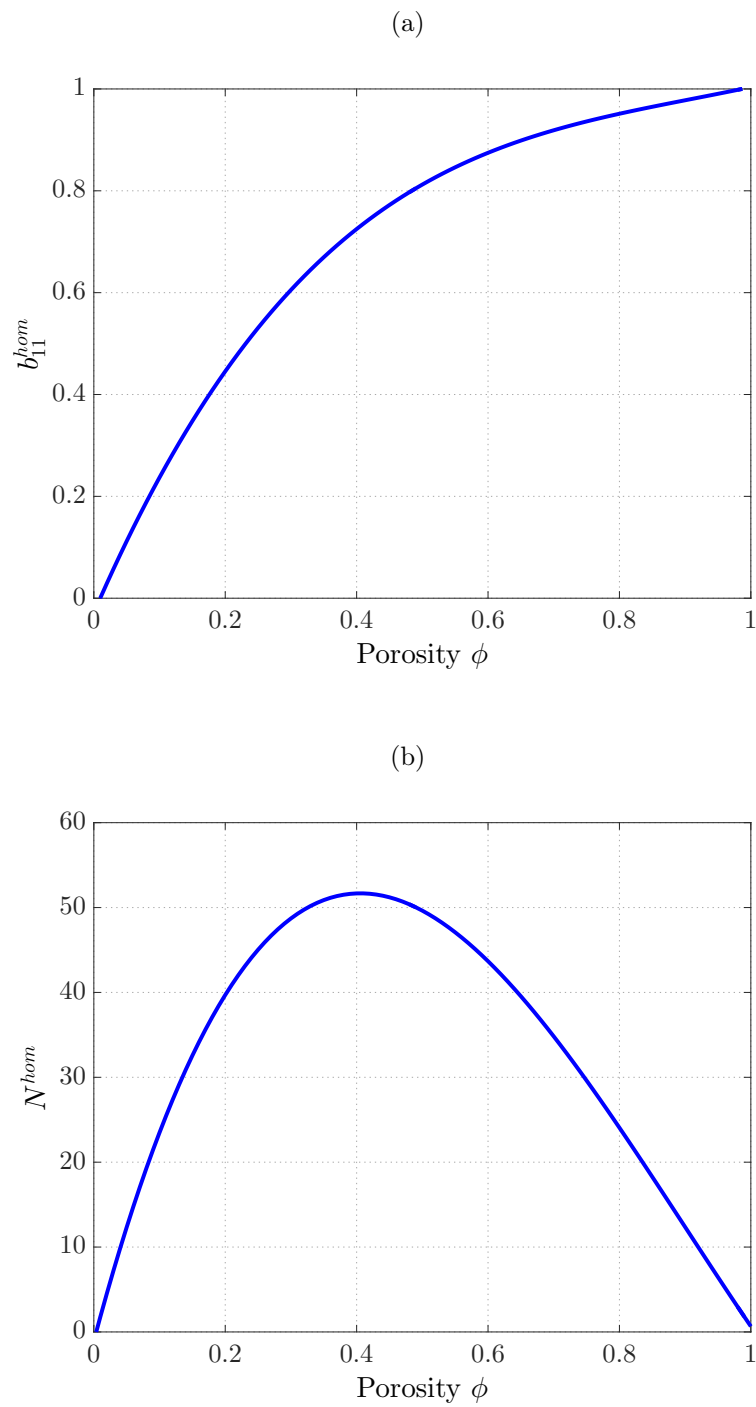


Figure 5.8: Poroelasticity of porous baghdadite scaffolds: (a) Biot coefficient as a function of porosity; (b) Biot modulus as a function of porosity

f_0^g , as “parents” X_p^g ,

$$X_p^g = \{\mu_0^g, s_0^g, f_0^g\}, \quad (5.25)$$

whereby the superscript g stands for the generation number, starting with $g = 1$. The strategy involves three subsequent steps:

I. Mutation

In the first step, each of these three parent values is mutated by adding a normally distributed random number,

$$X_m^g = X_p^g + Z^g \sigma, \quad (5.26)$$

where Z^g is generated from a normal distribution $\nu(0, \sigma)$, with mean 0 and standard deviation equal to the scattering parameter α , the size of which is discussed further below. This results in a new, mutated parent, with its mutated parameters:

$$X_m^g = \{\mu_m^g, s_m^g, f_m^g\}. \quad (5.27)$$

II. Recombination

In the next step, through recombination of the starting and the mutated parameters, one obtains a series of possible combinations of parameters $\{\mu_i^g, s_j^g, f_k^g\}$. As the mean value and standard deviation should stem from the same group, $i = j$, only four combinations remain possible, out of which three are the newly generated “offsprings”,

$$\begin{aligned} X_{O_1}^g &= \{\mu_0^g, s_0^g, f_m^g\}, \\ X_{O_2}^g &= \{\mu_m^g, s_m^g, f_0^g\}, \\ X_{O_3}^g &= \{\mu_m^g, s_m^g, f_m^g\}. \end{aligned} \quad (5.28)$$

III. Selection

In the final step, the CDF of the parent, CDF_P , and those of the offsprings, CDF_{O_l} , with $l = 1, 2, 3$ are generated. The set of parameters that fits the data best is the one whose CDFs minimize the error given in Eq. (5.18). This set (either the old parent or one of the offsprings) is then selected to become the parent of the new generation X_P^{g+1} :

$$X_P^{g+1} = \{\mu_P^{g+1}, s_P^{g+1}, f_P^{g+1}\}, \quad (5.29)$$

$$X_P^{g+1} = \begin{cases} X_{O_l}^g & \text{if } Error(X_{O_l}^g) < Error(X_P^g) \text{ with } l = 1, 2, 3 \\ X_P^g & \text{otherwise.} \end{cases} \quad (5.30)$$

Chapter 6

Ultrasonic elasticity determination of 45S5 Bioglass[®]-based scaffolds: Influence of polymer coating and crosslinking treatment

Authored by Wei Li, Maria-Ioana Pastrama, Yaping Ding, Kai Zheng, Christian Hellmich, and Aldo R. Boccaccini

Published in *Journal of the Mechanical Behavior of Biomedical Materials*, 40: 85–94, 2014

Highly porous 45S5 Bioglass[®]-based scaffolds with interconnected pore structure are promising candidates for bone tissue engineering due to their bioactivity, biocompatibility, osteogenic and angiogenic effects. In the present study, to ensure the mechanical competence of the 45S5 Bioglass[®]-based scaffolds, their stiffness was adjusted by applying polymer coatings and further crosslinking treatment. A non-destructive ultrasonic technique was used to determine the stiffness of the scaffolds. The stiffness of uncoated scaffolds was shown to increase by applying polymer coatings, and a further increase was achieved by crosslinking the used polymer coatings. All uncoated and polymer coated scaffolds were confirmed to exhibit stiffness values in the range of reported values in the literature for cancellous bone. A statistical evaluation of combined multiscale ultrasound-nanoindentation measurements indicated that the stiffness of the coated scaffold is directly dependent on the stiffness of the

polymer coating.

Collaboration

This paper results from a collaboration between the Institute for Mechanics of Materials and Structures of TU Wien and the Institute of Biomaterials, Department of Materials Science and Engineering at the University of Erlangen-Nuremberg, Germany. The purpose of Wei Li's research stay in Vienna, funded by Knowledge-based Multifunctional Materials AISBL (KMM-VIN), was to mechanically test the Bioglass[®] scaffolds and coatings he produced at the University of Erlangen-Nuremberg together with colleagues from the same institution. Maria-Ioana Pastrama supervised the ultrasonic testing, performed the nanoindentation of the Bioglass[®] and polymer coatings, as well as the statistical analysis of the results; these activities defined her as the second author of the paper. Christian Hellmich and Aldo R. Boccaccini directed the overall research strategy and the writing of the manuscript, as well as provided final corrections and approval for submission.

6.1 Introduction

In order to restore function of damaged bone tissue or to regenerate bone tissue, one important approach of bone tissue engineering involves the use of highly porous biodegradable scaffolds that are made of engineered materials (Rezwan et al., 2006). The relevant criteria for ideal scaffolds have been frequently discussed in the literature, and involve rather stringent requirements in terms of pore structure, mechanical properties and biological activity (Amini et al., 2012; Bose et al., 2012; Rezwan et al., 2006).

45S5 Bioglass[®] is promising for bone tissue engineering applications due to its excellent bioactivity, biocompatibility, osteogenic and angiogenic effects (Hench, 2006; Jones, 2013). Porous 45S5 Bioglass[®]-based scaffolds with interconnected pore structure have been successfully fabricated by the foam replication method since 2006 (Chen et al., 2006). These scaffolds are sufficiently robust for manual handling in cell biology studies (Chen et al., 2006; Yao et al., 2014), however higher values of mechanical properties (such as strength, toughness and stiffness) are still desired for warranting their wide applicability in bone tissue engineering (Amini et al., 2012; Bose et al., 2012; Rezwan et al., 2006). In order to improve the mechanical properties of 45S5 Bioglass[®]-based scaffolds, approaches based on polymer coatings are being applied, which have been shown to provide significant strengthening and toughening effects by the activation of a micron scale crack-bridging mechanism (Chen and Boccaccini, 2006; Peroglio et al., 2007; Yunos et al., 2008; Li et al., 2014a,b; Yao et al.,

2014). In this context, there is increasing interest in using natural polymers (such as gelatin with and without crosslinking, alginate and chitosan) to coat glass-ceramic based scaffolds (Bellucci et al., 2012; Erol et al., 2012a,b; Lozano et al., 2014; Yao et al., 2014), in this way producing composite scaffolds with superior properties. For example, natural polymer coatings have been shown to improve the compressive strength of inorganic scaffolds (Bellucci et al., 2012; Erol et al., 2012a,b; Lozano et al., 2014; Yao et al., 2014) and to be suitable as *in situ* carriers of therapeutic bioactive molecules such as antibiotics and growth factors (Lozano et al., 2014; Yao et al., 2014). Such natural polymer coated glass-ceramic scaffolds usually exhibit improved *in vitro* and *in vivo* biocompatibility (Lozano et al., 2014; Yao et al., 2014), which further indicates that they are promising for bone tissue engineering.

Besides strength and toughness, the stiffness of implants (here scaffolds) also plays an important role in their successful application, because stiffness predominantly determines the stress distribution in bone-implant systems (Huiskes et al., 1992; Ramaniraka et al., 2000; Rezwan et al., 2006; Ryan et al., 2006). Stiffness mismatch between biomaterials and the surrounding bone has been identified as a major reason for implant failure (Ryan et al., 2006). In addition, the stiffness of biomaterials could affect cell morphology, cytoskeletal structure and adhesion (Yeung et al., 2005; Skardal et al., 2013). Therefore, reasonable design, as well as accurate measurement of scaffold stiffness is critical for the development and successful application of scaffolds in the context of bone tissue engineering.

Normally, uniaxial compressive tests and three-point bending tests are used to measure the strength (e.g., compressive strength and bending strength) and toughness (e.g., work of fracture) of the scaffolds. However, it is very difficult or even impossible to determine the elastic modulus of the highly porous scaffolds from the stress-strain curves obtained in a mechanical test, because their highly porous and open pore structure lead to a zigzag type rather than monotonic type stress-strain curve (Chen et al., 2006; Li et al., 2014a,b; Yao et al., 2014). In other words, a “linear portion” or “linear region” needed for calculating the elastic modulus does not exist in the aforementioned stress-strain curves. Moreover, the determination of elastic properties of porous materials may be strongly biased by inelastic deformations occurring in the samples, especially in the vicinity of the load transfer device such as the loading platen (Kohlhauser et al., 2009; Luczynski et al., 2013). These problems can be avoided by applying ultrasonic measurement techniques, as they apply only very small stresses to the material, which avoid inelastic phenomena such as plasticity even in very small sized struts of the tested samples (Thelen et al., 2004). In previous studies, the elastic properties (stiffness) of porous 45S5 Bioglass[®]-based scaffolds have been successfully characterized by ultrasonic measurements (Kohl-

hauser et al., 2009; Hum et al., 2013). The latter indicated that the stiffness of these scaffolds could be increased through polycaprolactone and collagen coatings (Hum et al., 2013).

The elasticity of such a composite systems, here polymer coated scaffolds, is related to the elasticity of the components (material phases) (Zaoui, 2002). As shown in the literature (Bigi et al., 2002; Lee et al., 2006; Giofrè et al., 2012), the elastic modulus of natural polymers such as gelatin and alginate, which was extracted from stress-strain curves, could be adjusted by chemical crosslinking. Hence, for the natural polymer coated 45S5 Bioglass[®]-based composite scaffolds, it is anticipated that their elasticity can be conveniently tailored by further modifying the properties of the used polymer coatings (e.g., through chemical crosslinking). It should be noted that, although investigating the degradation behavior and bioactivity of the scaffolds is beyond the scope of this study, they should also be considered in designing the composition of this type of bone scaffolds. If the natural polymers are highly (or almost completely) crosslinked, they will degrade/dissolve more slowly, which delays the contact between the bioactive glass struts and the (simulated) body fluid. As a consequence, the bioactivity of the scaffolds may be significantly retarded. Thus, natural polymers used as coatings will need to be only partially crosslinked in order to balance the requirement for sound mechanical properties and sufficient bioactivity.

In the present study, 45S5 Bioglass[®]-based scaffolds were coated with synthetic (PHBV) and natural (gelatin and alginate) polymers. Furthermore, the natural polymer coatings (i.e., gelatin and alginate) were chemically crosslinked. The ultrasonic measurement technique was used to characterize the elasticity of these polymer-coated scaffolds with and without crosslinking. We anticipate that the non-destructive ultrasonic measurement could be an effective, reliable and convenient technique to determine the influence of polymer coatings and their property evolution on the overall elasticity of polymer-coated composite scaffolds. Moreover, as an attempt to establish a mathematical relationship between the stiffness of composite scaffolds and their constituents, a combined multiscale ultrasound-nanoindentation investigation was carried out.

To the best of our knowledge, the elastic properties of crosslinked polymer-coated scaffolds have never been characterized by the ultrasonic measurement technique, which was also only rarely performed on crosslinked gelatin- or alginate-related materials (Salsac et al., 2009).

6.2 Materials and methods

6.2.1 Materials

Commercially available melt-derived 45S5 Bioglass[®] powder with a particle size of $\sim 5 \mu\text{m}$ was used for fabricating scaffolds. Polyurethane (PU) foam (45 pores per inch) was supplied by Eurofoam (Troisdorf, Germany). Polyvinyl alcohol (PVA, completely hydrolyzed, MW $\sim 30,000$) was obtained from Merck (Darmstadt, Germany). The polymers used for coating the scaffolds were PHBV, gelatin and alginate. PHBV (PHV content 12 wt %) was purchased from Goodfellow (Huntingdon, UK). Gelatin (Type A from porcine skin) and alginate (sodium alginate) were obtained from Sigma-Aldrich (St. Louis, MO, USA). Crosslinking agents, i.e., genipin and calcium chloride dihydrate, were purchased from Wako (Osaka, Japan) and Sigma-Aldrich (St. Louis, MO, USA), respectively.

6.2.2 Fabrication of Bioglass[®]-based scaffolds

The scaffolds were fabricated by the foam replication method (Chen et al., 2006). Briefly, the slurry was prepared by dissolving 6% w/v PVA in deionized water at 80°C , and then 45S5 Bioglass[®] powder was added to the PVA solution up to a concentration of 50 wt %. Cylindrical PU foams with an approximate diameter of 12 mm and height of 12 mm were immersed in the slurry and rotated to ensure homogeneous slurry infiltration. Each procedure was carried out under vigorous stirring using a magnetic stirrer. The scaffolds were then extracted from the slurry, and the extra slurry was completely squeezed out. The samples were dried at room temperature for 24 h and then the procedure described above was repeated again. The samples were then heated at 400°C for 1 h in air atmosphere to decompose the PU foam, and at 1100°C for 2 h to densify the struts. The heating and cooling rates used were $2^\circ\text{C}/\text{min}$ and $5^\circ\text{C}/\text{min}$, respectively.

6.2.3 Polymer coating procedure

The Bioglass[®]-based scaffolds were coated with different polymers by the dip coating method. In order to obtain a comparable amount of polymer coating during the dip coating process in the present study, the same polymer concentration was used for PHBV and gelatin. However, the concentration of alginate solution was reduced, because the viscosity of this solution significantly increased as its concentration increased, which was undesirable as the polymer could have blocked the pores of the scaffolds. The amount of alginate coating was approximately increased to that of PHBV and gelatin coating by repeating the dip coating process. The coating procedures for the different polymers are described in the following paragraphs.

6.2.3.1 PHBV coated Bioglass[®]-based scaffolds

PHBV solution with a concentration of 5 % w/v was prepared by dissolving PHBV in chloroform (Merck, Germany) at room temperature. The sintered Bioglass[®] scaffolds were then completely immersed in the PHBV solution for 5 min. After that, the scaffolds were taken out and dried in fume hood at room temperature for 24 h.

6.2.3.2 Gelatin coated Bioglass[®]-based scaffolds

The coating solution was prepared by dissolving gelatin in distilled water at a concentration of 5 % w/v by magnetic stirring at 50° C. The sintered scaffolds were completely immersed in the gelatin solution for 5 min, and then taken out and dried in fume hood at room temperature for 72 h.

6.2.3.3 Crosslinked gelatin coated Bioglass[®]-based scaffolds

Gelatin-genipin solution with a concentration of 5 % w/v was prepared by dissolving gelatin and genipin together in distilled water by magnetic stirring at 50° C. The pH of the obtained solution was 5.5. The weight percentage of genipin in the gelatin-genipin mixture was 1 wt %. This genipin concentration was shown to be able to partially crosslink the gelatin in agreement with previous studies (Yao et al., 2004). The Bioglass[®]-based scaffolds were then completely immersed in the gelatin solution for 5 min. After that, the scaffolds were taken out and dried in fume hood at room temperature for 72 h. The color of the final obtained scaffolds was blue, which is a qualitative indication of the genipin crosslinked gelatin coating.

6.2.3.4 Alginate coated Bioglass[®]-based scaffolds

The coating solution was prepared by dissolving sodium alginate in distilled water at a concentration of 2 % w/v by vigorous magnetic stirring at room temperature. The sintered scaffolds were completely immersed in the alginate solution for 5 min, and then taken out and dried in fume hood at room temperature for 24 h. The coating process described above was repeated, and then the samples were dried in fume hood at room temperature for 72 h.

6.2.3.5 Crosslinked alginate coated Bioglass[®]-based scaffolds

Crosslinked alginate coated scaffolds were prepared by crosslinking the alginate coating present in the alginate coated scaffolds with CaCl₂ solution. The CaCl₂ solution was prepared by dissolving calcium chloride dihydrate in distilled water at a concentration of 0.1 mol/L. The alginate coated scaffolds, which were obtained as described

in the last section, were immersed in the CaCl_2 solution for 5 min, and then taken out and dried in fume hood at room temperature for 72 h.

6.2.4 Fabrication of polymer films and Bioglass[®] disk

In order to separately measure the elastic properties of the constituents of the coated “composite” scaffolds, namely those of the different polymers and of sintered Bioglass[®], samples consisting of polymer or Bioglass[®] only were produced, as well. As regards the polymers, films were prepared by solution casting using exactly the same polymer solution and crosslinking agent used for coating the scaffolds, since it is known that the physical properties of polymers, e.g., density and elastic modulus, are very sensitive to the processing history. Accordingly, also the drying process of these films was the same as the one applied to the polymer-coated scaffolds. For determining the elastic modulus of sintered Bioglass[®], a disk was produced by uniaxial pressing of the Bioglass[®] powder in a cylindrical die, followed by sintering using the same heat treatment used for the scaffolds.

6.2.5 Characterization methods

6.2.5.1 Density of polymers and sintered Bioglass[®]

The density of polymers and sintered Bioglass[®] was measured using a pycnometer and applying Eq. (6.1):

$$\rho_{\text{material}} = \frac{(M_2 - M_1)}{(M_4 - M_1) - (M_3 - M_2)} \rho_{\text{ethanol}}, \quad (6.1)$$

where M_2 is the mass of the sample and the pycnometer, M_1 is the mass of the pycnometer, M_4 is the mass of the fully filled amount of ethanol and the pycnometer, M_3 is the mass of the sample, the specific amount of immersion ethanol and the pycnometer, and ρ_{ethanol} is the density of ethanol at room temperature. Polymer films were cut into small pieces, and sintered Bioglass[®] scaffolds were ground into powder before measurement. Potential bubbles inside the pycnometer were removed in vacuum conditions before measurement. Ethanol was chosen as the immersion liquid in the present measurement, because none of the tested materials dissolve in ethanol.

6.2.5.2 Density and porosity of scaffolds

The density of the scaffolds (ρ_{scaffold}) was determined from the mass and volume of the scaffolds before and after coating with polymer. The porosities before (p_1) and after (p_2) coating were calculated by Eqs. (6.2) and (6.3), respectively:

$$p_1 = 1 - M_1 / (\rho_{\text{Bioglass}} V_1), \quad (6.2)$$

$$p_2 = 1 - (M_1/\rho_{\text{Bioglass}} + (M_2 - M_1)/\rho_{\text{polymer}})/V_2, \quad (6.3)$$

where (M_1, V_1) and (M_2, V_2) are the (mass, volume) of the scaffolds before and after coating with polymer, respectively; ρ_{Bioglass} is the density of sintered Bioglass[®], and ρ_{polymer} is the density of the used polymer.

6.2.5.3 Surface morphology

The microstructure of the scaffolds before and after coating was observed in a LEO 435 VP scanning electron microscope (SEM) (Cambridge, UK). Samples were sputter coated with gold in vacuum and observed at an accelerating voltage of 10 kV.

6.2.5.4 Ultrasonic measurement of elastic properties of scaffolds

Elastic properties of the scaffolds were obtained by acoustic measurements, and the measurements were performed in pulse transmission mode as described in a previously published protocol (Kohlhauser et al., 2009; Hum et al., 2013; Luczynski et al., 2013). The used ultrasonic device consists of a pulser-receiver (5077PR, Olympus NDT, USA), an oscilloscope (WaveRunner 62Xi, Lecroy, USA), and several ultrasonic transducers. The pulser unit can emit an electrical square-pulse of up to 400 V. The piezoelectric elements inside the transducers transform signals from electrical to mechanical when operating in the sending mode, and from mechanical to electrical when receiving mechanical signals from the opposite side of the sample. Honey was used as a coupling medium between transducers and sample. In the present study, ultrasonic waves were restricted to longitudinal waves, which means the directions of material particle movement and wave propagation were parallel. The receiver unit of the pulser-receiver has a bandwidth of 0.1–35 MHz and a voltage gain up to 59 dB. The amplified signal is displayed on an oscilloscope with a bandwidth of 600 MHz and a sample rate of 10 GS/s (Gigasamples per second). The oscilloscope enables the determination of the time of flight (Δt) of the longitudinal ultrasonic wave through the sample. The sample height (h) is the travel distance of the longitudinal wave through the sample, hence, the signal velocity was denoted as

$$v = \frac{h}{\Delta t}. \quad (6.4)$$

The wavelength of the transmitted longitudinal wave follows Newton's relationship

$$\lambda = \frac{v}{f}, \quad (6.5)$$

in which f is the frequency of signal, here 0.1 MHz. Reported data were obtained by averaging the results of at least five measurements.

6.2.6 Measurement of elastic modulus of polymers and Bioglass[®] by nanoindentation

The elasticity of the polymer films was determined by means of nanoindentation tests with a Berkovich diamond tip (TI 900, Hysitron, Minneapolis, MN, USA). Before testing, small coupons (approximately 7 mm × 7 mm) were cut from each film and glued onto metal sample holder disks. The samples were then manually polished with diamond spray with particle size of 3 μm and, subsequently, 1.5 μm. On each sample nine indentations were performed at equal distance from each other. Following pertinent studies in the field (Klapperich et al., 2000), the loading protocol consisted of a maximum indentation load of 600 μN, reached with a constant loading rate of 30 μN/s, and holding time of 10 s. The load-displacement curves were converted into elastic moduli through the standard technique of Oliver and Pharr (1992).

Similarly, the elastic modulus of sintered Bioglass[®] was measured by nanoindentation with a CSM Nano Hardness Tester[®], using a Berkovich tip. A Bioglass[®] disk with a diameter of 13 mm was glued onto a metal sample holder. Prior to testing, the sample was polished with increasingly fine sandpaper and finished with diamond spray with a particle size of 1.5 μm. During preparation, the sample was inspected with a microscope, to ensure the existence of sufficient scratch-free surfaces. 10 indentations were performed at maximum load of 15 mN, with a constant loading rate of 30 mN/min and a holding time of 10 s.

6.2.7 Statistical analysis

All data are presented as mean ± standard deviation (SD). Multi-linear regression was done using the statistical analysis software DataLab (<http://www.lohninger.com/datalab/>).

6.3 Results

6.3.1 Density of polymers and Bioglass[®]

Experimental values of density of the used polymers and sintered Bioglass[®] are given in Table 6.1. The measured density of PHBV is very close to the density of PHBV granules (1.25 g · cm⁻³) provided by the manufacturer. The measured density of gelatin is in the range of reported values (1.25 – 1.37 g · cm⁻³) (Mwangi and Ofner, 2004; Zhou et al., 2012). The measured density of crosslinked gelatin is shown to be similar to un-crosslinked gelatin. Also, the measured density of crosslinked alginate is close to that of un-crosslinked alginate. The obtained density of alginate in the present study is in good agreement with its density calculated with one water molecule per residue (1.60 g · cm⁻³), but it is slightly higher than the value obtained for the anhydrous molecule (1.45 g · cm⁻³) (Atkins et al., 1973). The density of

Table 6.1: Density of used polymers and sintered Bioglass[®]

Sample	Density [$\text{g} \cdot \text{cm}^{-3}$]
PHBV	1.26 ± 0.01
Gelatin	1.30 ± 0.02
Crosslinked gelatin	1.28 ± 0.01
Alginate	1.58 ± 0.02
Crosslinked alginate	1.61 ± 0.02
Sintered Bioglass [®]	2.74 ± 0.02

sintered Bioglass[®] determined from crushed Bioglass[®] scaffolds is slightly higher than the theoretical density of Bioglass (2.66 $\text{g} \cdot \text{cm}^{-3}$) (Hench, 1998), but it is still lower than the value obtained from sintered Bioglass[®] powder or frit (2.91 $\text{g} \cdot \text{cm}^{-3}$) (Lefebvre et al., 2008; Srivastava et al., 2012).

6.3.2 Nanoindentation-derived elastic modulus of polymers and sintered Bioglass[®]

The elastic modulus of different polymers used for coating the scaffolds is given in Table 6.2. PHBV exhibited the lowest value of elastic or Young's modulus. Also, as can be seen from the load-displacement curves (Figure 6.1), the highest indentation depth (over 600 nm) was reached when testing PHBV compared to the other polymers. The elastic modulus of gelatin was slightly reduced after crosslinking, although the stiffness component C_{1111} obtained by ultrasonic measurement was determined to be higher for crosslinked gelatin coated scaffolds (Table 6.5). Crosslinked alginate displayed a significantly higher elastic modulus than un-crosslinked alginate. The elastic modulus of sintered Bioglass[®] in the present study was determined to be 110 ± 13 GPa, which is in the range of reported values for Bioglass[®] after heat treatment (90–110 GPa) (Chen et al., 2012; Srivastava et al., 2012). The elastic modulus of sintered (crystallized) Bioglass[®] is much higher than that of (amorphous) Bioglass[®] as occurring before heat treatment, the latter modulus amounting to 35 GPa (Hench, 1998).

6.3.3 Structure characterization

The typical microstructure of uncoated Bioglass[®]-based scaffolds is shown in Figure 6.2(a). The pore size of the uncoated scaffolds was in the range of 200–500 μm . The highly interconnected porous structure was maintained in different polymer-coated scaffolds, thanks to an optimized coating procedure (Figure 6.2(b)–(f)). Only a few pores were clogged by the polymer coatings. The polymer coatings did not

Table 6.2: Elastic modulus of different polymers used for coating scaffolds

Sample	Elastic modulus [GPa]
PHBV	1.0 ± 0.1
Gelatin	4.2 ± 0.3
Crosslinked gelatin	3.8 ± 0.8
Alginate	5.6 ± 1.0
Crosslinked alginate	8.5 ± 0.7

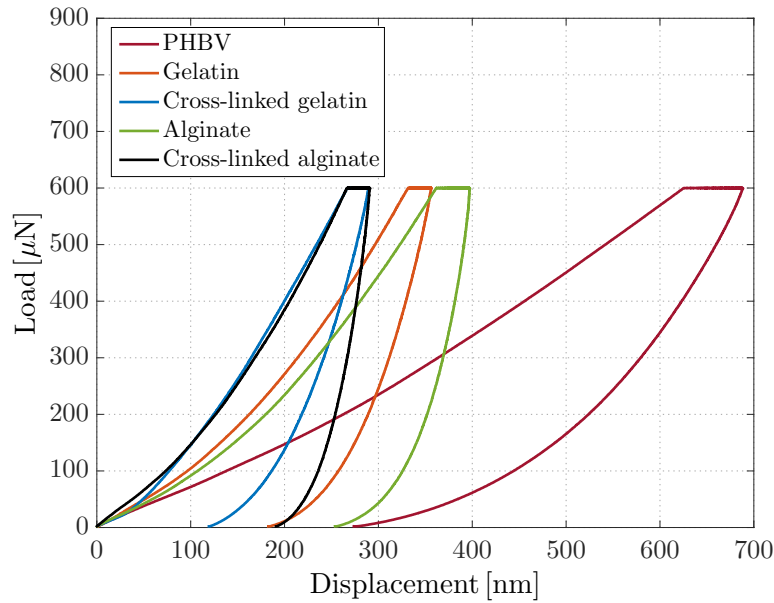


Figure 6.1: Typical load-displacement curves of different polymers used for coating the scaffolds

significantly change the pore size of any of the scaffolds, so that it remained in the range of 200–500 μm for all the polymer-coated scaffolds.

Table 6.3 shows the mass, dimensions, density and porosity of the investigated uncoated and polymer coated Bioglass[®]-based scaffolds. All of these scaffolds were of cylindrical shape, and they were similar in size. The porosity of uncoated scaffolds was as high as 95.2%. The polymer coatings only slightly reduced the porosity, down to 93.3–94.1%.

6.3.4 Ultrasound characterization of scaffolds

Wave propagation characteristics at 0.1 MHz signal frequency, such as time of flight, signal velocities, and wavelengths, are shown in Table 6.4. The relationship between signal velocities and elasticity tensor components which characterize the overall scaf-

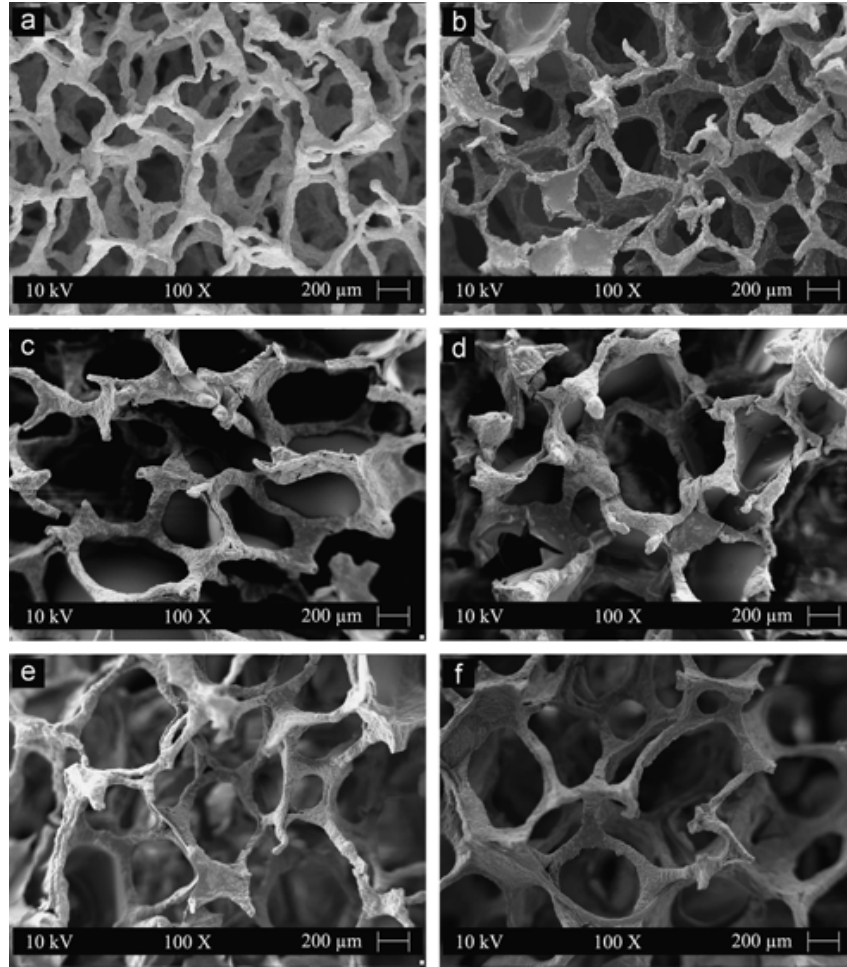


Figure 6.2: SEM images of (a) uncoated, (b) PHBV coated, (c) gelatin coated, (d) crosslinked gelatin coated, (e) alginate coated, and (f) crosslinked alginate coated Bioglass[®]-based scaffolds

Table 6.3: Characteristics of uncoated and polymer coated Bioglass[®]-based scaffolds: mass (m), diameter (D), height (h), mass density (ρ), and porosity (p)

Sample	m [g]	D [mm]	h [mm]	ρ [g · cm ⁻³]	p [%]
Uncoated	0.0691±0.0077	8.77±0.11	8.75±0.46	0.130±0.010	95.2±0.4
PHBV coated	0.0778±0.0087	8.78±0.24	8.44±0.33	0.127±0.007	93.3±0.8
Gelatin coated	0.0781±0.0130	8.82±0.31	8.70±0.51	0.129±0.013	93.9±0.6
Crosslinked gelatin coated	0.0711±0.0045	8.56±0.28	8.53±0.25	0.128±0.006	94.0±0.4
Alginate coated	0.0866±0.0135	9.06±0.22	8.90±0.14	0.134±0.016	94.0±1.0
Crosslinked alginate coated	0.0860±0.0065	9.06±0.19	9.14±0.21	0.128±0.006	94.1±0.2

Table 6.4: Time of flight (Δt), signal velocity (v), and wavelength (λ) of the transmitted signal in uncoated and polymer coated Bioglass[®]-based scaffolds

Sample	Δt [μs]	v [m/s]	λ [mm]
Uncoated	5.228 ± 0.214	1677.8 ± 140.0	16.8 ± 1.4
PHBV coated	4.127 ± 0.193	2050.1 ± 130.0	20.5 ± 1.3
Gelatin coated	4.339 ± 0.110	2007.5 ± 150.0	20.1 ± 1.5
Crosslinked gelatin coated	3.823 ± 0.129	2234.5 ± 103.9	22.3 ± 1.0
Alginate coated	4.670 ± 0.449	1919.3 ± 168.9	19.2 ± 1.7
Crosslinked alginate coated	3.816 ± 0.083	2396.4 ± 68.7	24.0 ± 0.7

folds or their solid compartments is mainly dependent on the sample geometry (diameter D and height h), the size of its microheterogeneities (d) and the wavelength (λ) of the transmitted signal. The size of the microheterogeneities (d) was equal to the diameter of the largest pores in the scaffolds, which was determined to be 0.5 mm (see Figure 6.2 and Section 6.3.3).

The ratio of sample geometry over wavelength determines whether a bulk wave travels through an approximately infinite medium, or whether the sample acts as an oscillating bar (Ashman et al., 1984). Specifically, bulk waves propagate when the diameter over height ratio (D/h) and the height over wavelength ratio (h/λ) fulfill the following relationship:

$$F_1(D/h, h/\lambda) = A \log(D/h) + B \log(h/\lambda) + 1 \geq 0, \quad (6.6)$$

with $A = 1.426$ and $B = 0.530$ (Kohlhauser and Hellmich, 2013).

At the frequency of 0.1 MHz, the measurements on all the scaffolds fulfill the requirement indicated in Eq. (6.6) (see fourth column of Table 6.5). Thus, this frequency triggers bulk waves. According to the theory of elastic waves (Carcione, 2007), the propagation velocity of such bulk waves gives access to the normal stiffness component of the investigated material,

$$C_{1111} = \rho \times v^2, \quad (6.7)$$

where ρ is the mass density of the material (Kohlhauser et al., 2009).

According to continuum micromechanics (Zaoui, 2002), the elasticity or stiffness of a material is related to a representative volume element (RVE) subjected to a homogeneous stress or strain state. On the one hand, the characteristic length of the RVE (l_{RVE}) should be significantly larger than the size d of microheterogeneities inside the RVE. On the other hand, the characteristic length of the RVE (l_{RVE}) needs to be considerably smaller than the wavelength λ of the signal which is transmitted

Table 6.5: Calculation of the normal stiffness tensor component of overall scaffolds from ultrasonic pulses with 0.1 MHz frequency, with F_1 according to Eq. (6.6)

Sample	D/h	h/λ	F_1	d/λ	C_{1111}^{scaff} [GPa]
Uncoated	1.00±0.06	0.52±0.02	0.85±0.04	0.029±0.002	0.373±0.095
PHBV coated	1.04±0.05	0.41±0.02	0.82±0.04	0.024±0.001	0.536±0.071
Gelatin coated	1.01±0.05	0.43±0.01	0.82±0.03	0.025±0.001	0.527±0.118
Crosslinked gelatin coated	1.00±0.03	0.38±0.01	0.78±0.02	0.022±0.001	0.639±0.050
Alginate coated	1.02±0.03	0.47±0.04	0.83±0.03	0.026±0.002	0.489±0.060
Crosslinked alginate coated	0.99±0.02	0.38± 0.01	0.77±0.01	0.020±0.001	0.734±0.065

through the investigated sample. Therefore, these requirements can be mathematically expressed as

$$d \ll l_{\text{RVE}} \ll \lambda. \quad (6.8)$$

The requirements in Eq. (6.8) were experimentally quantified in a previous study (Kohlhauser and Hellmich, 2013), and the results showed that the stiffness of the overall porous materials can be characterized when $d/\lambda \leq 0.03$ (see triangle labeled curve in Figure 10(a) of (Kohlhauser and Hellmich, 2013)). This prerequisite is fulfilled for the measurements carried out at 0.1 MHz in the present study (see column five of Table 6.5). Thus, Eq. (6.7) gives access to $C_{1111} = C_{1111}^{\text{scaff}}$, i.e., the normal stiffness component of the overall scaffold, as it is shown for all the uncoated and coated scaffolds in Table 6.5. It can be observed that the stiffness of uncoated scaffolds was increased by coating them with both synthetic polymer (PHBV) and natural polymers (gelatin and alginate). Moreover, the stiffness of gelatin and alginate coated scaffolds was further enhanced by crosslinking these natural polymers.

6.4 Discussion

The density and elastic modulus of polymers are highly dependent on their particular composition, molecular weight and processing history. As a consequence, the data collected from literature are often variable. In order to obtain reliable values for calculation and analysis in the present study, density and elastic modulus of the polymers as well as of sintered Bioglass[®] were measured. As shown in Table 6.1 and mentioned in Section 6.3.1, the measured densities are close to the values provided by the manufacturers or those reported in the literature. Thus, the density data is considered to be reliable for further calculation and analysis. As regards the elastic modulus, highly scattered data are reported for PHBV, gelatin and alginate,

while the elastic moduli of crosslinked gelatin or alginate-related materials are rarely reported at all. Therefore, in the present study, the elastic modulus of the used polymers was determined by nanoindentation, a widely used technique, which has been shown to be effective for measuring Young's modulus of polymers (Klapperich et al., 2000; Jee and Lee, 2010). In addition, the elastic modulus of sintered Bioglass[®] was also measured by nanoindentation, and the result was in good agreement with the values reported in the literature.

As shown in Figure 6.2, the highly interconnected porous structure of 45S5 Bioglass[®]-based scaffolds was retained after coating with different polymers. In addition, the average porosity of the scaffolds only slightly decreased after polymer coating (Table 6.3), and, as a consequence, the pore size of polymer coated scaffolds was still in the range of 200–500 μm . Therefore, the microstructure of uncoated and polymer coated scaffolds was nearly identical. On the one hand, from a biological point of view, it is of importance for polymer coated scaffolds to maintain the well-developed microstructure of uncoated scaffolds. Namely, scaffolds with a mean pore size of $\sim 300 \mu\text{m}$ were shown to be suitable for bone tissue engineering, as they exhibit increased osteoblast proliferation and differentiation throughout the entire 3D scaffold, due to enhanced oxygen and nutrient diffusion in comparison with scaffolds with small pore sizes (such as $< 200 \mu\text{m}$) (Amini et al., 2012; Karageorgiou and Kaplan, 2005; Rezwan et al., 2006). On the other hand, from a micromechanical point of view, the very similar microstructure of uncoated and polymer coated scaffolds allows for identification of one micromechanical morphology relevant for both coated and uncoated scaffolds, and, hence, for the use of one micromechanical model describing the behavior of all of these scaffolds.

As indicated in Table 6.5, the stiffness of uncoated scaffolds was increased by coating them with any of the used polymers. Moreover, after the crosslinking treatment, the stiffness of gelatin and alginate coated scaffolds was further increased. Therefore, the original assumption is confirmed, i.e., the stiffness of scaffolds can be conveniently tailored not only by applying polymer coatings, but also by further modifying the properties of the applied polymer coatings. These results provide a very simple and effective strategy of designing the stiffness of bone tissue engineering scaffolds based on bioactive glasses or bioceramics in general. In addition, the preliminary results obtained in the present study suggest that chemical crosslinking could also be an effective way to adjust the stiffness of polymer (e.g., alginate, gelatin, collagen, and chitosan) based scaffolds.

The elastic modulus of cancellous bone is dependent on its density (related to porosity) and the loading direction, and it was reported to be in the range of 0.1–0.85 GPa in the axial direction (Rohlmann et al., 1980; Linde and Hvid, 1989;

Giesen et al., 2001). The stiffness of the prepared uncoated scaffolds (0.373 GPa) and polymer-coated scaffolds (0.489–0.734 GPa) are all in the aforementioned range for cancellous bone. In other words, polymer coating and further crosslinking treatment facilitate the stiffness of the scaffolds to vary to a large extent, which could better match the specific stiffness of cancellous bone at different sites. Stiffness match of implants (here scaffolds) and their surrounding bone tissue could promote their enhanced *in vivo* performance, as stress shielding becomes negligible, thus avoiding bone resorption (Ryan et al., 2006).

From a micromechanical point of view, the elasticity of a composite is related to the elasticity of its constituents, their volume fractions and their mechanical interaction, in which the mechanical interaction is determined by the nature of the interface between the constituents and by the microstructural morphology (Zaoui, 2002). In the present study, the constituents of the scaffolds are Bioglass[®], polymer coating, and zero-stiffness macropores. As shown in Figure 6.2 and discussed above, the microstructure of uncoated and polymer coated scaffolds is very similar, which allows for introduction of one type of micromechanical structure-property relationship pertinent to all different coated and uncoated scaffolds. Moreover, the microstructure is made up of strut-type elements, as seen in Figure 6.2, and for such microstructures it has been shown that the discussion on the constituent stiffness values can be reduced to their elastic modulus (i.e., E_{Bioglass} and E_{polymer}) (Fritsch et al., 2013; Hum et al., 2013). As a consequence, the composite stiffness (C_{1111}^{scaff}) becomes a function F_2 , which represents the micromechanical interaction of the constituents of the composite in the scaffold struts. This function F_2 is expressed as

$$C_{1111}^{\text{scaff}} = F_2(E_{\text{Bioglass}}, E_{\text{polymer}}, f_{\text{Bioglass}}, f_{\text{polymer}}), \quad (6.9)$$

where f_{Bioglass} and f_{polymer} denote the volume fractions of Bioglass[®] and polymer coating, respectively. The remaining macroporosity fulfills $f_{\text{pore}} = 1 - f_{\text{Bioglass}} - f_{\text{polymer}}$.

A simple dimensional analysis provides the following relationship between dimensionless quantities (Barenblatt, 1996):

$$C_{1111}^{\text{scaff}}/E_{\text{Bioglass}} = F_2(E_{\text{polymer}}/E_{\text{Bioglass}}, f_{\text{Bioglass}}, f_{\text{polymer}}). \quad (6.10)$$

As shown in Table 6.6, f_{Bioglass} was almost constant for all types of scaffolds in the present study. Thus, Eq. (6.10) could be simplified to

$$C_{1111}^{\text{scaff}}/E_{\text{Bioglass}} = F_2(E_{\text{polymer}}/E_{\text{Bioglass}}, f_{\text{polymer}}). \quad (6.11)$$

A multi-linear regression (MLR) of the form $z = a \times x + b \times y + c$ performed on this dependence delivered $a = 6.06 \times 10^{-2}$, $b = 2.22 \times 10^{-1}$, $c = -1.04 \times 10^{-4}$ ($R^2 =$

Table 6.6: Volume fraction of pores (f_{pore}), Bioglass[®] (f_{Bioglass}), and polymer coating (f_{polymer}) in the scaffolds

Sample	f_{pore}	f_{Bioglass}	f_{polymer}
Uncoated	0.952±0.004	0.048±0.004	0
PHBV coated	0.933±0.008	0.047±0.003	0.020±0.006
Gelatin coated	0.939±0.006	0.048±0.005	0.013±0.002
Crosslinked gelatin coated	0.940±0.004	0.047±0.002	0.013±0.004
Alginate coated	0.940±0.010	0.049±0.006	0.011±0.005
Crosslinked alginate coated	0.941±0.002	0.047±0.002	0.011±0.002

0.72). A significance test showed that the statistical significance of the influence of $E_{\text{polymer}}/E_{\text{Bioglass}}$ on $C_{1111}^{\text{scaff}}/E_{\text{Bioglass}}$ is much higher than that of f_{polymer} . In fact, the confidence interval for the factor f_{polymer} in the MLR is approximately 61% (level of confidence $\alpha = 1 - 0.61 = 0.39$), which means that it can only be stated with a certainty of 61% that this factor may have an influence on the result. On the other hand, the level of confidence for $E_{\text{polymer}}/E_{\text{Bioglass}}$ is $\alpha = 0.19$. The 81% confidence interval confirms that this factor indeed has a more significant influence on the result. This may lead us to suggest approximating Eq. (6.11) through

$$C_{1111}^{\text{scaff}}/E_{\text{Bioglass}} = F_2(E_{\text{polymer}}/E_{\text{Bioglass}}). \quad (6.12)$$

This statistically suggested relationship once again reinforces the qualitative conclusions of the experimental results: coating of Bioglass[®] scaffolds with any of the used polymers indeed increases their overall stiffness. Moreover, there is a direct dependence of the resulting stiffness of the coated scaffold on the stiffness of the polymer coating. Therefore, the goal of tailoring the elasticity of the scaffolds by applying polymer coatings and further crosslinking these coatings is realized. Furthermore, the subtle variation of the elasticity values of these modified Bioglass[®] scaffolds is successfully detected by the non-destructive ultrasonic technique. It is therefore proposed that the micromechanical analysis based on the results obtained from ultrasonic measurements has a potential for improving the stiffness design of the scaffolds, which is usually done by a trial-and-error process.

6.5 Conclusions

The elastic properties predominantly determine the stress distribution in bone-implant systems, which have a great influence on the successful application of the implants, including scaffolds. Thus, it is of importance to properly design/adjust and accurately measure the elastic properties of the scaffolds. In the present study, the stiffness

of 45S5 Bioglass[®]-based scaffolds before and after polymer coating was successfully determined by the non-destructive ultrasonic technique. The results showed that the stiffness of uncoated scaffolds was increased by applying polymer coatings, and further increased by crosslinking the used natural polymer coatings. The combined multiscale ultrasound-nanoindentation measurement, as well as statistical analysis, indicated that there is a direct dependence of the resulting stiffness of the coated scaffold on the stiffness of the polymer coating.

6.6 Acknowledgements

Wei Li would like to acknowledge the European Virtual Institute on Knowledge-based Multifunctional Materials AISBL (KMM-VIN) and China Scholarship Council (CSC) for financial support. Christian Hellmich and Maria-Ioana Pastrama are grateful for financial support from the European Research Council, through project no. 257023 as part of call ERC-2010-StG. The authors thank Dr. Olaf Lahayne, Mr. Krzysztof Luczynski, Ms. Jasmin Hum, and Dr. Menti Goudouri for experimental support.

Chapter 7

Conclusions and outlook

The understanding of bone mechanobiology and the careful investigation of bone's mechanical properties are essential for the reasonable design of therapies for various bone-related diseases, as well as of implants and tissue regeneration strategies. In a way, these are the most important aspects biomedical engineers, working at the interface of mechanics, biology, biochemistry, physiology, mathematics, can contribute to the advancement of the field of medicine.

It is known that, to ensure the proper and reliable functioning of a tissue engineering scaffold seeded with cells and biochemical factors for bone regeneration, or that of a prosthesis, the mechanical properties of such constructs must match those of the surrounding bone tissue. Namely, a stiffness mismatch, causing the effect of stress shielding and bone resorption around the implant, is most undesirable and may lead to implant failure. Therefore, the mechanical properties of bone, as well as those of various ceramic materials for cell seeding in bone tissue engineering, have often been investigated. However, two aspects may have been underrated in these investigations, and exactly these have been detailed and emphasized in the current work:

- (i) Bone is a multiscale material, with a hierarchical structure revealing various compositions and mechanical properties at various length scales; the same might be the case for e.g., a bone tissue engineering scaffold, made up of a material with one or several levels of porosities. When matching the properties of implant and tissue, the level at which the mechanical properties are defined is essential. For instance, in Chapter 5, the elasticity of the intact baghdadite crystals was as high as 124 GPa, but that of the cylindrical scaffolds made of this material dramatically decreased with their porosity, that amounted up to 94%. In Chapter 6, the normal stiffness component of the highly porous Bioglass[®] scaffolds was in the range of that of cancellous bone, and therefore

these structures may be considered for regeneration of trabeculae;

- (ii) Even when testing at the desired length scale, i.e., by nanoindentation at the extracellular bone tissue scale, or the ceramic crystal scale in case of man-made bone regeneration materials, the test results may not exactly give the reliable information expected. It has been shown in Chapters 3, 4, and 5 that results from nanoindentation tests might, to a certain extent, deliver information on material phases damaged due to *a priori* existing microcracks, or due to microcracks resulted from the testing procedure itself. Then, the obtained elastic modulus might be lower than the actual one, and a mismatch between scaffold and tissue might ensue. The need for a method that characterizes only the intact material thus becomes quite clear – and this is exactly the method of statistical nanoindentation presented herein, for determination of Young’s modulus of intact human and bovine extracellular bone, as well as that of the intact ceramic material baghadadite for bone tissue engineering.

As regards bone mechanobiology, this topic was widely researched in the context of bone remodeling, where mechanotransduction plays an essential role in transmitting information on the mechanical loading conditions to the cells. The bone remodeling model in Chapter 2 considers this process to be driven by a novel mechanical stimulus, based on the hydrostatic pressures arising in the pore spaces of bone from macroscopic loading. A similar model (but with the strain energy density as mechanical stimulus) has already proven highly applicable in investigating the effect of the treatment of postmenopausal osteoporosis with the fully human monoclonal antibody denosumab (Scheiner et al., 2014). In the future, testing drugs for the treatment of bone diseases *in silico* rather than *in vivo* would represent a great advancement in computational biomedical engineering.

Another application of bone remodeling models that has known an increasing trend in the past years is in the endeavours to develop anti-cancer therapies. Ayati et al. (2010) and, shortly afterwards, Wang et al. (2011) have used a computational bone remodeling model to describe the progression of multiple myeloma, a cell malignancy characterized by osteolytic bone lesions and bone resorption. Cook et al. (2015, 2016) have developed a computational model for the evolution of bone metastatic prostate cancer cells and their interaction with the surrounding bone environment. These models are rather biology-based, lacking the mechanical feedback presented in Chapter 2. Once this essential mechanism in bone remodeling is also considered, it is hoped that such models may eventually be applied with the purpose of analyzing the efficacy of various therapeutic interventions, thus accelerating the process of finding cures for malignant bone tumours.

Nevertheless, current bone remodeling models also have a lot of potential for improvement.

First of all, there are many mechanisms that are not considered in these models – or maybe not *explicitly* considered – but which may reveal interesting features when introduced explicitly. In the bone remodeling model presented in Chapter 2, one aspect that could be explored more is related to the magnitude of osteocyte contribution to the remodeling process. These cells were considered as mechanosensors in the model, responding to the lacunar pore pressures and thus up-regulating preosteoblast proliferation. However, they might also produce even more RANKL, OPG or TGF β than the other cells (Heino et al., 2002; Bonewald, 2011); and apoptotic osteocytes could regulate the recruitment of osteoclast precursors and their differentiation by signalling their non-apoptotic neighbours, who produce RANKL or upregulate the expression of RANKL and decrease the expression of OPG, leading to increased bone resorption (Kennedy et al., 2012; O’Brien et al., 2013; Bellido, 2014). Another interesting aspect is the dynamics of the sclerostin-Wnt β pathway, that was only implicitly introduced in Chapter 2, but whose mechanisms could, in the future, be explicitly considered – e.g., by introducing a term for osteoblast precursor proliferation which is related to the amount of sclerostin expressed by a certain amount of osteocytes, in the line of Graham et al. (2013).

Secondly, the ideal scenario for developing bone remodeling models would imply concurrent modeling and experimental processes, in which there is constant feedback between the two aspects. One way in which this could work would be: the researchers working on the mathematical and computational issues develop a conceptual model, based on a set of parameters; the biologists measure these parameters on cells or tissue *in vivo*, and deliver their values to the modellers; the latter input the values and simulate the model, relying again on the experimental validation of the researchers in the laboratory. This is, of course, to a certain extent still utopic, as models are rarely based on fully measurable parameters, see e.g., the mechanosensitivity parameters in the model of Chapter 2; and simulations are not always fully reproducible in the laboratory, see e.g., the evolution of vascular porosity over years – or not always ethical, such as the long term evolution of porosity in postmenopausal osteoporosis with and without drug treatment.

To conclude, the author of this thesis has the hope that, with the work presented here, as well as with her future work, she can contribute, to however little extent, to the development of therapies for bone related diseases – the most critical of which, bone metastatic tumours, definitely require (more) cure options as soon as possible.

Bibliography

- (2008). *Indentation Software User's Manual*. CSM Instruments, Rue de la Gare 4, CH-2034 Peseux, Switzerland.
- Al-Hermezi, H. M., McKie, D., and Hall, A. J. (1986). Baghdadite, a new calcium zirconium silicate mineral from Iraq. *Mineralogical Magazine*, 50:119–123.
- Ali, M. A. and Singh, B. (1975). The effect of porosity on the properties of glass fibre-reinforced gypsum plaster. *Journal of Materials Science*, 10(11):1920–1928.
- Alliston, T., Choy, L., Ducey, P., Karsenty, G., and Derynck, R. (2001). TGF-beta-induced repression of CBFA1 by Smad3 decreases cbfa1 and osteocalcin expression and inhibits osteoblast differentiation. *EMBO Journal*, 20(9):2254–2272.
- Alon, U. (2007). *An Introduction to Systems Biology: Design Principles of Biological Circuits*. Chapman & Hall, Boca Raton, FL, USA.
- Amini, A. R., Laurencin, C. T., and Nukavarapu, S. P. (2012). Bone tissue engineering: Recent advances and challenges. *Critical Reviews in Biomedical Engineering*, 40(5):363–408.
- Ashman, R. B., Cowin, S. C., Van Buskirk, W. C., and Rice, J. C. (1984). A continuous wave technique for the measurement of the elastic properties of cortical bone. *Journal of Biomechanics*, 17(5):349–361.
- Atkins, A., Dean, M. N., Habegger, M. L., Motta, P. J., Ofer, L., Repp, F., Shipov, A., Weiner, S., Currey, J. D., and Shahar, R. (2014). Remodeling in bone without osteocytes: Billfish challenge bone structure-function paradigms. *Proceedings of the National Academy of Sciences*, 111(45):16047–16052.
- Atkins, E. D. T., Nieduszynski, I. A., Mackie, W., Parker, K. D., and Smolko, E. E. (1973). Structural components of alginic acid. II. The crystalline structure of poly- α -l-galuronic acid. Results of X-ray diffraction and polarized infrared studies. *Biopolymers*, 12(8):1879–1887.

- Atkins, P. W. (1998). *Physical Chemistry*. Oxford University Press, Oxford, UK.
- Aubin, J. (1998). Bone stem cells. *Journal of Cellular Biochemistry*, Supplements 30/31:73–82.
- Auriault, J.-L., Boutin, C., and Geindreau, C. (2009). *Homogenization of Coupled Phenomena in Heterogenous Media*. ISTE, London and John Wiley & Sons.
- Ayati, B. P., Edwards, C. M., Webb, G. F., and Wikswo, J. P. (2010). A mathematical model of bone remodeling dynamics for normal bone cell populations and myeloma bone disease. *Biology Direct*, 5(28).
- Badilatti, S. D., Christen, P., Levchuk, A., Hazrati Marangalou, J., van Rietbergen, B., Parkinson, I., and Müller, R. (2016). Large-scale microstructural simulation of load-adaptive bone remodeling in whole human vertebrae. *Biomechanics and Modeling in Mechanobiology*, 15(1):83–95.
- Bala, Y., Depalle, B., Douillard, T., Meille, S., Clément, P., Follet, H., Chevalier, J., and Boivin, G. (2011). Respective roles of organic and mineral components of human cortical bone matrix in micromechanical behavior: An instrumented indentation study. *Journal of the Mechanical Behavior of Biomedical Materials*, 4(7):1473–1482.
- Bala, Y., Farlay, D., and Boivin, G. (2013). Bone mineralization: from tissue to crystal in normal and pathological contexts. *Osteoporosis International*, 24(8):2153–2166.
- Bala, Y., Farlay, D., Delmas, P. D., Meunier, P. J., and Boivin, G. (2010). Time sequence of secondary mineralization and microhardness in cortical and cancellous bone from ewes. *Bone*, 46(4):1204–1212.
- Barenblatt, G. I. (1996). *Scaling, self-similarity, and intermediate asymptotics*. Cambridge University Press, Cambridge, UK.
- Bellido, T. (2014). Osteocyte-driven bone remodeling. *Calcified Tissue International*, 94(1):25–34.
- Bellucci, D., Sola, A., Gentile, P., Ciardelli, G., and Cannillo, V. (2012). Biomimetic coating on bioactive glass-derived scaffolds mimicking bone tissue. *Journal of Biomedical Materials Research Part A*, 100A(12):3259–3266.
- Bembey, A. K., Oyen, M. L., Bushby, A. J., and Boyde, A. (2006). Viscoelastic properties of bone as function of hydration state determined by nanoindentation. *Philosophical Magazine*, 86(33–35):5691–5703.

- Bergmann, G., Graichen, F., and Rohlmann, A. (1993). Hip joint loading during walking and running, measured in two patients. *Journal of Biomechanics*, 26(8):969–990.
- Bigi, A., Cojazzi, G., Panzavolta, S., Roveri, N., and Rubini, K. (2002). Stabilization of gelatin films by crosslinking with genipin. *Biomaterials*, 23(24):4827–4832.
- Black, J., Mattson, R., and Korostoff, E. (1974). Haversian osteons: Size, distribution, internal structure, and orientation. *Journal of Biomedical Materials Research*, 8:299–319.
- Bobji, M. S. and Biswas, S. K. (1998). Estimation of hardness by nanoindentation of rough surfaces. *Journal of Materials Research*, 13(11):3227–3233.
- Bobko, C. and Ulm, F.-J. (2008). The nano-mechanical morphology of shale. *Mechanics of Materials*, 40:318–337.
- Boivin, G. and Meunier, P. J. (2002). The degree of mineralization of bone tissue measured by computerized quantitative contact microradiography. *Calcified Tissue International*, 70(6):503–511.
- Bonewald, L. F. (2011). The amazing osteocyte. *Journal of Bone and Mineral Research*, 26(2):229–338.
- Bonewald, L. F. and Dallas, S. L. (1994). Role of active and latent transforming growth factor- β in bone formation. *Journal of Cellular Biochemistry*, 55(3):350–357.
- Bonfield, W. and Clark, E. A. (1973). Elastic deformation of compact bone. *Journal of Materials Science*, 8(11):1590–1594.
- Borgiani, E., Duda, G. N., Willie, B., and Checa, S. (2015). Bone healing in mice: Does it follow generic mechano-regulation rules? *Facta Universitatis, Series: Mechanical Engineering*, 13(3):217–227.
- Bose, S., Roy, M., and Bandyopadhyay, A. (2012). Recent advances in bone tissue engineering scaffolds. *Trends in Biotechnology*, 30(10):546–554.
- Boyce, B. F. and Xing, L. (2008). Functions of RANKL/RANK/OPG in bone modeling and remodeling. *Archives of Biochemistry and Biophysics*, 473(2):139–146.
- Boyce, T. M., Fyhrie, D. P., Glotkowski, M. C., Radin, E. L., and Schaffler, M. B. (1998). Damage type and strain mode associations in human compact bone bending fatigue. *Journal of Orthopaedic Research*, 16(3):322–329.

- Boyde, A., Bianco, P., Portigliatti Barbos, M., and Ascenzi, A. (1984). Collagen orientation in compact bone: I. A new method for the determination of the proportion of collagen parallel to the plane of compact bone sections. *Metabolic Bone Disease and Related Research*, 5(6):299–307.
- Brennan, O., Kuliwaba, J. S., Lee, T. C., Parkinson, I. H., Fazzalari, N. L., McNamara, L. M., and O'Brien, F. J. (2012). Temporal changes in bone composition, architecture, and strength following estrogen deficiency in osteoporosis. *Calcified Tissue International*, 91:440–449.
- Brighton, C. T., Fisher, J. R., Levine, S. E., Corsetti, J. R., Reilly, T., Landsman, A. S., Williams, J. L., and Thibault, L. E. (1996). The biochemical pathway mediating the proliferative response of bone cells to a mechanical stimulus. *The Journal of Bone and Joint Surgery*, 78(9):1337–1347.
- Brodts, M. D. and Silva, M. J. (2010). Aged mice have enhanced endocortical response and normal periosteal response compared with young-adult mice following 1 week of axial tibial compression. *Journal of Bone and Mineral Research*, 25(9):2006–2015.
- Buckwalter, J. A. and Cooper, R. R. (1987). Bone structure and function. In *Instructional Course Lectures, The American Academy of Orthopaedic Surgeons*, volume 36, pages 27–48. The American Academy of Orthopaedic Surgeons, Park Ridge, Illinois.
- Buckwalter, J. A., Glimcher, M. J., Cooper, R. R., and Recker, R. (1995a). Bone biology. Part I: Structure, blood supply, cells, matrix, and mineralization. *Journal of Bone and Joint Surgery – Series A*, 77(8):1256–1275.
- Buckwalter, J. A., Glimcher, M. J., Cooper, R. R., and Recker, R. (1995b). Bone biology. Part II. Formation, form, modeling, remodeling, and regulation of cell function. *Journal of Bone and Joint Surgery – Series A*, 77(8):1276–1289.
- Buenzli, P. R., Pivonka, P., and Smith, D. (2011). Spatio-temporal structure of cell distribution in cortical bone multicellular units: A mathematical model. *Bone*, 48:918–926.
- Burr, D. B. and Martin, R. B. (1993). Calculating the probability that microcracks initiate resorption spaces. *Journal of Biomechanics*, 26(4/5):613–616.
- Burr, D. B., Milgrom, C., Fyhrie, D., Forwood, M., Nyska, M., Finestone, A., Hoshaw, S., Saiag, E., and Simkin, A. (1996). *In vivo* measurement of human tibial strains during vigorous activity. *Bone*, 18(5):405–410.

- Busse, B., Djonic, D., Milovanovic, P., Hahn, M., Püschel, K., Ritchie, R., Djuric, M., and Amling, M. (2010). Decrease in the osteocyte lacunar density accompanied by hypermineralized lacunar occlusion reveals failure and delay of remodeling in aged human bone. *Aging Cell*, 9(6):1065–1075.
- Calori, G. M., Mazza, E., Colombo, M., and Ripamonti, C. (2011). The use of bone-graft substitutes in large bone defects: any specific needs? *Injury*, 42 Suppl 2:56–63.
- Carcione, J. M. (2007). *Wave fields in real media: Wave propagation in anisotropic, anelastic, porous and electromagnetic media*. Elsevier, Oxford, UK.
- Cardoso, L., Fritton, S. P., Galiani, G., Benalla, M., and Cowin, S. C. (2013). Advances in assessment of bone porosity, permeability and interstitial fluid flow. *Journal of Biomechanics*, 46(2):253–265.
- Carter, D. R., Orr, T. E., and Fyhrie, D. P. (1989). Relationships between loading history and femoral cancellous bone architecture. *Journal of Biomechanics*, 22(3):231–244.
- Çolak, A. (2006). Physical and mechanical properties of polymer-plaster composites. *Materials Letters*, 60(16):1977–1982.
- Chapurlat, R. D., Arlot, M., Burt-Pichat, B., Chavassieux, P., Roux, J. P., Portero-Muzy, N., and Delmas, P. D. (2007). Microcrack frequency and bone remodeling in postmenopausal osteoporotic women on long-term bisphosphonates: a bone biopsy study. *Journal of Bone and Mineral Research*, 22(10):1502–1509.
- Charles-Harris, M., del Valle, S., Hentges, E., Bleuet, P., Lacroix, D., and Planell, J. A. (2007). Mechanical and structural characterisation of completely degradable polylactic acid/calcium phosphate glass scaffolds. *Biomaterials*, 28(30):4429–4438.
- Charrière, E., Terrazzoni, S., Pittet, C., Mordasini, P., Dutoit, M., Lemaître, J., and Zysset, P. K. (2001). Mechanical characterization of brushite and hydroxyapatite cements. *Biomaterials*, 22(21):2937–2945.
- Chavassieux, P., Seeman, E., and Delmas, P. D. (2007). Insights into material and structural basis of bone fragility from diseases associated with fractures: how determinants of the biomechanical properties of bone are compromised by disease. *Endocrine Reviews*, 28(2):151–164.
- Checa, S., Prendergast, P. J., and Duda, G. N. (2011). Inter-species investigation of the mechano-regulation of bone healing: Comparison of secondary bone healing in sheep and rat. *Journal of Biomechanics*, 44(7):1237–1245.

- Chen, H., Zhou, X., Shoumura, S., Emura, S., and Bunai, Y. (2010). Age- and gender-dependent changes in three-dimensional microstructure of cortical and trabecular bone at the human femoral neck. *Osteoporosis International*, 21(4):627–636.
- Chen, Q. Z. and Boccaccini, A. R. (2006). Poly(D,L-lactic acid) coated 45S5 Bioglass[®]-based scaffolds: Processing and characterization. *Journal of Biomedical Materials Research Part A*, 77A(3):445–457.
- Chen, Q. Z., Thompson, I. D., and Boccaccini, A. R. (2006). 45S5 Bioglass[®]-derived glass-ceramic scaffolds for bone tissue engineering. *Biomaterials*, 27(11):2414–2425.
- Chen, Q. Z., Xu, J. L., Yu, L. G., Fang, X. Y., and Khor, K. A. (2012). Spark plasma sintering of sol-gel derived 45S5 Bioglass[®]-ceramics: Mechanical properties and biocompatibility evaluation. *Materials Science and Engineering C*, 32(3):494–502.
- Chu, T.-M. G., Orton, D. G., Hollister, S. J., Feinberg, S. E., and Halloran, J. W. (2002). Mechanical and *in vivo* performance of hydroxyapatite implants with controlled architecture. *Biomaterials*, 23:1283–1293.
- Coble, R. L. and Kingery, W. D. (1956). Effect of porosity on physical properties of sintered alumina. *Journal of the American Ceramic Society*, 39(11):377–385.
- Colloca, M., Blanchard, R., Hellmich, C., Ito, K., and van Rietbergen, B. (2014a). A multiscale analytical approach for bone remodeling simulations: Linking scales from collagen to trabeculae. *Bone*, 64:303–313.
- Colloca, M., Ito, K., and van Rietbergen, B. (2014b). An analytical approach to investigate the evolution of bone volume fraction in bone remodeling simulation at the tissue and cell level. *Journal of Biomechanical Engineering*, 136(3):031004 (8 pages).
- Constantinides, G., Ravi Chandran, K. S., Ulm, F.-J., and Van Vliet, K. J. (2006). Grid indentation analysis of composite microstructure and mechanics: Principles and validation. *Materials Science and Engineering A*, 430:189–202.
- Constantinides, G. and Ulm, F.-J. (2007). The nanogranular nature of C-S-H. *Journal of the Mechanics and Physics of Solids*, 55(1):64–90.
- Cook, L. M., Araujo, A., Basanta, D., and Lynch, C. C. (2015). Defining the temporal effects of TGF β inhibition on the cellular heterogeneity of the bone metastatic prostate cancer microenvironment. *Cancer Research*, 75(15 S):3751–3751.

- Cook, L. M., Araujo, A., Pow-Sang, J. M., Budzevich, M. M., Basanta, D., and Lynch, C. C. (2016). Predictive computational modeling to define effective treatment strategies for bone metastatic prostate cancer. *Scientific Reports*, 6, Article number: 29384.
- Cooper, D. M. L., Thomas, C. D. L., Clement, J. G., Turinsky, A. L., Sensen, C. W., and Hallgrímson, B. (2007). Age-dependent change in the 3D structure of cortical porosity at the human femoral midshaft. *Bone*, 40(4):957–965.
- Cooper, D. M. L., Turinsky, A. L., Sensen, C. W., and Hallgrímson, B. (2003). Quantitative 3D analysis of the canal network in cortical bone by micro-computed tomography. *Anatomical Record - Part B. The New Anatomist*, 274(1):169–179.
- Coussy, O. (2004). *Poromechanics*. John Wiley & Sons, Chichester, UK.
- Craciun, F., Galassi, C., Roncari, E., Filippi, A., and Guidarelli, G. (1998). Electro-elastic properties of porous piezoelectric ceramics obtained by tape casting. *Ferroelectrics*, 205(1):49–67.
- Currey, J. D. (1969a). The mechanical consequences of variation in the mineral content of bone. *Journal of Biomechanics*, 2:1–11.
- Currey, J. D. (1969b). The relationship between the stiffness and the mineral content of bone. *Journal of Biomechanics*, 2:477–480.
- Currey, J. D. (2006). *Bones: Structure and Mechanics*. Princeton University Press, Princeton, NJ, USA.
- Currey, J. D., Brear, K., and Zioupos, P. (1996). The effects of ageing and changes in mineral content in degrading the toughness of human femora. *Journal of Biomechanics*, 29(2):257–260.
- Cusack, S. and Miller, A. (1979). Determination of the elastic constants of collagen by Brillouin light scattering. *Journal of Molecular Biology*, 135(1):39–51.
- De With, G., Van Dijk, H. J. A., Hattu, N., and Prijs, K. (1981). Preparation, microstructure and mechanical properties of dense polycrystalline hydroxy apatite. *Journal of Materials Science*, 16(6):1592–1598.
- Dequeker, J., Remans, J., Franssen, R., and Waes, J. (1971). Ageing patterns of trabecular and cortical bone and their relationship. *Calcified Tissue International*, 7(1):23–30.

- Díaz, A. and Hampshire, S. (2004). Characterisation of porous silicon nitride materials produced with starch. *Journal of the European Ceramic Society*, 24:413–419.
- Doblaré, M. and García, J. M. (2002). Anisotropic bone remodelling model based on a continuum damage-repair theory. *Journal of Biomechanics*, 35(1):1–17.
- Dormieux, L., Kondo, D., and Ulm, F.-J. (2006). *Microporomechanics*. John Wiley & Sons, Chichester, UK.
- Drugan, W. R. and Willis, J. R. (1996). A micromechanics-based nonlocal constitutive equation and estimates of representative volume element size for elastic composites. *Journal of the Mechanics and Physics of Solids*, 44(4):497–524.
- Dunstan, C. R., Evans, R. A., Hills, E., Wong, S. Y., and Higgs, R. J. (1990). Bone death in hip fracture in the elderly. *Calcified Tissue International*, 47(5):270–275.
- Dunstan, C. R., Somers, N. M., and Evans, R. A. (1993). Osteocyte death and hip fracture. *Calcified Tissue International*, 53 (Suppl 1):S113–S116.
- Erlebacher, A., Filvaroff, E. H., Ye, J.-Q., and Derynck, R. (1998). Osteoblastic responses to TGF- β during bone remodeling. *Molecular Biology of the Cell*, 9(7):1903–1918.
- Erol, M., Mouriño, V., Newby, P., Chatzistavrou, X., Roether, J. A., Hupag, L., and Boccaccini, A. R. (2012a). Copper-releasing, boron-containing bioactive glass-based scaffolds coated with alginate for bone tissue engineering. *Acta Biomaterialia*, 8(2):792–801.
- Erol, M., Özyuğuran, A., Özarpat, O., and Küçükbayrak, S. (2012b). 3D composite scaffolds using strontium containing bioactive glasses. *Journal of the European Ceramic Society*, 32(11):2747–2745.
- Eshelby, J. (1957). The determination of the elastic field of an ellipsoidal inclusion, and related problems. *Proceedings of the Royal Society London, Series A*, 241:376–396.
- Espinoza Orías, A. A., Deuerling, J. M., Landrigan, M. D., Renaud, J. E., and Roeder, R. K. (2009). Anatomic variation in the elastic anisotropy of cortical bone tissue in the human femur. *Journal of the Mechanical Behavior of Biomedical Materials*, 2(3):255–263.
- Fan, X., Roy, E., Zhu, L., Murphy, T. C., Ackert-Bicknell, C., Hart, C. M., Rosen, C., Nanes, M. S., and Rubin, J. (2004). Nitric oxide regulates receptor activator of

- nuclear factor- κ B ligand and osteoprotegerin expression in bone marrow stromal cells. *Endocrinology*, 145(2):751–759.
- Fan, Z., Swadener, J. G., Rho, J. Y., Roy, M. E., and Pharr, G. M. (2002). Anisotropic properties of human tibial cortical bone as measured by nanoindentation. *Journal of Orthopaedic Research*, 20(4):806–810.
- Fazzalari, N. L., Forwood, M. R., Manthey, B. A., Smith, K., and Kolesik, P. (1998). Three-dimensional confocal images of microdamage in cancellous bone. *Bone*, 23(4):373–378.
- Fedorov, F. I. (1968). *Theory of Elastic Waves in Crystals*. Springer Science and Business Media, New York, USA.
- Feik, S. A., Thomas, C. D. L., Bruns, R., and Clement, J. G. (2000). Regional variations in cortical modeling in the femoral mid-shaft: sex and age differences. *American Journal of Physical Anthropology*, 112:191–205.
- Feng, L. and Jasiuk, I. (2011). Multi-scale characterization of swine femoral cortical bone. *Journal of Biomechanics*, 44(2):313–320.
- Follet, H., Boivin, G., Rumelhart, C., and Meunier, P. J. (2004). The degree of mineralization is a determinant of bone strength: a study on human calcanei. *Bone*, 34(5):783–789.
- Fölsch, C., Mittelmeier, W., Bilderbeek, U., Timmesfeld, N., von Garrel, T., and Matter, H. P. (2012). Effect of storage temperature on allograft bone. *Transfusion Medicine and Hemotherapy*, 39(1):36–40.
- Forwood, M. R. and Turner, C. H. (1995). Skeletal adaptations to mechanical usage: Results from tibial loading studies in rats. *Bone*, 17(4):197–205.
- Franzoso, G. and Zysset, P. K. (2009). Elastic anisotropy of human cortical bone secondary osteons measured by nanoindentation. *Journal of Biomechanical Engineering*, 131(2):021001–021011.
- Fritsch, A., Dormieux, L., and Hellmich, C. (2006). Porous polycrystals built up by uniformly and axisymmetrically oriented needles: Homogenization of elastic properties. *Comptes Rendus Mécanique*, 334(3):151–157.
- Fritsch, A., Dormieux, L., Hellmich, C., and Sanahuja, J. (2009a). Mechanical behaviour of hydroxyapatite biomaterials: An experimentally validated micromechanical model for elasticity and strength. *Journal of Biomedical Materials Research Part A*, 88:149–161.

- Fritsch, A. and Hellmich, C. (2007). "Universal" microstructural patterns in cortical and trabecular, extracellular and extravascular bone materials: Micromechanics-based prediction of anisotropic elasticity. *Journal of Theoretical Biology*, 244(4):597–620.
- Fritsch, A., Hellmich, C., and Dormieux, L. (2009b). Ductile sliding between mineral crystals followed by rupture of collagen crosslinks: experimentally supported micromechanical explanation of bone strength. *Journal of Theoretical Biology*, 260(2):230–252.
- Fritsch, A., Hellmich, C., and Young, P. (2013). Micromechanics-derived scaling relations for poroelasticity and strength of brittle porous polycrystals. *Journal of Applied Mechanics*, 80(2):020905 (12 pages).
- Fritton, J. C., Myers, E. R., Wright, T. M., and van der Meulen, M. C. H. (2005). Loading induces site-specific increases in mineral content assessed by microcomputed tomography of the mouse tibia. *Bone*, 36(6):1030–1038.
- Fritton, S. P., McLeod, K. J., and Rubin, C. T. (2000). Quantifying the strain history of bone: spatial uniformity and self-similarity of low-magnitude strains. *Journal of Biomechanics*, 33(3):317–325.
- Frost, H. M. (1964a). Dynamics of bone remodeling. In Frost, H. M., editor, *Bone Biodynamics*, pages 315–333. Churchill, Little Brown, Boston, USA.
- Frost, H. M. (1964b). *The laws of bone structure*. C.C. Thomas, Springfield, IL, USA.
- Frost, H. M. (1992). Perspectives: bone's mechanical usage windows. *Bone and Mineral*, 19(3):257–271.
- Frost, H. M. (1998). Changing concepts in skeletal physiology: Wolff's Law, the mechanostate, and the "Utah Paradigm". *American Journal of Human Biology*, 10(5):599–605.
- Fuchs, R. K., Warden, S. J., and Turner, C. H. (2009). Bone anatomy, physiology and adaptation to mechanical loading. In Planell, J. A., editor, *Bone Repair Biomaterials*, pages 25–68. Woodhead Publishing Limited, Cambridge, UK.
- Fuller, K., Lean, J. M., Bayley, K. E., Wani, M. R., and Chambers, T. J. (2000). A role for TGF- β 1 in osteoclast differentiation and survival. *Journal of Cell Science*, 113(13):2445–2453.

- Furin, I., Pastrama, M.-I., Kariem, H., Luczynski, K. W., Lahayne, O., and Hellmich, C. (2016). A new nanoindentation protocol for identifying the elasticity of undamaged extracellular bone tissue. *MRS Advances*, 1(11):693–704.
- Gardinier, J. D., Majumdar, S., Duncan, R. L., and Wang, L. (2009). Cyclic hydraulic pressure and fluid flow differentially modulate cytoskeleton re-organization in MC3T3 osteoblasts. *Cellular and Molecular Bioengineering*, 2(1):133–143.
- Gardinier, J. D., Townend, C. W., Jen, K.-P., Wu, Q., Duncan, R. L., and Wang, L. (2010). In situ permeability measurement of the mammalian lacunar-canalicular system. *Bone*, 46(4):1075–1081.
- Gaur, T., Lengner, C. J., Hovhannisyan, H., Bhat, R. A., Bodine, P. V., Komm, B. S., Javed, A., van Wijnen, A. J., Stein, J. L., Stein, G. S., and Lian, J. B. (2005). Canonical WNT signaling promotes osteogenesis by directly stimulating *Runx2* gene expression. *The Journal of Biological Chemistry*, 280(39):33132–33140.
- Gerhardt, L.-C. and Boccaccini, A. R. (2010). Bioactive glass and glass-ceramic scaffolds for bone tissue engineering. *Materials*, 3(7):3867–3910.
- Giesen, E. B. W., Ding, M., Dalstra, M., and van Eijden, T. M. G. J. (2001). Mechanical properties of cancellous bone in the human mandibular condyle are anisotropic. *Journal of Biomechanics*, 34(6):799–803.
- Gilmore, R. S. and Katz, J. L. (1982). Elastic properties of apatites. *Journal of Materials Science*, 17(4):1131–1141.
- Giofrè, M., Torricelli, P., Panzavolta, S., Rubini, K., and Bigi, A. (2012). Role of pH on stability and mechanical properties of gelatin films. *Journal of Bioactive and Compatible Polymers: Biomedical Applications*, 29:529–544.
- Glowacki, J., Cox, C. A., O’Sullivan, J., Wilkie, D., and Deftos, L. J. (1986). Osteoclasts can be induced in fish having an acellular bony skeleton. *Proceedings of the National Academy of Sciences of the United States of America*, 83:4104–4107.
- Goulet, J. A., Senunas, L. E., DeSilva, G. L., and Greenfield, M. L. (1997). Autogenous iliac crest bone graft. Complications and functional assessment. *Clinical Orthopaedics and Related Research*, 339(339):76–81.
- Graham, J. M., Ayati, B. P., Holstein, S. A., and Martin, J. A. (2013). The role of osteocytes in targeted bone remodeling: a mathematical model. *PloS One*, 8(5):e63884.

- Greenfield, E. M., Bi, Y., and Miyauchi, A. (1999). Regulation of osteoclast activity. *Life Sciences*, 65(11):1087–1102.
- Griffith, L. G. and Naughton, G. (2002). Tissue engineering – current challenges and expanding opportunities. *Science*, 295(5557):1009–1014.
- Grimal, Q., Rus, G., Parnell, W. J., and Laugier, P. (2011). A two-parameter model of the effective elastic tensor for cortical bone. *Journal of Biomechanics*, 44(8):1621–1625.
- Gupta, H. S., Stachewicz, U., Wagermaier, W., Roschger, P., Wagner, H. D., and Fratzl, P. (2006). Mechanical modulation at the lamellar level in osteonal bone. *Journal of Materials Research*, 21(8):1913–1921.
- Haglung, J. A. and Hunter, O. J. (1973). Elastic properties of polycrystalline monoclinic Gd_2O_3 . *Journal of the American Ceramic Society*, 56:327–330.
- Hashin, Z. (1983). Analysis of composite materials – a survey. *Journal of Applied Mechanics, Transactions ASME*, 50(3):481–505.
- Hegrenes, S. (2001). Diet-induced phenotypic plasticity of feeding morphology in the orangespotted sunfish, *Lepomis humilis*. *Ecology of Freshwater Fish*, 10:35–42.
- Heino, T. J., Hentunen, T. A., and Väänänen, H. K. (2002). Osteocytes inhibit osteoclastic bone resorption through transforming growth factor-beta: enhancement by estrogen. *Journal of Cellular Biochemistry*, 85(1):185–197.
- Heinonen, A., Sievänen, H., Kannus, P., Oja, P., and Vuori, I. (2002). Site-specific skeletal response to long-term weight training seems to be attributable to principal loading modality: a pQCT study of female weightlifters. *Calcified Tissue International*, 70(6):469–474.
- Hellmich, C., Barthélémy, J.-F., and Dormieux, L. (2004a). Mineral-collagen interactions in elasticity of bone ultrastructure – a continuum micromechanics approach. *European Journal of Mechanics - A/Solids*, 23(5):783–810.
- Hellmich, C., Celundova, D., and Ulm, F.-J. (2009). Multiporoelasticity of hierarchically structured materials: Micromechanical foundations and application to bone. *Journal of Engineering Mechanics (ASCE)*, 135(5):382–394.
- Hellmich, C. and Ulm, F.-J. (2002). Micromechanical model for ultra-structural stiffness of mineralized tissues. *Journal of Engineering Mechanics (ASCE)*, 128(8):898–908.

- Hellmich, C. and Ulm, F.-J. (2005). Microporodynamics of bones: prediction of the "Frenkel-Biot" slow compressional wave. *Journal of Engineering Mechanics (ASCE)*, 131(9):918–927.
- Hellmich, C., Ulm, F.-J., and Dormieux, L. (2004b). Can the diverse elastic properties of trabecular and cortical bone be attributed to only a few tissue-independent phase properties and their interactions? – Arguments from a multiscale approach. *Biomechanics and Modeling in Mechanobiology*, 2(4):219–238.
- Hench, L. L. (1998). Bioceramics. *Journal of the American Ceramic Society*, 81(7):1705–1727.
- Hench, L. L. (2006). The story of Bioglass[®]. *Journal of Materials Science: Materials in Medicine*, 17(11):967–978.
- Hengsberger, S., Kulik, A., and Zysset, P. K. (2002). Nanoindentation discriminates the elastic properties of individual human bone lamellae under dry and physiological conditions. *Bone*, 30:178–184.
- Henriksen, K., Karsdal, M., Delaissé, J.-M., and Engsig, M. T. (2003). RANKL and vascular endothelial growth factor (VEGF) induce osteoclast chemotaxis through an ERK1/2-dependent mechanism. *The Journal of Biological Chemistry*, 278(49):48745–48753.
- Hershey, A. V. (1954). The elasticity of an isotropic aggregate of anisotropic cubic crystals. *ASME Journal of Applied Mechanics*, 21:236–240.
- Hill, R. (1963). Elastic properties of reinforced solids: some theoretical principles. *Journal of Mechanics and Physics of Solids*, 11(5):357–372.
- Hill, R. (1965). Continuum micro-mechanics of elastoplastic polycrystals. *Journal of Mechanics and Physics of Solids*, 13(2):89–101.
- Hoffler, C. E., Guo, X. E., and Zysset, P. K. (2005). An application of nanoindentation technique to measure bone tissue lamellae properties. *Journal of Biomechanical Engineering*, 127(7):1046–1053.
- Hoffler, C. E., Moore, K. E., Kozloff, K., Zysset, P. K., Brown, M. B., and Goldstein, S. A. (2000a). Heterogeneity of bone lamellar-level elastic moduli. *Bone*, 26(7):603–609.
- Hoffler, C. E., Moore, K. E., Kozloff, K., Zysset, P. K., and Goldstein, S. A. (2000b). Age, gender, and bone lamellae elastic moduli. *Journal of Orthopaedic Research*, 18(3):432–437.

- Hollister, S. J. (2005). Porous scaffold design for tissue engineering. *Nature Materials*, 4(7):518–524.
- Hsieh, Y. F., Robling, A. G., Ambrosius, W. T., Burr, D. B., and Turner, C. H. (2001). Mechanical loading of diaphyseal bone *in vivo*: the strain threshold for an osteogenic response varies with location. *Journal of Bone and Mineral Research*, 16(12):2291–2297.
- Hsieh, Y. F. and Turner, C. H. (2001). Effects of loading frequency on mechanically induced bone formation. *Journal of Bone and Mineral Research*, 16(5):918–924.
- Huiskes, R., Ruimerman, R., van Lenthe, G. H., and Janssen, J. D. (2000). Effects of mechanical forces on maintenance and adaptation of form in trabecular bone. *Nature*, 405(6787):704–706.
- Huiskes, R., Weinans, H., Grootenboer, H. J., Dalstra, M., Fudala, B., and Slooff, T. J. (1987). Adaptive bone-remodeling theory applied to prosthetic-design analysis. *Journal of Biomechanics*, 20(11–12):1135–1150.
- Huiskes, R., Weinans, H., and van Rietbergen, B. (1992). The relationship between stress shielding and bone resorption around total hip stems and the effects of flexible materials. *Clinical Orthopaedics and Related Research*, 274:124–134.
- Hum, J., Luczynski, K. W., Noeaid, P., Newby, P., Lahayne, O., Hellmich, C., and Boccaccini, A. R. (2013). Stiffness improvement of 45S5 Bioglass[®]-based scaffolds through natural and synthetic biopolymer coatings: An ultrasonic study. *Strain*, 49(5):431–439.
- Hunter, G. K., Hauschka, P. V., Poole, A. R., Rosenberg, L. C., and Goldberg, H. A. (1996). Nucleation and inhibition of hydroxyapatite formation by mineralized tissue proteins. *Biochemical Journal*, 317(1):59–64.
- Hutmacher, D. W. (2000). Scaffolds in tissue engineering bone and cartilage. *Biomaterials*, 21(24):2529–2543.
- Huyseune, A., Sire, J. Y., and J, M. F. (1994). Comparative study of lower pharyngeal jaw structure in two phenotypes of *Astatoreochromis alluaudi* (*Teleostei, Cichlidae*). *Journal of Morphology*, 221:25–43.
- Jaindl, M., Reinbacher-Köstinger, A., Magele, C., and Renhart, W. (2009). Multi-objective optimization using evolution strategies. *Facta Universitatis, Series: Electronics and Energetics*, 22(2):159–174.

- Janssens, K., ten Dijke, P., Janssens, S., and Van Hul, W. (2005). Transforming growth factor- β 1 to the bone. *Endocrine Reviews*, 26(6):743–774.
- Jee, A. Y. and Lee, M. (2010). Comparative analysis on the nanoindentation of polymers using atomic force microscopy. *Polymer Testing*, 29(1):95–99.
- Jilka, R. L., Noble, B., and Weinstein, R. S. (2013). Osteocyte apoptosis. *Bone*, 54(2):264–271.
- Jilka, R. L. and O'Brien, C. A. (2016). The role of osteocytes in age-related bone loss. *Current Osteoporosis Reports*, 14(1):16–25.
- Jones, D. B., Nolte, H., Scholübbbers, J.-G., Turner, E., and Veltel, D. (1991). Biochemical signal transduction of mechanical strain in osteoblast-like cells. *Biomaterials*, 12(2):101–110.
- Jones, J. R. (2013). Review of bioactive glass: From Hench to hybrids. *Acta Biomaterialia*, 9(1):4457–4486.
- Judex, S., Lei, X., Han, D., and Rubin, C. T. (2007). Low-magnitude mechanical signals that stimulate bone formation in the ovariectomized rat are dependent on the applied frequency but not on the strain magnitude. *Journal of Biomechanics*, 40(6):1333–1339.
- Karageorgiou, V. and Kaplan, D. (2005). Porosity of 3D biomaterial scaffolds and osteogenesis. *Biomaterials*, 26(27):5474–5491.
- Kariem, H., Pastrama, M.-I., Roohani-Esfahani, S. I., Pivonka, P., Zreiqat, H., and Hellmich, C. (2015). Micro-poro-elasticity of baghdadite-based bone tissue engineering scaffolds: A unifying approach based on ultrasonics, nanoindentation, and homogenization theory. *Material Science and Engineering C*, 46:553–564.
- Kartsogiannis, V., Zhou, H., Horwood, N. J., Thomas, R. J., Hards, D. K., Quinn, J. M., Niforas, P., Ng, K. W., Martin, T. J., and Gillespie, M. T. (1999). Localization of RANKL (receptor activator of NF kappa B ligand) mRNA and protein in skeletal and extraskeletal tissues. *Bone*, 25(5):525–534.
- Kaspar, D., Seidl, W., Neidlinger-Wilke, C., Beck, A., Claes, L., and Ignatius, A. (2002). Proliferation of human-derived osteoblast-like cells depends on the cycle number and frequency of uniaxial strain. *Journal of Biomechanics*, 35(7):873–880.
- Katz, J. K. (1971). Hard tissue as a composite material - I. Bounds on the elastic behavior. *Journal of Biomechanics*, 4:455–473.

- Katz, J. L., Yoon, H. S., Lipson, S., Maharidge, R., Meunier, A., and Christel, P. (1984). The effects of remodelling on the elastic properties of bone. *Calcified Tissue International*, 36:S31–S36.
- Kazakia, G. J., Tjong, W., Nirody, J. A., Burghardt, A. J., Carballido-Gamio, J., Patsch, J. M., Link, T., Feeley, B. T., and Ma, C. B. (2014). The influence of disuse on bone microstructure and mechanics assessed by HR-pQCT. *Bone*, 63:132–140.
- Keller, T. S. (1994). Prediction of the compressive mechanical behavior of bone. *Journal of Biomechanics*, 27(9):1159–1168.
- Kennedy, O. D., Herman, B. C., Laudier, D. M., Majeska, R. J., Sun, H. B., and Schaffler, M. B. (2012). Activation of resorption in fatigue-loaded bone involves both apoptosis and active pro-osteoclastogenic signaling by distinct osteocyte populations. *Bone*, 50(5):1115–1122.
- Khanna, R., Katti, K. S., and Katti, D. R. (2009). Nanomechanics of surface modified nanohydroxyapatite particulates used in biomaterials. *Journal of Engineering Mechanics*, 135(5):468–478.
- Khanna, R., Katti, K. S., and Katti, D. R. (2012). Experiments in nanomechanical properties of live osteoblast cells and cell-biomaterial interface. *Journal of Nanotechnology in Engineering and Medicine*, 2(4):041005 (13 pages).
- Kiefer, B., Stixrude, L., Hafner, J., and Kresse, G. (2001). Structure and elasticity of wadsleyite at high pressures. *American Mineralogist*, 86:1387–1395.
- Klapperich, C., Komvopoulos, K., and Pruitt, L. (2000). Nanomechanical properties of polymers determined from nanoindentation experiments. *Journal of Tribology*, 123(3):624–631.
- Klein-Nulend, J., Van der Plas, A., Semeins, C. M., Ajubi, N. E., Frangos, J. A., Nijweide, P. J., and Burger, E. H. (1995). Sensitivity of osteocytes to biomechanical stress in vitro. *FASEB Journal*, 9(5):441–445.
- Klejna, K., Naumnik, B., Gasowska, K., and Myśliwiec, M. (2009). OP-G/RANK/RANKL signaling system and its significance in nephrology. *Folia Histochemica et Cytobiologica*, 47(2):199–206.
- Kohlhauser, C. and Hellmich, C. (2013). Ultrasonic contact pulse transmission for elastic wave velocity and stiffness determination: Influence of specimen geometry and porosity. *Engineering Structures*, 47:115–133.

- Kohlhauser, C., Hellmich, C., Vitale-Brovarone, C., Boccaccini, A. R., Rota, A., and Eberhardsteiner, J. (2009). Ultrasonic characterisation of porous biomaterials across different frequencies. *Strain*, 45(1):34–44.
- Kroll, M. H. (2000). Parathyroid hormone temporal effects on bone formation and resorption. *Bulletin of Mathematical Biology*, 62(1):163–188.
- Kutzner, I., Heinlein, B., Graichen, F., Bender, A., Rohlmann, A., Halder, A., Beier, A., and Bergmann, G. (2010). Loading of the knee joint during activities of daily living measured *in vivo* in five subjects. *Journal of Biomechanics*, 43(11):2164–2173.
- Lacey, D. L., Timms, E., Tan, H.-L., Kelley, M. J., Dunstan, C. R., Burgess, T., Elliott, R., Colombero, A., Elliott, G., Scully, S., Hsu, H., Sullivan, J., Hawkins, N., Davy, E., Capparelli, C., Eli, A., Qian, Y. X., Kaufman, S., Sarosi, I., Shalhoub, V., Senaldi, G., Guo, J., Delaney, J., and Boyle, W. J. J. (1998). Osteoprotegerin ligand is a cytokine that regulates osteoclast differentiation and activation. *Cell*, 93(2):165–176.
- Laib, A., Barou, O., Vico, L., Lafage-Proust, M. H., Alexandre, C., and Rügsegger, P. (2000). 3D micro-computed tomography of trabecular and cortical bone architecture with application to a rat model of immobilisation osteoporosis. *Medical and Biological Engineering and Computing*, 38:326–332.
- Langer, R. and Vacanti, J. P. (1993). Tissue engineering. *Science*, 260(5110):920–926.
- Lauffenburger, D. A. and Linderman, J. J. (1993). *Receptors – Models for Binding, Trafficking, and Signaling*. Oxford University Press, New York, USA.
- Lee, H. Y., Chan, L. W., Dolzhenko, A. V., and Heng, P. W. S. (2006). Influence of viscosity and uronic acid composition of alginates on the properties of alginate films and microspheres produced by emulsification. *Journal of Microencapsulation: Micro and Nano Carriers*, 23(8):912–927.
- Lees, S. (1982). Ultrasonic measurements of deer antler, bovine tibia and tympanic bulla. *Journal of Biomechanics*, 15(11):867–874.
- Lees, S. (1987). Considerations regarding the structure of the mammalian mineralized osteoid from viewpoint of the generalized packing model. *Connective Tissue Research*, 16(4):281–303.
- Lees, S., Ahern, J., and Leonard, M. (1983). Parameters influencing the sonic velocity in compact calcified tissues in various species. *Journal of the Acoustical Society of America*, 74(1):28–33.

- Lees, S., Hanson, D. B., and Page, E. A. (1996). Some acoustical properties of the otic bones of a fin whale. *Journal of the Acoustical Society of America*, 99(4):2421–2427.
- Lees, S., Heeley, J. D., and Cleary, P. F. (1979). A study of some properties of a sample of bovine cortical bone using ultrasound. *Calcified Tissue International*, 29(1):107–117.
- Lees, S., Prostack, K. S., Ingle, V. K., and Kjoller, K. (1994). The loci of mineral in turkey leg tendon as seen by atomic force microscope and electron microscopy. *Calcified Tissue International*, 55(3):180–189.
- Lees, S., Tao, N. J., and Lindsay, S. M. (1990). Studies of compact hard tissues and collagen by means of brillouin light scattering. *Connective Tissue Research*, 24(3-4):187–205.
- Lefebvre, L., Gremillard, L., Chevalier, J., Zenati, R., and Bernache-Assolant, D. (2008). Sintering behaviour of 45S5 bioactive glass. *Acta Biomaterialia*, 4(6):1894–1903.
- Lemaire, V., Tobin, F. L., Greller, L. D., Cho, C. R., and Suva, L. J. (2004). Modeling of the interactions between osteoblast and osteoclast activities in bone remodeling. *Journal of Theoretical Biology*, 229(3):293–309.
- Lewandrowski, K. U., Gresser, J. D., Wise, D. L., and Trantol, D. J. (2000). Biore-sorbable bone graft substitutes of different osteoconductivities: a histologic evaluation of osteointegration of poly(propylene glycol-co-fumaric acid)-based cement implants in rats. *Biomaterials*, 21(8):757–764.
- Li, W., Ding, Y., Rai, R., Roether, J. A., Schubert, D. W., and Boccaccini, A. R. (2014a). Preparation and characterization of PHBV microsphere/45S5 bioactive glass composite scaffolds with vancomycin releasing function. *Materials Science and Engineering C*, 41:320–328.
- Li, W., Noeaid, P., Roether, J. A., Schubert, D. W., and Boccaccini, A. R. (2014b). Preparation and characterization of vancomycin releasing PHBV coated 45S5 Bioglass[®]-based glass-ceramic scaffolds for bone tissue engineering. *Journal of the European Ceramic Society*, 34(2):505–514.
- Linde, F. and Hvid, I. (1989). The effect of constraint on the mechanical behaviour of trabecular bone specimens. *Journal of Biomechanics*, 22(5):485–490.

- Linde, F. and Sorensen, H. C. F. (1993). The effect of different storage methods on the mechanical properties of trabecular bone. *Journal of Biomechanics*, 26(10):1249–1252.
- Liu, D.-M. (1998). Preparation and characterisation of porous hydroxyapatite bioceramic via a slip-casting route. *Ceramics International*, 24(6):441–446.
- Locke, M. (2004). Structure of long bones in mammals. *Journal of Morphology*, 262(2):546–565.
- Lozano, D., Sánchez-Salcedo, S., Portal-Núñez, S., Vila, M., López-Herradón, A., Ardura, J. A., Mulero, F., Gómez-Barrena, E., Vallet-Regí, M., and Esbrit, P. (2014). Parathyroid hormone-related protein (107-111) improves the bone regeneration potential of gelatin-glutaraldehyde biopolymer-coated hydroxyapatite. *Acta Biomaterialia*, 10(7):3307–3316.
- Luczynski, K. W., Brynk, T., Ostrowska, B., Reihnsner, R., and Hellmich, C. (2013). Consistent quasi-static and acoustic elasticity determination of poly-L-lactide-based rapid-prototyped tissue engineering scaffolds. *Journal of Biomedical Materials Research Part A*, 101A(1):138–144.
- Luczynski, K. W., Steiger-Thirsfeld, A., Bernardi, J., Eberhardsteiner, J., and Hellmich, C. (2015). Extracellular bone matrix exhibits hardening elastoplasticity and more than double cortical strength: Evidence from homogeneous compression of non-tapered single micron-sized pillars welded to a rigid substrate. *Journal of the Mechanical Behavior of Biomedical Materials*, 52:51–62.
- Mader, K. S., Schneider, P., Müller, R., and Stampanoni, M. (2013). A quantitative framework for the 3D characterization of the osteocyte lacunar system. *Bone*, 57:142–154.
- Malandrino, A., Fritsch, A., Lahayne, O., Kropik, K., Redl, H., Noailly, J., Lacroix, D., and Hellmich, C. (2012). Anisotropic tissue elasticity in human lumbar vertebra, by means of a coupled ultrasound-micromechanics approach. *Materials Letters*, 78:154–158.
- Malasoma, A., Fritsch, A., Kohlhauser, C., Brynk, T., Vitale-Brovarone, C., Pakiela, Z., Eberhardsteiner, J., and Hellmich, C. (2008). Micromechanics of bioresorbable porous CEL2 glass ceramic scaffolds for bone tissue engineering. *Advances in Applied Ceramics*, 107(5):277–286.

- Manolagas, S. C. (2000). Birth and death of bone cells: Basic regulatory mechanisms and implications for the pathogenesis and treatment of osteoporosis. *Endocrine Reviews*, 21(2):115–137.
- Marotti, G., Favia, A., and Zambonin Zallone, Z. (1972). Quantitative analysis on the rate of secondary bone mineralization. *Calcified Tissue Research*, 10(1):67–81.
- Martin, E. and Shapiro, J. R. (2007). Osteogenesis imperfecta: Epidemiology and pathophysiology. *Current Osteoporosis Reports*, 5(3):91–97.
- Martin, R. B. (1984). Porosity and specific surface of bone. *Critical Reviews in Biomedical Engineering*, 10(3):179–222.
- Martin, R. B., Burr, D. B., and Sharkey, N. A. (1998). *Skeletal Tissue Mechanics*. Springer Science and Business Media, New York, USA.
- Martin, T. J. (2004). Paracrine regulation of osteoclast formation and activity: Milestones in discovery. *Journal of Musculoskeletal Neuronal Interactions*, 4(3):243–253.
- Meille, S. (2001). *Étude du comportement mécanique du plâtre pris en relation avec sa microstructure*. Ph.D. thesis, INSA de Lyon.
- Metz, L. N., Martin, R. B., and Turner, A. S. (2003). Histomorphometric analysis of the effects of osteocyte density on osteonal morphology and remodeling. *Bone*, 33(5):753–759.
- Meunier, P. J. and Boivin, G. (1997). Bone mineral density reflects bone mass but also the degree of mineralization of bone: therapeutic implications. *Bone*, 21(5):373–377.
- Meyer, A. (1987). Phenotypic plasticity and heterochrony in *Cichlasoma managuense* (Pisces, Cichlidae) and their implications for speciation in cichlid fishes. *Evolution*, 41:1357–1369.
- Mikić, B. and Carter, D. R. (1995). Bone strain gage data and theoretical models of functional adaptation. *Journal of Biomechanics*, 28(4):465–469.
- Miller, A. (1984). Collagen: the organic matrix of bone. *Philosophical Transactions of the Royal Society London B: Biological Sciences*, 304(1121):455–477.
- Miller, M., Bobko, C., Vandamme, M., and Ulm, F.-J. (2008). Surface roughness criteria for cement paste nanoindentation. *Cement and Concrete Research*, 38(4):467–476.

- Mohsin, S., O'Brien, F. J., and Lee, T. C. (2006). Osteonal crack barriers in ovine compact bone. *Journal of Anatomy*, 208(1):81–89.
- Moore, W. R., Graves, S. E., and Bain, G. I. (2001). Synthetic bone graft substitutes. *ANZ Journal of Surgery*, 71(6):354–361.
- Mori, T. and Tanaka, K. (1973). Average stress in matrix and average elastic energy of materials with misfitting inclusions. *Acta Metallurgica*, 21(5):571–574.
- Morin, C. and Hellmich, C. (2014). A multiscale poromicromechanical approach to wave propagation and attenuation in bone. *Ultrasonics*, 54(4):1251–1269.
- Mosley, J. R. and Lanyon, L. E. (1982). Strain rate as a controlling influence on adaptive modeling in response to dynamic loading of the ulna in growing male rats. *Bone*, 23(4):313–318.
- Mullender, M., El Haj, A. J., Yang, Y., van Duin, M. A., Burger, E. H., and Klein-Nulend, J. (2004). Mechanotransduction of bone cells in vitro: Mechanobiology of bone tissue. *Medical and Biological Engineering and Computing*, 42(1):14–21.
- Müllner, H. W., Fritsch, A., Kohlhauser, C., Reihnsner, R., Hellmich, C., Godlinski, D., Rota, A., Slesinski, R., and Eberhardsteiner, J. (2008). Acoustical and poromechanical characterisation of titanium scaffolds for biomedical applications. *Strain*, 44(2):153–163.
- Mundy, G. R., Boyce, B. F., Yoneda, T., Bonewald, L. F., and Roodman, G. D. (1996). Cytokines and bone remodeling. In Marcus, R., Feldman, D., and Kelsey, J., editors, *Osteoporosis*, pages 301–313. Academic Press, San Diego, CA.
- Muschick, M., Barluenga, M., Salzburger, W., and Meyer, A. (2011). Adaptive phenotypic plasticity in the Midas cichlid fish pharyngeal jaw and its relevance in adaptive radiation. *BMC Evolutionary Biology*, 11(116).
- Mwangi, J. W. and Ofner, C. M. (2004). Crosslinked gelatin matrices: release of a random coil macromolecular solute. *International Journal of Pharmaceutics*, 278(2):319–327.
- Nagatomi, J., Arulanandam, B. P., Metzger, D. W., Meunier, A., and Bizios, R. (2001). Frequency- and duration dependent effects of cyclic pressure on select bone cell functions. *Tissue Engineering*, 7(6):717–730.
- Nagatomi, J., Arulanandam, B. P., Metzger, D. W., Meunier, A., and Bizios, R. (2002). Effects of cyclic pressure on bone marrow cell cultures. *Journal of Biomechanical Engineering*, 124:308–314.

- Nagatomi, J., Arulanandam, B. P., Metzger, D. W., Meunier, A., and Bizios, R. (2003). Cyclic pressure affects osteoblast functions pertinent to osteogenesis. *Annals of Biomedical Engineering*, 31(8):917–923.
- Nakagawa, N., Kinoshita, M., Yamaguchi, K., Shima, N., Yasuda, H., Yano, K., Morinaga, T., and Higashio, K. (1998). RANK is the essential signaling receptor for osteoclast differentiation factor in osteoclastogenesis. *Biochemical and Biophysical Research Communications*, 253(2):395–400.
- Nakashima, T., Hayashi, M., Fukunaga, T., Kurata, K., Oh-hora, M., Feng, J. Q., Bonewald, L. F., Kodama, T., Wutz, A., Wagner, E. F., Penninger, J. M., and Takayanagi, H. (2011). Evidence for osteocyte regulation of bone homeostasis through RANKL expression. *Nature Medicine*, 17(10):1231–1234.
- Nazarian, A., Hermansson, B. J., Muller, J., Zurakowski, D., and Snyder, B. D. (2009). Effects of tissue preservation on murine bone mechanical properties. *Journal of Biomechanics*, 42(1):82–86.
- Nikander, R., Kannus, P., Rantalainen, T., Uusi-Rasi, K., Heinonen, A., and Sievänen, H. (2010). Cross-sectional geometry of weight-bearing tibia in female athletes subjected to different exercise loadings. *Osteoporosis International*, 21:1687–1694.
- Nix, W. D. and Gao, H. (1998). Indentation size effects in crystalline materials: A law for strain gradient plasticity. *Journal of the Mechanics and Physics of Solids*, 46(3):411–425.
- O’Brien, C. A., Nakashima, T., and Takayanagi, H. (2013). Osteocyte control of osteoclastogenesis. *Bone*, 54(2):258–263.
- O’Brien, F. J., Hardiman, D. A., Hazenberg, J. G., Mercy, M. V., Mohsin, S., Taylor, D., and Lee, C. (2005a). The behaviour of microcracks in compact bone. *European Journal of Morphology*, 42(1–2):71–79.
- O’Brien, F. J., Taylor, D., Dickson, G. R., and Lee, T. C. (2000). Visualisation of three-dimensional microcracks in compact bone. *Journal of Anatomy*, 197(3):413–420.
- O’Brien, F. J., Taylor, D., and Lee, T. C. (2005b). The effect of bone microstructure on the initiation and growth of microcracks. *Journal of Orthopaedic Research*, 23(2):475–480.

- Oliver, W. C. and Pharr, G. M. (1992). An improved technique for determining hardness and elastic modulus using load and displacement sensing indentation experiments. *Journal of Materials Research*, 7(6):1564–1583.
- Oyen, M. L. (2006). Nanoindentation hardness of mineralized tissues. *Journal of Biomechanics*, 39:2699–2702.
- Ozcivici, E., Luu, Y. K., Adler, B., Qin, Y.-X., Rubin, J., Judex, S., and Rubin, C. T. (2010). Mechanical signals as anabolic agents in bone. *Nature Reviews Rheumatology*, 6(1):50–59.
- Pabst, W., Gregorová, E., and Tichá, G. (2006). Elasticity of porous ceramics – a critical study of modulus-porosity relations. *Journal of the European Ceramic Society*, 26(7):1085–1097.
- Pabst, W., Gregorová, E., Tichá, G., and Týnová, E. (2004). Effective elastic properties of alumina-zirconia composite ceramics – Part 4. Tensile modulus of porous alumina and zirconia. *Ceramics-Silikáty*, 48(4):165–174.
- Peroglio, M., Gremillard, L., Chevalier, J., Chazeau, L., Gauthier, C., and Hamaide, T. (2007). Toughening of bio-ceramics scaffolds by polymer coating. *Journal of the European Ceramic Society*, 27:2679–2685.
- Phani, K. (1986). Young’s modulus-porosity relation in gypsum systems. *American Ceramic Society Bulletin*, 65:1584–1586.
- Pichler, B. and Hellmich, C. (2010). Estimation of influence tensors for eigenstressed multiphase elastic media with nonaligned inclusion phases of arbitrary ellipsoidal shape. *Journal of Engineering Mechanics (ASCE)*, 136(8):1043–1053.
- Pichler, B., Hellmich, C., and Eberhardsteiner, J. (2009). Spherical and acicular representation of hydrates in a micromechanical model for cement paste: Prediction of early-age elasticity and strength. *Acta Mechanica*, 203(3–4):137–162.
- Pitsillides, A. A., Rawlinson, S. C. F., Suswillo, R. F. L., Bourrin, S., Zaman, G., and Lanyon, L. E. (1995). Mechanical strain-induced NO production by bone cells: A possible role in adaptive bone (re)modeling? *FASEB Journal*, 9(15):1614–1622.
- Pivonka, P., Buenzli, P. R., and Dunstan, C. R. (2012). A systems approach to understanding bone cell interactions in health and disease. In Sivakumar, G., editor, *Cell Interaction*, pages 169–204. InTech Publishers, Rijeka, Croatia.

- Pivonka, P., Zimak, J., Smith, D. W., Gardiner, B. S., Dunstan, C. R., Sims, N. A., Martin, T. J., and Mundy, G. R. (2008). Model structure and control of bone remodeling: A theoretical study. *Bone*, 43(2):249–263.
- Pivonka, P., Zimak, J., Smith, D. W., Gardiner, B. S., Dunstan, C. R., Sims, N. A., Martin, T. J., and Mundy, G. R. (2010). Theoretical investigation of the role of the RANK-RANKL-OPG system in bone remodeling. *Journal of Theoretical Biology*, 262(2):306–316.
- Portigliatti Barbos, M., Bianco, P., and Ascenzi, A. (1983). Distribution of osteonic and interstitial components in the human femoral shaft with reference to structure, calcification and mechanical properties. *Acta Anatomica*, 115(2):178–186.
- Prostak, K. S. and Lees, S. (1996). Visualization of crystal-matrix structure. In situ demineralization of mineralized turkey leg tendon and bone. *Calcified Tissue International*, 59(6):474–479.
- Ramaniraka, N. A., Rakotomanana, L. R., and Leyvraz, P.-F. (2000). The fixation of the cemented femoral component. Effects of stem stiffness, cement thickness and roughness of the cement-bone surface. *Journal of Bone and Joint Surgery*, 82-B:297–303.
- Ramaswamy, Y., Wu, C., Van Hummel, A., Combes, V., Grau, G., and Zreiqat, H. (2008). The responses of osteoblasts, osteoclasts and endothelial cells to zirconium modified calcium-silicate-based ceramic. *Biomaterials*, 29(33):4392–4402.
- Reilly, D. T. and Burstein, A. H. (1975). The elastic and ultimate properties of compact bone tissue. *Journal of Biomechanics*, 8:393–405.
- Reilly, G. C., Knapp, H. F., Stemmer, A., Niederer, P., and Knothe Tate, M. L. (2001). Investigation of the morphology of the lacunocanalicular system of cortical bone using atomic force microscopy. *Annals of Biomedical Engineering*, 29(12):1074–1081.
- Reisinger, A. G., Pahr, D. H., and Zysset, P. K. (2011). Principal stiffness orientation and degree of anisotropy of human osteons based on nanoindentation in three distinct planes. *Journal of the Mechanical Behavior of Biomedical Materials*, 4(8):2113–2127.
- Reynaud, C., Thévenot, F., Chartier, T., and Besson, J.-L. (2005). Mechanical properties and mechanical behaviour of SiC dense-porous laminates. *Journal of the European Ceramic Society*, 25(5):589–597.

- Rezwan, K., Chen, Q. Z., Blaker, J. J., and Boccaccini, A. R. (2006). Biodegradable and bioactive porous polymer/inorganic composite scaffolds for bone tissue engineering. *Biomaterials*, 27(18):3413–3431.
- Rho, J. Y. (1996). An ultrasonic method for measuring the elastic properties of human tibial cortical and cancellous bone. *Ultrasonics*, 34:777–783.
- Rho, J. Y., Kuhn-Spearing, L., and Zioupos, P. (1998). Mechanical properties and the hierarchical structure of bone. *Medical Engineering & Physics*, 20:92–102.
- Rho, J. Y., Roy, M. E., Tsui, T. Y., and Pharr, G. M. (1999). Elastic properties of microstructural components of human bone tissue as measured by nanoindentation. *Journal of Biomedical Materials Research*, 45:48–54.
- Rho, J. Y., Tsui, T. Y., and Pharr, G. M. (1997). Elastic properties of human cortical and trabecular lamellar bone measured by nanoindentation. *Biomaterials*, 18(20):1325–1330.
- Rho, J. Y., Zioupos, P., Currey, J. D., and Pharr, G. M. (2002). Microstructural elasticity and regional heterogeneity in human femoral bone of various ages examined by nano-indentation. *Journal of Biomechanics*, 35:189–198.
- Riggs, B. L., Wahner, W., Seeman, E., Offord, K. P., Dunn, W. L., Mazess, R. B., Johnson, K. A., and Melton III, L. J. (1982). Changes in bone mineral density of the proximal femur and spine with aging. Differences between the postmenopausal and senile osteoporosis syndromes. *Journal of Clinical Investigations*, 70(4):716–723.
- Riggs, C. M., Lanyon, L. E., and Boyde, A. (1993). Associations between collagen fibre orientation and locomotor strain direction in cortical bone of the equine radius. *Anatomy and Embryology*, 187(3):231–238.
- Ritchie, R. O. (2011). The conflicts between strength and toughness. *Nature Materials*, 10:817–822.
- Robling, A. G., Castillo, A., and Turner, C. H. (2006). Biomechanical and molecular regulation of bone remodeling. *Annual Review of Biomedical Engineering*, 8:455–498.
- Robling, A. G., Hinant, F. M., Burr, D. B., and Turner, C. H. (2002). Improved bone structure and strength after long-term mechanical loading is greatest if loading is separated into short bouts. *Journal of Bone and Mineral Research*, 17(8):1545–1554.

- Robling, A. G., Niziolek, P. J., Baldrige, L. A., Condon, K. W., Allen, M. R., Alam, I., Mantila, S. M., Gluhak-Heinrich, J., Bellido, T. M., Harris, S. E., and Turner, C. H. (2008). Mechanical stimulation of bone *in vivo* reduces osteocyte expression of Sost/sclerostin. *Journal of Biological Chemistry*, 283(9):5866–5875.
- Rohlmann, A., Zilch, H., Bergmann, G., and Kolbel, R. (1980). Material properties of femoral cancellous bone in axial loading – Part I: Time independent properties. *Archives of Orthopaedic and Traumatic Surgery*, 97(2):95–102.
- Roodman, G. D. (1999). Cell biology of the osteoclast. *Experimental Hematology*, 27(8):1229–1241.
- Roohani-Esfahani, S. I., Dunstan, C. R., Davies, B., Pearce, S., Williams, R., and Zreiqat, H. (2012). Repairing a critical-sized bone defect with highly porous modified and unmodified baghdadite scaffolds. *Acta Biomaterialia*, 8(11):4162–4172.
- Rubin, C. T. and Lanyon, L. E. (1984). Regulation of bone formation by applied dynamic loads. *Journal of Bone and Joint Surgery. American Volume.*, 66(3):397–402.
- Rubin, C. T. and Lanyon, L. E. (1985). Regulation of bone mass by mechanical strain magnitude. *Calcified Tissue International*, 37(4):411–417.
- Rubin, C. T. and McLeod, K. J. (1994). Promotion of bony ingrowth by frequency-specific, low-amplitude mechanical strain. *Clinical Orthopaedics and Related Research*, 298:165–174.
- Rubin, C. T., Turner, A. S., Bain, S., Mallinckrodt, C., and McLeod, K. (2001). Anabolism: Low mechanical signals strengthen long bones. *Nature*, 412:603–604.
- Rubin, C. T., Turner, A. S., Mallinckrodt, C., Jerome, C., McLeod, K., and Bain, S. (2002a). Mechanical strain, induced noninvasively in the high-frequency domain, is anabolic to cancellous bone, but not cortical bone. *Bone*, 30(3):445–452.
- Rubin, C. T., Turner, A. S., Müller, R., Mittra, E., McLeod, K., Lin, W., and Qin, Y.-X. (2002b). Quantity and quality of trabecular bone in the femur are enhanced by a strongly anabolic, noninvasive mechanical intervention. *Journal of Bone and Mineral Research*, 17(2):349–357.
- Ruffoni, D., Fratzl, P., Roschger, P., Klaushofer, K., and Weinkamer, R. (2007). The bone mineralization density distribution as a fingerprint of the mineralization process. *Bone*, 40(5):1308–1319.

- Ruffoni, D., Fratzl, P., Roschger, P., Phipps, R., Klaushofer, K., and Weinkamer, R. (2008). Effect of temporal changes in bone turnover on the bone mineralization density distribution: A computer simulation study. *Journal of Bone and Mineral Research*, 23(12):1905–1914.
- Ryan, G., Pandit, A., and Apatsidis, D. P. (2006). Fabrication methods of porous metals for use in orthopaedic applications. *Biomaterials*, 27(13):2651–2670.
- Salençon, J. (2001). *Handbook of Continuum Mechanics*. Springer Verlag, Berlin.
- Salsac, A. V., Zhang, L., and Gherbezza, J. M. (2009). Measurement of mechanical properties of alginate beads using ultrasound. *Proceedings of the 19ème Congrès Français de Mécanique, Marseille, France*.
- Sanahuja, J., Dormieux, L., Meille, S., Hellmich, C., and Fritsch, A. (2010). Micromechanical explanation of elasticity and strength of gypsum: From elongated anisotropic crystals to isotropic porous polycrystals. *Journal of Engineering Mechanics*, 136(2):239–253.
- Sawamoto, H., Weidner, D. J., Sasaki, S., and Kumazawa, M. (1984). Single-crystal elastic properties of the modified spinel (beta) phase of magnesium orthosilicate. *Science*, 224(4650):749–751.
- Schaffler, M. B., Choi, K., and Milgrom, C. (1995). Aging and matrix microdamage accumulation in human compact bone. *Bone*, 17(6):521–525.
- Schaffler, M. B., Pitchford, W., Choi, K., and Riddle, J. M. (1994). Examination of compact bone microdamage using back-scattered electron microscopy. *Bone*, 15(5):483–488.
- Scheiner, S., Pivonka, P., and Hellmich, C. (2013). Coupling systems biology with multiscale mechanics, for computer simulations of bone remodeling. *Computer Methods in Applied Mechanics and Engineering*, 254:181–196.
- Scheiner, S., Pivonka, P., and Hellmich, C. (2016). Poromicromechanics reveals that physiological bone strains induce osteocyte-stimulating lacunar pressure. *Biomechanics and Modeling in Mechanobiology*, 15(1):9–28.
- Scheiner, S., Pivonka, P., Smith, D. W., Dunstan, C. R., and Hellmich, C. (2014). Mathematical modeling of postmenopausal osteoporosis and its treatment by the anti-catabolic drug denosumab. *International Journal for Numerical Methods in Biomedical Engineering*, 30(1):1–27.

- Scheiner, S., Sinibaldi, R., Pichler, B., Komlev, V., Renghini, C., Vitale-Brovarone, C., Rustichelli, F., and Hellmich, C. (2009). Micromechanics of bone tissue-engineering scaffolds, based on resolution error-cleared computer tomography. *Bio-materials*, 30(12):2411–2419.
- Schuhmacher, T. C., Volkmann, E., Yilmaz, R., Wolf, A., Treccani, L., and Rezwani, K. (2014). Mechanical evaluation of calcium-zirconium-silicate (baghdadite) obtained by a direct solid-state synthesis route. *Journal of the Mechanical Behavior of Biomedical Materials*, 34:294–301.
- Schulte, F. A., Ruffoni, D., Lambers, F. M., Christen, D., Webster, D. J., Kuhn, G., and Müller, R. (2013). Local mechanical stimuli regulate bone formation and resorption in mice at the tissue level. *PloS One*, 8(4):e62172.
- Schwiedrzik, J., Raghavan, R., Bürki, A., LeNader, V., Wolfram, U., Michler, J., and Zysset, P. K. (2014). *In situ* micropillar compression of lamellar bone reveals superior strength and ductility but no damage. *Nature Materials*, 13:740–747.
- Shahar, R. and Dean, M. N. (2013). The enigmas of bone without osteocytes. *BoneKEy Reports*, 2(434).
- Sietsema, W. K. (1995). Animal models of cortical porosity. *Bone*, 17(4):297S–305S.
- Silva, I. and Branco, J. C. (2011). RANK/RANKL/OPG: Literature review. *Acta Reumatologica Portuguesa*, 36:209–218.
- Simmons, E. D., Pritzker, K. P. H., and Grynblas, M. D. (1991). Age-related changes in the human femoral cortex. *Journal of Orthopaedic Research*, 9:155–167.
- Simonet, W. S., Lacey, D. L., Dunstan, C. R., Kelley, M., Chang, M. S., Lüthy, R., Nguyen, H. Q., Wooden, S., Bennett, L., Boone, T., Shimamoto, G., DeRose, M., Elliott, R., Colombero, A., Tan, H. L., Trail, G., Sullivan, J., Davy, E., Bucay, N., Renshaw-Gegg, L., Hughes, T. M., Hill, D., Pattison, W., Campbell, P., Sander, S., Van, G., Tarpley, J., Derby, P., Lee, R., and Boyle, W. J. (1997). Osteoprotegerin: a novel secreted protein involved in the regulation of bone density. *Cell*, 89(2):309–319.
- Skardal, A., Mack, D., Atala, A., and Soker, S. (2013). Substrate elasticity controls cell proliferation, surface marker expression and motile phenotype in amniotic fluid-derived stem cells. *Journal of the Mechanical Behavior of Biomedical Materials*, 17:307–316.

- Skerry, T. M. and Lanyon, L. E. (1995). Interruption of disuse by short duration walking exercise does not prevent bone loss in the sheep calcaneus. *Bone*, 16(2):269–274.
- Srivastava, A. K., Pyare, R., and Singh, S. P. (2012). Elastic properties of substituted 45S5 bioactive glasses and glass-ceramics. *International Journal of Scientific and Engineering Research*, 3(2):207–220.
- Sugiyama, T., Meakin, L. B., Browne, W. J., Galea, G. L., Price, J. S., and Lanyon, L. E. (2012). Bones' adaptive response to mechanical loading is essentially linear between the low strains associated with disuse and the high strains associated with the lamellar/woven bone transition. *Journal of Bone and Mineral Research*, 27(8):1784–1793.
- Suquet, P. M. (1997). *Continuum Micromechanics*, volume 377 of *CISM Courses and Lectures*. Springer Verlag, Wien, New York.
- Tai, K., Pelled, G., Sheyn, D., Bershteyn, A., Han, L., Kallai, I., Zilberman, Y., Ortiz, C., and Gazit, D. (2008). Nanobiomechanics of repair bone regenerated by genetically modified mesenchymal stem cells. *Tissue Engineering Part A*, 14(10):1709–1720.
- Tai, K., Ulm, F.-J., and Ortiz, C. (2006). Nanogranular origins of the strength of bone. *Nano Letters*, 6(11):2520–2525.
- Tatsumi, S., Ishii, K., Amizuka, N., Li, M., Kobayashi, T., Kohno, K., Ito, M., Takeshita, S., and Ikeda, K. (2007). Targeted ablation of osteocytes induces osteoporosis with defective mechanotransduction. *Cell Metabolism*, 5(6):464–475.
- Tazawa, E. (1998). Effect of self stress on flexural strength of gypsum-polymer composites. *Advanced Cement Based Materials*, 7(1):1–7.
- Thelen, S., Barthelat, F., and Brinson, L. C. (2004). Mechanics considerations for microporous titanium as an orthopedic implant material. *Journal of Biomedical Materials Research Part A*, 69A(4):601–610.
- Theoleyre, S., Wittrant, Y., Tat, S. K., Fortun, Y., Redini, F., and Heymann, D. (2004). The molecular triad OPG/RANK/RANKL: involvement in the orchestration of pathophysiological bone remodeling. *Cytokine & Growth Factor Reviews*, 15(6):457–475.
- Thomas, C. D. L., Feik, S. A., and Clement, J. G. (2005). Regional variation of intracortical porosity in the midshaft of the human femur: Age and sex differences. *Journal of Anatomy*, 206(2):219–230.

- Thomas, C. D. L., Feik, S. A., and Clement, J. G. (2006). Increase in pore area, and not pore density, is the main determinant in the development of porosity in human cortical bone. *Journal of Anatomy*, 209(2):219–230.
- Turner, C. H. (1998). Three rules for bone adaptation to mechanical stimuli. *Bone*, 23(5):399–407.
- Turner, C. H. and Akhter, M. P. (1999). The mechanics of bone adaptation. In *Mechanical Loading of Bones and Joints*. Springer Verlag, Tokyo, Japan.
- Turner, C. H. and Burr, D. B. (1993). Basic biomechanical measurements of bone: A tutorial. *Bone*, 14:595–608.
- Turner, C. H., Forwood, M. R., and Otter, M. W. (1994a). Mechanotransduction in bone: do bone cells act as sensors of fluid flow? *FASEB Journal*, 8:875–878.
- Turner, C. H., Forwood, M. R., Rho, J. Y., and Yoshikawa, T. (1994b). Mechanical loading thresholds for lamellar and woven bone formation. *Journal of Bone and Mineral Research*, 9(1):87–97.
- Turner, C. H., Owan, I., and Takano, Y. (1995). Mechanotransduction in bone: role of strain rate. *American Journal of Physiology*, 269(3 Pt 1):E438–442.
- Turner, C. H., Rho, J. Y., Takano, Y., Tsui, T. Y., and Pharr, G. M. (1999). The elastic properties of cortical and trabecular bone tissues are similar: results from two microscopic measurement techniques. *Journal of Biomechanics*, 32(4):437–441.
- Ueland, T., Yndestad, A., Øie, E., Florholmen, G., Halvorsen, B., Frøland, S. S., Simonsen, S., Christensen, G., Gullestad, L., and Aukrust, P. I. (2005). Dys-regulated osteoprotegerin/RANK ligand/RANK axis in clinical and experimental heart failure. *Circulation*, 111(19):2461–2468.
- Ulm, F.-J., Vandamme, M., Bobko, C., Alberto Ortega, J., Tai, K., and Ortiz, C. (2007). Statistical indentation techniques for hydrated nanocomposites: Concrete, bone, and shale. *Journal of the American Ceramic Society*, 90(9):2677–2692.
- Umemura, Y., Ishiko, T., Yamauchi, T., Kurono, M., and Mashiko, S. (1997). Five jumps per day increase bone mass and breaking force in rats. *Journal of Bone and Mineral Research*, 12(9):1480–1485.
- Urist, M. R., DeLange, R. J., and Finerman, G. A. M. (1983). Bone cell differentiation and growth factors. *Science*, 220(4598):680–686.

- Van Buskirk, W. C., Cowin, S. C., and Ward, R. N. (1981). Ultrasonic measurement of orthotropic elastic constants of bovine femoral bone. *Journal of Biomechanical Engineering*, 103(2):67–72.
- van Rietbergen, B., Huiskes, R., Weinans, H., Sumner, D. R., Turner, T. M., and Galante, J. O. (1993). The mechanism of bone remodeling and resorption around press-fitted THA stems. *Journal of Biomechanics*, 26(4–5):369–382.
- van Rietbergen, B., Weinans, H., Huiskes, R., and Odgaard, A. (1995). A new method to determine trabecular bone elastic properties and loading using micromechanical finite-element models. *Journal of Biomechanics*, 28(1):69–81.
- Vandamme, M. and Ulm, F.-J. (2009). Nanogranular origin of concrete creep. *Proceedings of the National Academy of Sciences*, 106(26):10552–10557.
- Vergne, L., Meunier, A., Adolphe, M., and Sedel, L. (1996). A new apparatus for studying the effect of hydrostatic pressure on cells in culture. *Cytotechnology*, 21(1):21–30.
- Vico, L. and Alexandre, C. (1992). Microgravity and bone adaption at the tissue level. *Journal of Bone and Mineral Research*, 7(S2):445–447.
- Vico, L., Collet, P., Guignandon, A., Lafage-Proust, M. H., Thomas, T., Rehalia, M., and Alexandre, C. (2000). Effects of long-term microgravity exposure on cancellous and cortical weight-bearing bones of cosmonauts. *The Lancet*, 355(9215):1607–1611.
- Vose, G. P. and Kubala, A. L. (1959). Bone strength – its relationship to z-ray determined ash content. *Human Biology*, 31:261–270.
- Vuola, J., Taurio, R., Göransson, H., and Asko-Seljavaara, S. (1998). Compressive strength of calcium carbonate and hydroxyapatite implants after bone-marrow-induced osteogenesis. *Biomaterials*, 19:223–227.
- Vuong, J. and Hellmich, C. (2011). Bone fibrillogenesis and mineralization: Quantitative analysis and implications for tissue elasticity. *Journal of Theoretical Biology*, 287:115–130.
- Wang, F.-S., Wang, C.-J., Chen, Y.-J., Huang, Y.-T., Huang, H.-C., Chang, P.-R., Sun, Y.-C., and Yang, K. D. (2004). Nitric oxide donor increases osteoprotegerin production and osteoclastogenesis inhibitory activity in bone marrow stromal cells from ovariectomized rats. *Endocrinology*, 145(5):2148–2156.

- Wang, X. and Ni, Q. (2003). Determination of cortical bone porosity and pore size distribution using a low field pulsed NMR approach. *Journal of Orthopaedic Research*, 21(2):312–319.
- Wang, Y., Pivonka, P., Buenzli, P. R., Smith, D. W., and Dunstan, C. R. (2011). Computational modeling of interactions between multiple myeloma and the bone microenvironment. *PloS One*, 6(11):e27494.
- Weicker, K. (2007). *Evolutionäre Algorithmen*. Vieweg & Teubner Verlag, Wiesbaden, Germany.
- Weiner, S., Arad, T., Sabanay, I., and Traub, W. (1997). Rotated plywood structure of primary lamellar bone in the rat: Orientation of the collagen fibril arrays. *Bone*, 20:509–514.
- Weiner, S. and Wagner, H. D. (1998). The material bone: Structure-mechanical function relations. *Annual Review of Materials Science*, 28(1):271–298.
- Weiss, R. E. and Watabe, N. (1979). Studies on the biology of fish bone. III. Ultrastructure of osteogenesis and resorption in osteocytic (cellular) and anosteocytic (acellular) bones. *Calcified Tissue International*, 28(1):43–46.
- Wenzel, T. E., Schaffler, B. A., and Fyhrie, D. P. (1996). *In vivo* trabecular microcracks in human vertebral bone. *Bone*, 19(2):89–95.
- Westendorf, J. J., Kahler, R. A., and Schroeder, T. M. (2004). Wnt signaling in osteoblasts and bone diseases. *Gene*, 341:19–39.
- Willems, N., Mulder, L., Bank, R. A., Grunheid, T., de Toonder, J. M. J., Zentner, A., and Langenbach, G. E. J. (2011). Determination of the relationship between collagen cross-links and the bone-tissue stiffness in the porcine mandibular condyle. *Journal of Biomechanics*, 44:1132–1136.
- Witten, P. E. and Huysseune, A. (2010). The unobtrusive majority: mononucleated bone resorbing cells in teleost fish and mammals. *Journal of Applied Ichthyology*, 26:225–229.
- Wolff, J. (1892). *Das Gesetz der Transformation der Knochen [Law of the Transformation of Bone]*. Hirschwald, Berlin, Germany.
- Wolfram, U., Wilke, H. J., and Zysset, P. K. (2010). Rehydration of vertebral trabecular bone: influences on its anisotropy, its stiffness and the indentation work with a view to age, gender and vertebral level. *Bone*, 46(2):348–354.

- Wong, S. Y., Evans, R. A., Needs, C., Dunstan, C. R., Hills, E., and Garvan, J. (1987). The pathogenesis of osteoarthritis of the hip. Evidence for primary osteocyte death. *Clinical Orthopaedics and Related Research*, 214:305—312.
- Yao, C.-H., Liu, B.-S., Chang, C.-J., Hsu, S.-H., and Chen, Y.-S. (2004). Preparation of networks of gelatin and genipin as degradable biomaterials. *Materials Chemistry and Physics*, 83(2–3):204—208.
- Yao, Q., Noeaid, P., Detsch, R., Roether, J. A., Dong, Y., Goudouri, O.-M., Schubert, D. W., and Boccaccini, A. R. (2014). Bioglass[®]/chitosan-polycaprolactone bilayered composite scaffolds intended for osteochondral tissue engineering. *Journal of Biomedical Materials Research Part A*, 102(12):4510–4518.
- Yeung, T., Georges, P. C., Flanagan, L. A., Marg, B., Ortiz, M., Funaki, M., Zahir, N., Ming, W., Weaver, V., and Janmey, P. A. (2005). Effects of substrate stiffness on cell morphology, cytoskeletal structure, and adhesion. *Cell Motility and Cytoskeleton*, 60(1):24–34.
- Yoon, H. S. and Katz, J. L. (1976a). Ultrasonic wave propagation in human cortical bone—I. Theoretical considerations for hexagonal symmetry. *Journal of Biomechanics*, 9:407–464.
- Yoon, H. S. and Katz, J. L. (1976b). Ultrasonic wave propagation in human cortical bone—II. Measurements of elastic properties and microhardness. *Journal of Biomechanics*, 9:459–464.
- Yunos, D. N., Bretcanu, O., and Boccaccini, A. R. (2008). Polymer-bioceramic composites for tissue engineering scaffolds. *Journal of Materials Science*, 43:4433–4442.
- Zaoui, A. (1997). Structural morphology and constitutive behavior of microheterogeneous materials. In Suquet, P. M., editor, *Continuum Micromechanics*, chapter 6, pages 291–347. Springer Verlag, Wien, New York.
- Zaoui, A. (2002). Continuum micromechanics: Survey. *Journal of Engineering Mechanics (ASCE)*, 128(8):808–816.
- Zhou, J., Fang, T., Wang, Y., and Dong, J. (2012). The controlled release of vancomycin in gelatin/ β -TCP composite scaffolds. *Journal of Biomedical Materials Research Part A*, 100 A(9):2295–2301.
- Zysset, P. K., Guo, X. E., Hoffler, E., Moore, K. E., and Goldstein, S. A. (1999). Elastic modulus and hardness of cortical and trabecular bone measured by nanoindentation in the human femur. *Journal of Biomechanics*, 32:1005–1012.

Appendix

Appendix A: Matlab code for simulation of bone remodeling

This chapter gives a selection of computer codes written in Matlab programming language, which are related to the developments described in Chapter 2. The code, initially conceived by Stefan Scheiner, was adapted, modified and certain computational aspects were improved by the author of this thesis.

```
%% disuse_overuse_simulation.m: MAIN SCRIPT
% simulations for mouse & rat
```

```
clear all
close all
clc
delete *.dat
format long
tic
```

```
%%%%%%%%%%%%%%%%%%%%%%%%%%%%%%%%%%%%%%%%
% INPUT OF MODEL PARAMETERS %
%%%%%%%%%%%%%%%%%%%%%%%%%%%%%%%%%%%%%%%%
```

```
parameter_definition
```

```
%%%%%%%%%%%%%%%%%%%%%%%%%%%%%%%%%%%%%%%%
% SET GLOBAL VARIABLES %
%%%%%%%%%%%%%%%%%%%%%%%%%%%%%%%%%%%%%%%%
```

```
global steadystate
steadystate.BV = 0;
global fvas0...
    fvas_0...
    fbm_0...
    k...
    pvas0...
    plac0...
    OCY_exvas...
    Epeak;
```

```

%%%%%%%%%%%%%%%%%%%%%%%%%%%%%%%%%%%%%%%%%%%%%%%%%%%%%%%%%%%%%%%%%%%%%%%%
% Sugiyama's E_peak (mouse)%
%%%%%%%%%%%%%%%%%%%%%%%%%%%%%%%%%%%%%%%%%%%%%%%%%%%%%%%%%%%%%%%%%%%%%%%%

% 0: disuse, E_peak = 0 uE, BTV = -45.607%
% 300: disuse, E_peak = 300 uE, BTV = -32.653%
% 700: disuse, E_peak = 700 uE, BTV = -15.377%
% 1100: overuse, E_peak = 1100 uE, BTV = +1.899%
% 1400: overuse, E_peak = 1400 uE, BTV = +14.856%
% 1800: overuse, E_peak = 1800 uE, BTV = +32.132%
% 2200: overuse, E_peak = 2200 uE, BTV = +49.408%
% 2600: overuse, E_peak = 2600 uE, BTV = +66.684%
% 1056: steady-state, E_peak = 1056 uE, BTV = 0%

% 1: disuse, Laib (rat)

Epeak = 1;

% Osteocyte concentration
OCY_exvas = 5.9283e-2;
%OCY_exvas = 0; % to simulate no OCYs

% Define mechanics for OBp proliferation
global MECH %initial values
MECH.Pi_strain_steady = 0.155; % \hat{\pi}
MECH.ProfRate_calc = 1;
MECH.DOBu_frac = 0.1; % a_{OBp}
MECH.calibration = 1;

% Parameter storage variable
global ParameterWrite
ParameterWrite = 0; % not storing parameters at steady-state

%%%%%%%%%%%%%%%%%%%%%%%%%%%%%%%%%%%%%%%%%%%%%%%%%%%%%%%%%%%%%%%%%%%%%%%%
% SOLVE STEADY-STATE %
%%%%%%%%%%%%%%%%%%%%%%%%%%%%%%%%%%%%%%%%%%%%%%%%%%%%%%%%%%%%%%%%%%%%%%%%

% Initial, vascular concentrations (OBp, OBa, OCp, OCa); fvas0 = 0.05
cells_0 = [6.196390627918603e-004/fvas0, 5.583931899482344e-004/fvas0,...
          1.861904761904762e+000/(10*fvas0), 8.069635262731931e-004/fvas0];

% Due to non-linearity of the system, the re-calibration to vascular
% spaces requires to use:
% fvas0 = 0.05; 0.6; 0.7 -> 10*fvas0
% fvas0 = 0.2; 0.25; 0.8 -> 5*fvas0
% fvas0 = 0.1; 0.9 -> 3*fvas0
% fvas0 = 0.5; 0.4; 1 -> 1*fvas0

% fsolve-options optimization structure
options = optimset('TolFun',1e-14,'TolX',1e-14);

% Solve non-linear eq. system
cells_t0 = fsolve(@function_steadystate,cells_0,options);

% Cells at steady state, after solving

```

```

steadystate.OBp = cells_t0(1);    steadystate.OBa = cells_t0(2);
steadystate.OCP = cells_t0(3);    steadystate.OCa = cells_t0(4);

    % Resulting vascular concentrations (upscaling to macro by
    % multiplication with fvas0)
    % steadystate.OBp = 0.02;
    % steadystate.OBa = 0.01;
    % steadystate.OCP = 0.02;
    % steadystate.OCa = 0.002;

% Bone formation factor, k.res is defined in parameter_definition.m
k.form = k.res * steadystate.OCa / steadystate.OBa;

% Steady-state concentrations + fvas_0 = initial conditions for dynamics
x_t0 = [steadystate.OBp, steadystate.OBa, steadystate.OCP,...
        steadystate.OCa, fvas_0];

%return % if return here, obtain only solution of function_steadystate

%%%%%%%%%%%%%%%%%%%%%%%%%%%%%%%%%%%%%%%%%%%%%%%%%%%%%%%%%%%%%%%%%%%%%%%%
% DYNAMIC CALCULATION %
%%%%%%%%%%%%%%%%%%%%%%%%%%%%%%%%%%%%%%%%%%%%%%%%%%%%%%%%%%%%%%%%%%%%%%%%

% MaxStep = upper bound on solver step size
timestep = 1;

% Initial and end time of simulation
t_ini = 0;
t_end = 66;

% Define error tolerance (Rel Tol, AbsTol) for options of the solver
% -> they also have default values so it's not mandatory
error = 1e-6;

% Adjust the integration parameters of ODE solver
options = odeset('RelTol',error,'AbsTol',error,'MaxStep',timestep);

% Solve (stiff) differential equations (fct, integration interval, initial
% conditions, above options)
[timeVector,CellsVector] = ode15s('function_dynamics',...
    [t_ini t_end],x_t0,options);

% While solving, store all parameters in ParameterVector at each time point
% (see output of function_dynamics for a list of paramters)
ParameterWrite = 1;

for i=1:length(timeVector)
    ParameterVector(i,:) = function_dynamics(timeVector(i,1),...
        CellsVector(i,:));
    % Calculate change in BV/TV (=fbm = 1-fvas) to compare with experiments
    BVTV(i)=(1-CellsVector(i,5)-fbm_0)/fbm_0*100;
end

% Save the different workspaces (Sugiyama and Laib)

```

```

if Epeak == 0
    save S_disuse_0-45p607
elseif Epeak == 300
    save S_disuse_300-32p653
elseif Epeak == 700
    save S_disuse_700-15p377
elseif Epeak == 1100
    save S_overuse_1100_1p899
elseif Epeak == 1400
    save S_overuse_1400_14p856
elseif Epeak == 1800
    save S_overuse_1800_32p132
elseif Epeak == 2200
    save S_overuse_2200_49p408
elseif Epeak == 2600
    save S_overuse_2600_66p648
elseif Epeak == 1056
    save S_normal_simulation
elseif Epeak == 1;
    save Laib_simulation_mouse
end

%% Plot evolution of BV/TV (Laib): with bar plots
t_L = [6; 16];
BTVV_L = [0.17 0.09];
load Laib_simulation_mouse
BTVV_mod = [1-CellsVector(5604,5) 1-CellsVector(6603,5)];
B_all = [BTVV_L(1) BTVV_mod(1); BTVV_L(2) BTVV_mod(2)];
b=bar(t_L,B_all,1);
grid on
b(1).FaceColor = 'blue';
b(2).FaceColor = 'red';
legend('Laib et al. (2000): unloaded rat hindlimb tibia',...
    'Model simulation results: rat disuse')
set(legend,'FontSize',16,'FontName','Times New Roman','Location',...
    'northwest')
set(legend,'interpreter','latex')
legend boxoff
axis([0 22 0 0.24])
ax = gca;
ax.GridLineStyle = ':';
set(get(gcf,'CurrentAxes'),'FontName','Times New Roman','FontSize',22)
xlabel('$t$, [d]', 'FontSize',24,'FontName','Times New Roman',...
    'interpreter','latex')
ylabel('$f_{\mathrm{bm}}$', 'FontSize',24,'FontName','Times New Roman',...
    'interpreter','latex')

%% Plot evolution of (\Delta)BV/TV with each load case (Sugiyama)
hold on
load S_disuse_0-45p607
plot(timeVector-50,BTVV,'r—','LineWidth',3)
load S_disuse_300-32p653
plot(timeVector-50,BTVV,'b—','LineWidth',3)
load S_disuse_700-15p377
plot(timeVector-50,BTVV,'g—','LineWidth',3)

```

```

load S_normal_simulation
plot(timeVector-50,BTVV,'k-','LineWidth',3)
load S_overuse_1100_1p899
plot(timeVector-50,BTVV,'r-','LineWidth',3)
load S_overuse_1400_14p856
plot(timeVector-50,BTVV,'b-','LineWidth',3)
load S_overuse_1800_32p132
plot(timeVector-50,BTVV,'g-','LineWidth',3)
load S_overuse_2200_49p408
plot(timeVector-50,BTVV,'y-','LineWidth',3)
load S_overuse_2600_66p648
plot(timeVector-50,BTVV,'m-','LineWidth',3)
legend('disuse: $E^{\mathrm{peak}} = 0 \ \mu\epsilon$',...
      'disuse: $E^{\mathrm{peak}} = -300 \ \mu\epsilon$',...
      'disuse: $E^{\mathrm{peak}} = -700 \ \mu\epsilon$',...
      'steady-state: $E^{\mathrm{peak}} = -1056 \ \mu\epsilon$',...
      'overuse: $E^{\mathrm{peak}} = -1100 \ \mu\epsilon$',...
      'overuse: $E^{\mathrm{peak}} = -1400 \ \mu\epsilon$',...
      'overuse: $E^{\mathrm{peak}} = -1800 \ \mu\epsilon$',...
      'overuse: $E^{\mathrm{peak}} = -2200 \ \mu\epsilon$',...
      'overuse: $E^{\mathrm{peak}} = -2600 \ \mu\epsilon$')
set(legend,'FontSize',16,'FontName','Times New Roman','Location',...
    'northwest')
set(legend,'interpreter','latex')
legend boxoff
axis([0 16 -50 140])
ax = gca;
ax.GridLineStyle = ':';
set(get(gcf,'CurrentAxes'),'FontName','Times New Roman','FontSize',22)
grid on
xlabel('$t$',[d],'FontName','Times New Roman','FontSize',24,...
    'interpreter','latex')
ylabel('$\Delta f_{\mathrm{bm}}/f_{\mathrm{bm,ini}}$',[ \% ]$','FontName',...
    'Times New Roman','FontSize',24,'interpreter','latex')

%% Plot pvas AND plac
figure
load S_disuse_700-15p377
hold on
plot(timeVector-50,ParameterVector(:,11)*0.1/(pvas0*0.1),'k-',...
    'LineWidth',3)
grid on
plot(timeVector-50,ParameterVector(:,12)*0.1/(plac0*0.1),'k-',...
    'LineWidth',2)
load S_overuse_1800_32p132
plot(timeVector-50,ParameterVector(:,11)*0.1/(pvas0*0.1),'b-',...
    'LineWidth',3)
grid on
plot(timeVector-50,ParameterVector(:,12)*0.1/(plac0*0.1),'b-',...
    'LineWidth',2)
legend('mouse disuse ($E^{\mathrm{peak}} = -700 \ \mu\epsilon$):'...'
      '$p^{\mathrm{peak}}_{\mathrm{vas}}\mathrm{f}/'...'
      '\overline{p^{\mathrm{peak}}_{\mathrm{vas}}\mathrm{f}}$',...
      'mouse disuse ($E^{\mathrm{peak}} = -700 \ \mu\epsilon$):'...'
      '$p^{\mathrm{peak}}_{\mathrm{lac}}\mathrm{f}/'...'
      '\overline{p^{\mathrm{peak}}_{\mathrm{lac}}\mathrm{f}}$',...

```

```

        'mouse overuse ($E^\mathrm{peak} = -1800 \mu\epsilon)$:'...
        '$p^\mathrm{peak}_\mathrm{vas}\mathrm{f}/'...
        '\overline{p^\mathrm{peak}_\mathrm{vas}\mathrm{f}}$',...
        'mouse overuse ($E^\mathrm{peak} = -1800 \mu\epsilon)$:'...
        '$p^\mathrm{peak}_\mathrm{lac}\mathrm{f}/'...
        '\overline{p^\mathrm{peak}_\mathrm{lac}\mathrm{f}}$')
legend boxoff
set(legend, 'FontSize',16, 'FontName', 'Times New Roman', 'interpreter',...
    'latex', 'Location', 'northwest')
axis([-0.1 max(timeVector-50) 0 3])
ax = gca;
ax.GridLineStyle = ':';
set(gca, 'FontSize',22, 'FontName', 'Times New Roman')
grid on
xlabel('$t$, [d]', 'FontSize',24, 'FontName', 'Times New Roman',...
    'interpreter', 'latex')
ylabel('$p^\mathrm{peak}\mathrm{f}/\overline{p^\mathrm{peak}\mathrm{f}}$',...
    'FontSize',24, 'FontName', 'Times New Roman', 'interpreter', 'latex')

%% Plot cells
figure
hold on
load S_disuse_700-15p377
plot(timeVector-50, CellsVector(:,2)/steadystate.OBa, 'k-', 'LineWidth',3)
plot(timeVector-50, CellsVector(:,4)/steadystate.OCa, 'k—', 'LineWidth',3)
load S_overuse_1800_32p132
plot(timeVector-50, CellsVector(:,2)/steadystate.OBa, 'b-', 'LineWidth',3)
plot(timeVector-50, CellsVector(:,4)/steadystate.OCa, 'b—', 'LineWidth',3)
legend('mouse disuse ($E^\mathrm{peak} = -700 \mu\epsilon)$:'...
    '$C_\mathrm{OBa}^\mathrm{vas}/C_\mathrm{OBa,ini}^\mathrm{vas}$',...
    'mouse disuse ($E^\mathrm{peak} = -700 \mu\epsilon)$:'...
    '$C_\mathrm{OCa}^\mathrm{vas}/C_\mathrm{OCa,ini}^\mathrm{vas}$',...
    'mouse overuse ($E^\mathrm{peak} = -1800 \mu\epsilon)$:'...
    '$C_\mathrm{OBa}^\mathrm{vas}/C_\mathrm{OBa,ini}^\mathrm{vas}$',...
    'mouse overuse ($E^\mathrm{peak} = -1800 \mu\epsilon)$:'...
    '$C_\mathrm{OCa}^\mathrm{vas}/C_\mathrm{OCa,ini}^\mathrm{vas}$')
legend boxoff
axis([0 max(timeVector-50) 0.8 1.6])
set(legend, 'FontSize',16, 'FontName', 'Times New Roman', 'interpreter',...
    'latex', 'Location', 'northwest')
ax = gca;
ax.GridLineStyle = ':';
set(gca, 'FontSize',22, 'FontName', 'Times New Roman')
grid on
xlabel('$t$, [d]', 'FontSize',24, 'FontName', 'Times New Roman',...
    'interpreter', 'latex')
ylabel('$C^\mathrm{vas}_\mathrm{i}/C_\mathrm{vas,i,ini}$',...
    'FontSize',24, 'FontName', 'Times New Roman', 'interpreter', 'latex')

toc



---



%% parameter_definition.m: INPUT PARAMETERS FOR THE MODEL
% called in disuse_overuse_simulation.m

```

```

global DiffRate...
    ApRate...
    K...
    k...
    P_d...
    tD...
    B...
    conc...
    beta...
    var_factors...
    fvas0...
    fbm0;

% Value for concentration re-calibrations to vascular pore spaces
fvas0 = 0.05;
fbm0 = 1-fvas0;

%%%%%%%%%%%%%%%%%%%%%%%%%%%%%%%%%%%%%%%%%%%%%%%%%%%%%%%%%%%%%%%%%%%%%%%%
% RELATIVE RATE OF BONE RESORPTION %
%%%%%%%%%%%%%%%%%%%%%%%%%%%%%%%%%%%%%%%%%%%%%%%%%%%%%%%%%%%%%%%%%%%%%%%%

% [1/(pM.day)] normalized with respect to normal bone resorption
k.res = 20; % mouse/rat

%%%%%%%%%%%%%%%%%%%%%%%%%%%%%%%%%%%%%%%%%%%%%%%%%%%%%%%%%%%%%%%%%%%%%%%%
% OSTEOBLAST-SPECIFIC PARAMETERS %
%%%%%%%%%%%%%%%%%%%%%%%%%%%%%%%%%%%%%%%%%%%%%%%%%%%%%%%%%%%%%%%%%%%%%%%%

% Differentiation rate of osteoblast progenitors in vascular pores [1/day]
% D_OBu^{vas}
DiffRate.OBu = 7.000e-04;

% Differentiation rate of responding osteoblasts in vascular pores[1/day]
% D_OBp^{vas}
DiffRate.OBp = 1.656963129760296e-001;

% Apoptosis rate of active osteoblasts in vascular pores [1/day]
% A_OBa^{vas}
ApRate.OBa = 2.110726258064961e-001;

%%%%%%%%%%%%%%%%%%%%%%%%%%%%%%%%%%%%%%%%%%%%%%%%%%%%%%%%%%%%%%%%%%%%%%%%
% OSTEOCLAST-SPECIFIC PARAMETERS %
%%%%%%%%%%%%%%%%%%%%%%%%%%%%%%%%%%%%%%%%%%%%%%%%%%%%%%%%%%%%%%%%%%%%%%%%

% Differentiation rate of osteoclast progenitors in vascular pores [1/day]
% D_OCu^{vas}
DiffRate.OCu = 4.200000000000000e-003;

% Differentiation rate of osteoclast precursors in vascular pores [1/day]
% D_O Cp^{vas}
DiffRate.OCp = 2.100000000000000e+000;

```

```

% Apoptosis rate of active osteoclasts in vascular pores [1/day]
% A_OCa^{vas}
ApRate.OCa = 5.648744684096325e+000;

%%%%%%%%%%%%%%%%%%%%%%%%%%%%%%%%%%%%%%%%%%%%%%%%%%%%%%%%%%%%%%%%%%%%%%%%
% COEFFICIENTS FOR ACTIVATOR/REPRESSOR FUNCTIONS %
%%%%%%%%%%%%%%%%%%%%%%%%%%%%%%%%%%%%%%%%%%%%%%%%%%%%%%%%%%%%%%%%%%%%%%%%

% Activation coefficients related to TGF-beta binding on OBU and OCa [pM]
% activation of differentiation OBU -> OBp: K_{act,TGF-b}^{OBU->OBp,vas}
K.actOBuTGFb = 5.632788096754291e-004/fvas0;

% activation of OCa apoptosis: K_{act,TGF-b}^{OCa->+,vas}
K.actOCaTGFb = K.actOBuTGFb;

% K.actOBuTGFb = 0.011265576193509;      % resulting vascular concentration

% Repression coefficient related to TGF-beta binding on OBp [pM]
% repression of differentiation OBp -> OBa: K_{rep,TGF-b}^{OBp->OBa,vas}
K.repOBpTGFb = 1.754260518210943e-004/fvas0;

% K.repOBpTGFb = 0.003508521036422;      % vascular concentration

% Activation coefficient for RANKL production related to PTH binding [pM]
% activator function of OBa and OBp to produce RANKL in the presence of
% PTH: K_{act,PTH}^{maxRANKL/OBp,vas}
K.actOBPTH = 1.5e+2/fvas0;

% K.actOBPTH = 3000; % vascular concentration

% Repression coefficient for OPG production related to PTH binding [pM]
% repression function of OBa to produce OPG in the presence of PTH:
% K_{rep,PTH}^{OPG/OBa,vas}
K.repOBPTH = 2.225814277099542e-001/fvas0;

% K.repOBPTH = 4.451628554199083;      % vascular concentration

% Activation coefficient related to RANKL binding to RANK [pM]:
% K_{act,[RANKL-RANK]}^{OCp->OCa,vas}
K.actOCpRANKL = 5.679718330610479e+000/fvas0;

%K.actOCpRANKL = 1.135943666122096e+02;      % vascular concentration

% Activation coefficient related to MCSF binding on OCu [pM]
K.actOCuMCSF = 1.000e-03/fvas0; % not needed in function_dynamics

% K.actOCuMCSF = 0.020000000000000;      % vascular concentration

%%%%%%%%%%%%%%%%%%%%%%%%%%%%%%%%%%%%%%%%%%%%%%%%%%%%%%%%%%%%%%%%%%%%%%%%
% EXTERNAL (DOSAGE) PRODUCTION RATES % all zero, none of them is needed
%%%%%%%%%%%%%%%%%%%%%%%%%%%%%%%%%%%%%%%%%%%%%%%%%%%%%%%%%%%%%%%%%%%%%%%%

% External RANKL-injection [pM/day]
% non-zero if PMO is initiated via extra RANKL, see subprogram_loadcase

```

```
P_d.RANKL = 0;

% External OPG injection [pM/day]
P_d.OPG = 0;

% External PTH injection [pM/day]
P_d.PTH = 0;

% External OBa injection [pM/day]
P_d.OBa = 0;

% External OBp injection [pM/day]
P_d.OBp = 0;

% external OCY injection [pM/day]
P_d.OCY = 0;

% External OCp injection [pM/day]
P_d.OCp = 0;

% External OCa injection [pM/day]
P_d.OCa = 0;

%%%%%%%%%%%%%%%%%%%%%%%%%%%%%%%%%%%%%%%%%%%%%%%%%%%%%%%%%%%%%%%%%%%%%%%%
% CONSTANT DEGRADATION RATES %
%%%%%%%%%%%%%%%%%%%%%%%%%%%%%%%%%%%%%%%%%%%%%%%%%%%%%%%%%%%%%%%%%%%%%%%%

% Degradation rate of PTH [1/day]: %D_{PTH}^{vas}
tD.PTH = 8.6e+1;

% Degradation rate of OPG [1/day]: %D_{OPG}^{vas}
tD.OPG = 3.5e-1;

% Degradation rate of RANKL [1/day]: %D_{RANKL}^{vas}
tD.RANKL = 1.0132471014805027e+1;

%%%%%%%%%%%%%%%%%%%%%%%%%%%%%%%%%%%%%%%%%%%%%%%%%%%%%%%%%%%%%%%%%%%%%%%%
% PRESCRIBED FIXED CONCENTRATION %
%%%%%%%%%%%%%%%%%%%%%%%%%%%%%%%%%%%%%%%%%%%%%%%%%%%%%%%%%%%%%%%%%%%%%%%%

% Maximum possible OPG concentration [pM]: % C_{OPG,max}^{vas}
conc.OPGmax = 2e+8/fvas0;

% conc.OPGmax = 4.000000000000000e+09;      % vascular concentration

% Maximum possible RANKL production: C_{RANKL,max}^{vas} -> calculate

%%%%%%%%%%%%%%%%%%%%%%%%%%%%%%%%%%%%%%%%%%%%%%%%%%%%%%%%%%%%%%%%%%%%%%%%
% ASSOCIATION BINDING CONSTANTS %
%%%%%%%%%%%%%%%%%%%%%%%%%%%%%%%%%%%%%%%%%%%%%%%%%%%%%%%%%%%%%%%%%%%%%%%%

% Association binding constant for RANKL-OPG [1/pM]:
% K_{a,[RANKL-OPG]}^{vas}
```

```

B.RANKL_OPG = 1.0000000000000000e-003*fvas0;

%B.RANKL_OPG = 5.0000000000000000e-05;      % vascular concentration (*fvas0!)

% Association binding constant for RANKL-RANK [1/pM]:
%  $K_{a, [RANKL-RANK]}^{\{vas\}}$ 
B.RANKL_RANK = 3.411764705882353e-002*fvas0;

%B.RANKL_RANK = 0.001705882352941;          % vascular concentration (*fvas0!)

%%%%%%%%%%%%%%%%%%%%%%%%%%%%%%%%%%%%%%%%%%%%%%%%%%%%%%%%%%%%%%%%%%%%%%%%
% PROPORTIONALITY BETWEEN RESORPTION AND TGF-BETA CONTENT %
%%%%%%%%%%%%%%%%%%%%%%%%%%%%%%%%%%%%%%%%%%%%%%%%%%%%%%%%%%%%%%%%%%%%%%%%

% Apparently, it is difficult to determine the constant degradation rate of
% TGF-beta, thus it is assumed that the sink/source term equals zero, and
%  $\alpha^{\{TGF-b\}} * k_{res} / \tilde{D}_{\{TGF-beta\}}$  is considered as ONE factor
% ALPHA; at a later stage, the unknown components should be clarified as
% currently a sink/source term cannot be introduced!
%  $(\alpha_{\{TGF-b\}} * k_{res}) / \tilde{D}_{\{TGF-b\}}$ 
var_factors.Alpha = 1; % [dimensionless]

%%%%%%%%%%%%%%%%%%%%%%%%%%%%%%%%%%%%%%%%%%%%%%%%%%%%%%%%%%%%%%%%%%%%%%%%
% INTRINSIC PRODUCTION RATES %
%%%%%%%%%%%%%%%%%%%%%%%%%%%%%%%%%%%%%%%%%%%%%%%%%%%%%%%%%%%%%%%%%%%%%%%%

% Intrinsic production rate of PTH [pM/day] (assumed to be constant):
%  $\beta_{\{PTH\}}^{\{vas\}}$ 
beta.PTH = 2.50e+2/fvas0;

% beta.PTH = 5000;                          % vascular concentration

% Intrinsic production rate of RANKL [pM/day]
%  $\beta_{\{RANKL\}}^{\{vas\}}$  (OBp), old
beta.RANKL = 1.684195714712206e+002/fvas0;

% beta.RANKL = 3.368391429424412e+03;      % vascular concentration

% Intrinsic production rate of OPG [pM/day]: beta.OPG ( $\beta_{\{OPG\}}^{\{vas\}}$ )...
% => calculate in function_steadystate (appears explicited in paper)

%%%%%%%%%%%%%%%%%%%%%%%%%%%%%%%%%%%%%%%%%%%%%%%%%%%%%%%%%%%%%%%%%%%%%%%%
% OPG PRODUCTION-GOVERNING PARAMETERS %
%%%%%%%%%%%%%%%%%%%%%%%%%%%%%%%%%%%%%%%%%%%%%%%%%%%%%%%%%%%%%%%%%%%%%%%%

% Rate of OPG production per cell:
%  $p^{\{OBp\}}_{\{OPG\}} = p^{\{OBa\}}_{\{OPG\}} = p^{\{OB\}}_{\{OPG\}}$ 
var_factors.OPGrate_per_cell = 1.624900337835679e+008;

% Boolean variable determining which cells produce OPG: 0 = no, 1 = yes
var_factors.OPGprod_OBp = 0;
var_factors.OPGprod_OBa = 1; % OBAs produce OPG

```

```

%%%%%%%%%%%%%%%%%%%%%%%%%%%%%%%%%%%%%%%%%%%%%%%%%%%%%%%%%%%%%%%%%%%%%%%%
% RANK(L) PRODUCTION-GOVERNING PARAMETERS %
%%%%%%%%%%%%%%%%%%%%%%%%%%%%%%%%%%%%%%%%%%%%%%%%%%%%%%%%%%%%%%%%%%%%%%%%

% Constant describing how much RANK is produced per cell (OCp) [pM/pM]
% \rho_{RANK}
var_factors.RANKprod = 1.000e+004;

% Production rate of RANKL per cell [pM/pM] (OBp and OBa)
% N^{OBp}_{RANKL} = N^{OBa}_{RANKL} = N^{OB}_{RANKL}
var_factors.RANKLrate = 2.703476379131062e+006;

% Boolean variable determining which cells produce RANKL: 0 = no, 1 = yes
var_factors.RANKLprod_OBp = 1;      % OBps produce RANKL
var_factors.RANKLprod_OBa = 0;

%%%%%%%%%%%%%%%%%%%%%%%%%%%%%%%%%%%%%%%%%%%%%%%%%%%%%%%%%%%%%%%%%%%%%%%%

%% function_steadystate.m
% FUNCTION DETERMINING THE CELL CONCENTRATIONS AND PARAMETERS NECESSARY FOR
% THE BONE REMODELING MODEL AT STEADY-STATE
% called in disuse_overuse_simulation.m

function F_cells = function_steadystate(CV)

global DiffRate...
    ApRate...
    K...
    P_d...
    tD...
    B...
    conc...
    beta...
    var_factors...
    fvas0...
    fvas_0...
    fbm_0...
    pvas0...
    plac0...
    ratio...
    Epeak;

% Value from which the simulation starts
% mouse (Sugiyama) 0.8, rat 0.81 (Laib), (human 0.05)
fvas_0 = 0.81;
fbm_0 = 1-fvas_0;

%%%%%%%%%%%%%%%%%%%%%%%%%%%%%%%%%%%%%%%%%%%%%%%%%%%%%%%%%%%%%%%%%%%%%%%%
% INPUT OF INITIAL OSTEOBLAST AND OSTEOCLAST NUMBERS %
%%%%%%%%%%%%%%%%%%%%%%%%%%%%%%%%%%%%%%%%%%%%%%%%%%%%%%%%%%%%%%%%%%%%%%%%

OBp = CV(1); OBa = CV(2); OCp = CV(3); OCa = CV(4);

%%%%%%%%%%%%%%%%%%%%%%%%%%%%%%%%%%%%%%%%%%%%%%%%%%%%%%%%%%%%%%%%%%%%%%%%
% MCSF-RELATED ACTIVATION/REPRESSION FUNCTIONS %

```



```

%%%%%%%%%%%%%%%%%%%%%%%%%%%%%%%%%%%%%%%%%%%%%%%%%%%%%%%%%%%%%%%%%%%%%%%%
% Proportionality constants quantifying the OPG production of OB precursors
% and active ones [1/day]
P.OBpOPG = var_factors.OPGrate_per_cell*var_factors.OPGprod_OBp;
% = 0; OBps don't produce OPG -> only OBas
P.OBaOPG = var_factors.OPGrate_per_cell*var_factors.OPGprod_OBa;
% = just OPGrate_per_cell = n_{OPG/OBa}

% Intrinsic OPG production rate [pM/day]: % \beta_{OPG}^{vas}, appears
% explicitly in the paper
beta.OPG = (P.OBpOPG*OBp+P.OBaOPG*OBa)*Pi_PTH_rep;

% Concentration of OPG [pM]: C_{OPG}^{vas}
conc.OPG = (P_d.OPG+beta.OPG)/(beta.OPG/conc.OPGmax+tD.OPG);

%%%%%%%%%%%%%%%%%%%%%%%%%%%%%%%%%%%%%%%%%%%%%%%%%%%%%%%%%%%%%%%%%%%%%%%%
% RANK(L)-RELATED ACTIVATION/REPRESSION FUNCTIONS %
%%%%%%%%%%%%%%%%%%%%%%%%%%%%%%%%%%%%%%%%%%%%%%%%%%%%%%%%%%%%%%%%%%%%%%%%

% Proportionality constants quantifying the OPG production of OB precursors
% and active ones [pM/pM]
P.OBpRANKL = var_factors.RANKLprod_OBp*var_factors.RANKLrate;
% = just RANKLrate = n_{RANKL/OBp}
P.OBaRANKL = var_factors.RANKLprod_OBa*var_factors.RANKLrate;
% = 0; OBas don't produce RANKL -> only OBps

% Concentration of RANK [pM]: C_{RANK}^{vas}
conc.RANK = var_factors.RANKprod*OCp;

% Effective RANKL concentration [pM] = max. RANKL conc:
% C_{RANKL,max}^{vas}
conc.RANKLeff = (P.OBpRANKL*OBp+P.OBaRANKL*OBa)*Pi_PTH_act;

% Old concentration of RANKL [pM] - for the case of no OCYs
% C_{RANKL}^{vas} with MRP_new = P^{mech_RANKL}
conc.RANKL = conc.RANKLeff*(beta.RANKL+P_d.RANKL)/...
            ((1+B.RANKL_OPG*conc.OPG+B.RANKL_RANK*conc.RANK)*...
            (beta.RANKL+conc.RANKLeff*tD.RANKL));

% Old, endogeneous RANKL production
Prankl_e = beta.RANKL*(1-conc.RANKL*(1+B.RANKL_OPG*conc.OPG+B.RANKL_RANK*...
            conc.RANK)/conc.RANKLeff);

% Ratio Prankl_e_OBp/Prankl_e
ratio.Prankl = 0.574; % trabecular bone (mouse, rat)

% Prankl_e must remain the same, but is now produced by BOTH OBps and OCYs...
% => Prankl_e = Prankl_eOBp + beta.OCY_exvas*(1-fvas)/fvas
% So beta is (\beta_{RANKL}^{vas}(OCY)):
beta.OCY_exvas = Prankl_e*(1-ratio.Prankl)*fvas_0/(1-fvas_0);

% The final conc. of RANKL is then: % C_{RANKL}^{vas}, new
conc.RANKL_final = (Prankl_e+P_d.RANKL)/(tD.RANKL*(1+B.RANKL_OPG*conc.OPG+...
            B.RANKL_RANK*conc.RANK));

```

```

% Calculate the new beta.RANKL:
% \beta_{RANKL}^{\text{vas}(\text{OBp})}, new
beta.RANKL_new = conc.RANKLeff*Prankl_e*ratio.Prankl/(conc.RANKLeff-...
                conc.RANKL_final*(1+B.RANKL_OPG*conc.OPG+B.RANKL_RANK*...
                conc.RANK));

% Concentrations of the complexes RANKL-OPG and RANKL-RANK [pM]
% C_{[RANKL-OPG]}^{\text{vas}}
conc.RANKL_OPG = B.RANKL_OPG*conc.OPG*conc.RANKL_final;
% C_{[RANKL-RANK]}^{\text{vas}}
conc.RANKL_RANK = B.RANKL_RANK*conc.RANKL_final*conc.RANK;

% Activator function related to RANK-RANKL binding
% \pi_{\text{act}, [RANKL-RANK]}^{\text{OCp} \rightarrow \text{OCa}}
Pi_RANK_act = conc.RANKL_RANK./(K.actOCpRANKL+conc.RANKL_RANK);

%%%%%%%%%%%%%%%%%%%%%%%%%%%%%%%%%%%%%%%%%%%%%%%%%%%%%%%%%%%%%%%%%%%%%%%%
% INTERRELATION BETWEEN DIFFERENTIATION AND PROLIFERATION RATE %
%%%%%%%%%%%%%%%%%%%%%%%%%%%%%%%%%%%%%%%%%%%%%%%%%%%%%%%%%%%%%%%%%%%%%%%%

% D_OBu is composed of a differentiation and proliferation term
% D_OBu_1 ... differentiation - 1/3 ... related to diff
% D_OBu_2 ... proliferation - 2/3 ... related to prolif

D_OBu_1 = 1.00/3.00*DiffRate.OBu;
D_OBu_2 = 2.00/3.00*DiffRate.OBu;
P_OBp_t0 = D_OBu_2/Pi_WNT_act; % Pi_WNT_act = 1
% D_{OBu}^{\text{vas}}, only for steady-state:
D_OBu = (D_OBu_1+P_OBp_t0*Pi_WNT_act)*Pi_TGFb_OBu_act;

%%%%%%%%%%%%%%%%%%%%%%%%%%%%%%%%%%%%%%%%%%%%%%%%%%%%%%%%%%%%%%%%%%%%%%%%
% POROMECHANICS %
%%%%%%%%%%%%%%%%%%%%%%%%%%%%%%%%%%%%%%%%%%%%%%%%%%%%%%%%%%%%%%%%%%%%%%%%

Cexlac(:, :) = load('Cec.mat') ; Cec=Cexlac.Cec;
Placunae(:, :) = load('Plac.mat'); Plac=Placunae.Psph_ultra;

IIII = eye(6);
II = [1 1 1 0 0 0]';

blac = [1 1 1 0 0 0]';
bvas = [1 1 1 0 0 0]';

barflac = 0.1;

Aexcell = IIII*inv(barflac*inv(IIII-Plac*Cec)+(1-barflac)*IIII);
Alac = inv(IIII-Plac*Cec)*inv(barflac*inv(IIII-Plac*Cec)+(1-barflac)*...
        IIII);

bexaslac = barflac*II'*Alac;

Nexas = (-blac'*inv(Cec)*(barflac*blac-bexaslac'))^-1;

```

```

Mexvaslac = (barflac/2.3+1/Nexvas)^-1;

Cexvaslacdr = (1-barflac)*Cec*Aexcell;
Cexasundr = Cexvaslacdr+bexvaslac'*bexvaslac*Mexvaslac;

inc_phi = 2*pi/50;
Pcyl = FU_P_cylincl_orthomat(Cexvaslacdr,inc_phi);

flac = (1-fvas_0)*barflac;

% Concentration tensors
Aexvaslacdr = IIII*inv(fvas_0*inv(IIII-Pcyl*Cexvaslacdr)+(1-fvas_0)*IIII);
Avaslacdr = inv(IIII-Pcyl*Cexvaslacdr)*inv(fvas_0*inv(IIII-Pcyl*...
Cexvaslacdr)+(1-fvas_0)*IIII);

% Biot tensors: b_{macro}^{lac}, b_{macro}^{vas}
bcortlac = (1-fvas_0)*bexvaslac*Aexvaslacdr;
bcortvas = fvas_0*II'*Avaslacdr;

% Biot moduli: N_{macro}^{i,j}, {i,j} = {lac,vas}
Ncortlaclac = ((1-fvas_0)/Nexvas+bexvaslac*inv(Cexvaslacdr)*((1-fvas_0)*...
bexvaslac-bcortlac)')^-1;
Ncortvasvas = (-bvas'*inv(Cexvaslacdr)*((fvas_0)*bvas-bcortvas)')^-1;
Ncortlacvas = (bexvaslac*inv(Cexvaslacdr)*(fvas_0*bvas-bcortvas)')^-1;

% Coussy moduli: M_{macro}^{i}, i = {lac,vas}
Mcortlac = (flac/2.3+1/Ncortlaclac)^-1;
Mcortvas = (fvas_0/2.3+1/Ncortvasvas)^-1;

Ccortlacvasdr = (1-fvas_0)*Cexvaslacdr*Aexvaslacdr;
Ccortvasdr = Ccortlacvasdr+bcortlac'*bcortlac*Mcortlac;
% Homogenized stiffness tensor of RVE (undrained lac and vas pores):
% C_{macro}^{lac,vas-u}
Ccortundr = Ccortlacvasdr+bcortlac'*(Mcortlac*Ncortlacvas/...
(Ncortlacvas^2-Mcortlac*Mcortvas)*(bcortvas*Mcortvas+...
bcortlac*Ncortlacvas))+bcortvas'*(Mcortvas*Ncortlacvas/...
(Ncortlacvas^2-Mcortlac*Mcortvas)*(bcortlac*Mcortlac+...
bcortvas*Ncortlacvas));

% Skempton tensors:
% (B_{macro}^{lac})_{lac,vas-u}
Bcortlac = Mcortlac*Ncortlacvas/(-Mcortlac*Mcortvas+Ncortlacvas^2)*...
(bcortvas*Mcortvas+bcortlac*Ncortlacvas)*inv(Ccortundr);
% (B_{macro}^{vas})_{lac,vas-u}
Bcortvas = Mcortvas*Ncortlacvas/(-Mcortlac*Mcortvas+Ncortlacvas^2)*...
(bcortlac*Mcortlac+bcortvas*Ncortlacvas)*inv(Ccortundr);

% Stress tensor (see function_dynamics)
if Epeak == 1; % rat (Laib)
SIG_macro_normal = [0 0 0;0 0 0; 0 0 -3.854]*10^-3; % GPa
else % mouse (Sugiyama)
SIG_macro_normal = [0 0 0;0 0 0;0 0 -4.055]*10^-3; % GPa
end

% Transformation of matrix to vector: \Sigma_{macro}, steady-state
SIG_macro_normal_vector = FU_mat2vec(SIG_macro_normal);

```

```

% Vascular and lacunar pressure, steady-state: \overline{p_i}, i={lac,vas}
pvas0 = -Bcortvas*SIG_macro_normal_vector';
plac0 = -Bcortlac*SIG_macro_normal_vector';

% Macroscopic strain tensor at steady-state
Emacro0 = Ccortundr^-1*SIG_macro_normal_vector';

% E33 at steady-state: \overline{E^{peak}}
E0 = Emacro0(3);

%%%%%%%%%%%%%%%%%%%%%%%%%%%%%%%%%%%%%%%%%%%%%%%%%%%%%%%%%%%%%%%%%%%%%%%%
% SYSTEM OF GOVERNING EQUATIONS %
%%%%%%%%%%%%%%%%%%%%%%%%%%%%%%%%%%%%%%%%%%%%%%%%%%%%%%%%%%%%%%%%%%%%%%%%

% OBps
F1 = D_OBu*(1/fvas0)-DiffRate.OBp*OBp*Pi_TGFb_OBp_rep;
% old eq: 1 = C_OBu_vas

% OBas
F2 = DiffRate.OBp*Pi_TGFb_OBp_rep*OBp-(ApRate.OBa)*OBa;

% OCps
F3 = DiffRate.OCu*Pi_MCSF_act*Pi_RANK_act*(1/fvas0)-DiffRate.OCp*...
    Pi_RANK_act*OCp;
% old eq: 1 = C_OCu_vas

% OCas
F4 = DiffRate.OCp*Pi_RANK_act*OCp - ApRate.OCa*Pi_TGFb_OCa_act*OCa;

% Vector of all eqs at steady-state
F_cells = [F1;F2;F3;F4];

%%%%%%%%%%%%%%%%%%%%%%%%%%%%%%%%%%%%%%%%%%%%%%%%%%%%%%%%%%%%%%%%%%%%%%%%

%% function_dynamics.m: FUNCTION FOR RUNNING ALL THE DYNAMIC SIMULATIONS
% called in disuse_overuse_simulation.m

function xdot = function_dynamics(Time,CV)

global DiffRate...
    ApRate...
    K...
    P_d...
    tD...
    B...
    conc...
    beta...
    var_factors...
    steadystate...
    ParameterWrite...
    MECH...
    k...;
    ProfRate...
    fvas0...

```

```

    pvas0...
    plac0...
    MPS_new...
    MRP_new...
    lambda...
    OCY_exvas...
    Epeak;

% CV = vector of all solutions
OBp=CV(1); OBa=CV(2); OCp=CV(3); OCa=CV(4); fvas=CV(5);

% Input of model parameters
parameter_definition

%%%%%%%%%%%%%%%%%%%%%%%%%%%%%%%%%%%%%%%%%%%%%%%%%%%%%%%%%%%%%%%%%%%%%%%%
% DEFINITION OF MACROSCOPIC STRESS TENSORS %
%%%%%%%%%%%%%%%%%%%%%%%%%%%%%%%%%%%%%%%%%%%%%%%%%%%%%%%%%%%%%%%%%%%%%%%%
% \Sigma_{macro}, steady-state
SIG_macro_normal = [0 0 0;0 0 0; 0 0 -4.055]*10^-3; % GPa

%%%%%%%%%%%%%%%%%%%%%%%%%%%%%%%%%%%%%%%%%%%%%%%%%%%%%%%%%%%%%%%%%%%%%%%%
% DISUSE/ OVERUSE SIMULATION %
%%%%%%%%%%%%%%%%%%%%%%%%%%%%%%%%%%%%%%%%%%%%%%%%%%%%%%%%%%%%%%%%%%%%%%%%
% Sugiyama's E_peak (mouse)

% 0: disuse, E_peak = 0 uE, BVTV = -45.607%
% 300: disuse, E_peak = 300 uE, BVTV = -32.653%
% 700: disuse, E_peak = 700 uE, BVTV = -15.377%
% 1100: overuse, E_peak = 1100 uE, BVTV = +1.899%
% 1400: overuse, E_peak = 1400 uE, BVTV = +14.856%
% 1800: overuse, E_peak = 1800 uE, BVTV = +32.132%
% 2200: overuse, E_peak = 2200 uE, BVTV = +49.408%
% 2600: overuse, E_peak = 2600 uE, BVTV = +66.684%
% 1056: steady-state, E_peak = 1056 uE, BVTV = 0%

% 1: disuse, Laib (rat)

if Time>=50
    if Epeak == 0
        SIG_macro = [0 0 0;0 0 0; 0 0 -0.0001]*10^-3;% GPa
    elseif Epeak == 300
        SIG_macro = [0 0 0;0 0 0; 0 0 -1.152]*10^-3; % GPa
    elseif Epeak == 700
        SIG_macro = [0 0 0;0 0 0; 0 0 -2.688]*10^-3; % GPa
    elseif Epeak == 1100
        SIG_macro = [0 0 0;0 0 0; 0 0 -4.225]*10^-3; % GPa
    elseif Epeak == 1400
        SIG_macro = [0 0 0;0 0 0; 0 0 -5.377]*10^-3; % GPa
    elseif Epeak == 1800
        SIG_macro = [0 0 0;0 0 0; 0 0 -6.913]*10^-3; % GPa
    elseif Epeak == 2200
        SIG_macro = [0 0 0;0 0 0; 0 0 -8.448]*10^-3; % GPa
    elseif Epeak == 2600
        SIG_macro = [0 0 0;0 0 0; 0 0 -9.985]*10^-3; % GPa

```

```

elseif Epeak == 1056
    SIG_macro = SIG_macro_normal;
elseif Epeak == 1;
    SIG_macro = [0 0 0;0 0 0; 0 0 -0.33]*10^-3; % GPa
end
else
    if Epeak == 1;
        SIG_macro =[0 0 0;0 0 0; 0 0 -3.854]*10^-3;
        % Laib has fvas_0=0.81, adjust SIG_normal so that Epeak,0=1056 uE
    else
        SIG_macro = SIG_macro_normal;
    end
end

SIG_macro_vector = FU_mat2vec(SIG_macro);

%%%%%%%%%%%%%%%%%%%%%%%%%%%%%%%%%%%%%%%%%%%%%%%%%%%%%%%%%%%%%%%%%%%%%%%%
% Call function to calculate (poro)micromechanics%
%%%%%%%%%%%%%%%%%%%%%%%%%%%%%%%%%%%%%%%%%%%%%%%%%%%%%%%%%%%%%%%%%%%%%%%%

micromech=f_micromech(SIG_macro_vector,fvas);

pvas = micromech(1);
plac = micromech(2);
E = micromech(3);

%%%%%%%%%%%%%%%%%%%%%%%%%%%%%%%%%%%%%%%%%%%%%%%%%%%%%%%%%%%%%%%%%%%%%%%%
% Mechanosensing: this part drives all the simulations%
%%%%%%%%%%%%%%%%%%%%%%%%%%%%%%%%%%%%%%%%%%%%%%%%%%%%%%%%%%%%%%%%%%%%%%%%

if Time>=50
    if MECH.calibration == 1

        %% 1. Dynamic calculation:
        % MPS = Mechanically-induced proliferation of OBps - Pi^mech_act

        % lambda.OBp,new for quantification only of MPS by OBps:
        % \lambda_{OBp}^{\vas}; mouse (Sugiyama)/ rat (Laib) irrelevant (disuse)
        lambda.OBP = 2;

        % lambda.OCY (Wnt/sclr), for the new contribution of OCYs to MPS
        % \lambda_{Wnt/sclr}^{\vas}; mouse/ rat irrelevant (disuse)
        lambda.OCY = 100;

        % lambdas calibrated such that the contribution of OBps to the
        % total MPS = C_OBp^macro/(C_OBp^macro+C_OCY^macro)

        %% 2. Dynamic calculation:
        % MRP = Mechanically produced RANKL - P^mech_RANKL

        % k.OBp,new for quantification only of MRP_OBp: \kappa
        % mouse/rat
        k.OBP = 3.5e4;
    end
end

```

```

    % k.OCY, for the new contribution of OCYs to MRP: \kappa
    k.OCY = k.OBP;
    %k.OCY = 0; % to simulate no OCYs

    MECH.calibration = 0;

    end

% Mechanosensing mechanisms: mechanical stimulus is pressure x frequency

% Sugiyama's frequency: \mathfrak{f}
f=0.1;

% MPS = Additional, mechanically-induced OBp proliferation with increased
% loading
MPS1 = 0; % \Pi_{act,OBp}^{mech,vas} - OBp&pvas term
MPS2 = 0; % \Pi_{act,OBp}^{mech,vas} - OCY&plac term

% MRP = Additional, mechanically-induced RANKL production with loading
MRP1 = 0; % P_{RANKL}^{mech,vas} - OBp&pvas term
MRP2 = 0; % P_{RANKL}^{mech,vas} - OCY&plac term

if pvas*f > pvas0*f    % if pvas*f is higher than the steadystate pvas0*f
    MPS1 = lambda.OBP*(pvas*f-pvas0*f)/(pvas0*f);
end

if pvas*f < pvas0*f    % if pvas*f is lower than the steadystate pvas0*f
    MRP1 = k.OBP*OBp*(pvas0*f-pvas*f)/(pvas0*f);
end

if plac*f > plac0*f    % if plac*f is higher than the steadystate plac0*f
    MPS2 = lambda.OCY*OCY_exvas*(plac*f-plac0*f)/(plac0*f)*(1-fvas)/fvas;
end

if plac*f < plac0*f    % if plac*f is lower than the steadystate plac0*f
    MRP2 = k.OCY*OCY_exvas*(plac0*f-plac*f)/(plac0*f)*(1-fvas)/fvas;
end

% Total \Pi_{act,OBp}^{mech,vas}
MPS_new = MECH.Pi_strain_steady*(1+MPS1+MPS2);

% Calculate the contribution of OBPs to the total MPS at the first dynamic
% step -> equal to C_OBp^macro/(C_OBp^macro+C_OCY^macro)
%if Time == 50
    % MPS1/(MPS1+MPS2)
%end

if MPS_new > 1
    MPS_new = 1; % max is MPS = 1
end

% Total P_{RANKL}^{mech,vas}
MRP_new = MRP1 + MRP2;

else % if Time < 50, pvas*f = pvas0*f; plac*f = plac0*f
    % => just normal loading;

```

```

MPS_new = MECH.Pi_strain_steady;
MRP_new = 0;
end

%%%%%%%%%%%%%%%%%%%%%%%%%%%%%%%%%%%%%%%%%%%%%%%%%%%%%%%%%%%%%%%%%%%%%%%%
% TGF-BETA RELATED ACTIVATION/REPRESSION FUNCTIONS %
%%%%%%%%%%%%%%%%%%%%%%%%%%%%%%%%%%%%%%%%%%%%%%%%%%%%%%%%%%%%%%%%%%%%%%%%

% activation/repression functions due to the presence of TGF-beta in the
% system, note: as no reasonable determination of the TGF-beta degradation
% rate was/is achieved, a factor Alpha was introduced, unifying all factors
% and rates to one number (while assuming that the source/sink term equals
% zero)

% \pi_{act,TGF-b}^{OBu->OBp}
Pi_TGFb_OBu_act = (var_factors.Alpha*OCa)/...           % C_TGF-\beta
                 (K.actOBuTGFb+var_factors.Alpha*OCa);
% \pi_{act,TGF-b}^{OCa->+}
Pi_TGFb_OCa_act = (var_factors.Alpha*OCa)/...
                 (K.actOCaTGFb+var_factors.Alpha*OCa);
% \pi_{rep,TGF-b}^{OBp->OBa}
Pi_TGFb_OBp_rep = 1/(1+var_factors.Alpha*OCa/K.repOBpTGFb);

%%%%%%%%%%%%%%%%%%%%%%%%%%%%%%%%%%%%%%%%%%%%%%%%%%%%%%%%%%%%%%%%%%%%%%%%
% PTH-RELATED ACTIVATION/REPRESSION FUNCTIONS %
%%%%%%%%%%%%%%%%%%%%%%%%%%%%%%%%%%%%%%%%%%%%%%%%%%%%%%%%%%%%%%%%%%%%%%%%

% PTH-concentration [pM], assuming constant production and degradation
% rates, and no further regulation (Pi=1):
% % C_{PTH}^{vas}
conc.PTH = (beta.PTH+P_d.PTH)/tD.PTH;
% \pi_{act,PTH}^{maxRANKL}
Pi_PTH_act = (conc.PTH)/(conc.PTH+K.actOBPTH);
% \pi_{rep,PTH}^{OPG/OBa}
Pi_PTH_rep = 1/(1+conc.PTH/K.repOBPTH);

%%%%%%%%%%%%%%%%%%%%%%%%%%%%%%%%%%%%%%%%%%%%%%%%%%%%%%%%%%%%%%%%%%%%%%%%
% OPG-RELATED FUNCTIONS %
%%%%%%%%%%%%%%%%%%%%%%%%%%%%%%%%%%%%%%%%%%%%%%%%%%%%%%%%%%%%%%%%%%%%%%%%

% Proportionality constants quantifying the OPG production of OB precursors
% and active ones [1/day]
P.OBpOPG = var_factors.OPGrate_per_cell*var_factors.OPGprod_OBp;
% = 0; OBps don't produce OPG -> only OBas
P.OBaOPG = var_factors.OPGrate_per_cell*var_factors.OPGprod_OBa;
% = just OPGrate_per_cell = n_{OPG/OBa}

% Intrinsic OPG production rate [pM/day]: % \beta_{OPG}^{vas}, appears
% explicitly in the paper
beta.OPG = (P.OBpOPG*OBp+P.OBaOPG*OBa)*Pi_PTH_rep;

% Concentration of OPG [pM]: C_{OPG}^{vas}
conc.OPG = (P_d.OPG+beta.OPG)/(beta.OPG/conc.OPGmax+tD.OPG);

```

```

%%%%%%%%%%%%%%%%%%%%%%%%%%%%%%%%%%%%%%%%%%%%%%%%%%%%%%%%%%%%%%%%%%%%%%%%
% RANKL-RELATED ACTIVATION/REPRESSION FUNCTIONS %
%%%%%%%%%%%%%%%%%%%%%%%%%%%%%%%%%%%%%%%%%%%%%%%%%%%%%%%%%%%%%%%%%%%%%%%%

% Proportionality constants quantifying the RANKL production of OB
% precursors and active ones [pM/pM]
P.OBpRANKL = var_factors.RANKLprod_OBp*var_factors.RANKLrate;
% = just RANKLrate = n_{RANKL/OBp}
P.OBaRANKL = var_factors.RANKLprod_OBa*var_factors.RANKLrate;
% = 0; OBas don't produce RANKL -> only OBps

% Concentration of RANK [pM]: C_{RANK}^{vas}
conc.RANK = var_factors.RANKprod*OCp;

% Effective RANKL concentration [pM] = max. RANKL conc:
% C_{RANKL,max}^{vas}
conc.RANKLeff = (P.OBpRANKL*OBp+P.OBaRANKL*OBa)*Pi_PTH_act;

% Old concentration of RANKL [pM] - for the case of no OCYs
% C^{vas}_{RANKL} with MRP_new = P^mech_RANKL
conc.RANKL = conc.RANKLeff*(beta.RANKL+P_d.RANKL+MRP_new)/...
            ((1+B.RANKL_OPG*conc.OPG+B.RANKL_RANK*conc.RANK)*...
            (beta.RANKL+conc.RANKLeff*tD.RANKL));

% Production rate of RANKL per extravascular osteocyte concentration(1/day)
k.p_OCY = beta.OCY_exvas/OCY_exvas;
% k.p_OCY = 0; % to simulate no OCYs

% The final conc. of RANKL with OCYs is then:
% C_{RANKL}^{vas}, new, with mech production of RANKL!
conc.RANKL_final = conc.RANKLeff*(beta.RANKL_new+P_d.RANKL+k.p_OCY...
            *OCY_exvas*(1-fvas)/fvas+MRP_new)/...
            ((1+B.RANKL_OPG*conc.OPG+B.RANKL_RANK*conc.RANK)*...
            (beta.RANKL_new+conc.RANKLeff*tD.RANKL));

% Concentrations of the complexes RANKL-OPG and RANKL-RANK [pM]
% C_{[RANKL-OPG]}^{vas}
conc.RANKL_OPG = B.RANKL_OPG*conc.OPG*conc.RANKL_final;
% to simulate no OCYs new conc.RANKL = old one
%conc.RANKL_OPG = B.RANKL_OPG*conc.OPG*conc.RANKL;
% C_{[RANKL-RANK]}^{vas}
conc.RANKL_RANK = B.RANKL_RANK*conc.RANKL_final*conc.RANK;
% to simulate no OCYs new conc.RANKL = old one
%conc.RANKL_RANK = B.RANKL_RANK*conc.RANKL*conc.RANK;

% Activator function related to RANK-RANKL binding
% \pi_{act,[RANKL-RANK]}^{OCp->OCa}
Pi_RANK_act = conc.RANKL_RANK./(K.actOCpRANKL+conc.RANKL_RANK);

% Calculate ProfRate.OBp only for the first step of dynamic simulation
if MECH.ProfRate_calc == 1

    % Mechanical proliferation of OBps, P_{OBp}^{vas}
    ProfRate.OBp = DiffRate.OBu*MECH.DOBu_frac*(1/fvas0)*...

```

```

        Pi_TGFb_OBu_act/steadystate.OBp/MPS_new;

    MECH.ProfRate_calc = 0;
end

%%%%%%%%%%%%%%%%%%%%%%%%%%%%%%%%%%%%%%%%%%%%%%%%%%%%%%%%%%%%%%%%%%%%%%%%
% SYSTEM OF GOVERNING EQUATIONS %
%%%%%%%%%%%%%%%%%%%%%%%%%%%%%%%%%%%%%%%%%%%%%%%%%%%%%%%%%%%%%%%%%%%%%%%%

% 1: Vascular concentration change of OBps with time
dOBpdt = DiffRate.OBu*(1-MECH.DOBu_frac)*Pi_TGFb_OBu_act*(1/fvas0)+...
        ProfRate.OBp*OBp*MPS_new-...
        DiffRate.OBp*Pi_TGFb_OBp_rep*OBp+...
        P_d.OBp - OBp*(OCa*k.res-OBa*k.form);

% 2: Vascular concentration change of OBAs with time
dOBadt = DiffRate.OBp*Pi_TGFb_OBp_rep*OBp-(ApRate.OBa)*OBa+P_d.OBa...
        - OBa*(OCa*k.res-OBa*k.form);

% 3: Vascular concentration change of OCps with time
dOCpdt = 0;

% 4: Vascular concentration change of OCas with time
dOCadt = DiffRate.OBp*Pi_RANK_act*OCp-ApRate.OCa*Pi_TGFb_OCa_act*OCa+...
        P_d.OCa - OCa*(OCa*k.res-OBa*k.form);

% 5: Change of fvas with time
dfvasdt = (OCa*k.res-OBa*k.form)*fvas;

% Vector of all eqs
xdot = [dOBpdt;dOBadt;dOCpdt;dOCadt;dfvasdt];

% After solving, give all parameters in ParameterVector

    if ParameterWrite == 1

xdot = [conc.OPG; ... % 1
        conc.RANK; ... % 2
        conc.RANKLeff; ... % 3
        conc.RANKL_final; ... % 4
        conc.RANKL_RANK; ... % 5
        Pi_TGFb_OBu_act; ... % 6
        Pi_TGFb_OCa_act; ... % 7
        Pi_TGFb_OBp_rep; ... % 8
        Pi_RANK_act; ... % 9
        Time; ... % 10
        pvas; ... % 11
        plac;... % 12
        MPS_new;... % 13
        MRP_new;... % 14
        E*1e6;]; % 15 [in uE]

    end

```

```

%% f_micromech.m: FUNCTION CALCULATING ALL THE POROMICROMECHANICS;
% called in function_dynamics.m

function micromech = f_micromech(SIG,fvas)

%%%%%%%%%%%%%%%%%%%%%%%%%%%%%%%%%%%%%%%%%%%%%%%%%%%%%%%%%%%%%%%%%%%%%%%%
% INITIAL CONFIGURATION %
%%%%%%%%%%%%%%%%%%%%%%%%%%%%%%%%%%%%%%%%%%%%%%%%%%%%%%%%%%%%%%%%%%%%%%%%

% Initial volume fractions (porosity, bone matrix)
fbm = 1-fvas;

%%%%%%%%%%%%%%%%%%%%%%%%%%%%%%%%%%%%%%%%%%%%%%%%%%%%%%%%%%%%%%%%%%%%%%%%
% POROMECHANICS %
%%%%%%%%%%%%%%%%%%%%%%%%%%%%%%%%%%%%%%%%%%%%%%%%%%%%%%%%%%%%%%%%%%%%%%%%

Cexlac(:, :)=load('Cec.mat') ; Cec=Cexlac.Cec;
Placunae(:, :)=load('Plac.mat'); Plac=Placunae.Psph_ultra;

IIII = eye(6);
II = [1 1 1 0 0 0]';

blac = [1 1 1 0 0 0]';
bvas = [1 1 1 0 0 0]';

barflac = 0.1;

Aexcell = IIII*inv(barflac*inv(IIII-Plac*Cec)+(1-barflac)*IIII);
Alac = inv(IIII-Plac*Cec)*inv(barflac*inv(IIII-Plac*Cec)+(1-barflac)*...
    IIII);

bexaslac = barflac*II'*Alac;

Nexas = (-blac'*inv(Cec)*(barflac*blac-bexaslac'))^-1;

Mexvaslac = (barflac/2.3+1/Nexas)^-1;

Cexaslacdr = (1-barflac)*Cec*Aexcell;
Cexasundr = Cexaslacdr+bexaslac'*bexaslac*Mexaslac;

inc_phi = 2*pi/50;
Pcyl = FU_P_cylincl_orthomat(Cexaslacdr,inc_phi);

flac = (1-fvas)*barflac;

% Concentration tensors
Aexaslacdr = IIII*inv(fvas*inv(IIII-Pcyl*Cexaslacdr)+(1-fvas)*IIII);
Avaslacdr = inv(IIII-Pcyl*Cexaslacdr)*inv(fvas*inv(IIII-Pcyl*...
    Cexaslacdr)+(1-fvas)*IIII);

% Biot tensors: b_{macro}^{lac}, b_{macro}^{vas}
bcortlac = (1-fvas)*bexaslac*Aexaslacdr;
bcortvas = fvas*II'*Avaslacdr;

% Biot moduli: N_{macro}^{i,j}, {i,j} = {lac,vas}
Ncortlac = ((1-fvas)/Nexas+bexaslac*inv(Cexaslacdr))*((1-fvas)...

```

```

        *bexvaslac-bcortlac')^-1;
Ncortvasvas = (-bvas'*inv(Cexvaslacdr)*((fvas)*bvas-bcortvas'))^-1;
Ncortlacvas = (bexvaslac*inv(Cexvaslacdr)*(fvas*bvas-bcortvas'))^-1;

% Coussy moduli: M_{macro}^{i}, i = {lac,vas}
Mcortlac    = (flac/2.3+1/Ncortlaclac)^-1;
Mcortvas    = (fvas/2.3+1/Ncortvasvas)^-1;

Ccortlacvasdr = (1-fvas)*Cexvaslacdr*Aexvaslacdr;
Ccortvasdr    = Ccortlacvasdr+bcortlac'*bcortlac*Mcortlac;
% Homogenized stiffness tensor of RVE (undrained lac and vas pores):
% C_{macro}^{lac,vas-u}
Ccortundr     = Ccortlacvasdr+bcortlac'*(Mcortlac*Ncortlacvas/...
                (Ncortlacvas^2-Mcortlac*Mcortvas)*(bcortvas*Mcortvas+...
                bcortlac*Ncortlacvas))+bcortvas'*(Mcortvas*Ncortlacvas/...
                (Ncortlacvas^2-Mcortlac*Mcortvas)*(bcortlac*Mcortlac+...
                bcortvas*Ncortlacvas));

% Skempton tensors
% (B_{macro}^{lac})_{lac,vas-u}
Bcortlac      = Mcortlac*Ncortlacvas/(-Mcortlac*Mcortvas+Ncortlacvas^2)*...
                (bcortvas*Mcortvas+bcortlac*Ncortlacvas)*inv(Ccortundr);
% (B_{macro}^{vas})_{lac,vas-u}
Bcortvas      = Mcortvas*Ncortlacvas/(-Mcortlac*Mcortvas+Ncortlacvas^2)*...
                (bcortlac*Mcortlac+bcortvas*Ncortlacvas)*inv(Ccortundr);

% Vascular and lacunar pressures: p_{vas}, p_{lac}
% SIG = \Sigma_{macro}
pvas = -Bcortvas*SIG';
plac = -Bcortlac*SIG';

% Macroscopic strain tensor
Emacro = Ccortundr^-1*SIG';

% E33: E^{peak}
E = Emacro(3);

micromech = [pvas... % vascular pore pressure
             plac... % lacunar pore pressure
             E];    % macroscopic strain tensor component 33

```

```

%% FU_mat2vec.m: FUNCTION TRANSFORMING MATRIX INTO VECTOR

function mat = FU_mat2vec(mat_macro)

mat = [mat_macro(1,1) ...
       mat_macro(2,2) ...
       mat_macro(3,3) ...
       2*mat_macro(1,2) ...
       2*mat_macro(2,3) ...
       2*mat_macro(3,1)];

```

```

%% FU_P_cylincl_orthomat.m:
% FUNCTION DETERMINING THE HILL TENSOR FOR CYLINDRICAL INCLUSIONS IN AN
% ORTHOTROPIC MATRIX

```

```

function Pcyl = FU_P_cylincl_orthomat(Cultra_ORTH,inc_phi)

```

```

C_LOCAL(1,1,1,1) = Cultra_ORTH(1,1);
C_LOCAL(1,1,2,2) = Cultra_ORTH(1,2);
C_LOCAL(1,1,3,3) = Cultra_ORTH(1,3);
C_LOCAL(1,1,2,3) = Cultra_ORTH(1,4)/sqrt(2);
C_LOCAL(1,1,3,2) = Cultra_ORTH(1,4)/sqrt(2);
C_LOCAL(1,1,1,3) = Cultra_ORTH(1,5)/sqrt(2);
C_LOCAL(1,1,3,1) = Cultra_ORTH(1,5)/sqrt(2);
C_LOCAL(1,1,1,2) = Cultra_ORTH(1,6)/sqrt(2);
C_LOCAL(1,1,2,1) = Cultra_ORTH(1,6)/sqrt(2);
C_LOCAL(2,2,1,1) = Cultra_ORTH(2,1);
C_LOCAL(2,2,2,2) = Cultra_ORTH(2,2);
C_LOCAL(2,2,3,3) = Cultra_ORTH(2,3);
C_LOCAL(2,2,2,3) = Cultra_ORTH(2,4)/sqrt(2);
C_LOCAL(2,2,3,2) = Cultra_ORTH(2,4)/sqrt(2);
C_LOCAL(2,2,1,3) = Cultra_ORTH(2,5)/sqrt(2);
C_LOCAL(2,2,3,1) = Cultra_ORTH(2,5)/sqrt(2);
C_LOCAL(2,2,1,2) = Cultra_ORTH(2,6)/sqrt(2);
C_LOCAL(2,2,2,1) = Cultra_ORTH(2,6)/sqrt(2);
C_LOCAL(3,3,1,1) = Cultra_ORTH(3,1);
C_LOCAL(3,3,2,2) = Cultra_ORTH(3,2);
C_LOCAL(3,3,3,3) = Cultra_ORTH(3,3);
C_LOCAL(3,3,2,3) = Cultra_ORTH(3,4)/sqrt(2);
C_LOCAL(3,3,3,2) = Cultra_ORTH(3,4)/sqrt(2);
C_LOCAL(3,3,1,3) = Cultra_ORTH(3,5)/sqrt(2);
C_LOCAL(3,3,3,1) = Cultra_ORTH(3,5)/sqrt(2);
C_LOCAL(3,3,1,2) = Cultra_ORTH(3,6)/sqrt(2);
C_LOCAL(3,3,2,1) = Cultra_ORTH(3,6)/sqrt(2);
C_LOCAL(2,3,1,1) = Cultra_ORTH(4,1)/sqrt(2);
C_LOCAL(3,2,1,1) = Cultra_ORTH(4,1)/sqrt(2);
C_LOCAL(2,3,2,2) = Cultra_ORTH(4,2)/sqrt(2);
C_LOCAL(3,2,2,2) = Cultra_ORTH(4,2)/sqrt(2);
C_LOCAL(2,3,3,3) = Cultra_ORTH(4,3)/sqrt(2);
C_LOCAL(3,2,3,3) = Cultra_ORTH(4,3)/sqrt(2);
C_LOCAL(2,3,2,3) = Cultra_ORTH(4,4)/2;
C_LOCAL(2,3,3,2) = Cultra_ORTH(4,4)/2;
C_LOCAL(3,2,3,2) = Cultra_ORTH(4,4)/2;
C_LOCAL(3,2,2,3) = Cultra_ORTH(4,4)/2;
C_LOCAL(2,3,1,3) = Cultra_ORTH(4,5)/2;
C_LOCAL(2,3,3,1) = Cultra_ORTH(4,5)/2;
C_LOCAL(3,2,3,1) = Cultra_ORTH(4,5)/2;
C_LOCAL(3,2,1,3) = Cultra_ORTH(4,5)/2;
C_LOCAL(2,3,1,2) = Cultra_ORTH(4,6)/2;
C_LOCAL(2,3,2,1) = Cultra_ORTH(4,6)/2;
C_LOCAL(3,2,2,1) = Cultra_ORTH(4,6)/2;
C_LOCAL(3,2,1,2) = Cultra_ORTH(4,6)/2;
C_LOCAL(1,3,1,1) = Cultra_ORTH(5,1)/sqrt(2);
C_LOCAL(3,1,1,1) = Cultra_ORTH(5,1)/sqrt(2);
C_LOCAL(1,3,2,2) = Cultra_ORTH(5,2)/sqrt(2);
C_LOCAL(3,1,2,2) = Cultra_ORTH(5,2)/sqrt(2);
C_LOCAL(1,3,3,3) = Cultra_ORTH(5,3)/sqrt(2);

```

```

C_LOCAL(3,1,3,3) = Cultra_ORTH(5,3)/sqrt(2);
C_LOCAL(1,3,2,3) = Cultra_ORTH(5,4)/2;
C_LOCAL(1,3,3,2) = Cultra_ORTH(5,4)/2;
C_LOCAL(3,1,3,2) = Cultra_ORTH(5,4)/2;
C_LOCAL(3,1,2,3) = Cultra_ORTH(5,4)/2;
C_LOCAL(1,3,1,3) = Cultra_ORTH(5,5)/2;
C_LOCAL(1,3,3,1) = Cultra_ORTH(5,5)/2;
C_LOCAL(3,1,3,1) = Cultra_ORTH(5,5)/2;
C_LOCAL(3,1,1,3) = Cultra_ORTH(5,5)/2;
C_LOCAL(1,3,1,2) = Cultra_ORTH(5,6)/2;
C_LOCAL(1,3,2,1) = Cultra_ORTH(5,6)/2;
C_LOCAL(3,1,2,1) = Cultra_ORTH(5,6)/2;
C_LOCAL(3,1,1,2) = Cultra_ORTH(5,6)/2;
C_LOCAL(1,2,1,1) = Cultra_ORTH(6,1)/sqrt(2);
C_LOCAL(2,1,1,1) = Cultra_ORTH(6,1)/sqrt(2);
C_LOCAL(1,2,2,2) = Cultra_ORTH(6,2)/sqrt(2);
C_LOCAL(2,1,2,2) = Cultra_ORTH(6,2)/sqrt(2);
C_LOCAL(1,2,3,3) = Cultra_ORTH(6,3)/sqrt(2);
C_LOCAL(2,1,3,3) = Cultra_ORTH(6,3)/sqrt(2);
C_LOCAL(1,2,2,3) = Cultra_ORTH(6,4)/2;
C_LOCAL(1,2,3,2) = Cultra_ORTH(6,4)/2;
C_LOCAL(2,1,3,2) = Cultra_ORTH(6,4)/2;
C_LOCAL(2,1,2,3) = Cultra_ORTH(6,4)/2;
C_LOCAL(1,2,1,3) = Cultra_ORTH(6,5)/2;
C_LOCAL(1,2,3,1) = Cultra_ORTH(6,5)/2;
C_LOCAL(2,1,3,1) = Cultra_ORTH(6,5)/2;
C_LOCAL(2,1,1,3) = Cultra_ORTH(6,5)/2;
C_LOCAL(1,2,1,2) = Cultra_ORTH(6,6)/2;
C_LOCAL(1,2,2,1) = Cultra_ORTH(6,6)/2;
C_LOCAL(2,1,2,1) = Cultra_ORTH(6,6)/2;
C_LOCAL(2,1,1,2) = Cultra_ORTH(6,6)/2;

w1 = [1;0;0]; w2 = [0;1;0]; w3 = [0;0;1];
Pcyl_LOCAL = zeros(3,3,3,3);

for phi_1 = 0:inc_phi:2*pi-inc_phi
    xi = cos(phi_1)*w1+sin(phi_1)*w2;
    Khelp = zeros(3,3,3);
    K1 = zeros(3,3);
    for i=1:3
        for j=1:3
            for k=1:3
                Khelp(i,j,k) = xi(1)*C_LOCAL(1,i,j,k)+xi(2)*...
                    C_LOCAL(2,i,j,k)+xi(3)*C_LOCAL(3,i,j,k);
            end
        end
    end
    for i=1:3
        for j=1:3
            K1(i,j) = Khelp(i,j,1)*xi(1)+...
                Khelp(i,j,2)*xi(2)+Khelp(i,j,3)*xi(3);
        end
    end
    Klinv = inv(K1);
    for i=1:3
        for j=1:3

```

```

        for k=1:3
            help(i,j,k) = Klinv(i,j)*xi(k);
        end
    end
end
for i=1:3
    for j=1:3
        for k=1:3
            for l=1:3
                help1(i,j,k,l) = xi(i)*help(j,k,l);
            end
        end
    end
end
for i=1:3
    for j=1:3
        for k=1:3
            for l=1:3
                Gamma_LOCAL_inc(i,j,k,l) = ...
                    (help1(i,j,k,l)+help1(i,j,l,k)+...
                    help1(j,i,k,l)+help1(j,i,l,k))/4;
            end
        end
    end
end
Pcyl_LOCAL = Pcyl_LOCAL+Gamma_LOCAL_inc*inc_phi/(2*pi);
end

Pcyl = [1*Pcyl_LOCAL(1,1,1,1)      1*Pcyl_LOCAL(1,1,2,2)      ...
        1*Pcyl_LOCAL(1,1,3,3)      sqrt(2)*Pcyl_LOCAL(1,1,2,3)      ...
        sqrt(2)*Pcyl_LOCAL(1,1,3,1) sqrt(2)*Pcyl_LOCAL(1,1,1,2);      ...
        1*Pcyl_LOCAL(2,2,1,1)      1*Pcyl_LOCAL(2,2,2,2)      ...
        1*Pcyl_LOCAL(2,2,3,3)      sqrt(2)*Pcyl_LOCAL(2,2,2,3)      ...
        sqrt(2)*Pcyl_LOCAL(2,2,3,1) sqrt(2)*Pcyl_LOCAL(2,2,1,2);      ...
        1*Pcyl_LOCAL(3,3,1,1)      1*Pcyl_LOCAL(3,3,2,2)      ...
        1*Pcyl_LOCAL(3,3,3,3)      sqrt(2)*Pcyl_LOCAL(3,3,2,3)      ...
        sqrt(2)*Pcyl_LOCAL(3,3,3,1) sqrt(2)*Pcyl_LOCAL(3,3,1,2);      ...
        sqrt(2)*Pcyl_LOCAL(2,3,1,1) sqrt(2)*Pcyl_LOCAL(2,3,2,2)      ...
        sqrt(2)*Pcyl_LOCAL(2,3,3,3) 2*Pcyl_LOCAL(2,3,2,3)      ...
        2*Pcyl_LOCAL(2,3,1,3)      2*Pcyl_LOCAL(2,3,1,2);      ...
        sqrt(2)*Pcyl_LOCAL(1,3,1,1) sqrt(2)*Pcyl_LOCAL(1,3,2,2)      ...
        sqrt(2)*Pcyl_LOCAL(1,3,3,3) 2*Pcyl_LOCAL(1,3,2,3)      ...
        2*Pcyl_LOCAL(1,3,1,3)      2*Pcyl_LOCAL(1,3,1,2);      ...
        sqrt(2)*Pcyl_LOCAL(1,2,1,1) sqrt(2)*Pcyl_LOCAL(1,2,2,2)      ...
        sqrt(2)*Pcyl_LOCAL(1,2,3,3) 2*Pcyl_LOCAL(1,2,2,3)      ...
        2*Pcyl_LOCAL(1,2,1,3)      2*Pcyl_LOCAL(1,2,1,2)];

```

```

%% Sugiyama.m: SCRIPT CONTAINING EXPERIMENTAL DATA AND MODEL VALIDATION
% [Sugiyama et al. (2012), JBMR]

```

```

clc
%% Experimental data of Sugiyama et al. 2012 (JBMR)
% Peak strains & corresponding change in BTV after 16 days

```

```

% E^{peak} [uE]
E = [0 300 700 1100 1400 1800 2200 2600];
% \Delta f_{bm}/f_{bm,ini} [%]
BVTV = [-28.8 -34 -24.8 -5.4 4.8 42.2 30.2 87.2];
% y-points (BVTV[%]) on the linear fit applied to the above data
BVTV_fit = 0.04319*E - 45.61;

%% Model data
% E_model = same as Sugiyama's E (peak strains): E^{peak} [uE]
E_model = [0 300 700 1056.03 1100 1400 1800 2200 2600];
% Change in BVTV with the model after 16 days: \Delta f_{bm}/f_{bm,ini} [%]
BVTV_model = [-46.3716 -32.3014 -14.6874 0 1.7118 13.7201 30.9743...
    49.7802 70.3145];

%% Fits
% Linear fit of Sugiyama's data
[f,gof] = fit(E',BVTV','poly1');
% Linear fit of model data
[f2, gof2] = fit(E_model', BVTV_model','poly1');

%% Plots
% Model vs Sugiyama's experimental data
figure
hold on
grid on
plot(E,BVTV,'x','MarkerSize',18,'LineWidth',2)
plot(f,'b-')
plot(E_model, BVTV_model,'o','MarkerSize',18,'LineWidth',2)
plot(f2,'r-')
line([0,1056.03],[0,0], 'Color','black','LineStyle','--')
line([1056.03,1056.03],[0,-50], 'Color','black','LineStyle','--')
text(100,6,'$\Delta f_{bm}= 0$','FontSize',14,'FontName',...
    'Times New Roman','interpreter','latex')
text(1200,-50,'$\overline{E^{\mathrm{peak}}} = 1056 \mu\epsilon$','...
    'FontSize',14,'FontName','Times New Roman','interpreter','latex',...
    'rotation', 90)
legend('Sugiyama et al. (2012): mouse tibia, axial compression',...
    'Sugiyama et al. (2012): linear fit','Model simulation results',...
    'Model simulation: linear fit')
set(legend,'FontSize',16,'FontName','Times New Roman','Location','NorthWest')
set(legend,'interpreter','latex')
legend boxoff
axis([-50 2800 -50 110]);
ax = gca;
ax.GridLineStyle = ':';
set(gca,'FontSize',22,'FontName','Times')
xlabel('$-E^{\mathrm{peak}}$, [\mu\epsilon]$', 'FontSize',24,'FontName',...
    'Times New Roman','interpreter','latex')
ylabel('$\Delta f_{\mathrm{bm}}/f_{\mathrm{bm,ini}}$, [%]$', 'FontName',...
    'Times New Roman','FontSize',24,'interpreter','latex')

```

Appendix B: Matlab code for deconvolution of nanoindentation results with an evolutionary algorithm

This chapter gives a selection of computer codes written in Matlab programming language, which are related to the developments described in Chapters 3, 4, and 5. The code, initially conceived by Hawraa Kariem, was adapted, modified and improved by Irina Furin, and used by the author of this thesis for obtention of the results presented in Chapter 3.

```
%% Run_all_cdf_ntimes.m: MAIN SCRIPT
% runs the scripts over number of cycles ntimes
tic

clear all;
my_files = {'Sample_all.m'};
ntimes = 10;
n = ntimes;
str_n = num2str(ntimes);

Max_number_of_fits = 7;

% Initialize vectors of parameter results
% E-modulus
e_ntimes = zeros(Max_number_of_fits,n+1);
% Standard deviation
sigma_ntimes = zeros(Max_number_of_fits,n+1);
% R^2/ goodness of fit
r2_ntimes = zeros(Max_number_of_fits,n+1);
% Relative error
rel_err_ntimes = zeros(Max_number_of_fits,n+1);

e_ntimes(:,1) = (1:1:Max_number_of_fits)';
sigma_ntimes(:,1) = (1:1:Max_number_of_fits)';
r2_ntimes(:,1) = (1:1:Max_number_of_fits)';
rel_err_ntimes(:,1) = (1:1:Max_number_of_fits)';
```

```

% Calculate parameters for each cycle
for n = 1:ntimes
n
    str_n1 = num2str(n);
    filename = char(my_files);
    [Results,e] = Sample_all(Max_number_of_fits,n);
    e_ntimes(:,n+1) = Results(:,2);
    sigma_ntimes(:,n+1) = Results(:,3);
    r2_ntimes(:,n+1) = Results(:,4);
    rel_err_ntimes(:,n+1) = Results(:,5);
    min_rel_err = min(rel_err_ntimes(:,n+1))
    % Save workspace for each cycle
    save(['Sample_single_',str_n1,'cycle.mat']);
end

% Calculate means for each parameter
mean_e = mean(e_ntimes(:,2:end),2);
mean_sigma = mean(sigma_ntimes(:,2:end),2);
mean_r2 = mean(r2_ntimes(:,2:end),2);
mean_rel_err = mean(rel_err_ntimes(:,2:end),2);

Results_means=[(1:Max_number_of_fits)',mean_e,mean_sigma,mean_r2,...
                mean_rel_err];

toc



---



%% Sample_all.m
% FUNCTION DETERMINING PARAMETERS FOR A NUMBER OF FITS FROM 1 TO MAX
% NUMBER OF FITS

function[Results,e] = Sample_all(Max_number_of_fits,n)

% Choose data file & extract values for E-moduli from nanoindentation
filename = 'New_Prox_269_AP_P_endosteal.xlsx';
emodulus = xlsread(filename);

% Sort E-moduli
e = sort(emodulus);
e = unique(e);

% Max_number_of_fits=10;
fits_data = struct();

a = 0.001; % initial p (mean and std deviation) scatter ratio
b = 1; % initial weight scatter ratio
Results = zeros(Max_number_of_fits,5);

% Plot original values
Fit_color = [1 .7 1;1 0 1;1 0 0;0 1 1;0 1 0;0 0 1;0 0 0;0.5 0.5 1;...
            0.5 0 0.5;0 0.5 1];
fig = figure;
grid on;

```

```

plot(e);
title('Original E-modulus Data from Indentation Experiments');
xlabel('Number of Indents');
ylabel('E-modulus Values [GPa]');
print(fig, 'Sample_all_E_modulus.tiff', '-dtiff');
close(fig);

% Empirical Cumulative Distribution Function (CDF) of measured E moduli
[f, x_e] = ecdf(e);
f = f';
x_e = x_e';

% Coefficient of determination (R^2)
mean_f = sum(f)/length(f);
sst = sum((f-mean_f).^2);

% Determine parameters for each number of fits with evolutionary algorithm
for fits = 1:Max_number_of_fits

    fits_str = ['fit', num2str(fits)];
    Printfn = ['Sample_all_estimated_pd', fits_str, '.tiff'];

    % Create estimated parent values of mu and sigma of normal...
    % distribution fits - call CreateFit
    [pd_mean, pd_std] = CreateFit(emodulus, Printfn, fits);
    fits_data.(fits_str).p_mean = pd_mean;
    fits_data.(fits_str).p_std = pd_std;
    fits_data.(fits_str).r2 = 0;

    c = a; % initial scatter ratio for mean and std will be adjusted
    d = b; % initial scatter ratio for weight will be adjusted
    k = 1; % break

    % While R^2 < 0.98
    while fits_data.(fits_str).r2 < 0.98

        if fits == 1 && fits_data.(fits_str).r2 > 0.8
            break
        end

        fits_data.(fits_str).w = zeros(1, fits); % weights
        for i=1:fits
            fits_data.(fits_str).w(i) = 1/fits;
        end

        % Apply mutation cycles - call Mutate function
        [ncdf_p, ncdf_p_fits, p_mean, p_std, w, ssr, r2] = ...
        Mutate(fits_data.(fits_str).p_mean, fits_data.(fits_str).p_std, ...
        fits_data.(fits_str).w, e, f, sst, fits, c, d);

        fits_data.(fits_str).ncdf = ncdf_p;
        fits_data.(fits_str).ncdf_fits = ncdf_p_fits;
        fits_data.(fits_str).p_mean = p_mean;
        fits_data.(fits_str).p_std = p_std;
        fits_data.(fits_str).w = w;
        fits_data.(fits_str).ssr = ssr;
    end
end

```

```

fits_data.(fits_str).r2 = r2; % coefficient of determination

c = c*1.2; % scatter ratio for p increases with 20%
k = k+1;
if k > 100
    d = d*1.2; % scatter ratio for weight increases
    if k == 300
        break
    end
end
end

end

% Calculate relative error with integral
E_max = max(e);
E_min = min(e);
Integral_ncdf = trapz(ncdf_p,e);
Integral_ecdf = trapz(f(2:end),e);
fits_data.(fits_str).rel_err = abs(Integral_ncdf-Integral_ecdf)/...
(E_max-E_min)*100;

str_n1 = num2str(n);

% Plot the mutated weighted distributions – call PrintFit
[Fit] = PrintFit(emodulus,fits_data.(fits_str).p_mean,...
    fits_data.(fits_str).p_std,w,Printfn,fits,n);

% Plot the cumulated mutated weighted ncdfs
figure
hold on;
LegHandles = []; LegText = {};
str_i=num2str(fits);
hLine = plot(e,fits_data.(fits_str).ncdf,'LineWidth',3,'Color','Red');
LegHandles(end+1) = hLine;
LegText{end+1} = ['Theoretical: cumulation of ',str_i,' Gaussian CDFs'];

hold all
for i = 1:fits
    hLine = plot(e,fits_data.(fits_str).ncdf_fits(:,i)*...
        fits_data.(fits_str).w(i),'LineWidth',1,'Color',Fit_color(i,:));
    LegHandles(end+1) = hLine;
    str_i = num2str(i);
    LegText{end+1} = ['Theoretical: Gaussian CDF of Fit',str_i];
    hold on
end

hLine = plot(x_e,f,'MarkerEdgeColor','b','MarkerFaceColor','b',...
    'MarkerSize',10);
LegHandles(end+1) = hLine;
LegText{end+1} = 'Experimental Data';

hold off
set(gca,'XTick')
hLegend = legend(LegHandles,LegText,'Orientation','vertical',...
    'Location','NorthWest');
set(gca,'XTickLabel')

```

```

title(['ECDF & NCDF, Empirical and Normal Cumulative Distribution'...
      'Functions of all Samples']);
xlabel('Elastic modulus E [GPa]');
ylabel('Cumulative distribution function');
grid on;
Printfn=['Sample_all_ecdf_',str_n1,fits_str];
print(Printfn, '-dtiff');
savefig(Printfn)

close(figure);

% Save results for each number of fits
Results(fits,:) = [fits,max(fits_data.(fits_str).p_mean),...
                  max(fits_data.(fits_str).p_std),fits_data.(fits_str).r2,...
                  fits_data.(fits_str).rel_err];

end

end

```

```

%% CreateFit.m
% FUNCTION CREATING ESTIMATED PARENTS VALUES OF MU AND SIGMA OF NORMAL
% ...DISTRIBUTION
% called in Sample_all.m

function [pd_mean,pd_std] = CreateFit(emodulus,Printfn,fits)

% Sort E-moduli
e = sort(emodulus);
e = e(:);
fits_str = num2str(fits);
mfd = 6; % minimum number of fitted data
w = zeros(fits); % weights
for i = 1:fits
    w(i) = 1/fits;
end

% Create estimated exclusion limits: the values where the fitted data is
% divided, where the new curve begins
e_min = min(e);
e_max = max(e);
place_e_min = find(e==e_min);
place_e_max = find(e==e_max);

% 1. Exclude the first smallest measured values, which have a difference...
% greater than the interval of the fits, as they obviously represent a...
% measurement error

for i = 2:length(e)
    if e(i)-e(i-1) > (e_max-e_min)/fits
        place_e_min = i;
        e_min = e(place_e_min);
    end
end

```

```

end

% 2. Calculate the exclusion limits of the fitted intervals
if fits == 1
    ex = 1;
else
    ex = zeros(fits-1,1);
end

for i = 1:(fits-1)
    ex(i) = (e_max-e_min)*i/fits+e_min;
end

% Check if Fit is possible on the interval: number of minimum fitted
% data is reached. If not, the limits are moved
interval = zeros(fits,1);

for i = 1:fits
    if i == 1
        interval(i)=length(e(e >= e_min & e < ex(i)));
    elseif i == fits
        interval(i)=length(e(e > ex(i-1) & e <= e_max));
        ex(i) = e_max;
    else
        interval(i) = length(e(e > ex(i-1) & e < ex(i)));
    end
end

if fits > 1

    for i = 1:fits
        k = 1;

        while interval(i) < mfd
            lim_int_up = place_e_min-1;
            lim_int_low = place_e_min;

            for j = 1:i
                lim_int_up = lim_int_up+interval(j);
                if j == i
                    break
                end
                lim_int_low = lim_int_low+interval(j);
            end

            if i == 1
                ex(i) = e(lim_int_up+1);
                interval(i) = interval(i)+1;
                interval(i+1) = interval(i+1)-1;
            end

            if i == fits
                ex(i-1) = e(lim_int_low-1);
                interval(i) = interval(i)+1;
                interval(i-1) = interval(i-1)-1;
            end
        end
    end
end

```

```

        if i < fits
            ex(i) = e(lim_int_up+1);
            interval(i) = interval(i)+1;
            interval(i+1) = interval(i+1)-1;
        end

        k = k+1;
        if k == 100
            break
        end
    end
end

% Create fit
pd_mean = zeros(1,fits);
pd_std = zeros(1,fits);

if fits == 1
    pd1 = fitdist(e, 'normal');
    pd_mean(i)=mean(pd1);
    pd_std(i)=std(pd1);
else
    for i = 1:fits

        if i == 1
            Excluded = (e > e_min & e < ex(i));
        elseif i == fits
            Excluded = (e > ex(i-1) & e < e_max);
        else
            Excluded = (e > ex(i-1) & e < ex(i));
        end

        Data = e(Excluded);
        pd1 = fitdist(Data, 'normal');
        pd_mean(i) = mean(pd1);
        pd_std(i) = std(pd1);

    end
end

%% Mutate.m
% FUNCTION PERFORMING MUTATION CYCLES
% called in Sample_all.m

function[ncdf_p,ncdf_p_fits,p_mean,p_std,w,ssr,r2] = ...
    Mutate(p_mean,p_std,w,e,f,sst,fits,c,d)

p_mean_mut=zeros(1,fits);
p_std_mut=zeros(1,fits);

```

```

w_mut=zeros(1,fits);

% z,z_std,z_w: random parameters for max. 5000 mutations
z = normrnd(0,1,fits,5000);
z_std = normrnd(0,1,fits,5000);
z_w = rand(fits,5000);
s_mean = (rand(1,fits))*c; % scattering for mean with ratio (c,d): weight...
% scatter to mean and std scatter
s_std = (rand(1,fits))*c; % scattering for std
s_w = (rand(1,fits))*d; % scattering for w

h = 0.85; % stepsize
k = 0; % counter
t = 0; % counter w_mut
tol = 0.00009; %tolerance
pm = ones(1,5000);
RR = ones(1,5000);

for i=1:size(z,2)

    % Mutation sequence

    % Mutation mean values & standard deviation = ...
    % parent value+scatter*random
    for j = 1:size(z,1)
        p_mean_mut(j) = p_mean(j)+(s_mean(j)*z(j,i)) ;
        p_std_mut(j) = p_std(j)+(s_std(j)*z_std(j,i));
    end

    % Mutation of weighting factor
    for j = 1:size(z_w,1)
        w_mut(j) = w(j)+(s_w(j)*z_w(j,i));
    end

    while (sum(w_mut)~=1) % sum of w must be 1!!
        w_mut = w_mut/sum(w_mut);
        t = t+1;
        if (t > 1000)
            break;
        end
    end

    ncdf_p_fits = zeros(size(e,1),fits);
    ncdf_p_mut_fits = zeros(size(e,1),fits);
    ncdf_p = zeros(size(e,1),1);
    ncdf_pmut = zeros(size(e,1),1);
    ncdf_wmut = zeros(size(e,1),1);
    ncdf_pmut_wmut = zeros(size(e,1),1);

    for j=1:fits
        % ncdf curves for all the fits
        ncdf_p_fits(:,j) = normcdf(e,p_mean(j),p_std(j));
        % Mutated ncdf curves for all the fits
        ncdf_p_mut_fits(:,j) = normcdf(e,p_mean_mut(j),p_std_mut(j));
        % 1. Original distribution & original weighting
        ncdf_p = ncdf_p+ncdf_p_fits(:,j)*w(j);
    end
end

```

```

    % 2. Calculating offspring with original distribution &...
    % mutated weighting
    ncdf_wmut = ncdf_wmut+ncdf_p_fits(:,j)*w_mut(j);
    % 3. Mutated distribution & original weighting
    ncdf_pmut = ncdf_pmut+ncdf_p_mut_fits(:,j)*w(j);
    % 4. Calculate offspring with mutated distribution &...
    % mutated weighting
    ncdf_pmut_wmut = ncdf_pmut_wmut+ncdf_p_mut_fits(:,j)*w_mut(j);
end

% Calculate error for all combinations
e_ncdf_p = zeros(length(e));
e_ncdf_wmut = zeros(length(e));
e_ncdf_pmut = zeros(length(e));
e_ncdf_pmut_wmut = zeros(length(e));

for j=1:length(e)
    e_ncdf_p(j) = (ncdf_p(j)-f(j+1))^2;
    e_ncdf_wmut(j) = (ncdf_wmut(j)-f(j+1))^2;
    e_ncdf_pmut(j) = (ncdf_pmut(j)-f(j+1))^2;
    e_ncdf_pmut_wmut(j) = (ncdf_pmut_wmut(j)-f(j+1))^2;
end

error_ncdf_p = sum(e_ncdf_p(:));
error_ncdf_wmut = sum(e_ncdf_wmut(:));
error_ncdf_pmut = sum(e_ncdf_pmut(:));
error_ncdf_pmut_wmut = sum(e_ncdf_pmut_wmut(:));
err=[error_ncdf_p error_ncdf_wmut error_ncdf_pmut error_ncdf_pmut_wmut];

% Find minimum error to decide parents for next generation
if (min(err) == err(2)) % p original w mutated
    w = w_mut;
    k = k+1;
end

if (min(err) == err(3)) % p mutated w original
    p_mean = p_mean_mut;
    p_std=p_std_mut;
    k=k+1;
end

if (min(err) == err(4)) % p mutated w mutated
    p_mean = p_mean_mut;
    p_std = p_std_mut;
    w = w_mut;
    k = k+1;
end

ifp = fits*3-1; % number of independently fitted paramters

if (mod((i/ifp),10) == 0)
    if (k < (ifp*2)) % 1/5 success rule
        s_mean = s_mean/h; % adopt step size
        s_std = s_std/h; % adopt step size
        s_w = s_w/h;
    end
end

```

```

        if (k > (ifp*2))
            s_mean = s_mean*h;
            s_std = s_std*h; % adopt step size
            s_w = s_w*h;
        end
    end

    if (mod((i/ifp),10) == 0)
        k = 0; % reset counter
    end

    % If parameters are within the tolerance in the 1000 cycles
    ncdf_p = zeros(size(e,1),1);
    ncdf_p_fits = zeros(size(e,1),fits);

    for j=1:fits
        ncdf_p_fits(:,j) = normcdf(e,p_mean(j),p_std(j));
        ncdf_p = ncdf_p+ncdf_p_fits(:,j)*w(j);
    end

    % R^2
    ssr = sum((f(2:end)-ncdf_p').^2);
    r2 = 1-(ssr/sst);
    pm(i) = r2;

    % Relative error within the mutation cycle
    E_max = max(e);
    E_min = min(e);
    Integral_ncdf = trapz(ncdf_p,e);
    Integral_ecdf = trapz(f(2:end),e);
    rel_err(i) = abs(Integral_ncdf-Integral_ecdf)/(E_max-E_min)*100;

    if (i > 1000)
        con = abs(pm(i)-(mean(pm(i-1000):pm(i))));
        if con < tol
            break;
        end
    end
end

```

end

```

%% PrintFit.m: FUNCTION CREATING PLOTS OF FITS
% called in Sample_all.m

```

```

function [Fit]=PrintFit(emodulus,p_mean,p_std,w,Printfn,fits,n)

```

```

figfunc=figure;
emodulus = emodulus(:);

```

```

% Prepare figure
clf;
hold on;
LegHandles = []; LegText = {};

```

```

% Plot data originally in dataset "emodulus data"
[CdfF,CdfX] = ecdf(emodulus,'Function','cdf'); % compute empirical cdf
BinInfo.rule = 3; % number of bins given
BinInfo.nbins = 50;
[~,BinEdge] = internal.stats.histbins(emodulus,[],[],BinInfo,CdfF,CdfX);
[BinHeight,BinCenter] = ecdfhist(CdfF,CdfX,'edges',BinEdge);
hLine = bar(BinCenter,BinHeight,'hist');
set(hLine,'FaceColor',[.8 .8 .8],'EdgeColor','black',...
      'LineStyle','-','LineWidth',1);
xlabel('Elastic Modulus E [GPa]');
ylabel('Density')
LegHandles(end+1) = hLine;
LegText{end+1} = 'Empirical Cumulative Distribution Histogram';

% Create grid where function will be computed
XLim = get(gca,'XLim');
XLim = XLim+[-1 1]*0.01*diff(XLim);
XGrid = linspace(0,XLim(2),100);

% Create fit
SumFit = 0;

for i = 1:fits
    fits_str = num2str(i);
    Fit = ProbDistUnivParam('normal',[ p_mean(i), p_std(i)]);
    YPlot = pdf(Fit,XGrid)*w(i);

    if i == fits
        hLine = plot(XGrid,YPlot,'Color','red','LineStyle','-','...
            'LineWidth',3,'Marker','none','MarkerSize',6);
        LegHandles(end+1) = hLine;
        LegText{end+1} = ['Theoretical distribution number ',fits_str,...
            ' - intact phase'];
    else
        hLine_blue = plot(XGrid,YPlot,'--rs','Color','blue','LineWidth',1,...
            'Marker','none','MarkerSize',6);
    end

    SumFit=SumFit+YPlot;

end

if i~=1
    LegHandles(end+1) = hLine_blue;
    LegText{end+1} = ...
        'Theoretical distributions - damaged material phases';
end

hLine = plot(XGrid,SumFit,'Color','k','LineStyle','-','LineWidth',1,...
    'Marker','none','MarkerSize',6);
LegHandles(end+1) = hLine;
LegText{end+1} = ['Sum of ',fits_str,' theoretical distributions'];

% Adjust figure
grid on;

```

```
box on;
hold off;

% Create legend from accumulated handles and labels
hLegend = legend(LegHandles,LegText,'Orientation','vertical','Location',...
    'NorthWest');
set(hLegend,'Interpreter','none');
fits_str = ['fit',num2str(fits)];
str_n1 = num2str(n);
Printfn = ['Sample_all_fitted_pd_',str_n1,fits_str];
print(figfunc,'-dtiff',Printfn);
savefig(Printfn)

close(figfunc);
```

Curriculum Vitae

Personal Data

Name	Maria-Ioana Pastrama
Address	Neubaugasse 5/18H, 1070 Vienna, Austria
Phone number	+43 680 23 55 017
E-Mail address	maria-ioana.pastrama@tuwien.ac.at
Birth date (city, country)	February 24, 1988 (Bucharest, Romania)

Work experience

April 2013 – present	Project assistant , <i>Institute for Mechanics of Materials and Structures, Vienna University of Technology, Austria</i> ; Research work and dissemination thereof by conference participation and scientific publishing Teaching activities: Exercise on Multiscale Material Modeling, 2.0 semester hours, 2 ECTS (Summer Semester 2015 & 2016, ATHENS programme) Supervision activities: two master's students and their theses Committee membership: Study commission Biomedical Engineering; Civil Engineering Faculty Council (Fakultätsrat Bauingenieurwesen)
September 2009 – September 2010	Sales assistant , <i>Byblos S.A.</i> , Bucharest, Romania; Type of business: import of books in foreign languages

Education

April 2013 – present	PhD studies , <i>Institute for Mechanics of Materials and Structures, Vienna University of Technology, Austria</i> Topic: Multiscale biomechanics and mechanobiology for orthopaedics and bone regenerative medicine
----------------------	--

- 2010 – 2013 **Master’s studies in Biomedical Engineering** (Dipl.-Ing.), specialization Biomechanics and Biomaterials, *Vienna University of Technology*, Austria (graduated with highest honors)
Title of thesis: *Computer Tomography of aluminum oxide parts fabricated by Additive Manufacturing Technology*
- 2006 – 2010 **Bachelor’s studies in Industrial Engineering** (BSc), *Faculty for Engineering in Foreign Languages (German)*, *Politehnica University of Bucharest*, Romania
- 2002 – 2006 **Highschool degree**, *Colegiul National Bilingv “George Cosbuc”* (bilingual: Romanian-English), Bucharest, Romania

Conference Presentations and Posters

- July 24 – 29, 2016 M.-I. Pastrama, S. Scheiner, P. Pivonka, C. Hellmich: *Mechanosensing in the different pore spaces of bone: Arguments from a multiscale bone remodeling model, coupled with multiscale poromicromechanics* (oral presentation)
12th World Congress on Computational Mechanics, Seoul, South Korea
- November 9 – 11, 2015 M.-I. Pastrama, S. Scheiner, P. Pivonka, C. Hellmich: *Updates on: A multiscale systems biology approach for computer simulation-based prediction of bone remodeling* (oral presentation)
20th Inter-Institute Seminar for Young Researchers, Cracow, Poland
- September 14 – 16, 2015 M.-I. Pastrama, S. Scheiner, P. Pivonka, C. Hellmich: *Updates on: A multiscale systems biology approach for computer simulation-based prediction of bone remodeling* (oral presentation)
6th International Conference on Computational Bioengineering, Barcelona, Spain

- June 09 – 10, 2015 M.-I. Pastrama, S. Scheiner, P. Pivonka, C. Hellmich: *Updates on: A multiscale systems biology approach for computer simulation-based prediction of bone remodeling* (oral presentation)
1st Vienna Young Scientist Symposium, Vienna, Austria
- May 06 – 08, 2015 M.-I. Pastrama, S. Scheiner, P. Pivonka, C. Hellmich: *A multiscale systems biology approach for computer simulation-based prediction of bone remodeling* (poster presentation)
9th Conference of the German Society of Biomechanics, Bonn, Germany
- September 24 – 27, 2014 H. Kariem, M.-I. Pastrama, S. Roohani-Esfahani, P. Pivonka, H. Zreiqat, C. Hellmich: *Micro-elasticity of porous ceramic baghdadite: A combined acoustic-nanoindentation approach supported by homogenization theory* (poster presentation)
31st Danubia-Adria Symposium on Advances in Experimental Mechanics, Kempten, Germany

Publications in peer-reviewed journals

- 2016 I. Furin, M.-I. Pastrama, H. Kariem, K.W. Luczynski, O. Lahayne, C. Hellmich. *A new nanoindentation protocol for identifying the elasticity of undamaged extracellular bone tissue*. MRS Advances, 1(11): 693–704
- 2015 H. Kariem, M.-I. Pastrama, S. Roohani-Esfahani, P. Pivonka, H. Zreiqat, C. Hellmich: *Micro-poro-elasticity of baghdadite-based bone tissue engineering scaffolds: A unifying approach based on ultrasonics, nanoindentation, and homogenization theory*. Materials Science and Engineering C, 46: 553–564
- 2014 W. Li, M.-I. Pastrama, Y. Ding, K. Zheng, C. Hellmich, A.R. Boccaccini: *Ultrasonic elasticity determination of 45S5 Bioglass[®]-based scaffolds: Influence of polymer coating and crosslinking treatment*. Journal of the Mechanical Behavior of Biomedical Materials, 40: 85–94

Publications submitted to or in preparation for peer-reviewed journals

- 2016 M.-I. Pastrama, S. Scheiner, P. Pivonka, C. Hellmich: *Multiscale systems biology of bone, accounting for pore space-specific mechanosensation. In preparation for submission to Bone*
- 2016 M.-I. Pastrama, R. Blanchard, D. Thomas, J. Clement, P. Pivonka, C. Hellmich: *Spatial variation of longitudinal and transverse elastic properties in mid femur cortical cross sections, as assessed by statistical nanoindentation. In preparation for submission to Journal of Bone and Mineral Research*

International exchange

- February 2016 **Guest researcher**, *St. Vincent's Department of Surgery, The University of Melbourne, Australia* (grant for short research stays abroad from Vienna University of Technology)
Topic: modeling of bone remodeling and direction-dependent nanoindentation of bone
- December 2012 – January 2013 **Guest researcher**, *Institute of Biomaterials, Department of Materials Science and Engineering, University of Erlangen-Nuremberg, Germany* (grant for short research stays abroad from Vienna University of Technology)
Topic: Bioglass[®] scaffolds for bone regeneration
- October 2008 – June 2009 **Erasmus exchange student**, *Vienna University of Technology, Austria*
- July – September 2007 **Intern, Leonardo DaVinci exchange program**, *Panalpina GmbH, Vienna, Austria*; Type of business: Import-Export

Other international experience

- November 2015 **ATHENS course**, *KU Leuven, Belgium*: “Small scale modeling techniques for materials” (participant)
- April 2014 **Training School COST Action NAMABIO MP1005** – 3rd course, *Zagreb, Croatia* (participant)

- November 2011 **ATHENS course**, *TU Delft*, The Netherlands: “Virtual models in engineering – Introduction to Finite Elements” (participant)
- July 2011 **BEST course**, *Technical University of Patras*, Greece: “Re-create engineering: Think out of the box!” (participant)
- July 2009 **BEST course**, *University of Coimbra*, Portugal: “iHealth: Be aware of the upcoming technologies in medicine!” (participant and co-organizer)
- April 2009 **BEST course**, *Grenoble Institute for Technology*, France: “Nano med, giga progress...Be nursed from inside” (participant)
- July 2008 **BEST course**, *TU Eindhoven*, The Netherlands: “Small things amuse big minds” (participant)

Awards

- July 2016 **Travel Award**, 12th World Congress on Computational Mechanics, July 24–29, Seoul, South Korea
- September 2014 **Prize for the best student poster**, 31st Danubia-Adria Symposium on Advances in Experimental Mechanics, September 24–27, Kempten, Germany
- 2006 – 2010 **Scholarship for excellent academic results**, Politehnica University of Bucharest, Romania
- March 2005 4th place in the **national English contest** (category: 11th & 12th grade), Bacau, Romania

Computer skills

- | | |
|------------------|---|
| Programming | Matlab |
| Finite Elements | ANSYS |
| CAD | CATIA, ADAMS |
| Image processing | ImageJ |
| Other | LaTeX; Adobe Illustrator; software for process simulation: Visio, Arena |

Language skills

- | | |
|-----------------|---------------|
| Romanian | mother tongue |
|-----------------|---------------|

English	proficient CAE (Cambridge Advanced English) certificate (Grade: A) IELTS (International English Language Testing System) certificate (Grade: 8.5/9)
German	proficient
French	intermediary level
Spanish	beginner
Italian	beginner

Extracurricular activities

Since July 2013	International Soft Skills Trainer for BEST (Board of European Students of Technology)
September 2012 – August 2013	BEST Vienna: Vice-President for Human Resources in the 11 th local board
July 2012	BEST Vienna: Main Organizer of the course "SecurITy Guide to the Galaxy", <i>Vienna University of Technology</i> , Austria
2007 – 2008	Senior Editor for the student newspaper Info@Poli, <i>Politehnica University of Bucharest</i> , Romania